Damage to and Copper Migration into Low-k Organosilicate Dielectrics from Vacuum-Ultraviolet Irradiation

by

Xiangyu Guo

A dissertation submitted in partial fulfillment of the requirements for the degree of

Doctor of Philosophy

(Electrical Engineering)

at the

UNIVERSITY OF WISCONSIN-MADISON

2016

Date of final oral examination: 08/30/2016

The dissertation is approved by the following members of the Final Oral Committee:

J. Leon Shohet, Professor, Electrical and Computer Engineering

Zhenqiang Ma, Professor, Electrical and Computer Engineering

Hongrui Jiang, Professor, Electrical and Computer Engineering

Mikhail Kats, Assistant Professor, Electrical and Computer Engineering

Xudong Wang, Associate Professor, Materials Science and Engineering

Damage to and Copper Migration into Low-k Organosilicate Dielectrics from Vacuum-Ultraviolet Irradiation

Under the supervision of Professor J. Leon Shohet

at the University of Wisconsin-Madison

Abstract

To extend Moore's law as far as possible, backend-of-the-line (BEOL) dielectrics, both intermetal and interlevel, with low dielectric constants (i.e. low-k) are needed to improve the performance of nano-electronic metal-interconnect structures in current and future integrated circuit. However, the reliability and yield issues associated with integration and implementation of such low-k dielectric materials are more challenging than expected. In this work, under the hypothesis that Cu migration into and breakdown of the organosilicate-based low-k dielectrics (a-SiOC:H) can be exacerbated by vacuum ultraviolet (VUV) irradiation, we characterize the VUV-induced damage to and Cu migration into a-SiOC:H low-k thin films. A state-of-the-art dense low-k a-SiOC:H dielectric thin film, which has being considered to be the next generation low-k capping layer dielectrics, was utilized in this work.

Using a synchrotron radiation system as a monochromatic VUV source, VUV-induced modifications to a-SiOC:H were examined mechanically, electrically and chemically. To examine the roles of VUV photons on the Cu migration into and related time-dependent breakdown of low-k a-SiOC:H dielectrics, XPS depth profiles were measured on both pristine and VUV-exposed dense a-SiOC:H/Cu film stacks under various bias-temperature stress (BTS) conditions. We found that Cu migration in VUV-exposed a-SiOC:H dielectrics depends on the VUV photon energy. A threshold photon energy of 8.3 eV was found by measuring the Cu migration as a function of photon energy. Above this value, VUV irradiation will cause the Cu to be oxidized. In the presence of an electric field, Cu ions drift into a-SiOC:H and deteriorate the time-dependent dielectric breakdown (TDDB). Finally, a combined band alignment and defect energy-level diagrams are presented, so as to illustrate the barrier potential at the Cu/a-SiOC:H interface, alignments of the valence and conduction bands in the dielectric and the energy levels of processing-induced defect states. This allows many reported electrical-leakage mechanisms and reliability issues in low-k dielectrics and integrated low-k/Cu interconnects to be determined in greater detail.

Acknowledgements

I have had the honor of working with many great people during my studies at the University of Wisconsin-Madison in the past five years. I would like to express my gratitude to all of them. Without their help, I would not be able to accomplish this thesis.

A very devoted and deepest thank you goes to my research advisor, Prof. J. Leon Shohet, who provided me with tremendous instruction and great help toward the fulfillment of my Ph.D degree. He helped me consistently and constructively since the days I began working in the field of plasma processing. I appreciate all his contributions of time, ideas, and support to make my Ph.D. experience productive and stimulating. I learnt a lot from him not only the research work but also enthusiastic attitude toward life, which will always inspire me for greater achievement.

I would like to thank the other members of my committee: Professor Zhenqiang Ma, Professor Hongrui Jiang, Professor Xudong Wang and Professor Mikhail Kats. I am grateful to Professor Yoshio Nishi of Stanford University for his knowledge and assistance for this work. I must thank Dr. Sean W. King at Intel for advice and for providing the state-of-the-art low-k samples. Special thanks go to Dr. Joseph E. Jakes at USDA Forest Service Forest Products Laboratory for his great help on measuring the mechanical properties of the low-k samples using nanoindentation. Thanks to Semiconductor Research Corporation and the National Science Foundation for their finical support on this research work.

I would also like to thank the researchers and staff at the UW-Madison Synchrotron Radiation Center, National Synchrotron Radiation Research Center (NSRRC), Materials

Science Center, and at the Wisconsin Center for Applied Microelectronics for their support. Many thanks go to my colleagues in the Plasma Processing & Technology Laboratory, Mike, Huifeng, Weiyi, Dongfei, Josh, Faraz, Panpan, Sang-Heum, Yu, Dan, Patrick and also Dr. Ha Nguyen.

Finally I would like to express my love and gratitude to my family. Heartfelt gratitude goes to my parents for their patience, understanding, and encouragement through my entire life. In particular, I must acknowledge my wife and best friend, Jun, who has seen, more than anyone, the emotional and intellectual ups and downs that this thesis has put me through. She has been a great source of strength all through this work, without whose love and encouragement I would not have finished this thesis. Unique thank you goes to Ethan, for the cute smile and the happiness brought to us.

Table of Contents

Chapter I Introduction ... 1
1.1 Low-k Dielectric Materials ... 4
1.1.1 Low-k Interlayer Dielectrics ... 9
1.1.2 Low-k Capping Layer Dielectrics ... 13
1.1.3 Low-k Etch-stop Dielectrics ... 14
1.2 Cu Metallization ... 16
1.3 Goal of the Work ... 20
1.4 Outline of Thesis ... 22
1.5 References ... 25

Chapter II Background ... 34
2.1 Plasma-Induced Damage to Cu/Low-k Interconnects ... 35
2.1.1. Chemical Damage ... 35
2.1.2. Mechanical Damage ... 43
2.1.3. Electrical Damage ... 44
2.2 Plasma Vacuum-Ultraviolet Photon Irradiation ... 48
2.3 Electrical-Conduction Mechanisms in Cu/Low-k Interconnects ... 53
2.4 Time-dependent Breakdown of Cu/Low-k Interconnects ... 55
2.4.1. Intrinsic TDDB in Low-k Organosilicates ... 56
2.4.2. Extrinsic TDDB in Low-k: Effects of Cu Migration ... 63
2.5 Summary ... 68
2.6 References ... 69

Chapter III Experimental Apparatus and Materials Diagnostics ... 84
3.1 Synchrotron VUV-Photon Source ... 85
3.2 Electron-Cyclotron-Resonance Plasma Reactor ... 90
3.3 Nanoindentation Measurements ... 93
3.4 X-ray Photoelectron Spectroscopy ... 99
3.4.1 Core-level X-ray Photoelectron Spectroscopy ... 101
3.4.2 Valence-band X-ray Photoelectron Spectroscopy ... 103
3.4.3 XPS Depth Profile ... 105
3.5 Fourier-Transform Infrared Spectroscopy ... 107
3.6 Electrical Characterization ... 111
3.7 References ... 114

Chapter IV VUV-induced Damage to Low-k Organosilicates ... 122
4.1 VUV-induced Mechanical Modifications ... 123
4.1.1 Mechanical-Property Changes Produced by VUV Irradiation ... 124
4.1.2 Chemical Analysis of Damage Mechanisms ... 126
4.1.3 Comparison with Ar Plasma Exposed a-SiOC:H ... 133
4.2 VUV-induced Leakage Currents ... 138
4.3 VUV-induced Moisture Uptake ... 141

4.4 Summary 145
4.5 References 147

Chapter V VUV-induced Cu Migration into a-SiOC:H and Time-Dependent Breakdown of Cu/Low-k Interconnects 154
5.1 Dense a-SiOC:H as a Low-k Capping Layer 155
5.2 Cu Migration into a-SiOC:H from VUV Irradiation 158
5.2.1 Cu Migration Rate in Pristine and VUV-exposed a-SiOC:H 159
5.2.2 VUV-induced Cu Oxidation and Mechanism Discussion 162
5.2.3 Effects of Photon Energy on Cu Migration Rate in a-SiOC:H 165
5.3 TDDB of Cu/Low-k Dielectric Interconnects 168
5.3.1 Intrinsic TDDB of Low-k a-SiOC:H Dielectrics 171
5.3.2 Extrinsic TDDB of Cu/Low-k a-SiOC:H Interconnects 174
5.4 TDDB for Cu/Low-k Interconnects from VUV Irradiation 177
5.5 Summary 180
5.6 References 181

Chapter VI Band Alignment for Cu/Low-k Dielectric Interconnects 188
6.1 Measurement of the Schottky Barrier Potential at the Cu/a-SiOC:H Interface 189
6.2 Defect-induced Bandgap Narrowing of Low-k Organosilicates 197
6.2.1 Bandgap Narrowing in Low-k a-SiOC:H Thin Films 200
6.2.2 Uplifting of the Valence Band Edge in a-SiOC:H 203
6.2.3 Defects in a-SiOC:H as Measured with Electron-Spin Resonance 205
6.3 Band Diagram for Cu/Low-k a-SiOC:H Interconnects 208
6.4 Summary 213
6.5 References 215

Chapter VII Conclusions and Future Directions 223
7.1 Summary of Results 223
7.1.1 VUV-induced Mechanical Modifications to a-SiOC:H 223
7.1.2 VUV-induced Moisture Uptake to a-SiOC:H 225
7.1.3 VUV-induced Exacerbation of Cu Migration into a-SiOC:H 226
7.1.4 VUV-induced Deterioration of Extrinsic TDDB of Cu/a-SiOC:H 227
7.1.5 Measurements of Schottky Barrier at Cu/a-SiOC:H Interface 228
7.1.6 Band Diagram for Cu/low-k Damascene Interconnects 229
7.2 Suggestions for Future Work 230
7.2.1 Temperature Dependence of VUV-induced Damages 231
7.2.2 Depth Profile of VUV-induced Damage in a-SiOC:H 231
7.2.3 Moisture-assisted TDDB of Cu/low-k Interconnects 232
7.2.4 Alternative Methods to Mitigate VUV-induced Damage 233
7.3 References 235

Chapter I

Introduction

In this work, under the hypothesis that Cu migration into and breakdown of organosilicate-based low-k dielectrics (a-SiOC:H) is exacerbated by vacuum-ultraviolet (VUV) irradiation, this work will concentrate on the effects of VUV irradiation on Cu migration, charge transport and breakdown behaviors in Cu/a-SiOC:H interconnects. Traditional Cu/low-k interconnects use metallic barriers (such as Ta, TaN) and dielectric capping layers (such as a-SiC_xN_y:H) to reduce Cu migration into the dielectric,[1],[2] and to prevent electrical leakage between adjacent metal lines.[3] While as the aggressive shrinking of via and trench sizes continues, the reliability and yield issues associated with integration and implementation of such Cu/low-k dielectric interconnects are becoming more challenging than expected.[4],[5] This is because (1) continuous technology scaling requires thinner and thinner barrier layers, which have to be smaller than 1.0 or even 0.5 nm,[6] and may eventually make the barrier layers so thin that the Cu lines are in

effectivelyu in direct contact with the low-k dielectric;[7] (2) as technology continues to downscale, the relative contribution of the capping layer k-value to the interlayer capacitance is growing and there is a critical requirement for alternative materials with lower dielectric constants, since the currently used capping layer materials (a-SiC_xN_y:H) currently have the highest k-values in conventional Cu interconnect structures.[8] For example, SiN has a k-value over 6.0, [9] and SiC and SiCN both have k-values between 4.0 and 5.0. [10],[11] In either scenario as described above, the low-k dielectric material will be in contact with the Cu wires directly.[8],[9] One must therefore fully examine the electrical properties of the Cu/low-k interconnect even without the a-SiC_xN_y:H capping layer.

A state-of-the-art dense nonporous low-k a-SiOC:H dielectric thin film, with a density of 1.5 g/cm^3 and a k-value of 3.2, will be used to examine the roles of VUV photons on the Cu migration into and related time-dependent breakdown of low-k a-SiOC:H dielectrics. These dense nonporous low-k a-SiOC:H is considered to be the next generation low-k capping layer dielectric in the 7 nm or beyond technology node, to replace the a-SiC_xN_y:H capping layer, as shown in the following **Figure 1-1**.

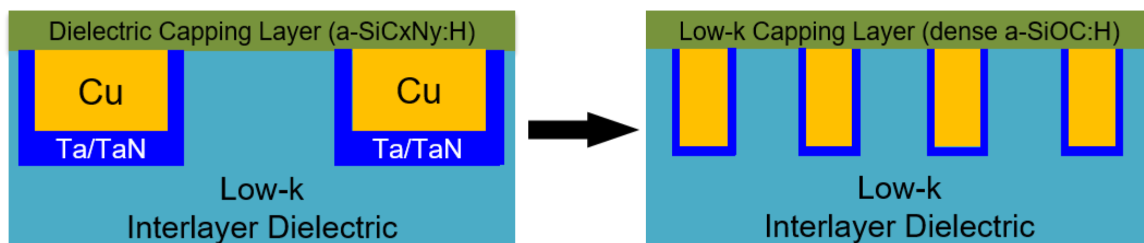

Figure 1-1 Drawing of the traditional capping layer (a-SiC_xN_y:H) configuration and the low-k capping layer (dense a-SiOC:H) configuration.

Since the capping layer dielectric materials have to be in contact with Cu directly, it requires that the dense low-k a-SiOC:H thin films have a good resistivity to Cu migration. **Figure 1-2** shows the concentration of Cu inside of an a-SiOC:H thin film (35% porosity, k = 2.2) measured with an XPS depth profile on a film stack of (a) porous a-SiOC:H(100 nm)/ a-SiCN:H(4 nm)/Cu (b) porous a-SiOC:H(100 nm)/dense a-SiOC:H(4 nm)/Cu after annealing at a temperature of 225°C for 24 hours. It shows that the dense a-SiOC:H exhibit a similar resistance to Cu migration as does a-SiCN. However, after a long-time temperature stress (225°C for 24 hours), Cu can still penetrate through the capping layer (either a-SiCN or dense a-SiOC:H) enter into the bulk of the porous low-k a-SiOC:H. As a result, it is critical to characterize the behavior of Cu migration into low-k a-SiOC:H thin films and determine the effect of VUV photon irradiation on this process.

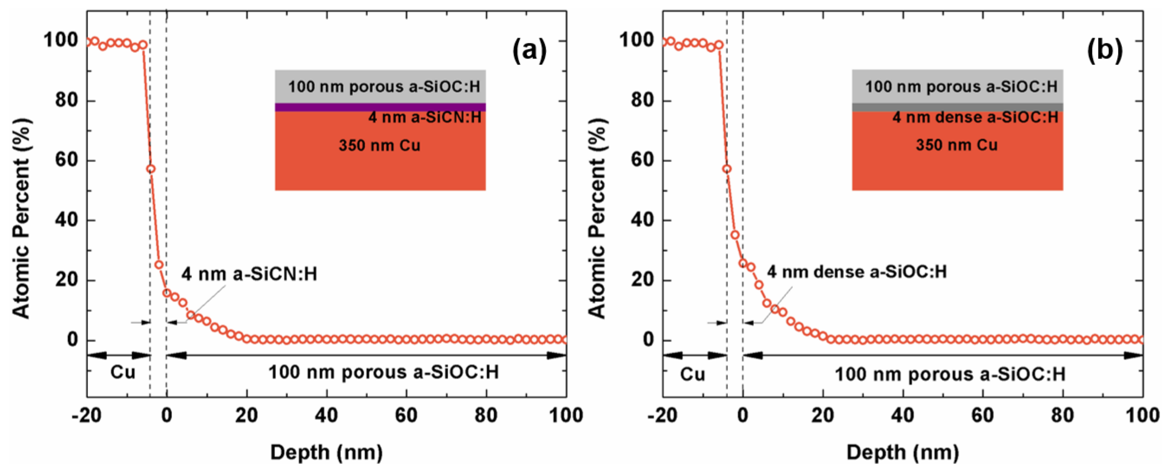

Figure 1-2 XPS depth profile on film stack of (a) porous a-SiOC:H(100 nm)/ a-SiCN:H(4 nm)/Cu (b) porous a-SiOC:H(100 nm)/dense a-SiOC:H(4 nm)/Cu after annealing at a temperature of 225°C for 24 hours. The porous low-k a-SiOC:H thin film has a k value of 2.2 and a porosity of 35%.

To make it clear, it would benefit to mention that Cu migration should include both diffusion of Cu atoms, which originates from density gradients, and drift of Cu ions, which, because of the electro-positivity of Cu ions, will take place in the presence of an electric field.

1.1 Low-k Dielectric Materials

Over the past few decades, performance of microelectronic integrated circuits (ICs), for the most part, has been improved by increasing transistor speed, reducing transistor size, and packing more transistors onto a single chip. While the feature size of ICs has decreased into the nanometer range, the limiting factor has now shifted from the traditional front-end attributes of gate length and gate thickness, to back-end interconnect properties such as the conductivity of the metal lines, parasitic capacitances of the back-end interlayer dielectrics (ILD), and the compatibility of these materials.

Increased resistance-capacitance (RC) delay, brought about by continuous transistor dimensional scaling, can severely limit the operating speed and overall performance of the integrated system. As can be observed in **Figure 1-3**, when the device feature size scales down to 250 nm, the interconnect delay is comparable to the gate delay and contributes increasingly larger portions of the total signal propagation delay between devices. As such, over the past decade, the primary focus for improving the performance of nanoelectronic metal-interconnect structures has been via the utilization of insulating dielectrics with low values of the dielectric constant (*i.e.* low-k) and metal lines with high conductivity, such as Cu, to reduce the impact of RC delays.[12],[13]

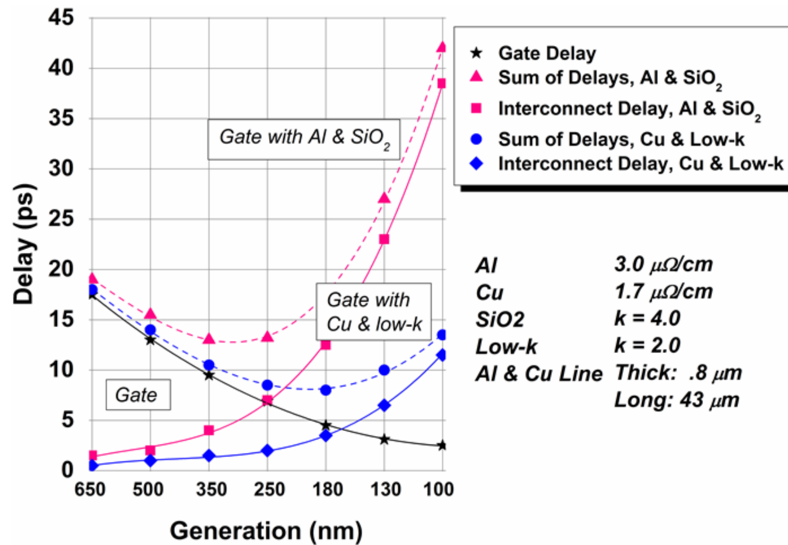

Figure 1-3 Comparison of the signal-propagation delay from device interconnects with the transistor gate delay.[14]

To reduce the k-value, two approaches are currently used: (1) reducing the polarizability of the dielectric by increasing the level of low-electronic-polar bonds, mainly carbon-containing components (like C-C, C-H, $Si\text{-}CH_3$, etc.); (2) reducing the material density by increasing the free volume (the volume between molecules,) through rearranging the material structure or introducing porosity. [15] The two methods can be combined to achieve even lower k values. Typical low-k dielectrics that are being currently investigated have k-values ranging from 2.0 to 2.5 (with a continuous push to decrease it), a porosity of 30%-50%, and a pore size of 2-3nm. [13],[16] There are also different types of low-k matrix [16] materials, such as organic polymers, organosilicate glass (OSG) and methylsilsesquioxane (MSQ).[4] Here, a matrix refers to the precursors used for the deposition of low-k thin films.

To reduce the resistance of the interconnect wires, the primary conductor material was changed from Al to Cu (36% decrease in resistivity). However, this requires that the damascene process[17] becomes the dominant interconnect-fabrication process, since Cu cannot be patterned by the previous techniques of photoresist masking and plasma etching that had been used with great success with Al.[17] **Figure 1-4** shows the cross-section of the 64-bit high-performance microprocessor built with IBM's 90 nm Server-Class CMOS technology with Cu/low-k interconnects. As can be seen, the metallization schemes involve a large number of metal/dielectric layers. The first dielectric level, encapsulating the active area, is doped SiO_2 glass with metal-filled (*e.g.,* tungsten) contacts to the transistors (source, drain, and gates). All subsequent dielectric layers consist of low-k material, such as organosilicate glass. Trenches (for *intra*level interconnects) and vias (for *inter*level interconnects) are formed within these layers through plasma etching, and are filled in subsequent steps with Cu and planarized with the damascene process, *i.e.,* Chemical Mechanical Polishing (CMP). The resulting structure is a planar surface on which the next level is built in a similar way.

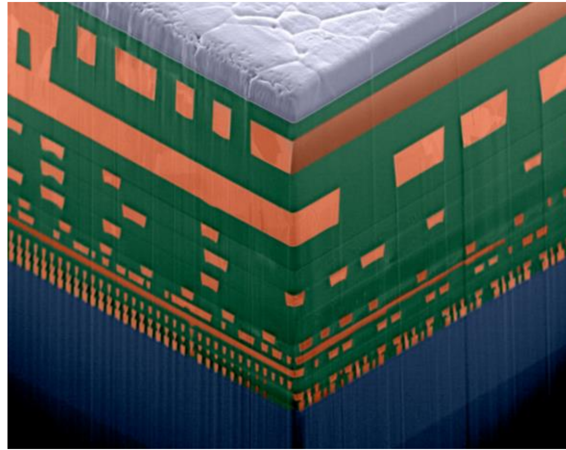

Figure 1-4 Cross-section of 64-bit high-performance microprocessor chip built with IBM's 90-nm Server-Class CMOS technology with Cu/low-interconnect (Figure located at the URL https://www-03.ibm.com/press/us/en/photo/19014.wss)

The dual-damascene scheme,[4],[17] in which trenches and vias are formed before the Cu-fill step, is the latest evolution of Cu-interconnect implementation. There are several ways to create a dual-damascene structure with and without an intermediate etch layer that provides an etch-stop for the trench etching, *i.e.*, the "Trench first, via last" approach and "Via first, trench last" approach.

In the "trench first, via last" approach, as shown in **Figure 1-5**, a trench etch-stop layer is used. After deposition of the low-k dielectric, trenches are patterned first by standard lithographic techniques and then etched with plasma to a finite depth into the dielectric. Anti-reflective coatings (ARC) and capping layers (which could be either SiO_2 or SiN_x) are usually used in the dual-damascene structure.[3],[18] The ARC layer can serve in a dual role as an antireflective layer as well as a pattern-transfer layer. After resist removal, another lithographic step defines a via, and the etch process continues all the

way to form a contact to the metal level below. A capping layer on top of the metal below is then etched in a low-bias process to reduce sidewall formation.[17]

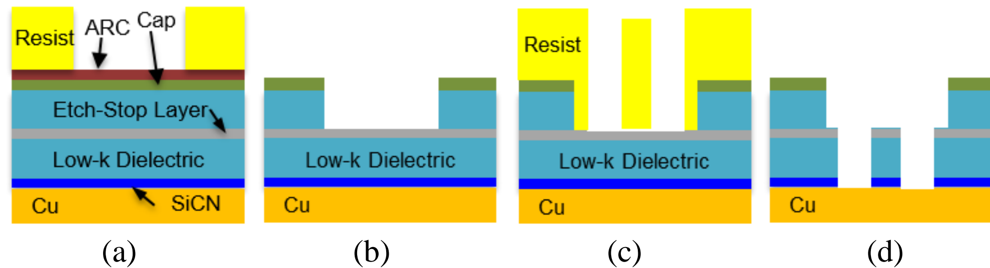

Figure 1-5 "Trench first, via last" dual damascene process flow: (a) Trench patterning (Litho); (b) Trench etching, stopped on an etch-stop layer; (c) Via patterning; (d) Via etching, resist stripping and barrier etching.[17]

The "via first, trench last" approach, which is shown in **Figure 1-6**, has evolved with time and has been the preferred implementation of dual-damascene structures since no trench etch-stop layer is present within the low-k dielectric. In this approach, the via is etched to completion, resist is stripped, followed by lithographic and etch steps to form the trench. A planarizing layer, capping layer and ARC are also shown. The role of the planarizing layer is to smooth the topography and, combined with the capping layer, it enables the use of a thin imaging layer. The pattern is first transferred to the capping layer followed by a pattern transfer to the planarizing layer. The etch chemistry for the latter step is either O_2 or CO_2 based; the latter gives a more anisotropic profile than the former. [4],[17]

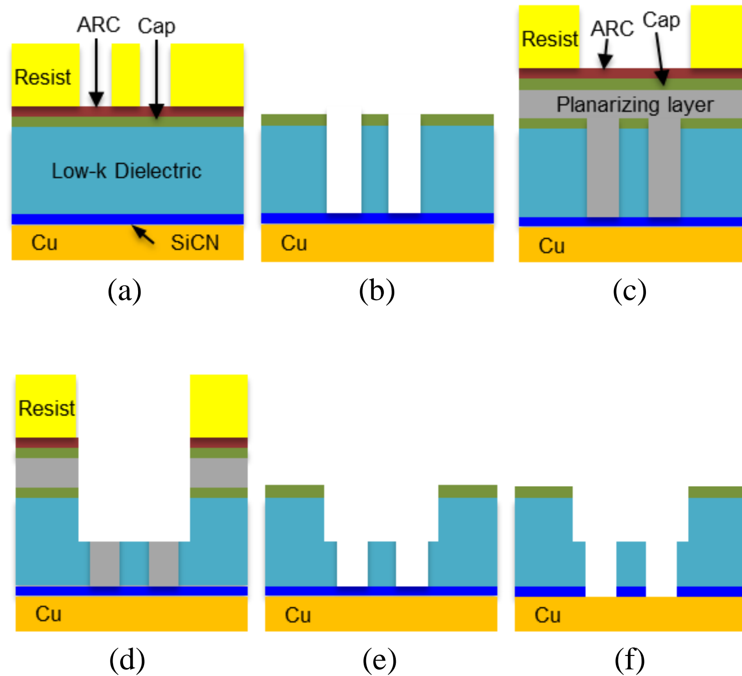

Figure 1-6 "Via first, trench last" dual damascene process flow: (a) Via patterning (Litho); (b) Via etching and resist stripping; (c) Trench patterning; (d) Trench etching; (e) Planarizing layer removal and resist stripping; (f) Barrier etching.[17]

In the early implementations of low-k dielectric materials, they were mainly considered as interlayer dielectrics to replace the traditional SiO_2. As continuous down-scaling of devices proceeded, additional low-k dielectrics became needed to serve as either a diffusion barrier, a Cu capping layer, or an etch-stop and/or polish-stop layer, depending on the details of the interconnect fabrication scheme. This section will introduce them briefly, including their functionality, requirements and progression.

1.1.1 Low-k Interlayer Dielectrics

Low-k interlayer dielectrics (ILD) serve the basic purpose of establishing a medium in which metal lines can be inlaid and remain electrically isolated from each other, as shown in **Figure 1-7**. The low-k ILD also provides some mechanical support to

metal lines during downstream processing of multiple metal layers and packaging. This requires the low-k dielectrics (1) to be electrical insulators that exhibit both extremely low leakage currents and high dielectric-breakdown strength, and (2) to provide reinforcing mechanical support for the various metal layers and to help distribute thermal and shear stresses produced during downstream processing and packaging.

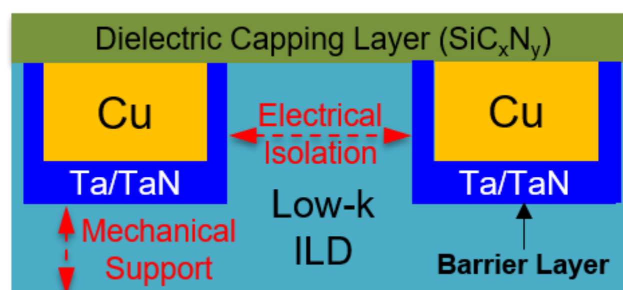

Figure 1-7 Schematic diagram illustrating the different functionalities of a low-k ILD in a low-k/Cu interconnect.

Currently porous organosilicate-based dielectric thin films (a-SiOC:H) deposited with plasma-enhanced chemical-vapor deposition (PECVD) techniques were the dominant choice for low-k ILD ($k > 2.2$) in the past decade and are also potential candidates for ultralow-k ILD ($k < 2.2$) applications in the future. **Figure 1-8** shows the general processes to deposit porous SiOC:H thin films. During the deposition, sacrificial organic polymers (porogens), such as tetramethyl-cyclotetrasiloxane (TMCTS) [4], are co-deposited with matrix materials, such as a silica-like matrix [4]. The sacrificial porogens are used to create porous structure inside of the material.

During the curing step, most of this organic material is thermally decomposed, whereby the original occupied sites are converted into microporus/nanoporous sites. The k-value and quality of the low-k film highly depends on the matrix, the porogen deposition

and the curing conditions.[4] Different matrix and porogen compositions can result in various new types of network structures in the final film.[19],[20]

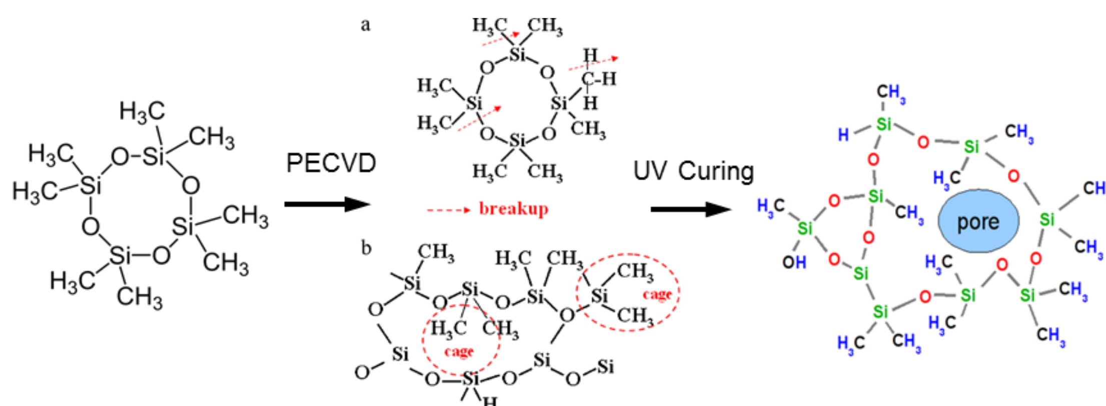

Figure 1-8 Deposition of porous low-k SiOC:H thin films and its chemical structure.[21]

Compared with SiO_2, whose leakage currents are typically $<10^{-8}$ A/cm^2 (up to 6-8 MV/cm) [22] and breakdown strengths of > 10 MV/cm,[23] low-k a-SiOC:H (k > 2.2) materials, with a breakdown strength of 3-5 MV/cm,[4] are fairly weak dielectrics. In addition, relative to SiO_2, which exhibits a reasonably robust Young's modulus (60-80 GPa)[24] and fracture toughness values (0.6-0.8 MPa$\sqrt{m}$)[25] respectively, a-SiOC:H exhibits substantially reduced values for Young's modulus (3-10 GPa)[24],[26] and fracture toughness (< 0.2 MPa$\sqrt{m}$).[27] Unfortunately, the reduction in the electrical and mechanical properties scales with a continuous decrease in the k-value, and is one of the contributing factors for why low-k ILD materials with increasingly lower values of k have been so challenging to integrate.

Figure 1-9 shows the progression of ILD k-values reported in the International Technology Roadmap for Semiconductors (ITRS). To keep an annual 20% improvement of these devices, the k-value of the ILDs has to be 1.65 or even smaller by the end of 2025.

Because of the introduction of high porosity to achieve lower k-values, these low-k dielectrics normally possess poor mechanical properties as compared with SiO_2, which results in great difficulties in being able to maintain their integrity during chemical-mechanical polishing (CMP) and consequently results in adhesion failure, fractures, cracks or peeling.[4] Additionally, the increased surface area from the pore structure also renders the material vulnerable to moisture uptake [5],[28],[29] and Cu diffusion, [30] both of which increase leakage currents, leading to electrical instabilities and accelerated dielectric breakdown. Hence, there is a need to devise strategies to inhibit chemical and mechanical instabilities of low-k ILDs that are often produced by the introduction of porosity and carbon doping.

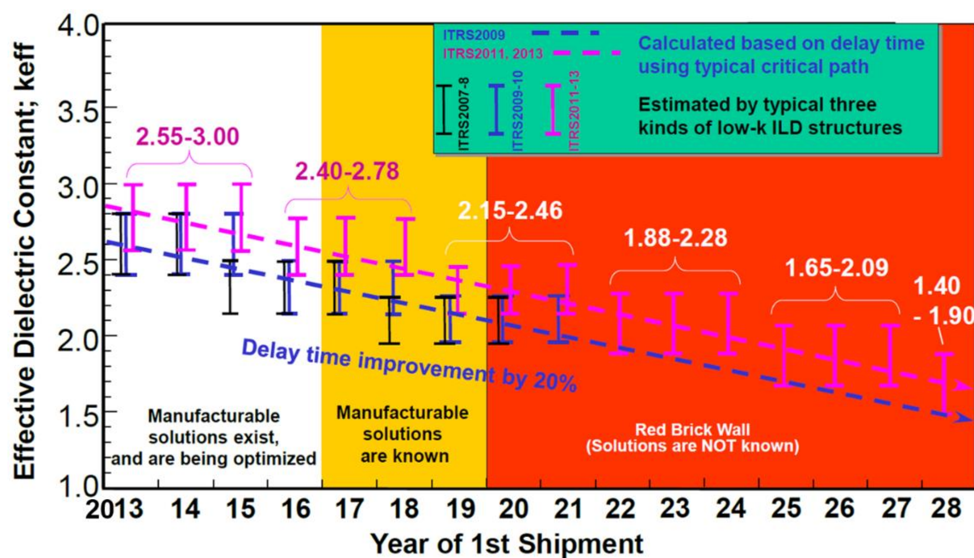

Figure 1-9 Progression of ILD k-values from International Technology Roadmap for Semiconductors (ITRS) 2013.

1.1.2 Low-k Capping Layer Dielectrics

Due to the fairly reduced properties of low-k ILDs, capping layer are usually needed in the dual-damascene process (1) to prevent in-diffusion of moisture and other aqueous cleaning chemicals that will cause corrosion of Cu wires and ILD layers underneath;[31],[32] (2) to prevent Cu out-diffusion into overlying metal layers;[33] (3) to passivate the top surface of the Cu lines to enhance the electromigration (EM) resistance;[34] (4) to improve the interlayer adhesions, etc.[35] **Figure 1-10** illustrates the functionality of a capping layer in a low-k/ Cu interconnect schematically.[9] In early implementations, due to differences in dry-etch selectivity and other considerations like low leakage current, robust mechanical properties, a-SiO_2, a-SiN, and a-SiC_xN_y:H related complements were the primary choice as the capping layer in Cu interconnect structures.[9],[36],[10],[11]

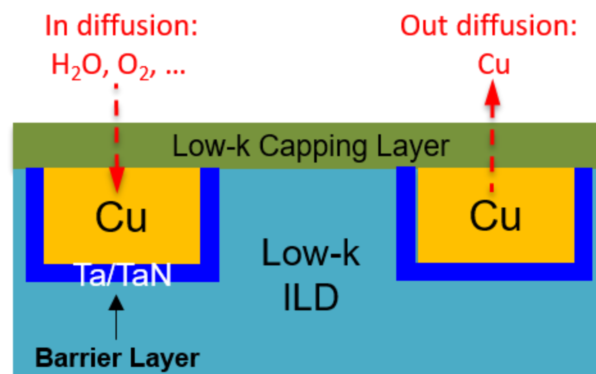

Figure 1-10 Schematic diagram illustrating the location and functionality of a capping layer in a low-k/ Cu interconnect.

The capping layers typically have the highest k-values in conventional Cu interconnect structures. For a-SiC_xN_y:H related materials, their k-values are all larger than

that of PECVD SiO_2 (k = 4.0–4.4). For example, PECVD SiN:H has a k-value over 6.0,[9],[36] and SiC and SiCN both have k-values larger than 4.5,[10],[11] as listed in **Table 1-1**. As technology continues to downscale, the relative contribution of the capping layer k-value to the interlayer capacitance is growing, and a requirement for alternative low-k materials as a capping layer becomes even more critical. Recently, dense low-k a-SiOC:H (~2.0 g/cm^3) dielectric materials have attracted much attention because of their significantly reduced k-values relative to conventional a-SiC_xN_y:H dielectric materials [37] and as a result, are the main subject of this work.

Table 1-1 Comparison of dielectric constant of a-SiC_xN_y:H related materials with ILDs.

Type	Materials	Dielectric Constant
Interlayer Dielectrics	PECVD a-SiO_2	4.0 ~ 4.4
	PECVD a-SiOC:H	< 3.2
Capping Layer Dielectrics	PECVD SiN:H	6.5 ~ 7.0
	PECVD SiC:H	4.5 ~ 7.0
	PECVD SiCN:H	4.5 ~ 5.8
	PECVD dense s-SiOC:H	3.2

As depicted in **Figure 1-10**, these low-k capping layers will contact the Cu wires directly in the dual-damascene structures. As a result, it is critical to determine the interactions at the low-k capping-layer dielectric and Cu line interface. Examples of these are line-to-line leakages, Cu transport, yield degradation, and other reliability related issues.

1.1.3 Low-k Etch-stop Dielectrics

In the dual-damascene process, the trench/via structure is patterned by etching the shape of the structure in the underlying ILD materials. Since the trench and via usually have different shapes and dimensions, they cannot be opened up simultaneously so via-

trench alignment is absolutely critical. Therefore, there is a need for an etch-stop layer to prevent over-etching, especially for the "trench first, via last" scheme as described above.[17] Thus, an etch-stop layer is embedded in low-k ILDs. Via patterning is carried out in the embedded etch-stop layer after the first half of the ILD is laid down with the trench pattern, as illustrated in **Figure 1-5**. In addition, an etch-stop layer is used between different metal layers, stopping the trench or via ILD etch to prevent over-etching into the underlying metal layer,[38] as illustrated in **Figure 1-11**. In order for a material to be used as an etch stop for trench or via patterning of an SiO_2 or low-k a-SiOC:H ILDs, the material must exhibit some resistance to typical fluorinated plasma etches utilized to transfer optical lithographically defined photoresist patterns into the ILDs.[39]

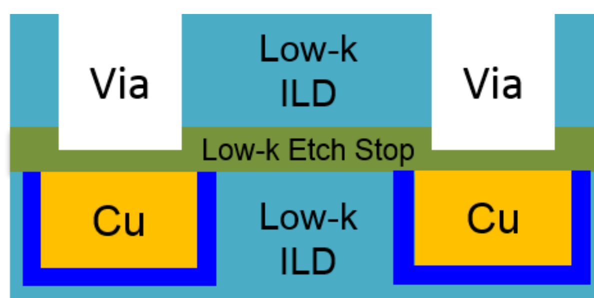

Figure 1-11 Schematic diagram illustrating functionality of a low-k etch-stop layer in a low-k/ Cu interconnect for stopping via etching over contacts.

Similarly to the capping layer, as device scaling continues, there is also a need for alternative materials with low dielectric constants to replace the traditional silicon nitride etch-stop layers. Low-k dense a-SiC:H etch stop materials,[9] as shown in **Figure 1**-12,

have been reported to exhibit high etch selectivities (2–10) relative to SiO_2,[17],[40] making them be potential candidates for the low-k etch-stop layer.

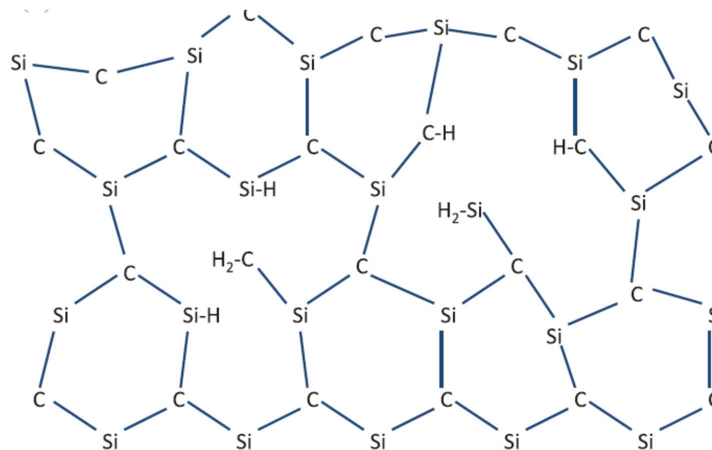

Figure 1-12 Schematic diagrams illustrating the dense structure in a low-k a-SiC:H.[9]

1.2 Cu Metallization

Cu metallization for interconnects has advantages of low resistivity and ease of deposition using existing process methods that can offer improvements to device performance. However, this also presents numerous integration and reliability challenges, like poor adhesion and high diffusivity along with the creation of deep levels in the silicon band gap. Compared with Al, Cu readily diffuses into silicon and most dielectrics. This progress can also be greatly enhanced by electric fields imposed between adjacent leads during device operation (10 V/cm). While the transport of Cu, including atomic diffusion and ion injection in porous low-k dielectrics is a complicated process, it is generally accepted that the main driving forces for Cu atomic diffusion and ion injection are the Cu concentration gradient and internal electric fields. Both chemical interactions and surface

passivation contribute to increased Cu-migration rates.[41]. Cu atomic diffusion, produced by the density gradients, is dominant when no Cu oxidation takes place and the temperature is higher than room temperature. If the Cu layer is oxidized, drifts of Cu ions, in the presence of external electric field, will dominate.[42]

Since the Cu ions are electropositive rather than electroneutral, drifts of Cu ions into the dielectric materials can cause charge accumulation in the bulk of dielectric and cause more serious reliability challenges than diffusion of Cu atoms alone. This will also be discussed in detail later in this Chapter. As such, in the initial inlay of Cu wires into dielectric trenches or vias during the damascene process, the Cu leads must be encapsulated with metallic (such as Ta, TaN) and dielectric (such as SiN, SiC, SiCN) diffusion barriers to prevent Cu transport between adjacent metal leads and also to prevent any in-diffusion of oxidizing material, such as H_2O, O_2.

However, it is increasingly more challenging to contain Cu within lines by implanting Cu seeds into the trenches/vias etched on low-k dielectrics, since the continual downscaling of interconnect dimensions results in significant shrinking of via and trench size, and require thinner and thinner barrier layers. More details about the requirement of the barrier dimensions can be found the International Technology Roadmap for Semiconductors (ITRS) 2013 [6] guidelines as summarized in **Table 1-2**. As can be seen, in the next decade, the thickness of the barrier layer needs to be made smaller than 1.0 nm or even 0.5 nm for continuous performance improvement and downscaling of device dimensions.

Table 1-2 ITRS 2013 guidelines for Cu diffusion-barrier thickness in advanced interconnects.[6]

Year	2010	2011	2012	2013	2014	2015	2016	2017
Barrier Thickness (nm)	3.3	2.9	2.6	2.4	2.1	1.9	1.7	1.5
Year	2018	2019	2020	2021	2022	2023	2024	2030
Barrier Thickness (nm)	1.3	1.2	1.1	1.0	0.9	0.8	0.7	<0.5

Legend (cell colour)	Meaning
(white)	*Manufacturable solutions exist, and are being optimized*
(yellow)	*Manufacturable solutions are known*
(red)	*Manufacturable solutions are NOT known*

Continuous technology scaling may eventually eliminate barrier layers entirely and expose Cu lines directly to low-k dielectrics.[7] As a result, Cu-diffusion-induced instabilities have generated extensive interest in determining the mechanisms of Cu diffusion into the low-k ILDs. The other driving force that requires characterization of Cu migration into low-k dielectrics is the need for low-k capping and/or etch stop layers as discussed above. Thus, the properties of the Cu/low-k dielectric interface are of considerable interest and have become a focus of study.[42],[8],[43]

Figure 1-13 illustrates one of many proposed mechanisms for electrical leakages in an advanced Cu/low-k interconnect structure.[44] According to this proposed mechanism, the presence of defect states below the conduction band results in low-energy pathways for electrons to move inside the dielectric. As shown, these conduction pathways enable Poole-Frenkel conduction, which can be thought of as electrons "hopping" between defect states.[45] With an applied electric field, Cu ions can drift into the low-k dielectrics.

These Cu ions provide additional low-energy conduction pathways for electrons. Furthermore, over an extended time frame, the drift process results in Cu ions building up at the a-SiOC:H/Cu interface.[44]) The presence of this net positive charge near the interface results in a bending of the conduction band in the bulk of the dielectric.[46] Electrons are then able to tunnel through the interfacial energy barrier by Fowler-Nordheim tunneling.[44]

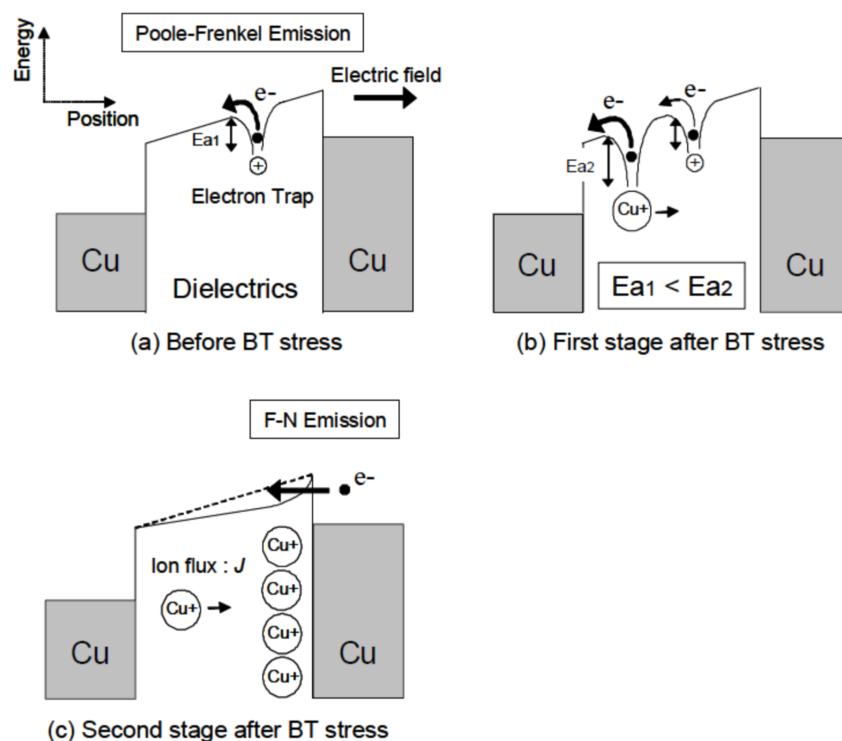

Figure 1-13 Leakage-current mechanisms produced by Cu migration into dielectrics.[44]

During the IC fabrication process, there are several plasma-processing steps required for successful integration of low-k materials. These include: (1) initial deposition (in the case of PECVD dielectrics), (2) hard-mask deposition, (3) etching vias and/or trenches, (4) removal (stripping) of photoresist, (5) deposition of diffusion barriers, and (6) chemical-mechanical polishing (CMP). As is well known, a plasma is an aggressive

medium with the presence of photons (from deep VUV to infrared), energetic ions, electrons, and highly reactive radicals. Due to the low density and porous structure of the low-k materials, the reactivity and penetration depth of reactive species from a plasma will be significantly increased,[47] which will consequently affect the behaviors of Cu migration into the materials.[48] The reliability and yield issues associated with integration of these materials with dual-damascene Cu lines is more challenging than expected.[49]

Currently, various points of view exist in the literature regarding the reliability of Cu/low-k dielectric interconnects. In addition, work has seldom been carried out to determine the influence of VUV irradiation on Cu-migration properties into low-k dielectrics.[45,49] To accomplish this goal, it is necessary to carry out systematic experiments that compare Cu-migration properties into dielectrics using the same set of measurement data before and after plasma processing. In addition, to predict reliability limits of the advanced Cu/low-k interconnects at operational conditions, leakage-current mechanisms and time-dependent dielectric breakdown (TDDB) modes have to be identified by considering the drift of Cu^{+} ions inside the dielectric.[49]

1.3 Goal of the work

The goal of this work is to investigate damage to and Cu migration into low-k organosilicate (a-SiOC:H) dielectrics from vacuum-ultraviolet irradiation during plasma processing. We hypothesize that for advanced Cu/low-k dielectric interconnects, Cu

migration into and breakdown of low-k dielectrics can be exacerbated by VUV irradiation. To verify this hypothesis, we need to answer the following questions:

(1) What kinds of damage can VUV cause to low-k a-SiOC:H dielectrics, how does it happen and what are the differences between pure VUV-photon induced damage and plasma-induced damage?

(2) How do VUV photons affect Cu migration into low-k dielectrics in Cu/a-SiOC:H interconnects and is this effect energy-dependent?

(3) What are the effects of VUV irradiation on extrinsic (including the effect of Cu migration) TDDB of a-SiOC:H?

(4) How to avoid or minimize degradation of Cu/low-k dielectric interconnects from VUV photons?

To verify this hypothesis, we first systemically examine VUV-irradiation-induced modifications, (mechanical, electrical and chemical) to low-k dielectrics, and compare these modifications to those produced from exposure to an electron-cyclotron-resonance (ECR) argon plasma. Then we investigate how these modifications affect the transport properties of Cu into the low-k dielectrics under various bias-temperature stresses (BTS). Next, the characteristics of TDDB of VUV-exposed Cu/low-k a-SiOC:H dielectric stacks involving Cu migration were investigated to determine the effects of VUV irradiation on the device lifetime.

To determine the electrical leakage paths and breakdown mechanisms of Cu/low-k dielectric interconnects, the barrier height at the Cu/low-k dielectric interface and the location of the valence-band edge of low-k a-SiOC:H dielectrics was measured. Defect-

induced band offsets at the Cu/low-k interface will also be investigated to further examine the leakage current and breakdown mechanisms. Based on these results, a band diagram for low-k/Cu interconnects can be developed so as to explain and predict the observed reliability issues reported for low-k/Cu interconnects. Finally, based on this work, we discuss alternative solutions for mitigation of the damage.

The key merits of this work for future applications are: 1) A threshold energy has been found to exist for VUV photon caused degradations of Cu/low-k dielectric interconnects, which correspond to the dissociation energy of Si-O chemical bonds (8.3 eV). This is important because it means one can avoid VUV-induced damage by choosing etch gases which do not emit photons with energies higher than 8.3 eV. For example, a recent work measuring the VUV emission of a CF_3I (Trifluoroiodomethane) plasma shows that very few VUV photons with energies larger than 8.3 eV were emitted.[50] This might be a promising etchant for low-k a-SiOC:H from the point of view of mitigating VUV-induced damage; 2) This work provides guidance for developing new precursors and/or manufacturing methods for novel low-k dielectrics to achieve even lower k-values without losing mechanical/electrical strength. For example, it is possible to increase the degree of cross-linking inside the low-k dielectrics to increase the material mechanical strength.

1.4 Outline of Thesis

Based on the introduction and proposed work as described above, this thesis is organized as follows:

Chapter II provides background information for this research work. It includes previous work on plasma-processing-induced reliability issues of low-k dielectric thin films, VUV photon irradiation during processing plasmas, breakdown mechanisms of Cu/low-k interconnects and the TDDB models to predict the failure taking place in the Cu/low-k dielectric interconnects. Plasma-caused damage to Cu/low-k interconnects are summarized from three aspects: chemical, mechanical and electrical. Then, VUV emission spectra from an oxide-etch plasma are introduced, to compare with the synchrotron radiation used in this work, giving an estimation of the photon energy and flux of VUV-irradiation during plasma processing of low-k dielectrics. At the end of this Chapter, a number of existing failure models for Cu/low-k dielectrics are reviewed and compared, which will help one to realize the limitations of previous results and the necessity of this work. Some of the reported models are even contradictory.[51],[49]

Chapter III describes the experimental apparatus and characterization methods that have been utilized in this this research. Two exposure systems, (1) synchrotron radiation and (2) electron-cyclotron resonance (ECR) plasma, are introduced. Some VUV exposures were obtained at the National Synchrotron Radiation Research Center (NSRRC) in Taiwan with the help of other lab members (Dongfei Pei and Weiyi Li) due the limited travel funds available. Diagnostic techniques used to characterize low-k a-SiOC:H thin films before, during and after VUV photon irradiation are discussed. A methodology to evaluate Cu migration and migration-induced degradation is introduced in detail.

Chapter IV presents a systematic study of the damage to various low-k a-SiOC:H dielectrics from VUV irradiation using a synchrotron as a VUV-photon source. The effects of VUV irradiation on the mechanical properties, such as hardness, elastic modulus and

crack threshold, will be investigated with nanoindentation. Mechanisms of VUV-induced modification are proposed, based on Fourier transform infrared spectroscopy (FTIR) and X-ray photoelectron spectroscopy (XPS) measurements. The effects of VUV irradiation on the electrical properties, such as leakage current, breakdown voltage and k-values, are evaluated with I-V and C-V measurements. By comparing the synchrotron VUV-exposed samples to the ECR Ar-plasma exposed samples, we will show the damage mechanisms for both energetic ions and VUV photons coming from the plasma.

In Chapter V, the effects of VUV irradiation on Cu migration into low-k dielectrics and time-dependent breakdown of Cu/low-k interconnects involved Cu migration are investigated. By employing XPS depth-profile measurements, the diffusivity of Cu into as-deposited and VUV-irradiated low-k a-SiOC:H dielectrics will be evaluated under different temperature and bias conditions. As described in the beginning of this chapter, Cu migration includes both diffusion of Cu atoms, which originates from density gradients, and drift of Cu ions, which is because of the electro-positivity of Cu ions and will take place in the presence of an electric field.

The energy-dependent exacerbation of Cu migration from VUV can be determined by examining the migration rate as a function of photon energy. Mechanisms for energy-dependent Cu migration are proposed and discussed. At the end of this Chapter, extrinsic TDDB (by taking into account of Cu migration) of a-SiOC:H and the effect of VUV irradiation on them are measured. Constant-voltage time-to-failure (TTF) measurements are performed on (i) a-SiOC:H (ii) a-SiOC:H/Cu and (iii) VUV exposed a-SiOC:H/Cu stacks. Weibull statistics are used to determine the characteristic lifetime (63.2 % TTF) and

shape factor (defined as the slope of the breakdown probability plot using the Weibull scale) of each type of sample as a function of electric stress over repeated measurements.

Chapter VI depicts a band diagram for low-k/Cu interconnects which is used to explain and predict some of the observed reliability issues as shown in previous chapters. The Schottky barrier at the low-k/Cu interface is measured using VUV photoemission spectroscopy. The surface bandgap and valence-band edge for various porous and non-porous low-k a-SiOC:H dielectrics are then determined from core-level and valence XPS, respectively. Combined with electron paramagnetic resonance (EPR) results measured on exposed a-SiOC:H dielectrics, a band diagram for low-k/Cu interconnects, including all possible defect states within the band, is developed.

Chapter VII summarizes the significant findings of this work, discusses several alternative solutions that can be used to mitigate the VUV-induced damage to the low-k dielectrics and provides some directions for possible future research.

1.5 References

[1] C. W. Chen, P. T. Liu, T. C. Chang, J. H. Yang, T. M. Tsai, H. H. Wu, and T. Y. Tseng, "Cu-penetration induced breakdown mechanism for a-SiCN," *Thin Solid Films*, Vol. **469–470**, pp.388-392 (2004).

[2] S. W. King, D. Jacoba, D. Vanleuvena, B. Colvina, J. Kellya, M. Frencha, J. Bielefeldb, D. Duttac, M. Liuc, and D. Gidleyc, "Film Property Requirements for

Hermetic Low-k a-SiOxCyNz:H Dielectric Barriers," *Ecs J Solid State Sc*, Vol. **1**, pp.N115-N122 (2012).

[3] S. W. King, D. Jacob, D. Vanleuven, B. Colvin, J. Kelly, G. Xu, M. French, D. Dutta, and D. Gidley, "Role of Nano-Porosity in Plasma Enhanced Chemical Vapor Deposition of Hermetic low-k a-SiOCN:H Dielectric Barrier Materials," *Ecs Transactions*, Vol. **45**, pp.27-45 (2013).

[4] M. R. Baklanov, J. F. de Marneffe, D. Shamiryan, A. M. Urbanowicz, H. L. Shi, T. V. Rakhimova, H. Huang, and P. S. Ho, "Plasma processing of low-k dielectrics," *Journal of Applied Physics*, Vol. **113**, 041101 (2013).

[5] C. Wu, Y. Li, M. R. Baklanov, and K. Croes, "Electrical Reliability Challenges of Advanced Low-k Dielectrics," *Ecs J Solid State Sc*, Vol. **4**, pp.N3065-N3070 (2015).

[6] International Technology Roadmap for Semiconductors (ITRS): 2013, (Semiconductor Industry Association, San Jose, CA, 2013).

[7] M. He, S. Novak, L. Vanamurthy, H. Bakhru, J. L. Plawsky, and T. Lu, "Cu penetration into low-k dielectric during deposition and bias-temperature stress," *Applied Physics Letters*, Vol. **97**, 252901 (2010).

[8] X. Guo, D. Pei, H. Zheng, S. W. King, Y.-H. Lin, H.-S. Fung, C.-C. Chen, Y. Nishi, and J. L. Shohet, "Measurements of Schottky barrier at the low-k SiOC:H/Cu interface using vacuum ultraviolet photoemission spectroscopy," *Applied Physics Letters*, Vol. **107**, 232905 (2015).

[9] S. W. King, "Dielectric Barrier, Etch Stop, and Metal Capping Materials for State of the Art and beyond Metal Interconnects," *Ecs J Solid State Sc*, Vol. **4**, pp.N3029-N3047 (2015).

[10] S. W. King, J. D. Bielefeld, G. Xu, W. A. Lanford, Y. Matsuda, R. H. Dauskardt, N. H. Kim, D. Hondongwa, L. Olasov, B. Daly, G. Stan, M. Liu, D. Dutta, and D. Gidley, "Influence of network bond percolation on the thermal, mechanical, electrical and optical properties of high and low-k a-SiC:H thin films," *J Non-Cryst Solids*, Vol. **379**, pp.67-79 (2013).

[11] A. Mallikarjunan, A. D. Johnson, L. Matz, R. N. Vrtis, A. Derecskei-Kovacs, X. Jiang, and M. Xiao, "Silicon precursor development for advanced dielectric barriers for VLSI technology," *Microelectronic Engineering*, Vol. **92**, pp.83-85 (2012).

[12] A. Grill, V. Patel, K. L. Saenger, C. J. Jahnes, S. A. Cohen, and A. G. Schrott, "Diamondlike carbon materials as low-k dielectrics for multilevel interconnects in ULSI," *Mater Res Soc Symp P*, Vol. **443**, pp.155-164 (1997).

[13] K. Maex, M. R. Baklanov, D. Shamiryan, F. Iacopi, S. H. Brongersma, and Z. S. Yanovitskaya, "Low dielectric constant materials for microelectronics," *Journal of Applied Physics*, Vol. **93**, pp.8793-8841 (2003).

[14] M. T. Bohr, "Interconnect scaling - The real limiter to high performance ULSI," *International Electron Devices Meeting, 1995 - Iedm Technical Digest*, Vol., pp.241-244 (1995).

[15] A. Grill, L. Perraud, V. Patel, C. Jahnes, and S. Cohen, "Low dielectric constant SiCOH films as potential candidates for interconnect dielectrics," *Mater Res Soc Symp P*, Vol. **565**, pp.107-116 (1999).

[16] M. Baklanov, M. Green, and K. Maex, "Dielectric Films for Advanced Microelectronics". (John Wiley & Sons, Ltd, Chichester, England; Hoboken, NJ, 2007).

[17] V. M. Donnelly and A. Kornblit, "Plasma etching: Yesterday, today, and tomorrow," *Journal of Vacuum Science & Technology A*, Vol. **31**, 050825 (2013).

[18] N. Jourdan, Y. Barbarin, K. Croes, Y. K. Siew, S. Van Elshocht, Z. Tokei, and E. Vancoille, "Plasma Enhanced Chemical Vapor Deposition of Manganese on Low-k Dielectrics for Copper Diffusion Barrier Application," *Ecs Solid State Lett*, Vol. **2**, pp.25-27 (2013).

[19] A. Grill, S. M. Gates, T. E. Ryan, S. V. Nguyen, and D. Priyadarshini, "Progress in the development and understanding of advanced low k and ultralow k dielectrics for very large-scale integrated interconnects-State of the art," *Appl Phys Rev*, Vol. **1**, 011306 (2014).

[20] K. Vanstreels, C. Wu, M. Gonzalez, D. Schneider, D. Gidley, P. Verdonck, and M. R. Baklanov, "Effect of Pore Structure of Nanometer Scale Porous Films on the Measured Elastic Modulus," *Langmuir*, Vol. **29**, pp.12025-12035 (2013).

[21] Dongfei Pei, "The Effects of Vacuum Ultraviolet Irradiation on the Electrical Properties of Porous Low-k Organosilicate Glass," Doctor of Philosophy Thesis, University of Wisconsin-Madison, 2016.

[22] J. Batey and E. Tierney, "Low-temperature deposition of high-quality silicon dioxide by plasma-enhanced chemical vapor deposition," *Journal of Applied Physics*, Vol. **60**, pp.3136-3145 (1986).

[23] S. Lombardo, J. H. Stathis, B. P. Linder, K. L. Pey, F. Palumbo, and C. H. Tung, "Dielectric breakdown mechanisms in gate oxides," *Journal of Applied Physics*, Vol. **98**, 121301 (2005).

[24] G. Carlotti, P. Colpani, D. Piccolo, S. Santucci, V. Senez, G. Socino, and L. Verdini, "Measurement of the elastic and viscoelastic properties of dielectric films used in microelectronics," *Thin Solid Films*, Vol. **414**, pp.99-104 (2002).

[25] A. A. Volinsky, J. B. Vella, and W. W. Gerberich, "Fracture toughness, adhesion and mechanical properties of low-K dielectric thin films measured by nanoindentation," *Thin Solid Films*, Vol. **429**, pp.201-210 (2003).

[26] X. Guo, J. E. Jakes, M. T. Nichols, S. Banna, Y. Nishi, and J. L. Shohet, "The effect of water uptake on the mechanical properties of low-k organosilicate glass," *Journal of Applied Physics*, Vol. **114**, 084103 (2013).

[27] X. Guo, J. E. Jakes, S. Banna, Y. Nishi, and J. L. Shohet, "Effect of water uptake on the fracture behavior of low-k organosilicate glass," *Journal of Vacuum Science & Technology A*, Vol. **32**, 031512 (2014).

[28] T. M. Shaw, D. Jimerson, D. Haders, C. E. Murray, A. Grill, and D. C. Edelstein, "Moisture and oxygen uptake in low K copper interconnect structures," *Mat Res S C*, Vol., pp.77-84 (2004).

[29] H. S. Lu, K. Gottfried, N. Ahner, S. Schulz, and X. P. Qu, "Investigation of CH4, NH3, H2 and He plasma treatment on porous low-k films and its effects on resisting moisture absorption and ions penetratiorl," *Microelectronic Engineering*, Vol. **106**, pp.85-90 (2013).

[30] T. Abell, J. Schuhmacher, Z. Tokei, Y. Travaly, and K. Maex, "Lateral solvent diffusion characterization of low k dielectric plasma damage and ALD barrier film closure," *Microelectronic Engineering*, Vol. **82**, pp.411-415 (2005).

[31] C. Kubasch, H. Schumacher, H. Ruelke, U. Mayer, and J. W. Bartha, "Fourier Transform Infrared Spectroscopy of Moisturized Low-k Dielectric Materials," *IEEE Transactions on Electron Devices*, Vol. **58**, pp.2888-2894 (2011).

[32] Y. Cheng, W. Chang, and Y. Wang, "Moisture effect on electromigration characteristics for copper dual damascene interconnection," *Journal of Vacuum Science & Technology B*, Vol. **28**, pp.1322-1325 (2010).

[33] M. Vogt, M. Kachel, M. Plotner, and K. Drescher, "Dielectric barriers for Cu metallization systems," *Microelectronic Engineering*, Vol. **37-38**, pp.181-187 (1997).

[34] H. Miyazaki, H. Kojima, and K. Hinode, "Passivation effect of silicon nitride against copper diffusion," *Journal of Applied Physics*, Vol. **81**, pp.7746-7750 (1997).

[35] W. Shao, S. G. Mhaisalkar, T. Sritharan, A. V. Vairagar, H. J. Engelmann, O. Aubel, E. Zschech, A. M. Gusak, and K. N. Tu, "Direct evidence of Cu/cap/liner edge being the dominant electromigration path in dual damascene Cu interconnects," *Applied Physics Letters*, Vol. **90**, 052106 (2007).

[36] S. W. King, "Plasma enhanced atomic layer deposition of SiNx:H and SiO2," *Journal of Vacuum Science & Technology A*, Vol. **29**, 041501 (2011).

[37] S. W. King, M. French, M. Jaehnig, M. Kuhn, and B. French, "X-ray photoelectron spectroscopy investigation of the Schottky barrier at low-k a-SiO(C):H/Cu interfaces," *Applied Physics Letters*, Vol. **99**, 202903 (2011).

[38] A. Haruhiko, Y. Masahiro, and F. Nobuo, "Developments of Plasma Etching Technology for Fabricating Semiconductor Devices," *Japanese Journal of Applied Physics*, Vol. **47**, 1435 (2008).

[39] D. Eon, M. Darnon, T. Chevolleaua, T. David, L. Vallier, and O. Joubert, "Etch mechanisms of hybrid low-k material (SiOCH with porogen) in fluorocarbon based plasma," *Journal of Vacuum Science & Technology B*, Vol. **25**, pp.715-720 (2007).

[40] X. Hua, X. Wang, D. Fuentevilla, G. S. Oehrlein, F. G. Celii, and K. H. R. Kirmse, "Study of C4F8/N2 and C4F8/Ar/N2 plasmas for highly selective organosilicate glass etching over Si3N4 and SiC," *Journal of Vacuum Science & Technology A*, Vol. **21**, pp.1708-1716 (2003).

[41] J. Hernandez, P. Wrschka, and G. S. Oehrlein, "Surface Chemistry Studies of Copper Chemical Mechanical Planarization," *Journal of The Electrochemical Society*, Vol. **148**, pp.G389-G397 (2001).

[42] X. Guo, S. W. King, H. Zheng, P. Xue, Y. Nishi, and J. L. Shohet, "Effects of vacuum-ultraviolet irradiation on copper penetration into low-k dielectrics under bias-temperature stress," *Applied Physics Letters*, Vol. **106**, 012904 (2015).

[43] L. Zhao, M. Pantouvaki, K. Croes, Z. Tőkei, Y. Barbarin, C. J. Wilson, M. R. Baklanov, G. P. Beyer, and C. Claeys, "Role of copper in time dependent dielectric breakdown of porous organo-silicate glass low-k materials," *Applied Physics Letters*, Vol. **99**, 222110 (2011).

[44] N. Suzumura, S. Yamamoto, D. Kodama, K. Makabe, J. Komori, E. Murakami, S. Maegawa, and K. Kubota, "A new TDDB degradation model based on Cu ion drift in cu interconnect dielectrics," *Int Rel Phy*, Vol., pp.484-489 (2006).

[45] H. Miyazaki, D. Kodama, and N. Suzumura, "Phenomenological classification of stress-induced leakage current and time-dependent dielectric breakdown mechanism," *Journal of Applied Physics*, Vol. **106**, 104103 (2009).

[46] S. Lee, A. S. Oates, and K. M. Chang, "Fundamental understanding of porous low-k dielectric breakdown," 2009 IEEE International Reliability Physics Symposium, Montreal, QC, 2009.

[47] J. M. Atkin, D. Song, T. M. Shaw, E. Cartier, R. B. Laibowitz, and T. F. Heinz, "Photocurrent spectroscopy of low-k dielectric materials: Barrier heights and trap densities," *Journal of Applied Physics*, Vol. **103**, 094104 (2008).

[48] J. M. Atkin, E. Cartier, T. M. Shaw, R. B. Laibowitz, and T. F. Heinz, "Charge trapping at the low-k dielectric-silicon interface probed by the conductance and capacitance techniques," *Applied Physics Letters*, Vol. **93**, 122902 (2008).

[49] T. K. Wong, "Time Dependent Dielectric Breakdown in Copper Low-k Interconnects: Mechanisms and Reliability Models," *Materials*, Vol. **5**, pp.1602-1625 (2012).

[50] Z. el Otell, V. Šamara, A. Zotovich, T. Hansen, J. F. de Marneffe, and M. R. Baklanov, "Vacuum ultra-violet emission of CF4 and CF3I containing plasmas and their effect on low-k materials," *Journal of Physics D: Applied Physics*, Vol. **48**, 395202 (2015).

[51] C. Wu, Y. Li, I. Ciofi, Th. Kauerauf, J. Bömmels, I. De Wolf, Zs. Tőkei, and K. Croes, "Towards understanding intrinsic degradation and breakdown mechanisms in SiOCH low-k dielectrics," *Journal of Applied Physics*, Vol. **117**, 064101 (2015).

Chapter II

Background

This Chapter examines previous work on plasma processing-induced damage to Cu/low-k interconnects and the present understanding of Cu/low-k interconnect failure, including time-dependent dielectric breakdown (TDDB) lifetime degradation. The first section reviews existing work on all types of plasma-induced damage to low-k a-SiOC:H dielectric materials. The second section provides background information on VUV-photon spectra from processing plasmas and the estimated photon flux, showing VUV irradiation during plasma processing can be another important damage source in addition to energetic ions and reactive radicals. The third section discuss the likely dominant mechanisms for increased electrical conduction and shortened time-zero dielectric breakdown (TZDB) times.in low-k a-SiOC:H dielectrics. Lastly, an overview of the TDDB models of Cu/low-

k interconnects is provided based on the latest studies. Limitations of current work are examined to show the need for and importance of additional research in this area.

2.1 Plasma-Induced Damage to Cu/Low-k Interconnects

During the IC fabrication process, successful integration of Cu/low-k interconnects, either using a-SiC_xN_y:H dielectric as a capping layer or using a dense low-k dielectric as a capping layer as in this work requires several plasma-processing steps. These include layer deposition, comprising both interlayer dielectric and capping-layer dielectric layers, plasma-enhanced chemical vapor deposition (PECVD), etching of trenches and vias, photoresist ashing/stripping and surface polishing. [1] As is well known, plasmas are an aggressive medium because of the presence of photons (from deep VUV to infrared), energetic ions, electrons, and highly reactive radicals.[2],[3] Plasma-induced damage (PID) has been widely observed in low-k a-SiOC:H dielectric materials.[4],[5],[6],[7] The reliability and yield issues associated with integration of these materials with Cu wires have been discovered to be more challenging than expected.[8],[9],[10] A brief summary of PID will be presented below from three aspects: (1) chemical damage, (2) mechanical damage and (3) electrical damage.

2.1.1. Chemical Damage

For low-k organosilicates, a decrease in k-value is generally achieved by replacing some Si-O bonds with less polarizable Si-C bonds, and by increasing the overall porosity of the material.[11] However, this results in a greater susceptibility of the low-k dielectric material to both chemical attack and chemical deformation, such as composition change,

chemical-bond breaking and structural rearrangement. Many studies show that while exposed to plasma, the synergy between radicals, photons and ions has led to significant damage to chemical bonds and structures of low-k a-SiOC:H thin films.[4],[12],[13]

2.1.1.1. Carbon Depletion

Carbon depletion, also known as carbon loss or demethylation, has been a common feature of plasma-induced damage to a-SiOC:H materials. Compared with Si-O bonds, Si-C bonds are chemically weaker.[14] Reported carbon depletion in a-SiOC:H is a complex phenomenon involving both physical and chemical effects. The former arises from ion bombardment, where energetic ions break $-Si-CH_3$ bonds on the top surface of a-SiOC:H thin film. The latter involves chemical reactions between the plasma and low-k constituents, some of which can be induced by plasma radiation (photochemistry) or free radicals. These reactions can follow a diffusion-controlled mechanism and result in a thick damaged layer.[2]

For example, oxygen plasma, used to remove photoresist, can result in the depletion of carbon as evidenced by decreases in $-Si-CH_3$ intensity, as shown in **Figure 2-1**. Goldman *et al.* [15] have shown that in a-SiOC:H thin films, carbon depletion from O_2 plasma is not limited to the top surface. Damage can happen inside of the material since the damage here is dominated by the diffusion of O radicals. The thickness of the carbon-depletion layer, that can be up to 100 nm into low-k a-SiOC:H thin films, has been reported by several researchers.[16],[17] It should be noted that no capping layer was used in these studies, because most of the previous work focused on the studies of low-k dielectrics themselves.

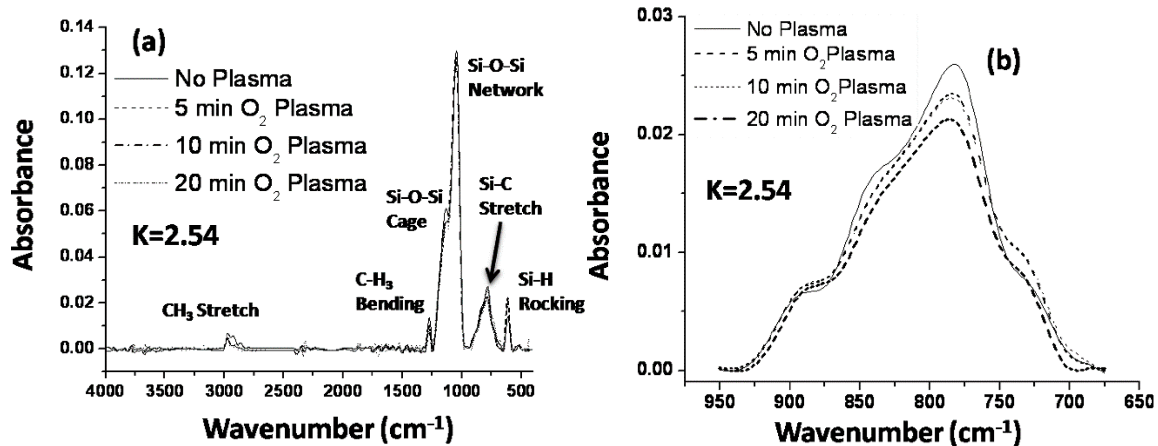

Figure 2-1 FTIR spectra of porous low-k a-SiOC:H film (k=2.54) as a function of O_2 plasma treatment. (a) Absorbance of 4000 - 500 cm^{-1} region and (b) expansion of $Si\text{-}CH_3$ stretch mode showing a monotonic decrease in intensity.[15]

For the $-Si\text{-}CH_3$ bonds, once some methyl groups are removed, some of the Si sites will exist as dangling bonds, if those sites were not already occupied by oxygen during the etching or ashing process.[2],[15] Upon subsequent exposure to air, these dangling bonds can react with moisture to form silanol groups (-Si-OH) at free Si sites.[5] The silanol group is known to increase the dielectric constant of low-k a-SiOC:H material.[2] It is also known that such a damaged low-k dielectric material is vulnerable to chemical attack during exposure to chemical cleanups, which results in significant critical-dimension loss of low-k a-SiOC:H insulating structures.[18] Similar effects may occur in other low-k dielectric materials with silicon-hydrocarbon bonds that are converted to silanol when exposed to oxidizing or reducing plasmas.[16],[19]

2.1.1.2. Defect generation

For low-k a-SiOC:H materials, it has been shown that electrical traps and defects can be created by downstream porogen removal and plasma-etching processes that expose the low-k material to intense UV/VUV radiation, energetic ions, and chemically active radicals.[20],[21],[22] It is not clear which one is the dominant process currently based on the published papers. The damage always varies with plasma conditions and material compositions. To make this clear, this work will focus on the VUV-induced modifications to the low-k dielectric materials by using synchrotron as the VUV photon source. Defects generated by active radicals will not be discussed here because it is out of the range of this work.

Plasma processes can break the chemical bonds of low-k a-SiOC:H and create large numbers of dangling bonds within the material. Using electron-spin resonance (ESR) spectroscopy, Afanas'ev *et al.* [23] addressed the atomic nature of the defects generated by ion bombardment in various a-SiOC:H (k=2.0-2.5) films, revealing the generation of Si-vacancy-related EX-centers and C dangling bonds in Si-C bonded clusters as the dominant pattern of defects in low-k organosilicates. Ren *et al.* [21] studied the defects generated from various plasma exposures (N_2, O_2 and air plasma), in which a paramagnetic defect state with a g-factor of 2.0033 was universally detected after plasma exposure, as shown in **Figure 2-2**, and the defect concentrations were estimated to be at the level of 10^{13} to 10^{14} cm^{-2}.[21],[24] Because both bulk defects and interface defects exist in low-k a-SiOC:H films, and also because the distribution of defects is not uniform in the bulk, the defect concentration is usually expressed in units of cm^{-2}, rather cm^{-3}.[21]

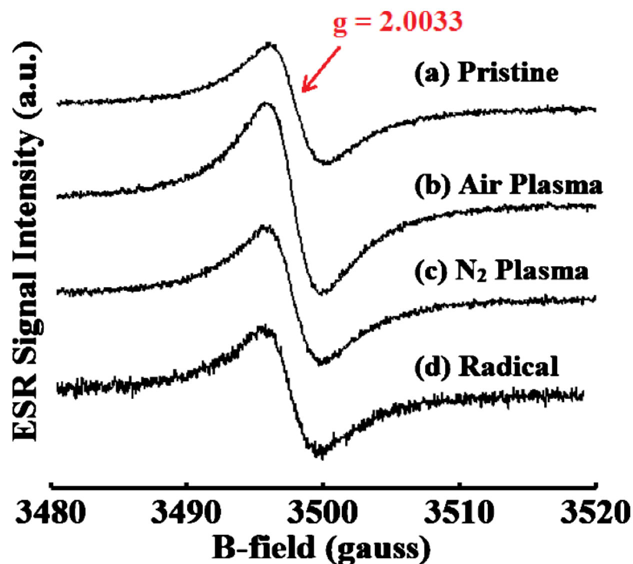

Figure 2-2 ESR signals for a-SiOC:H (k=2.65) with various plasma treatments.[21]

The bulk intra-gap traps or other defect states can significantly affect electron transport across low-k dielectric thin films. Numerous electrically based measurements have shown a direct correlation between trap/defect state concentration, leakage currents, breakdown voltages, and TDDB failures of low-k materials.[25],[26],[27]

2.1.1.3. Surface densification and roughening

During the etching process, in order to increase the etch rate and to have a better control of the etch profile (isotropic), an RF bias is usually coupled to the electrode to increase the ion energy, up to hundreds of electron-volts.[1] For porous low-k a-SiOC:H films, the physical bombardment from the ions causes densification of the a-SiOC:H surface to form a SiO_2-like layer on the top surface, which is related to the modification of pore density and pore interconnection in the top surface.[28] This effect gets even worse for high molecular-weight plasmas. It was reported that after Ar plasma exposure with a -100 V RF bias showed a 4.4% reduction in porosity of the low-k material compared with

the porosity after O_2 plasma exposure.[28] X-ray reflectivity data from Shi *et al.* [29] showed that the densified layer was up to 30 nm underneath the film surface. The densified SiO_2-like layer was reported to block in-diffusion of moisture, while at the same time, it can also block etch-gas radicals from diffusing inside the porous low-k dielectric, resulting in a change in the etch rate.[29]

Roughening of the sidewalls and the bottom of low-k trenches, due to collapse of pores or newly formed chemicals at the surface, has also been reported.[30] This induces severe electrical and reliability issues such as (1) a non-conformal barrier deposition that induces Cu diffusion; (2) a change in barrier and the Cu microstructure which can increase the Cu resistivity; (3) a variation in the critical dimension along the Cu lines which can induce both a change in interline capacity and Cu-line resistivity.[31],[32]

2.1.1.4. Hydrophilicity

Hydrophilicity is another common feature of plasma-induced damage to low-k a-SiOC:H dielectric materials.[5], [33],[34] The -Si-CH_3 groups in a-SiOC:H are originally hydrophobic. Once exposed to plasma, especially for photoresist stripping and cleaning using an oxygen plasma, the methyl terminals (-CH_3) are removed, as detailed previously, and result in the formation of hydrophilic -Si-OH groups.[5] These hydrophilic groups enable significant amounts of moisture to be absorbed from the ambient following diffusion into the bulk of a-SiOC:H through interconnected pores. As illustrated in **Figure 2-3**, FTIR spectra of low-k films after Ar, O_2, N_2, H_2 and N_2/H_2 plasma exposure, measured by Bao *et al.*[28], show an increase of the -Si-OH and H_2O peaks between 3200 and 3600 cm^{-1}, which is good evidence of plasma-induced surface hydrophilicity.

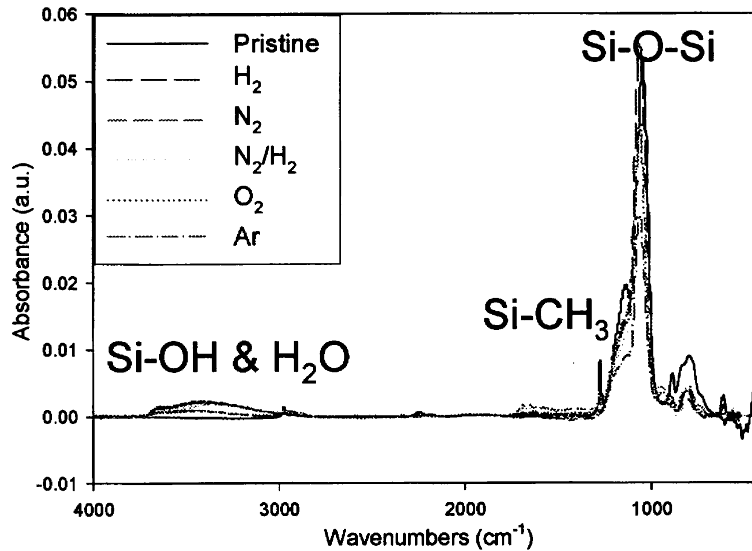

Figure 2-3 FTIR spectra of low-k films after Ar, O_2, N_2, H_2 and N_2/H_2 plasma exposure.[28]

It has been reported that there exist four types of water-related chemical groups attached to the -SiO_2• groups, as shown in **Figure 2-4**.[35] The α-bonded and β-bonded water components, often called physisorbed water and chemisorbed water, respectively, are water molecules that are hydrogen-bonded to the hydrophilic hydroxyl groups. Unlike α -bonded water molecules that are loosely bonded to each other and to surface hydroxyl groups, β -bonded water is tightly hydrogen-bonded to two neighboring hydroxyl groups. The γ_1 type of water-related group represents the hydrogen-bonded silanol (-Si-OH···HO-Si-) and the γ_2 type represents isolated silanol (-Si-OH).[36],[37]

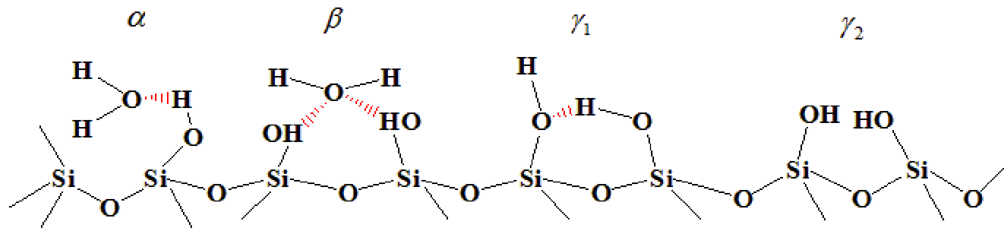

Figure 2-4 Schematic illustrating of the various -OH species existed in a-SiOC:H and their bond types to siloxane groups.[36] Red lines in the figure represents the hydrogen bond formed between absorbed water and the dielectric material.

The absorbed water, which has a dielectric constant over 70 for frequencies between 1-6 GHz, drastically increases the k-value of the low-k materials, [38] which will make the effort to decrease the interconnect capacitance null and void.

In addition, moisture uptake into the a-SiOC:H thin film can cause reliability issues both mechanically and electrically.[36],[39],[40],[41] One of our previous studies has shown that absorbed water within the a-SiOC:H thin films can cause a change of film hardness and elastic modulus.[36] Michelon *et al.* [39]demonstrated that by eliminating moisture, the leakage current can be significantly decreased. In addition, higher breakdown electric fields and longer dielectric lifetimes can be achieved. Kubasch *et al.* [40] reported that if water is in the dielectric film, the leakage-current density increased about 6 orders of magnitude due to the ionization of water molecules in presence of the applied electric field. Singh *et al.*[41] examined moisture-induced capacitance-voltage instabilities and illustrated that moisture can lead to flat-band shifts and C-V hysteresis. All of these results underlie the importance of preventing moisture uptake in low-k dielectric materials from the environment.

2.1.2. Mechanical Damage

The mechanical and fracture properties of porous ultralow-k dielectric films are closely linked with porosity, pore morphology, and network structure. During plasma processing, the chemical structures of a-SiOC:H thin films are modified through interactions with various plasma species. As a result, mechanical property changes occur inside the low-k materials. At the device-level, low-k thin films are integrated as a stack with other dielectric/metal layers. Thus, changes of mechanical properties such as hardness and elastic modulus can cause the accumulation of physical stress within these film stacks, resulting in major reliability issues, such as increased leakage current[42] and decreased breakdown voltage.[43]

Recent work has reported plasma-induced mechanical damage to a-SiOC:H low-k dielectrics.[44],[45],[46] One of our previous works[46] studied the effect of water uptake on the mechanical properties of these low-*k* dielectrics. However, the current understanding of plasma-induced mechanical-property changes is still limited. The reports of dominant mechanisms of plasma-induced mechanical property changes are not consistent. For example, Vanstreels *et al.* [44] investigated the modification of He/H_2 plasma exposure on a-SiOC:H low-*k* films. They concluded that He/H_2 plasma exposure results in a decrease in both film hardness and elastic modulus because of plasma removal of porogen residues. In another study, Broussous *et al.* [45] observed increases in both the hardness and elastic modulus of a-SiOC:H low-*k* films after He-plasma exposure and attributed the changes to subsurface densification and/or structural modifications. These inconsistent results might be because the researchers didn't distinguish the roles of energetic ions and VUV photons when examining the effects of plasma exposure on the mechanical properties of low-*k*

materials. The effects of charged-particle bombardment and photon irradiation have not yet been fully elucidated.

More recently, the impact of plasma processing on the fracture behavior of nanoporous dielectric film stacks were studied for various a-SiOC:H materials.[47],[48],[49] Vlassak *et al.* [48]demonstrated that the adhesion of the a-SiOC:H/SiCN interface decreases over time, since plasma-induced moisture uptake and the tendency of water molecules to diffuse along the a-SiOC:H/SiCN interface rather than through the bulk.[50] Guyer *et al.* [51] showed that besides moisture, other environmental species can also induce accelerated film cracking.

2.1.3. Electrical Damage

The most basic requirement for ILDs is that of good electrical insulation that exhibits extremely low leakage currents, high dielectric-breakdown strength and extreme resistance to time-dependent-dielectric breakdown (TDDB).[52] In this regard, plasma-induced damage to the electrical properties of low-k a-SiOC:H materials are of fundamental interest because the degradation of electrical property of low-k dielectrics limits the performance of the subsequent electronic device. Existing work about electrical damage from plasma exposure includes: (1) an increase in k value,[53] (2) charge accumulation, [54] (3) an increase in leakage current, [55] (4) TDDB degradation.[56] *etc*.

2.1.3.1. Increase of k-value

The k value the one of the most important properties of ILDs. For low-k a-SiOC:H, the ability to sustain the k-value during integration is an ideal characteristic. However,

much work has shown that the k-value for a-SiOC:H after plasma processing increases, either due to chemical reactions with the plasma or water absorption from the ambient or both. [53], [57] The k-value tends to increase as the -Si-CH_3 loss increases.[53] Based on Xu *et al.*'s work[57], O_2 plasma causes the most significant increase in the k-value even when it is highly diluted with He, as illustrated in the left part of **Figure 2-5**.

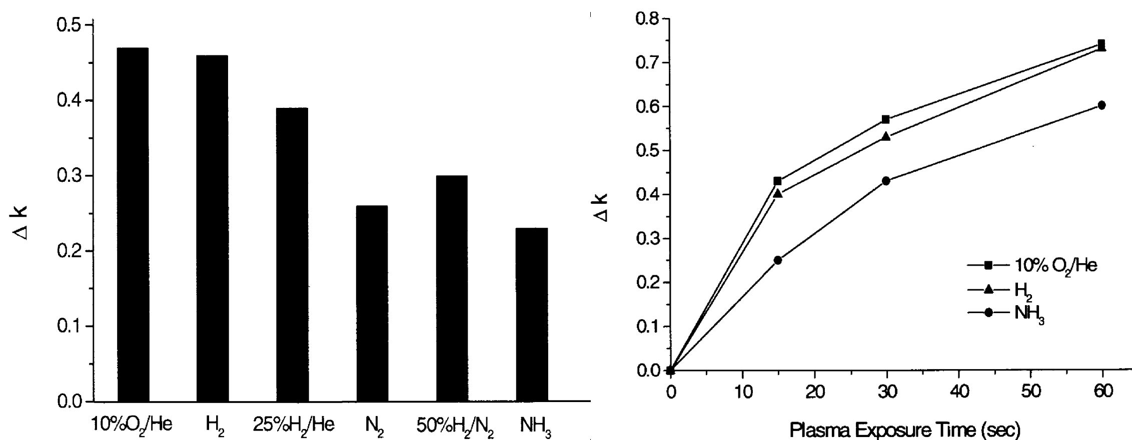

Figure 2-5 *Left*: Changes of k-value under several plasma chemistries when the plasma exposure time was 15 seconds; *Right*: Dependence of k-value change on plasma exposure time. For both figures, data was collected with r.f. source power = 600 W, and pressure = 10 mTorr.[57]

Dilution of the H_2 plasma with He helps to reduce the damage, but the reduction effect is still very limited. The k value after N_2 plasma exposure is much lower than that for the O_2 and H_2 cases. Adding H_2 into N_2 brings the k up again as shown for equally mixed H_2 and N_2. The extent of low-k damage increases with plasma exposure time, as shown in the right part of **Figure 2-5**. The k-value changes rapidly during the initial 10 s of exposure, especially in diluted O_2 and H_2 plasmas, and increases more slowly

afterwards. Baklanov *et al.* [58] showed that the change in k-value was also related to the RF bias and temperature during plasma exposure.

2.1.3.2. Charge accumulation

Plasma processing can cause generation of trap states and charge accumulation. This was observed in plasma-exposed low-k a-SiOC:H thin films.[59],[60] Both charged-particle bombardment and VUV-photon irradiation can contribute to charge accumulation.[54] The charge accumulation can be measured with a Kevin probe or from the C-V characteristics.[61] The surface potential is proportional to the charge density inside the dielectric material. With a higher fluence of ions or VUV photons from the plasma, the dielectric films tend to have higher surface potentials. Atkin *et al.*'s results for low-k films indicate the presence of a significant density of interfacial states and some of these states are attributed to defects associated with excess silicon or excess oxygen at or near the a-SiOC:H/Si interface.[61] Charged-trap states close to the interfaces in thin films of porous low-k dielectric materials are expected to affect interfacial barriers resulting in reliability in these materials.[61]

2.1.3.3. Increase in leakage current

Leakage current is another important electrical parameter of low-k dielectric materials and is directly related to the lifetime and power consumption of devices. Three conduction mechanisms have been commonly reported for low-k dielectrics: Schottky emission (SE), Poole-Frenkel (PF) emission and Fowler-Nordheim (FN) tunneling.[62] The dominant conduction mechanism is determined by the nature of any electrically active defects, such as trapped charges, oxide vacancies and/or fast surface states.[8] Plasma-

induced damage typically increases the defect density, resulting in an increased leakage current. **Figure 2-6** shows a typical leakage-current curve for pristine and Ar-plasma-treated low-k dielectric films. It can be seen that plasma exposure has increased the leakage current of the low-k film.[55]

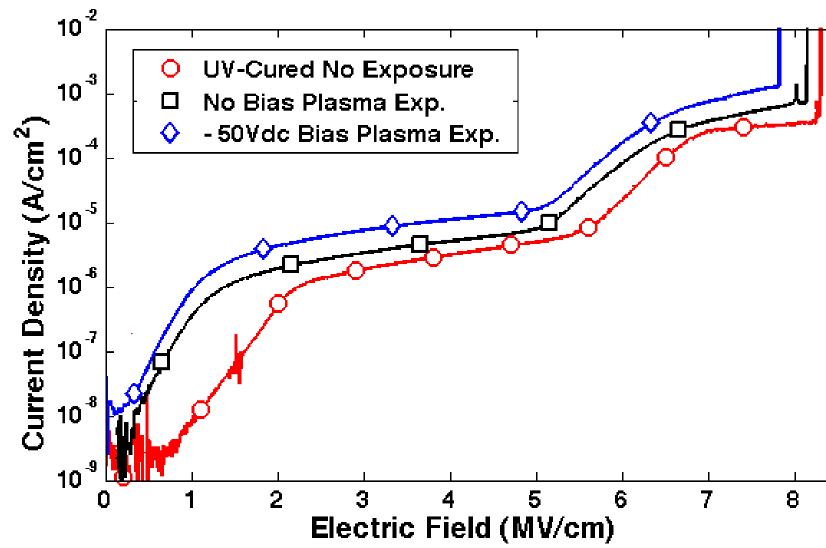

Figure 2-6 Effect of plasma exposure on leakage currents in k = 2.65 a-SiOC:H.[55]

2.1.3.4. Early breakdown

Time-dependent dielectric breakdown (TDDB), defined as spontaneous dielectric breakdown during long-term application of relatively low electric fields, is a major concern for low-k organosilicate dielectrics. Characteristic lifetimes of the dielectrics or device can be interpreted by examining the 63.2% Time-to-Failure (TTF) of the dielectric.[63] Breakdown of low-k dielectrics can be exacerbated by several effects including electric-field stress (resulting in damage-inducing leakage currents), thermal stress, as well as plasma-processing induced degradation of the electrical, chemical, and mechanical properties of the dielectric.[64]

Figure 2-7 shows the comparison of the Weibull statistics [26] characteristic failure percentages as a function of the applied electric field for pristine, VUV irradiated and plasma-exposed samples. Both VUV and plasma exposure resulted in reduced characteristic lifetimes relative to the pristine case. Reduced TTF implies an early breakdown and can result from an accumulation of defects from plasma exposure-induced damage.

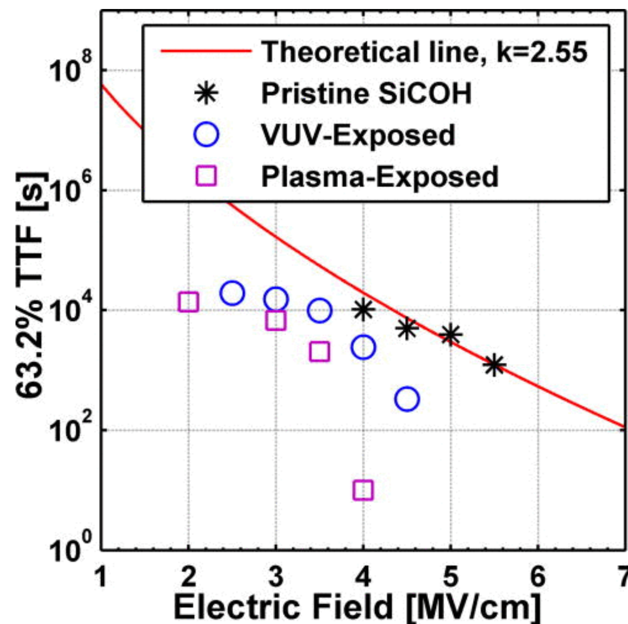

Figure 2-7 63.2% Time-to-Failure (TTF) versus electric field for pristine, VUV-exposed, and plasma-exposed a-SiOC:H thin films.[26]

2.2 Plasma Vacuum-Ultraviolet Photon Irradiation

Photons are emitted from a plasma when an electron transitions from an excited energy level to a lower energy level of atom or molecule. Photons produced in the plasma can also be emitted from free-free, free-bound or wall bremsstrahlung. Since the total power of photons due to bremsstrahlung is proportional to $T^{1/2}$, where T is the temperature

of the electrons, for a processing plasma, the number of photons due to bremsstrahlung is much smaller of electrons.[65],[66] As a result, the emitted photons from a processing plasma are mostly line radiation.[67] In addition, the photon energy of line radiation depends primarily on the electron orbits of the atoms or molecules used in the plasma. Processing plasmas used for semiconductor fabrication often have very strong line radiation in the vacuum-ultraviolet (VUV) region of the spectrum (6-22eV). These VUV photons have energies large enough to break most of the chemical bonds. Therefore, measuring the effects of VUV irradiation on electronic materials is very important.

Fundamental interest in this issue derives first from the need to determine, in general, the interactions of various plasma components (free radicals, ions, electrons, and photons) with electronic materials. In this work, especially for Cu/low-k organosilicate interconnects, we want to examine the effects of VUV irradiation during plasma exposure for three more reasons: (1) high photon energy compared with UV and visible photons, (2) high photon flux (fluence) and (3) deep penetration depth.

(1) High Photon Energy:

Table 2-1 shows the VUV photon energy emitted from fluorocarbon plasmas (CF_4, C_2F_6, CHF_3 and C_4F_8 *etc*, which are used for low-k dielectric etching), oxygen plasmas (which are used for photoresist removal (ashing)) and mixtures of C_2F_6 with argon and hydrogen (used for sidewall polymerization).[67] As can be seen, almost all of these plasmas can generate photons with energies higher than the bandgap energy of a-SiOC:H dielectrics, which were measured in the range of 6.8-8.3 eV. [25],[68],[69]

Table 2-1 VUV emission lines in dielectric-processing plasma discharges.[67]

Feed Gas	Operating Condition	Emission Lines	Photon Energy
CF_4	20 mTorr, 200W	95 nm, 165.7 nm, 202.6 nm	13.0 eV, 7.5 eV 6.1 eV
C_2F_6	20 mTorr, 200W	156.1 nm, 165.7 nm, 202.6 nm	7.9 eV, 7.5 eV 6.1 eV
CHF_3	20 mTorr, 200W	102.6 nm, 121.6 nm	12.1 eV, 10.2 eV
C_4F_8	20 mTorr, 300W	95 nm, 132.9 nm	13.0 eV, 9.3 eV
O_2	20 mTorr, 150W	130 nm, 135 nm, 197 nm	9.5 eV, 9.2 eV, 6.3 eV
Ar	20 mTorr, 200W	104.8nm, 106.6 nm	11.8 eV, 11.6 eV
C_2F_6/Ar	20 mTorr, 200W 1:1 gas mixture	104.8 nm, 106.6 nm, 156.1 nm, 165.7 nm, 202.6 nm	11.8 eV, 11.6 eV 7.9 eV, 7.5 eV 6.1 eV
C_2F_6/H_2/Ar	20 mTorr, 200W 1:1:1 gas mixture	104.8 nm, 106.6 nm, 121.6 nm, 156.1 nm, 165.7 nm, 202.6 nm.	11.6 eV, 11.8 eV 10.2 eV, 7.9 eV, 7.5 eV, 6.1 eV

VUV photons with energies greater than the bandgap energy in SiO_2-based dielectrics, like a-SiOC:H organosilicates, will be absorbed in the dielectric, producing electron-hole pairs and E' defect centers.[70] An E' center is formed from a silicon atom which is bonded only to three oxygen atoms and hence, has one dangling bond. Electron-hole pairs can also be created in the bulk of the low-k dielectrics by VUV photons.[59] These holes may become trapped near dielectric interfaces causing degradation in device characteristics such as dielectric breakdown[71], decreased lifetime of minority carriers, and a flatband voltage shift [70]. In addition, the photon energies listed in **Table 2-1** are higher than the strength of the chemical bonds existing in a-SiOC:H. For example: Si-O bonds (8.3 eV), Si-C bonds (4.7 eV), Si-H bonds (3.1 eV), Si-Si bonds (3.4 eV), C-H bonds

(3.5 eV) and O-H bonds (4.4 eV).[28] These high-energy photons can break these and other chemical bonds and generate other chemical defects besides the E' centers, such as C dangling bonds[25], making the material much more susceptible to damage.[13]

(2) High Photon-Fluence

The intensity of the VUV photon irradiation depends on plasma parameters, including the type of plasma reactor, RF power, pressure and gas flow etc., as well as the feed gas composition and exposure time.[72] Woodworth *et al.*[67] examined the photon flux that reached the wafer from inductively-coupled plasma (ICP) reactors. For pure fluorocarbon gases (*e.g*, C_2F_6, CHF_3 and C_4F_8) that were examined in their experiment, the flux of VUV photons to the wafer varied from 1 to 3×10^{15} photons/cm^2 s, which is equivalent to 1.5 to 5 mW/cm^2, expressed as power density. These measurements imply that for typical 20 mT, 200 W RF discharges, 0.1% - 0.3% of the RF source power to these discharges ends up hitting the wafer as VUV photons. For typical ''ashing'' discharges containing pure oxygen, the VUV flux intensities are slightly higher - about 5×10^{15} photons/cm^2 s, which is one order of magnitude larger than the ion flux (about 1×10^{14} ions/cm^2 s).[46]

When argon or hydrogen diluents are added to the fluorocarbon gases, the VUV intensities increase dramatically. A mixture of Ar/C_2F_6/H_2 in a plasma can yield VUV fluxe rates on the wafer up to 4×10^{16} photons/cm^2 s. [67] Such high-flux rate photons are a significant damage source and cannot be neglected.

(3) Photon Penetration Depth:

Unlike ions and radicals, VUV photons have a much deeper penetration depth into low-k a-SiOC:H materials and can cause bulk modifications. Under typical plasma processing conditions, the penetration depth of ions into a-SiOC:H is less than 2 nm,[46],[73] which means that the ions can only modify the top surface of low-k thin films. The penetration of radicals into an a-SiOC:H layer is diffusion-dominated, due to the concentration-gradient and the fact that the radicals are uncharged. [15] This step is slow and depends highly on the porosity and film density. However, for VUV photons passing into a SiO_2-based dielectric, the penetration depth of 8-eV photons can be up to 1 μm.[67]

Palik and Philip *et al.*[74] measured the photon-penetration depth of VUV light in amorphous SiO_2. At wavelengths shorter than 130 nm (photon energy > 9.5 eV), the penetration distances were in the range of 10 - 100 nm. Between 130 and 140 nm (photon energy: 8.8 - 9.5 eV), penetration distances are much larger, from 100 nm to 1μm.[67] For the case of porous a-SiOC:H low-k thin film, the photon-penetration depth is believed to be larger due to the decreased density of the dielectric. For example, a 9 eV photon can penetrate into a-SiOC:H (k=3.2) more than 100 nm[75].As a result, in real device scale, the VUV photons can penetrate through the low-k interlayer dielectrics and also the underneath capping layer dielectric materials or metal layer. Considering the high energy and high flux intensity of photons, as described earlier in this section, this may cause significant reliability issues.

2.3 Electrical-Conduction Mechanisms in Cu/Low-k Interconnects

Before addressing the breakdown mechanisms of Cu/low-k interconnects from VUV irradiation, it is first necessary to present a summary of the electrical conduction mechanisms through Cu/low-k organosiliate interconnects, because these conduction mechanisms are directly related to the breakdown characteristics, including TZDB and TDDB.[63] . Here, we need to know not only the conduction properties in the intrinsic low-k organosiliates but also the band alignment and defect states or traps at the interface between Cu and low-k dielectrics (such as dense low-k a-SiOC:H thin film, which has the potential to be used as either low-k ILD or low-k capping layer dielectric.

For intrinsic low-k dielectrics, three dominant conduction mechanisms have been commonly reported: Schottky emission (SE), Poole-Frenkel (PF) emission and Fowler-Nordheim (FN) tunneling. SE and PF emissions describe field-enhanced thermal excitation of electrons entering the conduction band from (1) the low-k interface or (2) the trap states with coulomb potentials, respectively. The FN tunneling conduction is caused by electrons tunneling from the metal Fermi energy or trapping sites in the material itself into the low-k dielectric conduction band. These studies or measurements were focused on low-k dielectric itself, using a-SiOC:H/Si film stack. There was no Cu layer, so no capping layer was needed for this work. The equations describing SE, PF emission and FN tunneling are listed below,[62]

Schottky emission

$$J_{SE} = A^{*} \cdot T^{2} \cdot exp\left[\frac{-q\left(\varphi_{SE}-\sqrt{qE/4\pi\varepsilon_{r}\varepsilon_{o}}\right)}{kT}\right] \quad (2\text{-}1)$$

Poole-Frenkel (PF) emission

$$J_{PF} \sim E \cdot \exp\left[\frac{-q\left(\varphi_{PF}-\sqrt{qE/4\pi\varepsilon_r\varepsilon_o}\right)}{kT}\right] \quad (2\text{-}2)$$

Fowler-Nodheim(FN) tunneling

$$J_{FN} \sim E^2 \cdot \exp\left[\frac{-8\pi\sqrt{2m^*}\,(q\varphi_{FN})^{3/2}}{3qhE}\right] \quad (2\text{-}3)$$

where J is the current density in amperes/^{m2}, $A*$ is the Richardson constant with a unit of ampere/(meter* Kelvin)^2, T is the temperature with a unit of degrees Kelvin, q is the elementary charge in coulombs, φ is the Schottky barrier height with a unit of volts, E is the electric field with a unit of volts/meter, ε_r is the dielectric constant which is dimensionless, ε_o is the permittivity of free space with a unit of farads/meter, $m*$ is the electron effective mass with a unit of kg, [76] and h is Planck's constant with a unit of m^2 kg/sec.

An efficient way to determine the dominant conduction mechanism is to study the leakage-current behavior as a function of field at different temperatures. If either SE or PF emission dominates, the slope extracted from the relation between ln(J) or ln(J/E) versus E$^{1/2}$ should be similar to the theoretical value as suggested by $\beta_{SE} \sim \beta_{PF} \sim\sqrt{q^3/\pi\varepsilon_r\varepsilon_o}$. If FN tunneling dominates, the leakage current exhibits a strong field dependency and is independent of temperature. The plot of ln(J/E^2) and 1/E should also yield a straight line. In addition, in each conduction mechanism, trap depth or barrier height φ can be extracted by employing appropriate fitting procedures.

For Cu/low-k interconnects, the band alignment between Cu and low-k dielectrics is critical to the fundamental mechanisms involved in electrical leakage. The barrier height at both the low-k/Si and the low-k/metal interfaces can be measured with internal

photoemission experiments. Atkin *et al.* [60] suggest that this value is 4.1 ± 0.4 eV for a low-k/Si interface. With a Ta or TaN_x metal capping layer, Shamuilia *et al.* [77] reported a barrier height close to 4.5 eV. The energy barrier did not significantly vary when Ta/TaN was used as the capping layer material.[77] This value is further substantiated by our latest work using VUV photoemission spectroscopy to measure the Schotttky barrier at the Cu/low-k interface.[78] Due to the barrier height being around 4 eV at the low-k dielectric interface, interface-controlled SE only happens when there are deep interface states/traps [8] or when there are changes to emission paths because of the existence of other low barrier-height interfaces, such as the etch-stop layer/metal interfaces (less than 2.0 eV).[79] As a result, PF emission is more likely the dominant conduction mechanism across the Cu/low-k interface, especially at low electric fields (1.0 - 4.0 MV/cm or less) .[80] FN-tunneling conduction can occur at high field ranges (6.0 - 7.0 MV/cm or above).[81]

2.4 Time-dependent Breakdown of Cu/Low-k Interconnects

Time-dependent dielectric breakdown (TDDB) of porous low-k dielectrics used in advanced BEOL interconnects is a serious reliability concern, which can be exacerbated by several influences including electric-field stress (which results in damage-induced leakage currents), thermal stress (which can increase the diffusivity of impurities and metal atoms from interconnects)[82], as well as plasma-processing-induced degradation of the chemical, mechanical, and electrical properties of the dielectric.[26],[83],[84] After describing the main dielectric-leakage mechanisms in Cu/low-k interconnects, this section will summarize the major TDDB models that have been reported in the literature.

Models proposed for dielectric reliability are the Lloyd model [80], the 1/E model [85], the thermochemical E model [86], the $E^{1/2}$ model [42], the E^2 model [87] and the Haase model [88]. These models can be broadly categorized into those that consider only intrinsic breakdown (Lloyd, 1/E, E and Haase models) and those that take into account Cu migration in low-k materials ($E^{1/2}$ models and E^2 model). Experimental attempts on validation of these Cu/low-k TDDB models using data obtained from different field stressing will be discussed as well.

2.4.1. Intrinsic TDDB in Low-k Organosilicates

2.4.1.1 Lloyd Model

This model was proposed by Lloyd *et al.* in 2005 and is also referred as the $\left(1/E+\sqrt{E}\right)$ model. [80] In this model, the damage to the low-k dielectric is assumed to be caused by energetic electrons. The electrons are injected into the dielectric and get accelerated under an electric field. After the electron has traversed a certain distance within the dielectric, it will undergo a scattering event and all the energy that it has acquired from the field up to that point will be dissipated. If the electron has more than a certain threshold energy, a new defect or trap can be generated, as illustrated in **Figure 2-8**. The accumulation of defects in the dielectric eventually leads to TDDB.

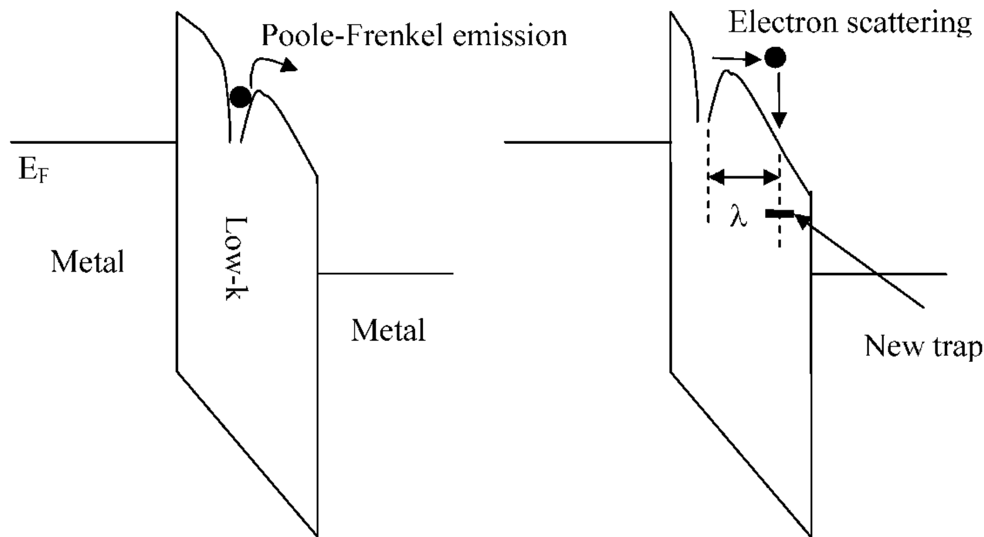

Figure 2-8 Energy bandgap diagram for the Lloyd model. [89]

There are several assumptions in this model: (1) electrons are injected by Poole-Frenkel tunneling; (2) the electron-free path between scattering events follows an exponential distribution; (3) there is a threshold energy for the electron to generate a new defect center and (4) the time to breakdown is dependent on the rate at which defects are generated. Accumulation of defects up to some threshold number N_f that will result in dielectric failure The failure time follows the following equation:

$$TTF = \frac{(N_f - N_0)}{AE} \exp(-\gamma\sqrt{E} + \frac{E_t}{\mu q E}) \quad (2\text{-}4)$$

where N_0 is the number of pre-existing defects, A and γ are the fitting parameters from the Pool-Frenkel equation, E is the electric field, N_f is the threshold number of defects when the dielectric breaks down, μ is the mean free path of the electron, q is the electron charge, and E_t is the threshold energy to create a new defect center.

The $\sqrt{E}$ dependence in Equation (2-4) is due to the Poole-Frenkel injection mechanism. At low fields, the *1/E* dependence will predominate. Despite the simplicity of the model, there is no information about the nature of the defects and how the defects eventually lead to the breakdown of the dielectric. It should be noted that there is no temperature-dependent term in Lloyd model, which cannot reflect the temperature-related TDDB.

2.4.1.2 *1/E* Model

The *1/E* model was first proposed by Chen *et al.* to explain TDDB in gate oxides and was modified later to describe TDDB in low-k dielectrics.[27],[90] This type of dielectric failure mechanism can be illustrated by examining the energy band diagram in **Figure 2-9**. In this model, one electrode is a metal while the other electrode is a semiconductor. During voltage stressing, a high electric field develops across the oxide and electrons tunnel into the oxide from the cathode by Fowler-Nordheim tunneling.

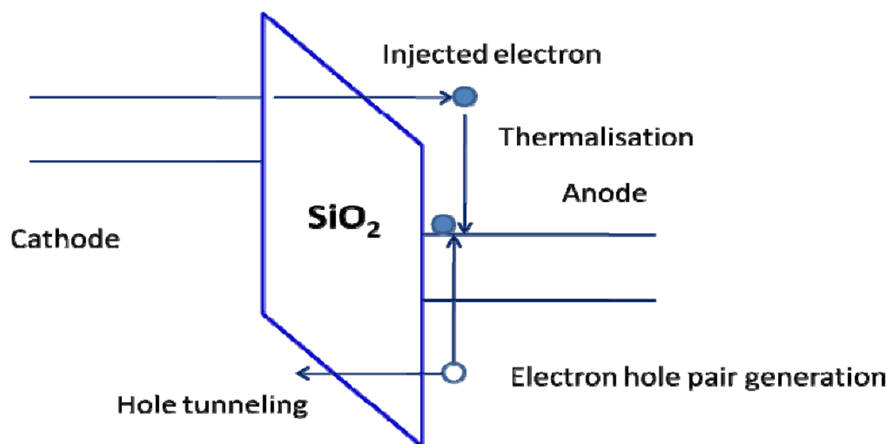

Figure 2-9 Energy-band diagram illustrating the anode hole-injection mechanism in the 1/E model. [89]

When these energetic electrons arrive at the anode, they will thermalize and their energy is used to generate hole-pairs in the anode. The holes, which are able to surmount the energy barrier at the valence band, are then injected back into the dielectric because of the direction of the applied field. Since holes have a greater effective mass than electrons, they are more easily trapped within the oxide layer. As a result, positive oxide-trapped charge will build up over time near the cathode. This will further increase the electric field near the cathode and lead to more Fowler-Nordheim injection of electrons into the oxide. Eventually, a positive feedback loop will develop and dielectric breakdown will ensue.

The TTF using the *1/E* model can be expressed as

$$TTF \propto \exp\left(\frac{\beta}{E}\right) \tag{2-5}$$

where β is the field acceleration parameter which is dimensionless, (equal to the slope of the line in a probability plot in Weibull scale and is related to the breakdown mechanism.) *E* is the electric field. At low fields, the prediction of the TTF from the *1/E* model tends to converge with that of the Lloyd model. Since one of the electrodes in the *1/E* model must be a semiconductor, it is usually applied to predict the intrinsic breakdown of low-k organosilicates, like a-SiOC:H/Si stacks, rather than that of a damascene Cu/low-k interconnect structure, in which there is a-SiOC:H/Cu stack.[63]

2.4.1.3 Thermochemical *E* Model

Under the thermochemical ***E*** model [86,91], TDDB occurs as a result of electric-field-induced breakage of weak chemical bonds in the dielectric network so that new defects (traps) are generated. When a sufficient density of traps is generated in the dielectric,

a conductive path linking the two electrodes will be formed and a large increase in current occurs. In this model, the chemical bonds that are broken by the weak electric field are found in E' defect centers in the dielectric.[92] E' centers are also called oxygen vacancies and their structure is illustrated in **Figure 2-10**. Under the electric field, the Si-Si bond in the E' center will be distorted. With some thermal excitations, this distorted Si-Si bond can be broken more easily. The model assumes that if enough Si-Si bonds in the E' centers are broken, then TDDB will take place.

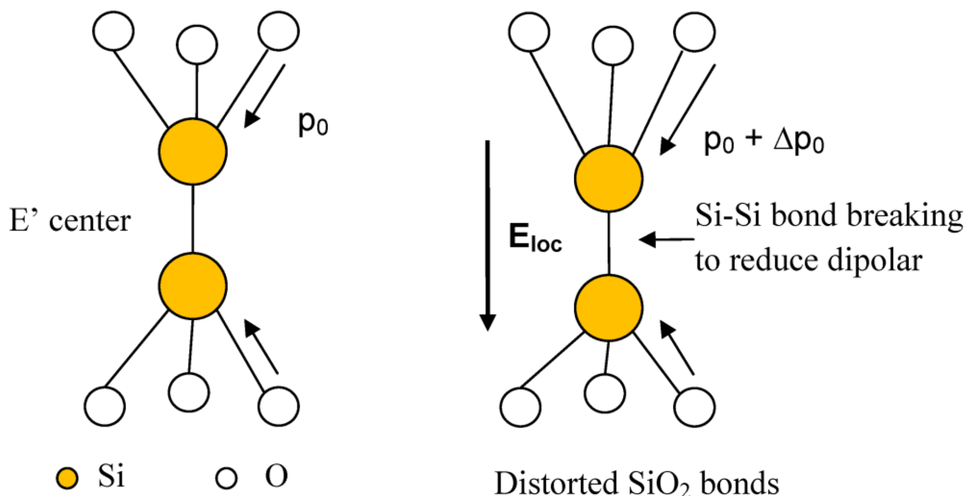

Figure 2-10 Schematic diagram of the Si-Si bond breaking process of the E' center in SiO_2 under voltage stress. Each Si-O bond has a permanent dipole moment p_o. An applied electric field distorts the Si-O bonds in the O_3Si-SiO_3 unit and makes it energetically favorable to break the Si-Si bond. [89]

Under the thermochemical *E* model, the TTF can be expressed as,

$$TTF \propto exp(\frac{\Delta H_0 - \alpha E}{k_B T}) \quad (2\text{-}6)$$

where ΔH_0 is the enthalpy (or activation energy) for the breaking of the Si-Si bond (in a range of 1.0 – 1.5 eV),[93] α is a constant related to the polarization of the chemical bond (Si-Si E' center), k_B is the Boltzmann constant, T is the temperature, and E is the electric field. The term a/k_BT is also generally known as the acceleration parameter during bias-temperature stress experiments. The thermochemical model is capable of fitting low-k TDDB data at high electric fields. In addition, extrapolation to lower fields using this model will tend to give the most conservative predictions.

2.4.1.4 Haase Model

The Lloyd model, the *1/E* model and the *E* model are all aimed to develop a predictive capability that relates the TTF to the electric field and/or temperature and to extrapolate the TDDB lifetime at low field conditions from data obtained at high electric field and/or high temperature conditions. The Haase model [88] was developed from the Lloyd model and does not aim to develop a TTF relationship on the grounds that some of the mechanisms used in the previous models lack empirical justification. Instead, it attempts to numerically simulate the low-k leakage current as a function of time and use the time-to-minimum-current (TTMC) as a criterion for dielectric failure, as shown in **Figure 2-11**.

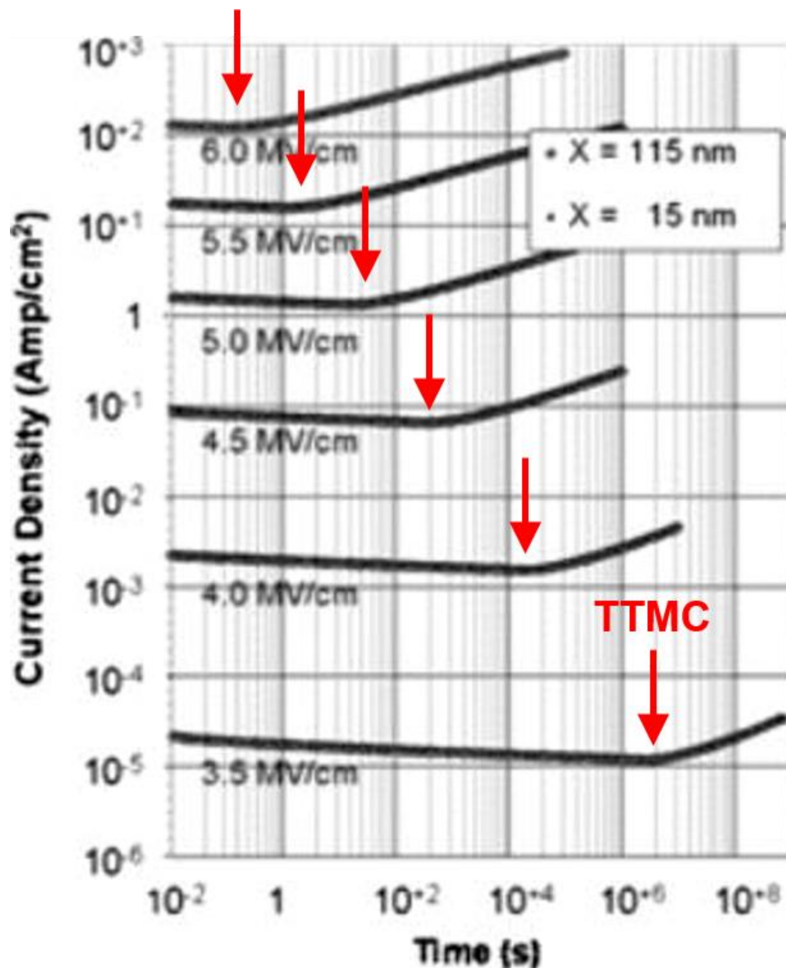

Figure 2-11 Leakage currents in a dielectric thin film as a function of time. The arrows in the figure show the location of time-to-minimum-current (TTMC).[88]

The assumptions made for the Haase model are similar to those for the Lloyd model.[80] The leakage current in the low-k dielectric is found by numerically solving three one-dimensional coupled partial-differential equations. They are: Poisson's equation, the continuity equation and the rate equation for the generation of traps within the low-k film simultaneously. Finite-element simulations have been employed for the calculation of the electric field from Poisson's equation, which could make the TTF in the Haase model much more complicated than that in other models In this model, three one-dimensional

coupled partial differential equations have to be solved. It is hard to say whether this model is better or not. The Haase model is based on simulation while the other models are based on experimental measurements. The Haase model is capable of fitting low-k TDDB date at low fields (1-2 MV/cm or less), while the Lloyd and thermochemical E model work better at high fields.

2.4.2. Extrinsic TDDB in Low-k: Effects of Cu Migration

Extrinsic TDDB in low-k dielectrics refers to the situation that the breakdown is caused by transport of external impurities into the sample. For Cu/low-k interconnects, the extrinsic TDDB is mainly Cu migration-induced TDDB. Cu migration, including both Cu atom diffusion and Cu-ion drift, has been a critical reliability concern for low-k organosilicates, used as either ILD or capping/etch-stop layers. Even with diffusion barriers, Cu atoms/ions can still diffuse or drift into low-k dielectrics [94], [95] and form a deep-level defects in the dielectric band gap, causing TDDB degradation. Hence, new models have been expressly developed to describe extrinsic TDDB in low-k dielectrics by taking into account the effects from Cu migration. These models include the Cu drift E model[96], the $\sqrt{E}$ model[42] and the E^2 model[87].

2.4.2.1 Cu Drift *E* Model

In one of the earliest attempts to develop a quantitative Cu/low-k interconnect TDDB reliability model, Wu *et al.* [96] considered the diffusion and drift of Cu^+ ions in a periodic potential with an external bias and developed the Cu drift $\boldsymbol{E}$ model. Cu^+ ions are thought to be generated in the metal by trapped oxides, such as H_2O or OH-.[97] The basic mechanism of failure is similar to that by Suzumura *et al*, where Cu+ ions form deep traps

in the dielectric and charge accumulates as a sheet of positive charge and increases band bending. The leakage mechanism then changes from the Poole-Frenkel to Fowler-Nordheim and the leakage current will increase further with time. When the concentration of Cu ions near the cathode exceeds a critical concentration, TDDB is assumed to occur. [98] The predicted TTF according to this model is:

$$TTF = \frac{B\exp\left(\frac{E_a}{k_B T}\right)}{\exp\left(\frac{q\lambda E}{k_B T}\right) - \exp\left(-\frac{q\lambda E}{k_B T}\right)} \quad (2\text{-}7)$$

where k_B is the Boltzmann constant, T is the temperature, λ is the periodicity of the potential. E_a is the activation energy that the Cu^+ ions have to overcome in order to jump to the adjacent potential well and B is a proportionality constant that depends on λ. In the limit of high fields, this TTF relationship reduces to the same form as the thermochemical E model, as described previously, with an acceleration parameter given by $q\lambda/k_B T$:

$$\mathrm{TTF} = B\exp\left(\frac{E_a - q\lambda E}{k_B T}\right) \quad (2\text{-}8)$$

For experimental verification of their model, Wu *et al.* [96] used the published data of Vogt *et al.* [97] and fitted the data for SiO_x and SiN_x to equation (2-7). For each dielectric, a good fit over a range of electric field and temperature could be obtained with one set of values for E_a and λ.

2.4.2.2 $\sqrt{E}$ Model

The $\sqrt{E}$ models [42,98] for low-k dielectrics involve migration of Cu into the low-k dielectric prior to breakdown, as shown in **Figure 2-12**. In the study by Suzumura *et al.*, as depicted in part (a) of **Figure 2-12**, the Cu^+ and electrons drift in different directions

under the electric field. The capping layer provides a path for Cu^+ between the metal lines. Initially, the conducting mechanism is Poole-Frenkel. Due to this leakage, Cu^+ will accumulate at one electrode and will shorten the distance between the two metal electrodes. If the distance is short enough, the conducting mechanism will be changed to Fowler-Nordheim and the dielectric will eventually break down if there is enough Cu^+ accumulation. Because Cu^+ forms deep trap centers in the capping layer (SiN), it will make electron tunneling more difficult. As a result, the leakage current will drop during the TDDB process. The TTF is given as

$$TTF \propto \frac{1}{E}\exp\left(-\frac{q}{kT}\left(\frac{q}{\pi\varepsilon}\right)\sqrt{E}\right) \quad (2\text{-}9)$$

where E is the electric field, ε is the dielectric permittivity, q is the charge of the ion, k is the Boltzmann constant and T is the temperature. The $\sqrt{E}$ model could well explain why the leakage current decreases before dielectric breakdown and fits well with experimental data.[99]

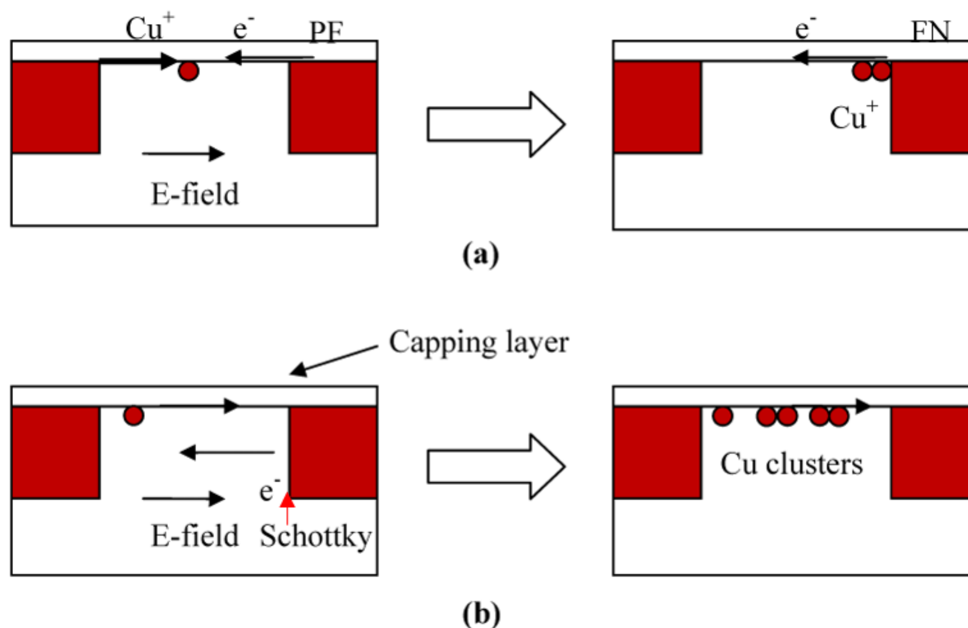

Figure 2-12 Schematic diagram of the process leading to dielectric breakdown in the $\sqrt{E}$ model of (a) Suzumura *et al.*[98] and (b) Chen *et al.*[42] ("Schottky" in the figure represents the Schottky barrier at the Cu/dielectric interface, as indicated by the arrow.)

In the study by Chen *et al.* [42], electrons are considered to be injected from the cathode into the low-k dielectric by Schottky emission (**Figure 2-12b**). Those electrons that do not undergo scattering within the low-k dielectric become energetic and can use their energy upon arrival at the anode to generate Cu+ ions. These Cu+ ions are then injected into the low-k dielectric at the low-k capping-layer interface and move towards the cathode. Two mechanisms by which the final breakdown may occur are proposed: (1) the Cu^{+} ions combine with electrons and become neutral Cu atoms. These atoms agglomerate into Cu clusters that over time can coalesce into a metallic bridging short; (2) the Cu atoms by virtue of their size can increase the local strain in the low-k dielectric and facilitate bond breakage.

2.4.2.3 E^2 Model

The E^2 model was proposed by Achanta *et al.* [87], which assumes that Cu^+ ion diffusion and drift play a major role in the TDDB of low-k dielectrics, like the $\sqrt{E}$ models. Under electrical stress, Cu^+ ions migrate into the low-k dielectric from the anode. After sufficient time, a layer of Cu^+ ions will accumulate at the cathode and result in an increase in the electric field nearby. A mass-transport model was developed for the diffusion/drift of Cu ions, in which the coupled Poisson equation and the continuity equations were solved simultaneously to yield the Cu^+ ion concentration and the potential within the dielectric. This is different from the $\sqrt{\mathbf{E}}$ model as discussed previously.

The time for the electric field at the cathode to increase to the breakdown field can be expressed as a function $f(C_e, T, E_{app})$ of ion solubility (refer to the maximum amount of Cu ions dissolved in the low-k dielectric at equilibrium) in a low-k dielectric (C_e), the absolute temperature T, and the applied field E_{app}. The function can be computed from the mass transport model.[87] Also, the model assumes that the enhanced electric field at the cathode will eventually lead to bond breakage at defects in the dielectric, instead of increased Fowler-Nordheim tunneling. The proposed TTF function is written as,

$$TTF \propto \exp\left(\frac{E_a - \gamma E_{app}^2}{kT}\right) f\left(C_e, T, E_{app}\right) \qquad (2\text{-}10)$$

where E_a is the activation energy of Si-O bond, γ is a constant related to the dipole moment of the Si-O bonds, E_{app} is the applied electric field, k is the Boltzmann constant and T is the temperature.

As discussed above, there is currently a large number of dielectric models all of which aim to predict the time to breakdown at electric fields and temperatures under actual use conditions from accelerated test data. There is as yet no consensus on the physical failure mechanism. One of the reasons is that different research groups often use different samples and different test structures. It is impossible to verify the model one by one. In order to narrow down the number of models, it may be useful to carry out a collaborative round-robin type experiment in which Cu low-k test structures fabricated at one laboratory are distributed to different research groups for testing and model verification.

Besides this, no one has considered the effects of VUV photon irradiation on the TDDB reliability of Cu/low-k interconnects. In this work, we focus on examining the VUV-induced TDDB of Cu/low-k interconnects.

2.5 Summary

In this Chapter, background information for understanding the problem of plasma-induced damage to Cu/low-k interconnects and the means necessary to measure VUV-induced damage, including Cu migration into and breakdown of low-k organosilicates, was discussed. First, an overview of past work on plasma-induced damage to low-k organosilicates was presented from three different perspectives, including chemical damage, mechanical damage and electrical damage. Next, details of VUV photons emitted from processing plasmas were discussed, with an emphasis on the importance of VUV photons as potential damage sources. A discussion of the the primary conduction mechanisms in low-k materials, namely Schottky emission, Poole-Frenkel conduction, and Fowler-Nordheim tunneling was presented. Finally, various TDDB models for Cu/low-k

interconnects were introduced, and a relevant summary of past work on TDDB was provided. With this background information, we are able to investigate the effects of VUV photon irradiation on TDDB of Cu/low-k interconnects.

2.6 References

[1] V. M. Donnelly and A. Kornblit, "Plasma etching: Yesterday, today, and tomorrow," *Journal of Vacuum Science & Technology A*, Vol. **31**, 050825 (2013).

[2] M. R. Baklanov, J. F. de Marneffe, D. Shamiryan, A. M. Urbanowicz, H. L. Shi, T. V. Rakhimova, H. Huang, and P. S. Ho, "Plasma processing of low-k dielectrics," *Journal of Applied Physics*, Vol. **113**, 041101 (2013).

[3] S. Rimal, T. Mukherjee, J. Abdelghani, A. Goswami, O. Chyan, J. Stillahn, Y. Chiba, and K. Maekawa, "Evaluation of Plasma Damage to Low-k Dielectric Trench Structures by Multiple Internal Reflection Infrared Spectroscopy," *Ecs Solid State Lett*, Vol. **3**, pp.N1-N4 (2014).

[4] J. Shoeb, M. M. Wang, and M. J. Kushner, "Damage by radicals and photons during plasma cleaning of porous low-k SiOCH. I. Ar/O2 and He/H2 plasmas," *Journal of Vacuum Science & Technology A*, Vol. **30**, 041303 (2012).

[5] J. Shoeb and M. J. Kushner, "Damage by radicals and photons during plasma cleaning of porous low-k SiOCH. II. Water uptake and change in dielectric constant," *Journal of Vacuum Science & Technology A*, Vol. **30**, 041304 (2012).

[6] K. Takeda, Y. Miyawaki, S. Takashima, M. Fukasawa, K. Oshima, K. Nagahata, T. Tatsumi, and M. Hori, "Mechanism of plasma-induced damage to low-k SiOCH

films during plasma ashing of organic resists," *Journal of Applied Physics*, Vol. **109**, 033303 (2011).

[7] H. Kazi and J. A. Kelber, "Plasma damage mechanisms in low k organosilicate glass and their inhibition by Ar ion bombardment," *Journal of Vacuum Science & Technology A*, Vol. **32**, 021302 (2014).

[8] C. Wu, Y. Li, M. R. Baklanov, and K. Croes, "Electrical Reliability Challenges of Advanced Low-k Dielectrics," *Ecs J Solid State Sc*, Vol. **4**, pp.N3065-N3070 (2015).

[9] K. Lionti, W. Volksen, T. Magbitang, M. Darnon, and G. Dubois, "Toward Successful Integration of Porous Low-k Materials: Strategies Addressing Plasma Damage," *Ecs J Solid State Sc*, Vol. **4**, pp.N3071-N3083 (2015).

[10] C. Labelle, R. Srivastava, J. Arnold, Y. Yin, M. Ishikawa, Y. Mignot, H. Yusuff, J. Linville, D. Horak, N. Fuller, R. Patz, A. Darlak, K. Zhou, Y. Zhou, and J. Pender, "Plasma Etch Challenges for Porous Low k Materials for 32nm and Beyond," *Ecs Transactions*, Vol. **34**, pp.329-334 (2011).

[11] G. A. Antonelli, G. Jiang, M. Sriram, K. Chattopadhyay, W. Guo, and H. H. Sawin, "Designing Ultra Low-k Dielectric Materials for Ease of Patterning," *MRS Online Proceedings Library Archive*, Vol. **1249**, pp.1249-F04-15 (2010).

[12] S. W. King, J. D. Bielefeld, G. Xu, W. A. Lanford, Y. Matsuda, R. H. Dauskardt, N. H. Kim, D. Hondongwa, L. Olasov, B. Daly, G. Stan, M. Liu, D. Dutta, and D. Gidley, "Influence of network bond percolation on the thermal, mechanical, electrical and optical properties of high and low-k a-SiC:H thin films," *J Non-Cryst Solids*, Vol. **379**, pp.67-79 (2013).

[13] B. Jinnai, T. Nozawa, and S. Samukawa, "Damage mechanism in low-dielectric (low-k) films during plasma processes," *Journal of Vacuum Science & Technology B*, Vol. **26**, pp.1926-1932 (2008).

[14] Tetsuya Homma, "Low dielectric constant materials and methods for interlayer dielectric films in ultralarge-scale integrated circuit multilevel interconnections," *Materials Science and Engineering: R: Reports*, Vol. **23**, pp.243-285 (1998).

[15] M. A. Goldman, D. B. Graves, G. A. Antonelli, S. P. Behera, and J. A. Kelber, "Oxygen radical and plasma damage of low-k organosilicate glass materials: Diffusion-controlled mechanism for carbon depletion," *Journal of Applied Physics*, Vol. **106**, 013311 (2009).

[16] Y. H. Wang, R. Kumar, X. Zhou, J. S. Pan, and J. W. Chai, "Effect of oxygen plasma treatment on low dielectric constant carbon-doped silicon oxide thin films," *Thin Solid Films*, Vol. **473**, pp.132-136 (2005).

[17] D. Shamiryan, K. Weidner, W. D. Gray, M. R. Baklanov, S. Vanhaelemeersch, and K. Maex, "Comparative study of PECVD SiOCH low-k films obtained at different deposition conditions," *Microelectronic Engineering*, Vol. **64**, pp.361-366 (2002).

[18] Eric Osei-Yiadom, "Effects of Plasma, Temperature and Chemical Reaction on Porous Low-k Dielectric Films for Semiconductor Devices " Doctor of Philosophy Thesis, University of North Texas, 2010.

[19] M. Creatore, W. M. M. Kessels, Y. Barrell, J. Benedikt, and M. C. M. van de Sanden, "Expanding thermal plasma for low-k dielectrics: engineering the film chemistry by means of specific dissociation paths in the plasma," *Mat Sci Semicon Proc*, Vol. **7**, pp.283-288 (2004).

[20] B. C. Bittel, P. M. Lenahan, and S. W. King, "Ultraviolet radiation effects on paramagnetic defects in low-k dielectrics for ultralarge scale integrated circuit interconnects," *Applied Physics Letters*, Vol. **97**, 063506 (2010).

[21] H. Ren, G. Jiang, G. A. Antonelli, Y. Nishi, and J. L. Shohet, "The nature of the defects generated from plasma exposure in pristine and ultraviolet-cured low-k organosilicate glass," *Applied Physics Letters*, Vol. **98**, 252902 (2011).

[22] H. Sinha, H. Ren, M. T. Nichols, J. L. Lauer, M. Tomoyasu, N. M. Russell, G. Jiang, G. A. Antonelli, N. C. Fuller, S. U. Engelmann, Q. Lin, V. Ryan, Y. Nishi, and J. L. Shohet, "The effects of vacuum ultraviolet radiation on low-k dielectric films," *Journal of Applied Physics*, Vol. **112**, 111101 (2012).

[23] V. V. Afanas'ev, A. P. D. Nguyen, M. Houssa, A. Stesmans, Z. Tokei, and M. R. Baklanov, "High-resolution electron spin resonance analysis of ion bombardment induced defects in advanced low-k insulators (k=2.0-2.5)," *Applied Physics Letters*, Vol. **102**, 172908 (2013).

[24] H. Ren, M. T. Nichols, G. Jiang, G. A. Antonelli, Y. Nishi, and J. L. Shohet, "Defects in low-k organosilicate glass and their response to processing as measured with electron-spin resonance," *Applied Physics Letters*, Vol. **98**, 102903 (2011).

[25] S. W. King, B. French, and E. Mays, "Detection of defect states in low-k dielectrics using reflection electron energy loss spectroscopy," *Journal of Applied Physics*, Vol. **113**, 044109 (2013).

[26] M. T. Nichols, H. Sinha, C. A. Wiltbank, G. A. Antonelli, Y. Nishi, and J. L. Shohet, "Time-dependent dielectric breakdown of plasma-exposed porous organosilicate glass," *Applied Physics Letters*, Vol. **100**, 112905 (2012).

[27] F. Chen and M. Shinosky, "Soft breakdown characteristics of ultralow-k time-dependent dielectric breakdown for advanced complementary metal-oxide semiconductor technologies," *Journal of Applied Physics*, Vol. **108**, 054107 (2010).

[28] J. Bao, H. Shi, J. Liu, H. Huang, P. S. Ho, M. D. Goodner, M. Moinpour, and G. M. Kloster, "Mechanistic study of plasma damage of low k dielectric surfaces," *Journal of Vacuum Science & Technology B*, Vol. **26**, pp.219-226 (2008).

[29] H. L. Shi, H. Huang, J. J. Bao, J. J. Liu, P. S. Ho, Y. F. Zhou, J. T. Pender, M. D. Armacost, and D. Kyser, "Role of ions, photons, and radicals in inducing plasma damage to ultra low-k dielectrics," *Journal of Vacuum Science & Technology B*, Vol. **30**, 011206 (2012).

[30] X. Hua, C. Stolz, G. S. Oehrlein, P. Lazzeri, N. Coghe, M. Anderle, C. K. Inoki, T. S. Kuan, and P. Jiang, "Plasma-surface interactions of nanoporous silica during plasma-based pattern transfer using C4F8 and C4F8/Ar gas mixtures," *Journal of Vacuum Science & Technology A*, Vol. **23**, pp.151-164 (2005).

[31] T. T. Olawumi, E. Levrau, M. Krishtab, C. Detavernier, J. W. Bartha, K. Xu, F. Lazzarino, and M. R. Baklanova., "Modification of Ultra Low-k Dielectric Films by O2 and CO2 Plasmas," *Ecs J Solid State Sc*, Vol. **4**, pp.N3048-N3057 (2015).

[32] S. A. Vitale and H. H. Sawin, "Etching of organosilicate glass low-k dielectric films in halogen plasmas," *Journal of Vacuum Science & Technology A*, Vol. **20**, pp.651-660 (2002).

[33] C. Kubasch, H. Schumacher, H. Ruelke, U. Mayer, and J. W. Bartha, "Fourier Transform Infrared Spectroscopy of Moisturized Low-k Dielectric Materials," *IEEE Transactions on Electron Devices*, Vol. **58**, pp.2888-2894 (2011).

[34] H. L. Shi, J. J. Baoi, J. J. Liu, H. Huang, R. S. Smith, Q. Zhao, P. S. Ho, M. D. Goodner, M. Moinpour, and G. M. Moster, "Dielectric recoveries on O2 plasma damaged organosilicate low-k dielectrics," *Mat Res S C*, Vol. **23**, pp.447-453 (2008).

[35] J. Proost, M. Baklanov, K. Maex, and L. Delaey, "Compensation effect during water desorption from siloxane-based spin-on dielectric thin films," *Journal of Vacuum Science & Technology B*, Vol. **18**, pp.303-306 (2000).

[36] X. Guo, J. E. Jakes, M. T. Nichols, S. Banna, Y. Nishi, and J. L. Shohet, "The effect of water uptake on the mechanical properties of low-k organosilicate glass," *Journal of Applied Physics*, Vol. **114**, 084103 (2013).

[37] J. Proost, E. Kondoh, G. Vereecke, M. Heyns, and K. Maex, "Critical role of degassing for hot aluminum filling," *Journal of Vacuum Science & Technology B*, Vol. **16**, pp.2091-2098 (1998).

[38] T. Meissner and F. J. Wentz, "The complex dielectric constant of pure and sea water from microwave satellite observations," *IEEE Transactions on Geoscience and Remote Sensing*, Vol. **42**, pp.1836-1849 (2004).

[39] J. Michelon and R. Hoofman, "Moisture Influence on Porous Low-k Reliability," *IEEE Transactions on Device and Materials Reliability*, Vol. **6**, pp.169-174 (2006).

[40] C. Kubascha, H. Ruelkeb, U. Mayerb, and J. W. Barthaa, "Leakage Current and Breakthrough Measurements on Moisturized SiCOH," *Ecs J Solid State Sc*, Vol. **4**, pp.N3118-N3121 (2015).

[41] A. P. Singh, P. Victor, P. G. Ganesan, O. Nalamasu, and G. Ramanath, "Moisture-induced capacitance-voltage instabilities in mesoporous silica thin films," *Applied Physics Letters*, Vol. **87**, 253506 (2005).

[42] F. Chen, O. Bravo, K. Chanda, P. McLaughlin, T. Sullivan, J. Gill, J. Lloyd, R. Kontra, and J. Aitken, "A comprehensive study of low-k SiCOH TDDB phenomena and its reliability lifetime model development," *Int Rel Phy*, Vol., pp.46-53 (2006).

[43] C. E. Murray, C. C. Goldsmith, T. M. Shaw, J. P. Doyle, and I. C. Noyan, "Thermal stress evolution in embedded Cu/low-k dielectric composite features," *Applied Physics Letters*, Vol. **89**, 011913 (2006).

[44] K. Vanstreels and A. M. Urbanowicz, "Nanoindentation study of thin plasma enhanced chemical vapor deposition SiCOH low-k films modified in He/H2 downstream plasma," *Journal of Vacuum Science & Technology B*, Vol. **28**, pp.173-179 (2010).

[45] L. Broussous, G. Berthout, D. Rebiscoul, V. Rouessac, and A. Ayral, "Mechanical properties of a plasma-modified porous low-k material," *Microelectronic Engineering*, Vol. **87**, pp.466-469 (2010).

[46] X. Guo, J. E. Jakes, S. Banna, Y. Nishi, and J. L. Shohet, "Effects of plasma and vacuum-ultraviolet exposure on the mechanical properties of low-k porous organosilicate glass," *Journal of Applied Physics*, Vol. **116**, 044103 (2014).

[47] Y. Lin, T. Y. Tsui, and J. J. Vlassak, "Water diffusion and fracture in organosilicate glass film stacks," *Acta Materialia*, Vol. **55**, pp.2455-2464 (2007).

[48] H. Li, T. Y. Tsui, and J. J. Vlassak, "Water diffusion and fracture behavior in nanoporous low-k dielectric film stacks," *Journal of Applied Physics*, Vol. **106**, 033503 (2009).

[49] E. P. Guyer and R. H. Dauskardt, "Fracture of nanoporous thin-film glasses," *Nature Materials*, Vol. **3**, pp.53-57 (2004).

[50] T. Y. Tsui, A. J. McKerrow, and J. J. Vlassak, "The effect of water diffusion on the adhesion of organosilicate glass film stacks," *Journal of the Mechanics and Physics of Solids*, Vol. **54**, pp.887-903 (2006).

[51] E. P. Guyer, J. Gantz, and R. H. Dauskardt, "Aqueous solution diffusion in hydrophobic nanoporous thin-film glasses," *J Mater Res*, Vol. **22**, pp.710-718 (2007).

[52] S. W. King, "Dielectric Barrier, Etch Stop, and Metal Capping Materials for State of the Art and beyond Metal Interconnects," *Ecs J Solid State Sc*, Vol. **4**, pp.N3029-N3047 (2015).

[53] Y. Iba, S. Ozaki, M. Sasaki, Y. Kobayashi, T. Kirimura, and Y. Nakata, "Mechanism of porous low-k film damage induced by plasma etching radicals," *Microelectronic Engineering*, Vol. **87**, pp.451-456 (2010).

[54] H. Sinha, A. Sehgal, H. Ren, M. T. Nichols, M. Tomoyasu, N. M. Russell, Y. Nishi, and J. L. Shohet, "Effect of the dielectric-substrate interface on charge accumulation from vacuum ultraviolet irradiation of low-k porous organosilicate dielectrics," *Thin Solid Films*, Vol. **519**, pp.5464-5466 (2011).

[55] M. T. Nichols, "The Effects of Processing Induced Damage on Electrical Conduction Mechanisms and Time-Dependent Dielectric Breakdown of Low-k Organosilicates," Doctor of Philosophy Thesis, University of Wisconsin, Madison, 2013.

[56] Dongfei Pei, "The Effects of Vacuum Ultraviolet Irradiation on the Electrical Properties of Porous Low-k Organosilicate Glass," Doctor of Philosophy Thesis, University of Wisconsin-Madison, 2016.

[57] S. L. Xu, C. Qin, L. Diao, D. Gilbert, L. Hou, A. Wiesnoski, E. Busch, R. McGowan, B. White, and F. Weber, "Study of plasma-induced damage of porous ultralow-k dielectric films during photoresist stripping," *Journal of Vacuum Science & Technology B*, Vol. **25**, pp.156-163 (2007).

[58] M. Baklanov, J. F. De Marneffe, L. P. Zhang, I. Ciofi, and Z. Tokei, "Cryogenic etching reduces plasma-induced damage of ultralow-k dielectrics," *Solid State Technol*, Vol. **57**, pp.25-27 (2014).

[59] J. L. Lauer, H. Sinha, M. T. Nichols, G. A. Antonelli, Y. Nishi, and J. L. Shohet, "Charge Trapping within UV and Vacuum UV Irradiated Low-k Porous Organosilicate Dielectrics," *Journal of the Electrochemical Society*, Vol. **157**, pp.G177-G182 (2010).

[60] J. M. Atkin, D. Song, T. M. Shaw, E. Cartier, R. B. Laibowitz, and T. F. Heinz, "Photocurrent spectroscopy of low-k dielectric materials: Barrier heights and trap densities," *Journal of Applied Physics*, Vol. **103**, 094104 (2008).

[61] J. M. Atkin, E. Cartier, T. M. Shaw, R. B. Laibowitz, and T. F. Heinz, "Charge trapping at the low-k dielectric-silicon interface probed by the conductance and capacitance techniques," *Applied Physics Letters*, Vol. **93**, 122902 (2008).

[62] S. M. Sze and K. K. Ng, "Physics of Semiconductor Devices", 3rd ed. (Wiley-Interscience, Hoboken, N.J., 2007).

[63] T. K. Wong, "Time Dependent Dielectric Breakdown in Copper Low-k Interconnects: Mechanisms and Reliability Models," *Materials*, Vol. **5**, pp.1602-1625 (2012).

[64] C. Guedj, E. Martinez, and G. Imbert, "Charging and Aging Effects in Porous ULK Dielectrics," *MRS Online Proceedings Library Archive*, Vol. **990**, pp.0990-B06-03 (8 pages) (2007).

[65] Gabriele Ghisellini, in *Radiative Processes in High Energy Astrophysics* (Springer International Publishing, Heidelberg, 2013), pp. 23-29.

[66] G. R. Blumenthal and R. J. Gould, "Bremsstrahlung, Synchrotron Radiation, and Compton Scattering of High-Energy Electrons Traversing Dilute Gases," *Reviews of Modern Physics*, Vol. **42**, pp.237-270 (1970).

[67] J. R. Woodworth, M. E. Riley, V. A. Arnatucci, T. W. Hamilton, and B. P. Aragon, "Absolute intensities of the vacuum ultraviolet spectra in oxide etch plasma processing discharges," *J Vac Sci Technol A*, Vol. **19**, pp.45-55 (2001).

[68] M. T. Nichols, W. Li, D. Pei, G. A. Antonelli, Q. Lin, S. Banna, Y. Nishi, and J. L. Shohet, "Measurement of bandgap energies in low-k organosilicates," *Journal of Applied Physics*, Vol. **115**, 094105 (2014).

[69] X. Guo, H. Zheng, S. W. King, V. V. Afanas'ev, M. R. Baklanov, J. F. de Marneffe, Y. Nishi, and J. L. Shohet, "Defect-induced bandgap narrowing in low-k dielectrics," *Applied Physics Letters*, Vol. **107**, 082903 (2015).

[70] T. Tetsuya, F. Seiichi, and K. Shingo, "Radiation Damage of SiO2 Surface Induced by Vacuum Ultraviolet Photons of High-Density Plasma," *Japanese Journal of Applied Physics*, Vol. **33**, 2175 (1994).

[71] S. Fang and J. P. McVittie, "Model for oxide damage from gate charging during magnetron etching," *Applied Physics Letters*, Vol. **62**, pp.1507-1509 (1993).

[72] J. R. Woodworth, M. G. Blain, R. L. Jarecki, T. W. Hamilton, and B. P. Aragon, "Absolute intensities of the vacuum ultraviolet spectra in a metal-etch plasma processing discharge," *J Vac Sci Technol A*, Vol. **17**, pp.3209-3217 (1999).

[73] W. M. Lau, I. Bello, L. J. Huang, X. Feng, M. Vos, and I. V. Mitchell, "Argon incorporation in Si(100) by ion bombardment at 15-100 eV," *Journal of Applied Physics*, Vol. **74**, pp.7101-7106 (1993).

[74] H. R. Philip, "Handbook of Optical Constants of Solids, edited by E. D. Palik*"*, 1st ed. (Academic Press, New York, 1985).

[75] X. Guo, S. W. King, H. Zheng, P. Xue, Y. Nishi, and J. L. Shohet, "Effects of vacuum-ultraviolet irradiation on copper penetration into low-k dielectrics under bias-temperature stress," *Applied Physics Letters*, Vol. **106**, 012904 (2015).

[76] M. T. Nichols, K. Mavrakakis, Q. Lin, and J. L. Shohet, "The effects of plasma exposure and vacuum ultraviolet irradiation on photopatternable low-k dielectric materials," *Journal of Applied Physics*, Vol. **114**, 104107 (2013).

[77] S. Shamuilia, V. V. Afanas'ev, Pi. Somers, A. Stesmans, Y.-L. Li, Z. Tokei, G. Groeseneken, and K. Maex, "Internal photoemission of electrons at interfaces of metals with low-k insulators," *Applied physics letters*, Vol. **89**, 2909 (2006).

[78] X. Guo, D. Pei, H. Zheng, S. W. King, Y.-H. Lin, H.-S. Fung, C.-C. Chen, Y. Nishi, and J. L. Shohet, "Measurements of Schottky barrier at the low-k SiOC:H/Cu interface using vacuum ultraviolet photoemission spectroscopy," *Applied Physics Letters*, Vol. **107**, 232905 (2015).

[79] F. Chen and M. A. Shinosky, "Electron fluence driven, Cu catalyzed, interface breakdown mechanism for BEOL low-k time dependent dielectric breakdown," *Microelectronics Reliability*, Vol. **54**, pp.529-540 (2014).

[80] J. R. Lloyd, E. Liniger, and T. M. Shaw, "Simple model for time-dependent dielectric breakdown in inter- and intralevel low-k dielectrics," *Journal of Applied Physics*, Vol. **98**, (2005).

[81] C. Wu, Y. Li, Y. Barbarin, I. Ciofi, K. Croes, J. Bömmels, I. De Wolf, and Zs. Tőkei, "Correlation between field dependent electrical conduction and dielectric breakdown in a SiCOH based low-k (k = 2.0) dielectric," *Applied Physics Letters*, Vol. **103**, 032904 (2013).

[82] E. T. Ogawa, J. Kim, G. S. Haase, H. C. Mogul, and J. W. McPherson, "Leakage, breakdown, and TDDB characteristics of porous low-k silica-based interconnect dielectrics," Reliability Physics Symposium Proceedings, 41st Annual. 2003 IEEE International, Texas, 2003.

[83] Y. L. Li, Z. Tokei, J. Van Aelst, L. Carbonell, M. R. Baklanov, O. Richard, H. Bender, G. Groeseneken, and K. Maex, "Plasma ash modulation of TDDB thermal

activation energy in damascene SiOC:H," *Semicond Sci Tech*, Vol. **22**, pp.320-325 (2007).

[84] T. Imada, Y. Nakata, S. Ozaki, Y. Kobayashi, K. Yoshikawa, and T. Nakamura, "TDDB characteristics of low-k dielectrics after plasma damage recovery process," *Mat Res S C*, Vol. **23**, pp.557-561 (2008).

[85] K. F. Schuegraf and C. M. Hu, "Hole Injection SiO2 Breakdown Model for Very-Low Voltage Lifetime Extrapolation," *IEEE Transactions on Electron Devices*, Vol. **41**, pp.761-767 (1994).

[86] J. W. McPherson and H. C. Mogul, "Underlying physics of the thermochemical E model in describing low-field time-dependent dielectric breakdown in SiO2 thin films," *Journal of Applied Physics*, Vol. **84**, pp.1513-1523 (1998).

[87] R. S. Achanta, J. L. Plawsky, and W. N. Gill, "A time dependent dielectric breakdown model for field accelerated low-k breakdown due to copper ions," *Applied Physics Letters*, Vol. **91**, 234106 (2007).

[88] G. S. Haase, "A model for electric degradation of interconnect low-k dielectrics in microelectronic integrated circuits," *Journal of Applied Physics*, Vol. **105**, 044908 (2009).

[89] T. K. S. Wong, "Time Dependent Dielectric Breakdown in Copper Low-k Interconnects: Mechanisms and Reliability Models," *Materials*, Vol. **5**, pp.1602-1625 (2012).

[90] F. Chen, O. Bravo, D. Harmon, M. Shinosky, and J. Aitken, "Cu/low-k dielectric TDDB reliability issues for advanced CMOS technologies," *Microelectronics Reliability*, Vol. **48**, pp.1375-1383 (2008).

[91] J. W. McPherson and R. B. Khamankar, "Molecular model for intrinsic time-dependent dielectric breakdown in SiO2 dielectrics and the reliability implications for hyper-thin gate oxide," *Semicond Sci Tech*, Vol. **15**, pp.462-470 (2000).

[92] J. Sune, I. Placencia, N. Barniol, E. Farres, F. Martin, and X. Aymerich, "On the Breakdown Statistics of Very Thin Sio2-Films," *Thin Solid Films*, Vol. **185**, pp.347-362 (1990).

[93] Y. S. Su and S. T. Pantelides, "Diffusion Mechanism of Hydrogen in Amorphous Silicon: Ab Initio Molecular Dynamics Simulation," *Physical Review Letters*, Vol. **88**, 165503 (2002).

[94] C. W. Chen, P. T. Liu, T. C. Chang, J. H. Yang, T. M. Tsai, H. H. Wu, and T. Y. Tseng, "Cu-penetration induced breakdown mechanism for a-SiCN," *Thin Solid Films*, Vol. **469–470**, pp.388-392 (2004).

[95] M. He, S. Novak, L. Vanamurthy, H. Bakhru, J. L. Plawsky, and T. Lu, "Cu penetration into low-k dielectric during deposition and bias-temperature stress," *Applied Physics Letters*, Vol. **97**, 252901 (2010).

[96] W. Wu, X. Duan, and J. S. Yuan, "Modeling of time-dependent dielectric breakdown in copper metallization," *IEEE Transactions on Device and Materials Reliability*, Vol. **3**, pp.26-30 (2003).

[97] M. Vogt, M. Kachel, M. Plotner, and K. Drescher, "Dielectric barriers for Cu metallization systems," *Microelectronic Engineering*, Vol. **37-38**, pp.181-187 (1997).

[98] N. Suzumura, S. Yamamoto, D. Kodama, K. Makabe, J. Komori, E. Murakami, S. Maegawa, and K. Kubota, "A new TDDB degradation model based on Cu ion drift in cu interconnect dielectrics," *Int Rel Phy*, Vol., pp.484-489 (2006).

[99] K.-Y. Yiang, H. W. Yao, A. Marathe, and O. Aubel, "New perspectives of dielectric breakdown in low-k interconnects," 47th Annual IEEE International Reliability Physics Symposium, Montreal, 2009.

Chapter III

Experimental Apparatus and Materials Diagnostics

In this Chapter, the experimental apparatus and characterization methods used in this work to measure the VUV-induced Cu migration into and breakdown of low-k a-SiOC:H organosilicates are described. It should be mentioned that some of the low-k dielectric materials under study are dense low-k a-SiOC:H with a k value of 3.2 and a density of 1.5 g/cm^3, which has the potential to be used as a low-k capping layer dielectric. This dense low-k capping layer material will also be compared with the widely used a-SiCN capping layer material. In the first section, details are given about (1) the monochromatic synchrotron VUV photon source used in this work and (2) VUV photoemission spectroscopy are described in detail. Next, an electron-cyclotron-resonance

(ECR) plasma reactor used to expose dielectric samples is presented. This allows a comparison of plasma-induced damage to the synchrotron radiation VUV-induced damage to a-SiOC:H. In the third section, nanoindentation measurements on the porous low-k organosilicates are detailed. In the fourth section, X-ray photoelectron spectroscopy (XPS) technology used for several distinct measurements is elaborated, including core-level XPS, valence-band XPS and depth-profile measurements. Fourier transform infrared spectroscopy (FTIR) is then discussed. And lastly, the electrical characterization test structure for the low-k a-SiOC:H thin films are discussed.

3.1 Synchrotron VUV-Photon Source

To get complete measurements of the effects of VUV photon irradiation on Cu migration into and breakdown of Cu/low-k interconnects, an appropriate VUV photon source is important. A useful VUV source should have the characteristics of variable energy, high photon flux, and high energy resolution, etc. Synchrotron radiation is such an ideal VUV photon source which can provide continuous, high-intensity monochromatic radiation over a wide range of wavelengths (from infrared to X-rays). In this work, the University of Wisconsin Synchrotron Radiation Center (SRC) in Madison, WI and the National Synchrotron Radiation and Research Center (NSRRC) in Taiwan were utilized as VUV photon sources. In both facilities, a particular beamline, equipped with a stainless-steel Seya-Namioka monochromator (SEYA), was used because it allows for exposure to photon energies from 4.5 eV up to 35 eV, which is comparable to those photon energies emitted from processing plasmas.[1]

The experimental apparatus is shown in **Figure 3-1**. The dielectric films were placed in the vacuum chamber, which was pumped down to a pressure of 10^{-8} Torr. As mentioned above, the VUV beam comes from the exit slit of a Seya-Namioka VUV monochromator with an output-energy range of 5-30 eV. The beam is oriented normally to the surface of the sample with an approximate cross-sectional area of 3.0×0.1 cm^2. The film position relative to the beam can be adjusted using a linear translator that is connected to the wafer plate. Since the VUV beam is fixed in position, the motion of the sample is equivalent to scanning the beam over the sample surface. The flux of the beam can be monitored *in situ* using a calibrated photodiode (AXUV100). During VUV exposure, the sample holder can be biased and a Keithley 486 pico-ammeter can be used to measure the substrate current.

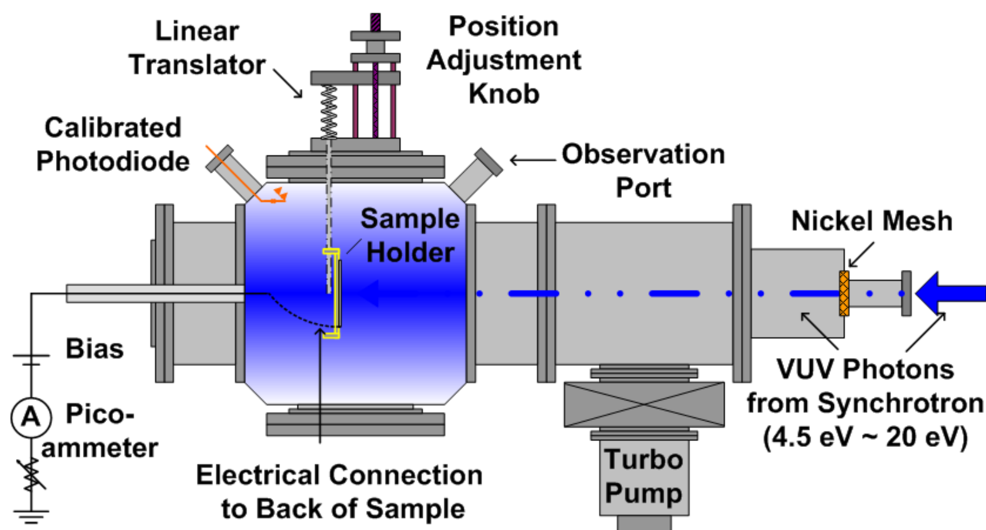

Figure 3-1. Schematic of the synchrotron VUV irradiation system.

Figure 3-2 shows the calibrated photon flux of the SEYA beamline at NSRRC for several widths of the exit (front) slit. The flux was measured with the photodiode located at the place of the sample holder. Energies between 5 and 17 eV using a 600 lines/mm

grating were measured. Energies higher than 17 eV could be utilized by installing a different grating. At the maximum slit opening (1.5mm), one can get the highest photon flux. Compared with the VUV photon flux in the ECR plasma,[2] the flux from the Seya beamline is smaller by two orders of magnitude. Thus, in order to achieve a similar total dose of VUV photons, the equivalent exposure using a synchrotron, radiation takes a much longer time.

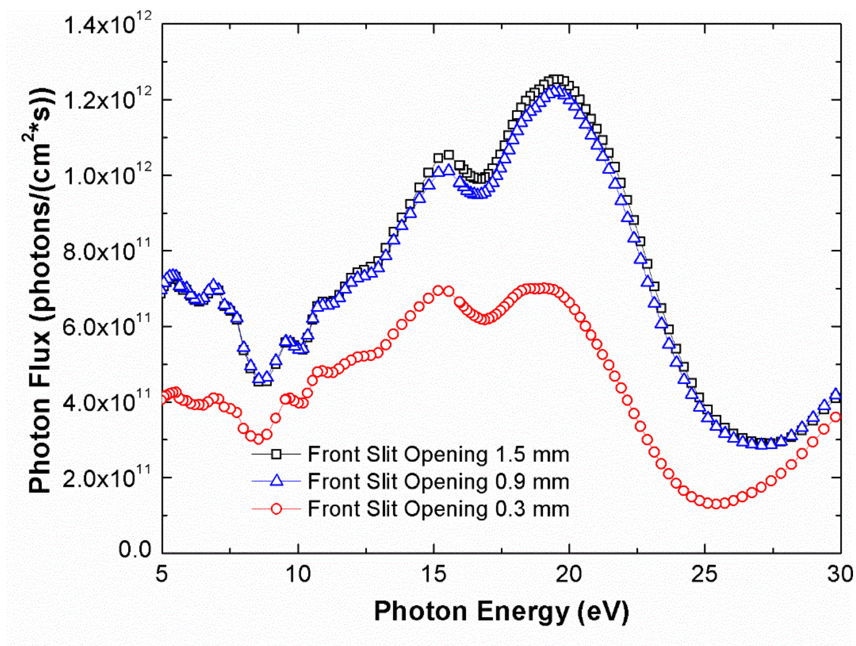

Figure 3-2 The calibrated photon flux of the SEYA beamline with different slit openings.

It is important to notice that increasing the slit opening increases the photon flux, as depicted in **Figure 3-2**, and also increases the bandwidth of the radiation that passes through the monochromator. When the slit is opened to its maximum (1.5mm), the full width at half maximum (FWHM) of the beam is approximately 1 nm. From the following expression for energy resolution, $\Delta E=hc\ (\Delta\lambda/\lambda^2)$, [3] where h is Planck's constant, c is the speed of light and λ is the wavelength, the energy resolution is 0.08 eV (less than 0.1 eV)

for 10 eV photons. It is likely to be poorer for higher photon energies (resolution is 0.18 eV for 15 eV photons). In this work, because sub-0.1 eV energy resolution is not needed for VUV irradiation with energy higher than 10 eV, the maximum slit opening was always used for VUV exposure to obtain the highest possible photon flux. This is because sub-0.1 eV energy resolution was only required when measuring the Schottky barrier using VUV spectroscopy.

The other reason that the widest slit opening was utilized is to have good spatial uniformity. **Figure 3-3** shows the spatial distribution of the photons from the SEYA beamline at NSRRC with different slit openings, as measured by Weiyi Li. As can be seen from **Figure 3-3** (left) for the vertical distribution, with a 1.5 mm slit opening, the beam size is about 12 mm and is relatively uniform in the center. For a 1.5 mm slit opening, the beam size is only about 4 mm. **Figure 3-3** (right) shown the horizontal distribution of the VUV beam. Since the exit slit is also horizontal, the opening of the slit does not affect the horizontal distribution of the VUV intensity significantly. For most of the materials diagnostic methods used in this work (XPS, FTIR, nanoidentation, ellipsometry, I-V, etc), a requirement of at least a 5mm × 5mm uniformly VUV-exposed area is needed. This can be achieved by adjusting the sample position during exposure, using the linear translator as described above.

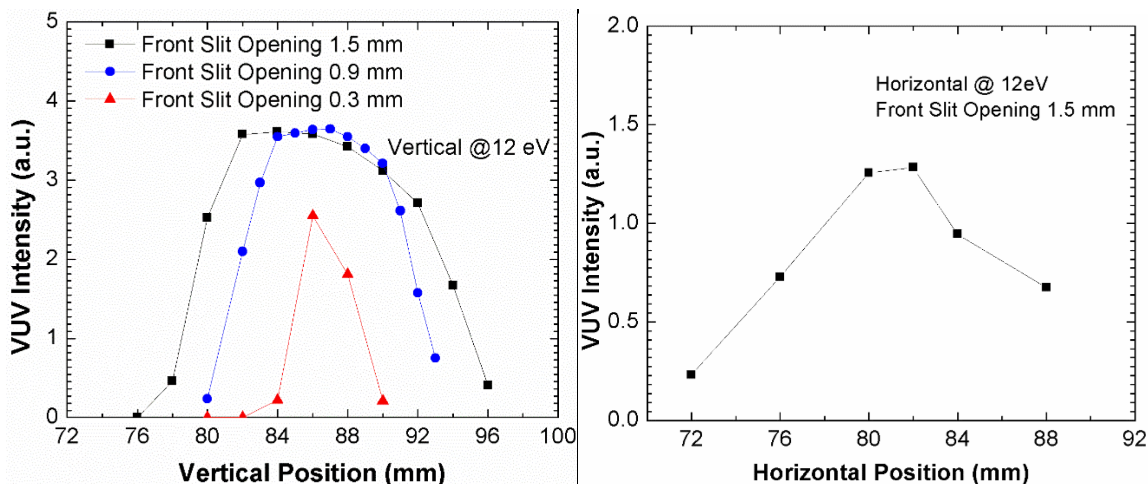

Figure 3-3 Spatial distribution of the photons from the SEYA beamline with different slit openings: (left) vertical distribution (right) horizontal distribution. (Data measured by Weiyi Li).

On the other hand, the VUV exposure apparatus used in this work allows *in-situ* sample diagnostics during or immediately after high-flux energetic photon exposures. Depending on the incident photon energy and the dielectric thickness, VUV irradiation can cause photoinjection, photoconduction, and photoemission of electrons.[4],[5] Electrons can be excited into the conduction band from the valence band or from defect states in the bandgap of the dielectric and travel in the dielectric and/or the substrate.[6] By exposing the materials to monochromatic VUV radiation at low flux (using a 0.3-mm slit opening) and rapidly scanning the photon energy over a wide range, the photoemission current from the low-k dielectric as a function of photon energy can be obtained using the set-up as shown in **Figure 3-4**.[7],[8] A picoammeter was connected to the silicon substrate of the wafer to monitor charge transfer into and out of the dielectric so as to measure the photoemission current during VUV irradiation, as indicated in the Figure..

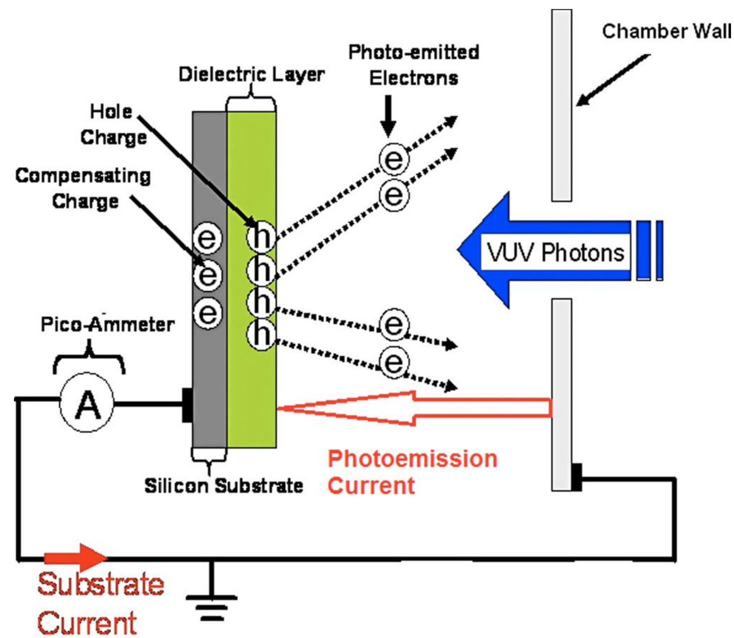

Figure 3-4 Setup for measuring the VUV photoemission current.[9]

It should be pointed out that the use of synchrotron radiation, both as a source of high-flux photon exposures and as a diagnostic tool, is fundamental for this work. As a diagnostic tool, VUV photoemission spectroscopy provides the possibility of *in-situ* sample characterization immediately after high-flux energetic photon exposures. We have successfully used this method to measure the Schottky barrier at the Cu/low-k a-SiOC:H interface,[10] which will be discussed in Chapter VI.

3.2 Electron-Cyclotron-Resonance Plasma Reactor

In this work, an electron-cyclotron-resonance (ECR) plasma reactor is also used to expose low-k a-SiOC:H samples, in order to compare VUV-only-induced and plasma-induced damage. In particular, the mechanical property changes of the thin film will be measured, as will be detailed in the following chapters.

ECR plasmas have a number of desirable characteristics, like low operating pressure[11] and high electron density[12], that make them particularly well suited for semiconductor processing.[13] Low-pressure operation is particularly useful for the deposition of high-quality films and is useful for anisotropic etching of high-aspect-ratio features, due to the reduction of ion collisions in the sheath.[14], [15] Also, because they are wave-heated discharges, ECR plasmas can be generated without the presence of internal electrodes, which can be potential contamination sources because of etching or sputtering of the electrode surfaces.[13]

Figure 3-5 shows a schematic diagram of the ECR plasma system used in this work. It utilizes a 2-kW magnetron power supply to generate a 2.45 GHz microwave field that is coupled to the reactor chamber through a gas-cooled quartz window. Once the microwaves are generated in the magnetron, they go through a circulator and then pass over a diode array that measures forward and reflected power. A three-stub dielectric tuner connected to the waveguide is used for impedance matching and to increase the efficiency of microwave power coupled into the plasma. The reflected power is absorbed by a dummy load as shown. Before they enter the cylindrical plasma chamber, a rectangular to circular waveguide converter was used to convert the microwaves from the TE_{10} (rectangular) mode to the TM_{01} (circular) mode. Because the TM_{01} mode is axially symmetric, the plasma induced by the microwaves will tend to be more uniform.[16] An 875-Gauss magnetic-mirror field is generated in the vacuum chamber by driving 1 kA through a set of magnet coils. Samples can be mounted on a heated movable stainless-steel wafer chuck placed axially inside the reactor.

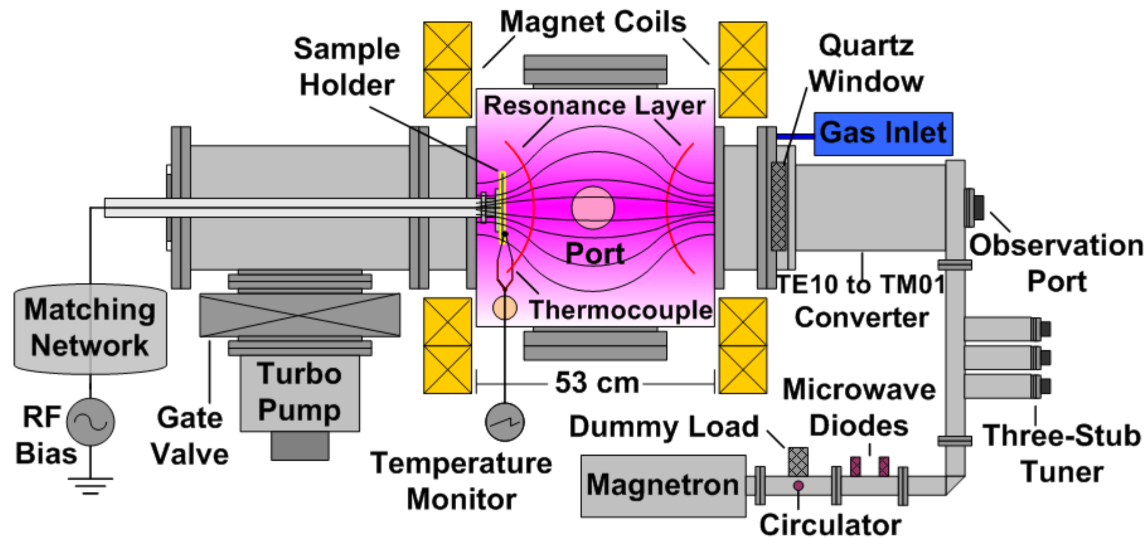

Figure 3-5. Schematic of the electron-cyclotron-resonance plasma-reactor.

In order to separate the effects of energetic charged particles and photon bombardment incident from the plasma, from chemical changes induced by free radicals, argon was used as the feed gas, under which the impact from free radicals is minimized.[17] The ion-impact energy at the surface of the wafer chuck can be modified with the addition of an external bias potential.[16] For conducting wafers or substrates, this can be accomplished with either a DC bias or an RF-induced DC bias (self-bias) voltage. For insulating wafers or substrates, an RF bias must be used.[18] An RF source (13.56 MHz, up to 1 kW) and an L-type matching network, as shown in **Figure 3-6**, were designed and incorporated into the ECR reactor.[16] The RF-induced DC bias can be up to -100 volts.

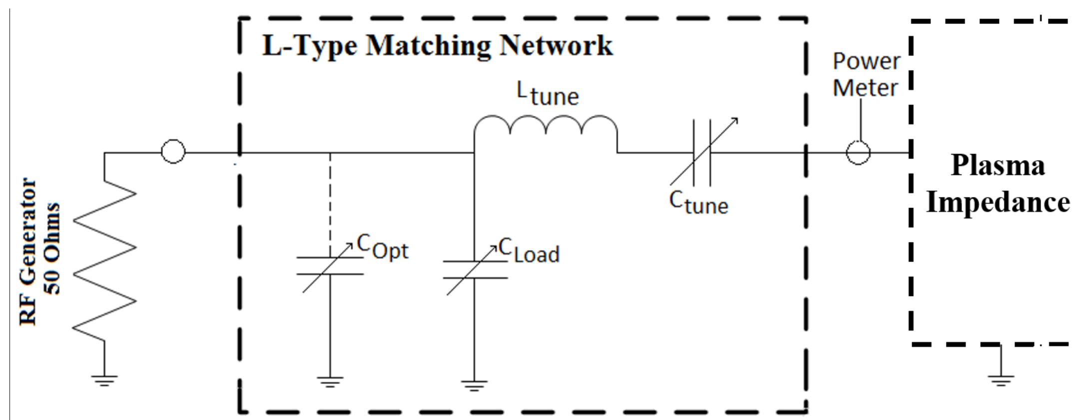

Figure 3-6 L-type matching network schematic showing simplified generator and plasma Impedances. C_{opt} represents a 100-pF capacitor, C_{load} represents a single 8-1000 pF variable capacitor and C_{tune} represents a variable vacuum capacitor placed in series with the inductor, which is tunable in a range of 8 to 1000 pF.

3.3 Nanoindentation Measurements

In this work, nanoindentation was used to measure the effect of VUV irradiation and plasma exposure on the mechanical properties of low-k organosilicates. Though nanoindentation has been widely used to characterize the mechanical properties of various materials, there are several challenges when it comes to measurements of layered samples in which a significant disparity exists between the properties of the materials in each layer.[19-21] Here, to carefully include the effects of multiple layers, modifications to the traditional nanoindentation test methods were made, based on Stone's Elasticity Model [22,23], to improve the accuracy and reliability of the measurements.

For a "standard" nanoidentation test, the indenter is controlled with a pre-set function to load it into and lift it off from the sample. As this takes place, the loading force and depth

(h) are monitored. From the load-depth traces, the initial unloading stiffness ($S = dP/dh$ at maximum load $P_{max,}$) can be assessed by fitting the unloading load-depth segment (the unloading part of the load-depth curve) to a power function. As a result, the hardness (H) and effective modulus (E_{eff}) of the material can be obtained by using the expressions $H = P_{max}/A_c$ and $E_{eff} = S/A_c^{1/2}$ respectively, where A_c is the contact area of the indenter with the sample surface, and P_{max} is the maximum load. For indentation against a homogeneous, isotropic, elastic half space, as depicted in **Figure 3-7 (a)**, E_{eff} is related to the material properties as follows:

$$\frac{1}{E_{eff}} = \frac{1}{\beta}\left(\frac{1-{\nu_s}^2}{E_s} + \frac{1-{\nu_d}^2}{E_d}\right) \quad (3\text{-}1)$$

where E_d and ν_d are the Young's modulus (1137 GPa) and Poisson's ratio (0.07) of the diamond probe [19] and E_s and ν_s are the same quantities for the specimen. β is a constant that depends on the geometry of the indenter. Once the Poisson ratio (the negative ratio of transverse to axial strain) of the specimen (ν_s) is known, the elastic modulus of the specimen (E_s) can be determined. This method is accurate for measurements on isotropic materials.[19] "Isotropic" here means the sample only has one layer.

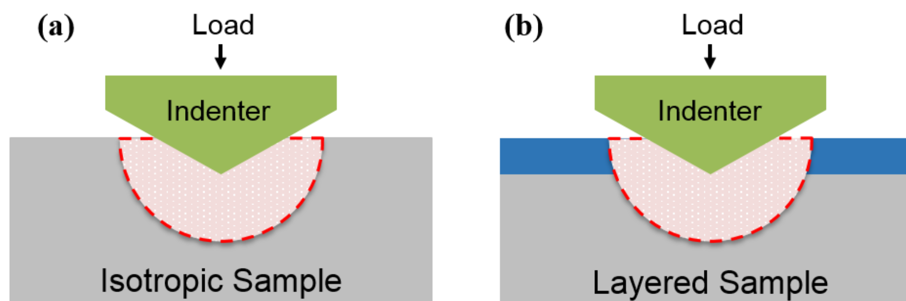

Figure 3-7 Schematic showing nanoindentation on (a) an isotropic and (b) a layered sample.

However, for indentation against a layered elastic half-space, such as a very thin film on a substrate, the underneath layer will have an increased effect on E_{eff} as the penetration-depth increases. What one measures here are not only the properties of the thin layer on the top, but also those of the substrate, as illustrated in **Figure 3-7 (b)**. For the case of a low-k a-SiOC:H thin film deposited on a silicon wafer, since Si is much mechanically stronger than a-SiOC:H, the measured results based on the traditional method, as discussed above, are usually overestimated and unconvincing because the effects from the Si substrate are not properly considered.[20] Furthermore, if the a-SiOC:H thin films are porous, film densification and delamination underneath the probe are significant during measurement, which brings additional challenges to the test.[21] Therefore, to obtain more reliable data, some necessary modifications are carried out in this work, as described in the following paragraphs.

First, an optimized load-function was used for each measurement, as shown in **Figure 3-8**. Nanoindentation tests were carried out using a Hysitron (Minneapolis, Minnesota, USA) TriboIndenter® equipped with a diamond Berkovich tip and operated in open-loop control. For each measurement, the indenter was operated in force-displacement mode and the tip oscillation frequency was 125 Hz. Machine compliance was assessed from a 0.01-1.2 mN series of load control indents on a fused silica standard using SYS correlation.[23] Both calibration and a-SiOC:H experiments utilized the same load-control indent function. In step (b), the slower loading ramp is important to eliminate film delamination.[19,24]

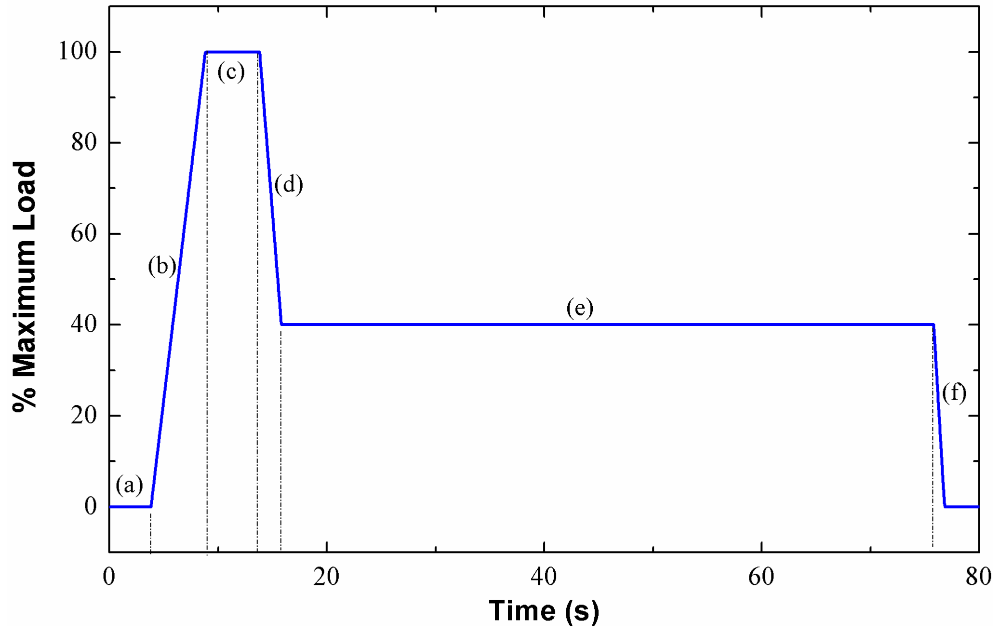

Figure 3-8 Load function used in this work, which consists of (a) an initial 20-nm lift-off and re-approach (which is done by lifting up the indenter tip and then movong it back to touch the sample surface) in order to define the initial contact point accurately, (b) a 5 s loading, (c) a 5 s hold at maximum load (P_{max}), (d) a 2 s unloading to 40% of the P_{max}, (e) a 60 s hold at 40% P_{max} to remove thermal drift effects, and (f) a 1 s final unload.

Second, the contact area (A_c) was recalibrated, as described below, at each indentation depth (h). After correcting the fused silica load-depth traces for machine compliance, the Oliver-Pharr method [25] was used to assess contact area based on initial unloading contact stiffness (S) and contact depth ($h_c = h - 0.75 \cdot P/S$) for each indent. The area function is determined by a calibration equation as follows[25]

$$A_c\,(h_c) = 24.5h_c^2 + C_1 h_c + C_2 h_c^{1/2} + C_3 h_c^{1/4} + C_4 h_c^{1/8} + C_5 h_c^{1/16} \qquad (3\text{-}2)$$

where C_1-C_5 are calibration constants of the indenter tip determined by the indentations on fused silica.

Third, Stone's elasticity model [22] was utilized to interpret the data measured on the layered sample and to remove the effect of the substrate, by comparing the experimental E_{eff} as a function of indent size to Stone's theoretical simulations. In the simulation, the elastic modulus and the Poisson's ratio of Si are set to be 161 GPa and 0.227 respectively[26] and the Poisson's ratio of a-SiOC:H was assumed to be 0.25.[27] The only fitting parameter here is the nanoindentation correction factor - β, as shown in equation (3-1), which is dependent on the indenter geometry, the tip bluntness and the Poisson's ratio of the material being indented. It was determined to be 1.23 in previous work.[28],[29]

Figure 3-9 shows the comparison of experimental E_{eff} (solid symbols) of a-SiOC:H (k=2.55) with calculated E_{eff} (open symbols) using Stone's model. The abscissa is the square root of the contact area ($\sqrt{A_c}$) normalized by the film thickness (h_f), which enables the simulations to be compared with films of arbitrary thickness. As one can see from **Figure 3-9**, the agreement between the experimental and the simulated E_{eff} is good when $\sqrt{A_c}/h_f < 1$. Above $\sqrt{A_c}/h_f = 1$, however, the experimental E_{eff} is higher than the simulated E_{eff}. As suggested by previous researchers,[21],[30] the deviation likely arises due to the porosity of the SiCOH films, because the stress state under an indenter is highly hydrostatic and causes the porous materials to densify during the loading step, which leads to a local increase in the stiffness. Furthermore, the harder substrate can also enhance densification underneath the indenter and thus lead to an even larger region of increased stiffness.[21] Therefore, only data below $\sqrt{A_c}/h_f = 1$ was used to assess E_{eff} of a-SiOC:H thin film.[19] Taking pristine a-SiOC:H with a k value of 2.55 as an example, the experimental E_s, as shown in Figure 3-5 is located between E_s =5.0 GPa and E_s =6.0 GPa in simulated curves when $\sqrt{A_c}/h_f < 1.0$, corresponding to a true E_s value of 5.3 ± 0.2 GPa.

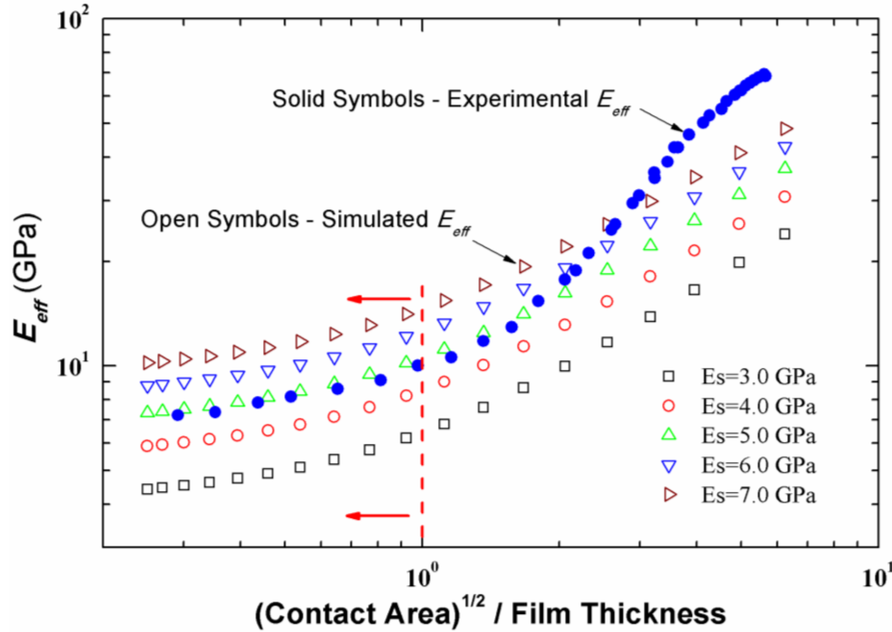

Figure 3-9 Comparison of experimental E_{eff} of pristine a-SiOC:H thin film (k=2.55) with simulated E_{eff} from Stone's elasticity model.

Figure 3-10 shows the measured hardness (*H*) of the pristine a-SiOC:H thin film (k=2.55) as a function of $\sqrt{A_c}/h_f$. At the onset of the indentation test, the curves level off and the measured *H* stays at a plateau value for shallow indentation depths. Then the measured *H* increases significantly with increased load. Finally, when the indenter probe approaches the film and substrate interface, a discontinuity appears in the curve. This discontinuity should be attributed to "pop-in" events, resulting from film cracking or adhesion loss (delamination) between the film and substrate.[31] Since hardness assesses the resistance of the material to plastic deformation underneath the indenter,[19] when a crack forms, the probe can more easily penetrate into the film/substrate system. This degenerated resistance induces a substantial increase in the contact area and a significant reduction in *H*, and the discontinuity appears in the *H* curve. As a result, to keep

coincidence with elastic modulus, hardness was measured over the same range $\sqrt{A_c}/h_f <$ 1.0. Measurements on non-porous low-k dielectric samples show the same trend. There is no difference between porous and non-porous samples.

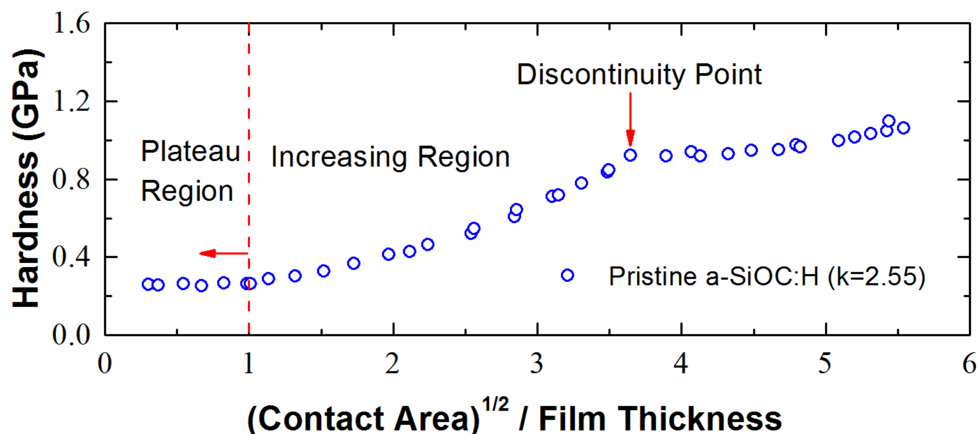

Figure 3-10 Measured hardness (H) of pristine a-SiOC:H thin film (k=2.55, porosity is approximately 15%.) as a function of $\sqrt{A_c}/h_f$. [19]

3.4 X-ray Photoelectron Spectroscopy

X-ray photoelectron spectroscopy (XPS) is a surface-sensitive quantitative spectroscopic technique that can probe electronic states and can give insight into the chemical and atomic composition of a material.[32] By irradiating a material with a beam of X-rays while simultaneously measuring the kinetic energy and number of electrons that escape from the material, an XPS spectrum can be obtained as a function of electron binding energy by using the equation of $E_{binding} = E_{photon} - (E_{kinetic} + \varphi)$,[33] where $E_{binding}$ is the binding energy (BE) of the electron, E_{photon} is the energy of the X-ray photons, $E_{kinetic}$ is the kinetic energy of the emitted electron as measured with the instrument and φ is the work function dependent on both the spectrometer and the material. The work function

term φ is an adjustable instrumental correction factor that accounts for the few eV of kinetic energy given up by the photoelectron as it becomes absorbed by the instrument's detector. It is a constant that rarely needs to be adjusted in practice and is always known for commercial XPS systems.[32] Because these experimentally determined BEs are characteristic of specific elements, they can be directly used to identify experimentally measured peaks of a material with unknown elemental composition.[32,33]

In this work, a Thermo Scientific K-alpha XPS system, equipped with an Al Kα X-ray source (E_{photon} = 1486.7 eV) [34], is used. It consists of a full 180-degree hemispherical analyzer (HSA) (125 mm mean radius), as shown in **Figure 3-11**. The emitted electrons from the sample surface can be transferred through the apertures and focused onto the energy-analyzer entrance slit. Electrostatic fields within the hemispherical energy analyzer are established to allow electrons of only of a given energy (the so called Pass Energy) to arrive at the detector slits and onto the detectors themselves. The energy resolution of the analyzer (ΔE, with a unit of eV), depends on the width of the entrance slit (W, with a unit of m), the mean radius of the hemispherical energy analyzer (R, with a unit of m), the pass energy (E_p) of the analyzer, and the acceptance angle (α, defined as the incident angle of the electrons on the detector surface). The relationship between these quantities to obtain the energy resolution is $\Delta E = E_p(W/2R + \alpha^2/2)$.[32] In this system, an absolute resolution of less than 0.5 eV can be achieved by setting the pass energy to be 21 eV. A combined low-energy electron/ion flood source is also available for charge neutralization, which is important for measurements on dielectrics [35], as will be detailed in the following chapters. Specific measurements from this system include: core-level XPS, valence-band

XPS, and XPS depth profile. All of these are utilized to measure the effects of VUV irradiation on Cu/low-k interconnects, as will be discussed in Chapter VI of this thesis.

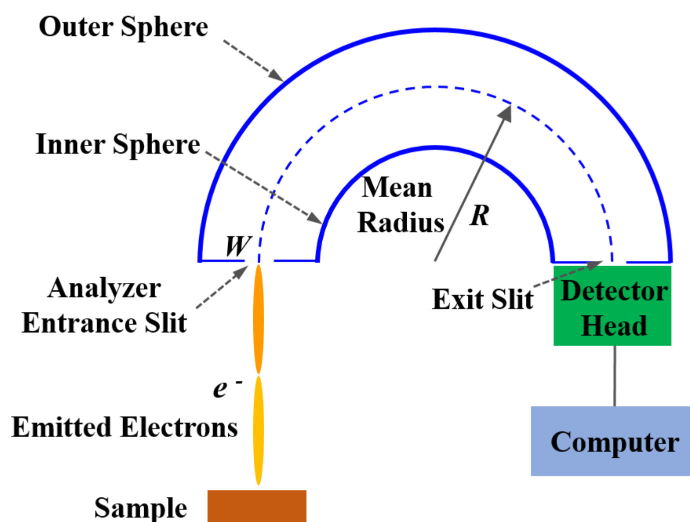

Figure 3-11 Schematic diagram of the XPS hemispherical energy analyzer.

3.4.1 Core-level X-ray Photoelectron Spectroscopy

Core-level XPS is normally employed to identify each element that exists on the surface or just below the surface (from the surface to 10 nm below the surface) of the material.[36] Characteristic peaks of the measured spectrum correspond to the electron configurations of the core-level electrons within the atoms, *e.g*, 1s, 2s, 2p, 3s, etc. The number of detected electrons at each of the characteristic peaks is directly related to the concentration of that particular element within the XPS sampling volume.[36] In a solid, inelastic scattering events also contribute to the photoemission process, generating electron-hole pairs which show up as an inelastic tail on the high BE side of the main core-level photoemission peak.[37] Therefore, core-level XPS can also be used to analyze the effects of inelastic collisions that occur during excitation and emission of electrons from

the sample. These inelastic processes include band-to-band electronic transitions and plasmon excitations.[38] This can either be a final-state effect caused by core-hole decay, which generates quantized electron-wave excitations in the solid (intrinsic plasmons), or it can be due to excitations induced by photoelectrons travelling from the emitter (the electron-occupied valence band) to the surface (extrinsic plasmons).[37,38] Analysis of these inelastic processes can be used to determine the bandgap energy near the surface of the dielectric. This method has been used to measure the bandgap narrowing occurring in the low-k a-SiOC:H thin films as will be discussed in Chapter VI of this thesis.

Figure 3-12 is an example showing the inelastic-loss spectra near the O 1s core-level peak collected from SiO_2, in which the data was measured by Michael Nichols.[39] The location of the O 1s core-level peak was determined to be 533.6 eV. As illustrated in **Figure 3-12**, by fitting a straight line to the inelastic loss spectra (the solid line) and extrapolating this to intersect with the background level (dashed horizontal line), the onset of inelastic losses is found to occur at 542.4 eV. Using the measured O 1s core-level peak energy of 533.6 eV, the bandgap energy was calculated to be E_g =8.8 eV, which is in good agreement with the literature-reported value [39]. It should be noted that though any core-level spectra of the material will exhibit the same inelastic losses, the O 1s core-level XPS peak was chosen here because of its higher cross section for absorption of X-ray photons and correspondingly higher photoelectron intensity, so that a sufficient signal-to-noise ratio can be achieved with suitably high resolution.[39]

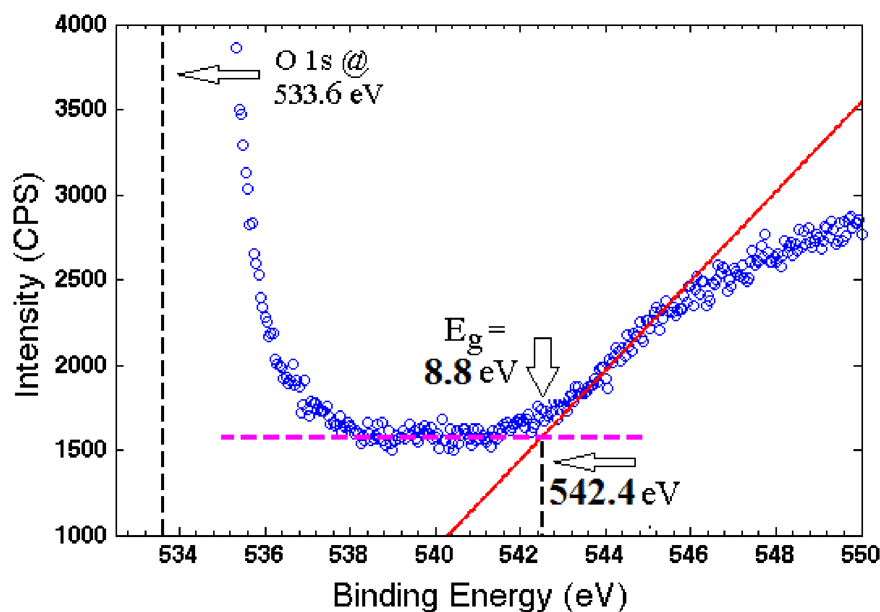

Figure 3-12 The inelastic-loss spectra near the O 1s core-level peak collected from SiO_2.[39]

The accuracy of this method can be ~ 0.5 eV or less if the electron density in the valence band near the surface is laterally homogeneous. [16,35] The largest source of error is from uncertainty in the process of linear extrapolation of the inelastic-loss spectra rising edge. By employing the same methods, the bandgap energy of various low-k a-SiOC:H have been successfully measured.[35],[39]

3.4.2 Valence-band X-ray Photoelectron Spectroscopy

Valence-band XPS measurements have emerged as a useful technique because the spectra are essentially proportional to the total density of states (DOS).[40],[41] A knowledge of the valence-band DOS and/or the valence-band edge (VBE) of a material can yield considerable information about that material's electronic-band structure, which is of fundamental importance for a dielectric in measuring its properties and possible

conduction mechanisms.[41,42] In this work, valence-band XPS has been measured on various low-k a-SiOC:H thin films before and after processing and is used to obtain the valence-band edge of the samples.

Figure 3-13 shows the valence-band XPS measured on dense a-SiOC:H (k=3.2) thin films, in which the "0" binding energy corresponds to the energy of the Fermi level. The low binding-energy region (0-20 eV) contains the "valence band" which typically consists of electrons that are shared between atoms in chemical bonds. By making a linear fit to the rising edge of valence band XPS spectra and extrapolating this to intersect with the background level, as depicted in the inset in **Figure 3-13**, the valence-band edge of the material can be determined.[35] The uncertainty of this method can be less than 0.1 eV. For an a-SiOC:H (k=3.2) film, the VBE is approximately 4.1 eV below the Fermi level, which is reasonable for undoped intrinsic materials with a measured bandgap of 8.1 eV [43].

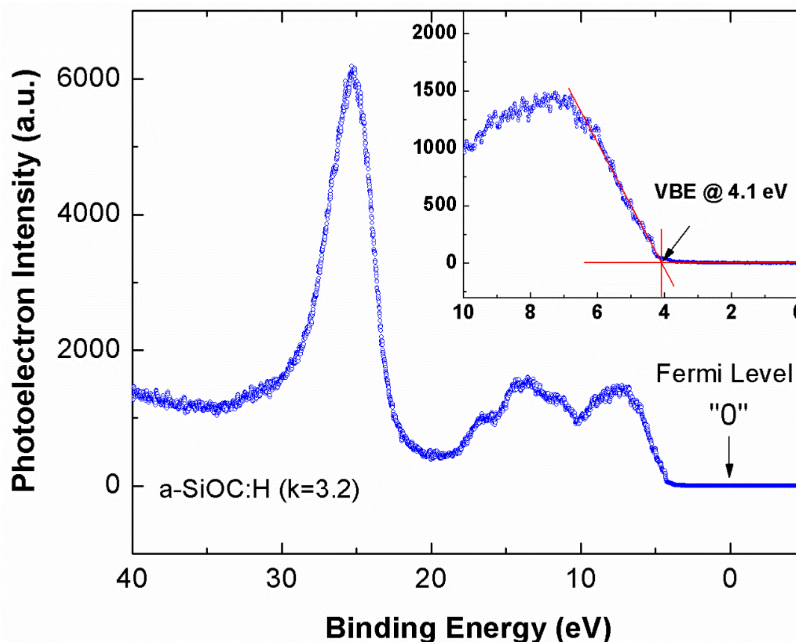

Figure 3-13 Valence-band XPS measured on a-SiOC:H thin film.

3.4.3 XPS Depth Profile

A depth profile of the sample in terms of XPS quantities can be obtained by combining a sequence of ion-gun sputter cycles interleaved with XPS measurements from the surface. To investigate the depth profile, an ion gun is used to sputter the material for a period of time before being turned off. The XPS spectra are acquired during this off time. Each ion gun sputter cycle exposes a new surface, and the XPS spectra provide the means to analyze the composition of these surfaces. The actual depth for each XPS analysis is dependent on the sputter-rate of the ion-gun, which in turn depends on the material and also the ion energy and flux generated from the ion gun.[44]

In this work, XPS depth profiles are used mainly to characterize the Cu migration into low-k a-SiOC:H thin films. If Cu diffuses/drifts into low-k a-SiOC:H, the distribution of Cu can be explored by measuring its relative concentration as a function of depth. **Figure**

3-14 is one example of the XPS depth profile measured on a 100nm porous a-SiOC:H (porosity is 35%) deposited on Cu with and without an additional a-SiCN:H capping layer.

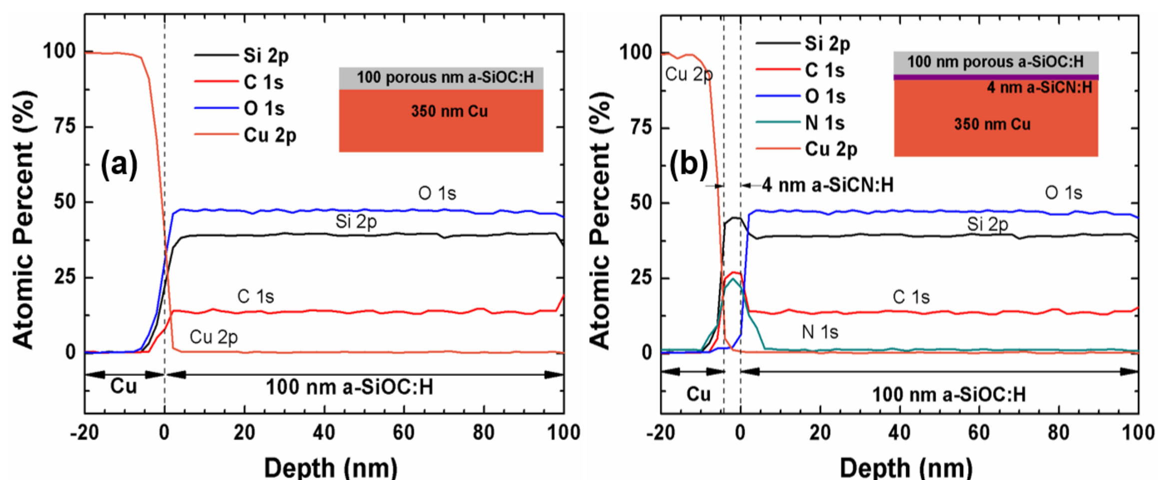

Figure 3-14 XPS depth profile of (a) 100nm porous a-SiOC:H deposited on a layer of 350 nm Cu; (b) 100 nm porous a-SiOC:H deposited on a layer of 350 nm Cu with 4 nm a-SiCN:H capping layer. Inset shows the schematic of the sample structure utilized.[44]

Following is more information about the XPS depth-profile measurements used in this work. The energy of the ions generated by a monochromatic argon ion gun is 1.5 keV and the ion-beam current is 15 μA/cm^2, enabling a measured material removal rate of about 0.2 nm/s. The depth profile was obtained by scanning over an area of about 1.5mm × 1.5mm to ensure a laterally homogeneous ion-current distribution. The sample is rotated during sputtering to minimize sputter-induced roughening. For each sputter step, the sputtering time was 15 seconds, enabling a depth resolution of 2 nm to 3 nm, depending on the porosity of the a-SiOC:H.

3.5 Fourier-Transform Infrared Spectroscopy

Fourier-transform infrared (FTIR) spectroscopy is a well-established analytic method used to investigate the chemical composition of organic or inorganic materials, along with the analysis of the bonding types, the structure, and the interface phenomena. It has the major advantages of rapid and nondestructive analysis, high resolution and sensitivity, self-calibration, mechanical simplicity, extreme accuracy and reproducible results. All of these make the FTIR technique well suited to detect changes of the chemical structure of bulk low-k organosilicates, as well as adsorbed water in dielectric materials. Because of these features, FTIR spectroscopy is the most widely used method of blanket low-k film damage assessments. It has been demonstrated, for example, in refs. [45] and [46].

A detailed instrumental diagram of a single-beam FTIR is shown in **Figure 3-15**. An IR source that can be adjusted to operate in the near region (12800-4000 cm^{-1}), the mid region (4000-200 cm^{-1}) or the far region (200-10 cm^{-1}) sends infrared (IR) light into an interferometer where it travels through the beam splitter to a fixed or movable mirror. Once the IR light impacts a mirror, the IR light travels into the sample compartment and into the IR transducer. The two beams produced by the beam splitter interact with each other producing an interferogram. Once the combined signal has entered the transducer, the interferogram is Fourier transformed into a spectrum. The laser is used as a calibration technique for the movable mirror in the interferometer.

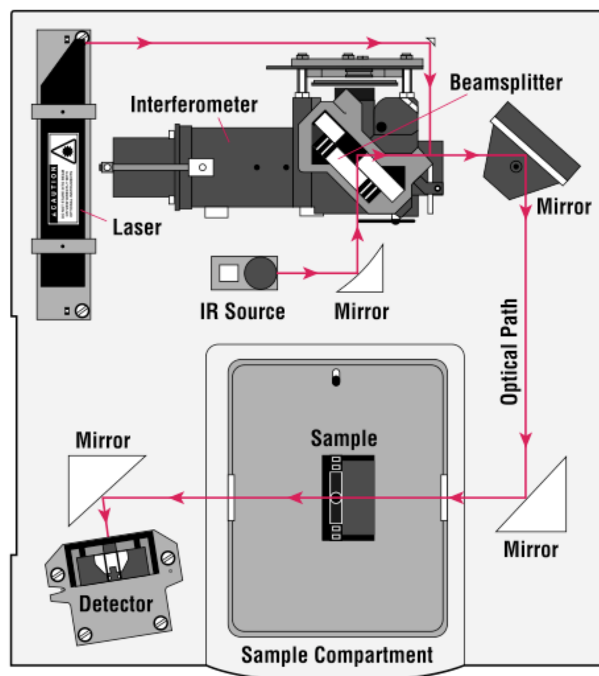

Figure 3-15 Diagram showing the layout of commercial FTIR spectrometer.[47]

The most common interferometer used in FTIR spectroscopy is a Michelson interferometer, as shown in **Figure 3-16**. When the coherent infrared light with wavelength λ travels to the beam splitter, it is split into two beams. After which, one beam is reflected by a stationary mirror with a fixed path length and the other beam is reflected by a moving mirror that moves over a distance Δl. Thus, the moving mirror reflects the second beam with a specific phase with respect to the first beam, and the phase changes as a function of mirror position. The difference in the path lengths is called the optical path difference or retardation (δ). The two beams are recombined at the beam splitter and then interfere constructively (δ = nλ, where n is an integer) and destructively (δ = nλ/2, where n is odd).[48] For each λ, one obtains a sinusoidal signal as a function of mirror position. An interferogram, which is the retardation (δ) plotted against the signal intensity of the detector, will then get Fourier Transformed and generate a spectrum. By choosing the interferogram

of the beams reflected from the sample or transmitted through the sample, reflectance or transmission FTIR spectroscopy can be obtained.

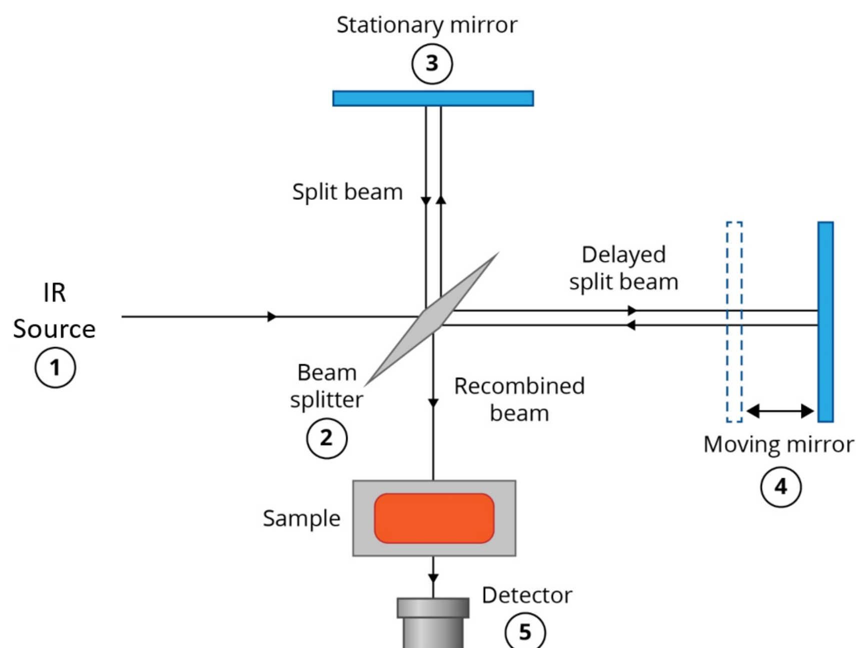

Figure 3-16 Schematic diagram of a Michelson interferometer.[49]

In this research work, a Thermo Nicolet Magna 550 series II FTIR spectrometer with a mid-IR source (4000-400 cm^{-1}) is used. During the measurement, the sample compartment is purged with dry nitrogen, to minimize contamination, such as moisture, from the ambient or reactive gases. A calibration is also applied to each measured spectrum minimizing the effects from H_2O and CO_2 in the light path. Before each measurement, it is important to monitor the C=O bond peak (around 1740 cm^{-1}) from the FTIR spectrum to make sure that the CO_2 level is low enough for accurate measurement. For low-k a-SiOC:H dielectrics, we are mostly interested in Si-related and C-related chemical bonds (as well as water-related bonds). We need to determine their intensities, peak widths and area ratios

(which is defined as the ratio of the area under the peak of FTIR spectrum) before and after any plasma-processing steps. **Table 3-1** is a summary of the FTIR peak values of the various chemical bonds that could exist in a-SiOC:H based on the work of Grill *et al*. [45] and Das *et al*.[46]

Table 3-1 FTIR band peaks in terms of their atomic-unit configuration, observed wavenumber, and vibrational mode: v = stretching, δ = bending, ρ = rocking, a = antisymmetric and s = symmetric. Data from Reference [45] and [46].

Chemical Group	Wavenumber (cm^{-1})	Mode
Si-OH	3620	ν^s O-H
Absorbed H_2O	3385	ν^s O-H
sp^3 -CH_3	2965	ν^a C-H
	2875	ν^s C-H
sp^3 -CH_2	2930	ν^a C-H
	2860	ν^s C-H
sp^3 -CH	2910	ν^s C-H
O_3Si-(CH_3)	1270	δ^s CH_3
O_2Si-$(CH_3)_2$	1260	δ^s CH_3
Si-O-Si cage structure bonding angle > 144°	1140	ν^a Si-O-Si
Si-O-Si network structure bonding angle ~ 144°	1060-1065	ν^a Si-O-Si
Silicon suboxides bonding angle < 144°	1035	ν^a Si-O-Si
Si-OH	920	ν^s Si-OH
H-SiO_3	890	δ H-Si-O
Si-$(CH_3)_3$	~850	ν Si-C; ρ^a CH_3
Si-O-Si network smaller angle	~800	ν Si-O-Si
Si-$(CH_3)_2$	~800	ν Si-C; ρ^a CH_3
Si-$(CH_3)_2$	~760	ν Si-C, ρ Si-CH_3; ρ^a CH_3
Si-O-Si network and ring opening	450	ρ Si-O-Si

3.6 Electrical Characterization

In this work, a Metal-Insulator-Semiconductor (MIS) structure is used for electrical characterization of the low-k a-SiOC:H thin films, which are deposited directly on a 300-mm diameter Si wafer. These structures are designed to closely mimic a parallel-plate capacitor comprised of a metal electrode, the low-k dielectric material under test, and the Si semiconducting substrate. A solid pin probe from a probe station (Signatone S-1160) was used to make separate electrical contacts at the top metal electrode and the bottom semiconducting electrode so as to facilitate leakage current and TDDB measurements.

Figure 3-17 shows an optical micrograph of the deposited metal electrodes and a cross section of the MIS structures. The metal electrode is deposited on top of the low-k dielectrics using e-beam evaporation. The electrode patterns are defined using commercially available transmission electron microscope (TEM) grids that have a hexagonal-array pattern. The area of each hexagon is about 2.8×10^{-4} cm^2. The deposited metal electrode has two layers, as shown in **Figure 3-17**. The bottom layer is 100 nm of titanium (Ti) and is directly in contact with the a-SiOC:H. Since the diffusivity of Ti into a-SiOC:H is much smaller than that of Cu, utilizing Ti electrodes can effectively avoid contamination of low-k dielectrics from metal diffusion. On top of the 100 nm Ti layer, a 200-nm layer of silver (Ag) is deposited using the same hexagonal-array-patterned mask. The purpose of this 200-nm Ag layer is to minimize the physical-stress pressure from the sharp pin probe during electrical test, because low-k a-SiOC:H thin films usually have weak mechanical strength. This external physical stress could cause damage resulting in higher leakage currents and lowering of the breakdown voltage.

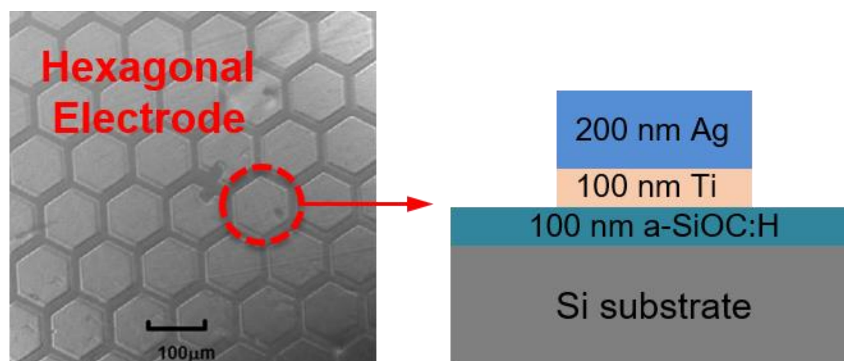

Figure 3-17 Hexagonal pattern of the metal layer on top of the dielectric film and the MIS structure used for electrical characterization test.

Metal-Insulator-Metal (MIM) testing structures are also used in this work for measurements on low-k/Cu thin film stacks, as illustrated in

Figure 3-18, in which there is layer of 100-nm thermally grown SiO_2 on top of the Si substrate. Thus, the previously described MIS test structure does not work. Because Cu was found to diffuse into low-k organosilicates after deposition of Cu electrodes on the a-SiOC:H using either e-beam evaporation or sputter deposition [50], the sample preparation procedure was optimized as follows. First, 100 nm of SiO_2 was thermally grown as an adhesion layer on the Si wafer. Next, a Ta/TaN barrier layer was deposited on the SiO_2 followed by electroplating a layer of Cu. Then, the Cu layer was chemically-mechanically-polished (CMP) to 350 nm and the surface of the Cu was treated with H_2 plasma to remove the Cu corrosion inhibitors and to reduce Cu surface oxides formed by ambient exposure. Finally, the a-SiOC:H thin film (k=3.2, density 1.5g/cm^3) was deposited at a thickness of 100 nm on the Cu film at temperatures of the order of 400 ^oC using a standard commercially available 300-mm PECVD tool. Additional details concerning PECVD processing and

thin-film measurements have been previously reported.[43,51] These low-k/Cu stacks are well suited to study Cu migration into low-k a-SiOC:H from VUV irradiation.

The MIM structure is fabricated as follows. (1) the top electrode is still the hexagon-patterned Ti/Ag metal dot, which is identical to the one used in the MIS structure as discussed above, (2) the bottom electrode is a Cu layer underneath the low-k organosilicate, which is formed by sputtering the low-k a-SiOC:H thin film using the 3 keV ion gun from the XPS system.

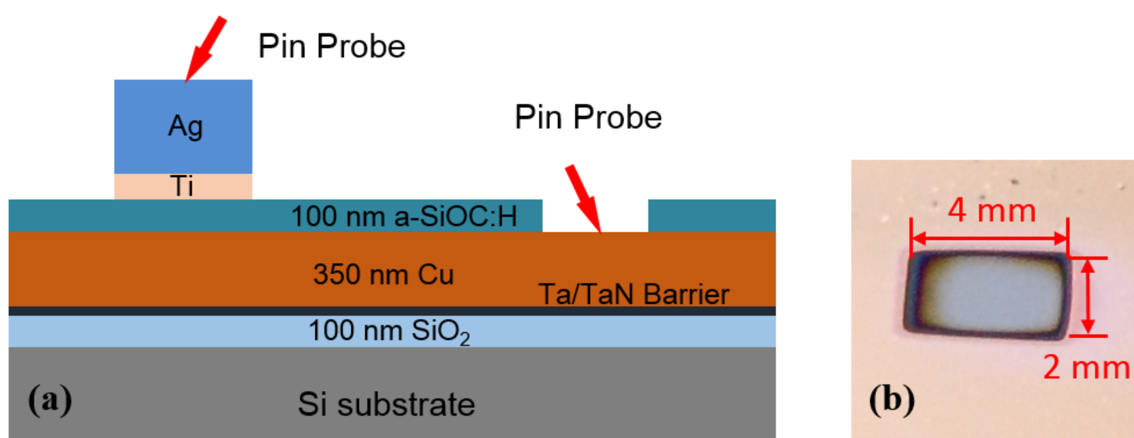

Figure 3-18 (a) MIM structure used for electrical characterization test of a-SiOC:H deposited on a 350-nm Cu layer. The Cu layer was plated on a Si wafer above a Ta/TaN barrier layer and a 100-nm thermal-grown SiO_2 adhesion layer. (b) Top view of the Cu electrode generated on the film stack by ion sputtering, with a size of 4 mm × 2mm.

Figure 3-18 (b) shows the top view of the Cu electrode generated on the film stack by ion sputtering, with a size of 4 mm × 2 mm. This MIM structure, electrically in contact with the pin probes, enables one to make the I-V, C-V and TDDB measurements on a-SiOC:H by taking account of the effect of Cu migration, because Cu can diffuse into the

dielectric because of the concentration gradient at the Cu/dielectric interface. It should be noted that the 100 nm a-SiOC:H thin film is dense a-SiOC:H and is considered to be a candidate low-k capping layer. The MIM structure illustrated here has also been used to measure the samples with a-SiCN:H capping layers. We observed that under the bias-temperature-bias (225 ºC, 2.5 MV/cm) over 5 hours, Cu can penetrate through a 10 nm capping layer of a-SiCN:H and enter into the bulk of low-k dielectric, which will be described in details in Chapter V.

It should also be noted that through it can make rapid, non-destructive contacts on a sample for electrical characterization, a mercury probe is not suited for electrical testing on the porous low-k organosilicates, because recent work found that mercury can easily diffuse into the low-k organosilicates under electrical bias and cause sample contamination and degradation of their electrical properties[52].

3.7 References

[1] J. R. Woodworth, M. E. Riley, V. A. Arnatucci, T. W. Hamilton, and B. P. Aragon, "Absolute intensities of the vacuum ultraviolet spectra in oxide etch plasma processing discharges," *J Vac Sci Technol A*, Vol. **19**, pp.45-55 (2001).

[2] X. Guo, J. E. Jakes, S. Banna, Y. Nishi, and J. L. Shohet, "Effects of plasma and vacuum-ultraviolet exposure on the mechanical properties of low-k porous organosilicate glass," *Journal of Applied Physics*, Vol. **116**, 044103 (2014).

[3] R. Brooks, M. Ingle, J. Milnes, J. Howorth, and J. Hutchings, "Wavelength-dependent resolution and electron energy distribution measurements of image intensifiers," Proc. SPIE 6294, San Diego, CA, 2006.

[4] J. L. Lauer, J. L. Shohet, C. Cismaru, R. W. Hansen, M. Y. Foo, and T. J. Henn, "Photoemission and conduction currents in vacuum ultraviolet irradiated aluminum oxide," *Journal of Applied Physics*, Vol. **91**, pp.1242-1246 (2002).

[5] J. L. Lauer, H. Sinha, M. T. Nichols, G. A. Antonelli, Y. Nishi, and J. L. Shohet, "Charge Trapping within UV and Vacuum UV Irradiated Low-k Porous Organosilicate Dielectrics," *Journal of the Electrochemical Society*, Vol. **157**, pp.G177-G182 (2010).

[6] R. J. Powell, "Hole photocurrents and electron tunnel injection induced by trapped holes in SiO2 films," *Journal of Applied Physics*, Vol. **46**, pp.4557-4563 (1975).

[7] H. Sinha, M. T. Nichols, A. Sehgal, M. Tomoyasu, N. M. Russell, G. A. Antonelli, Y. Nishi, and J. L. Shohet, "Effect of vacuum ultraviolet and ultraviolet irradiation on mobile charges in the bandgap of low-k-porous organosilicate dielectrics," *Journal of Vacuum Science & Technology A*, Vol. **29**, 010601 (2011).

[8] H. Sinha, J. L. Lauer, M. T. Nichols, G. A. Antonelli, Y. Nishi, and J. L. Shohet, "Effect of vacuum ultraviolet and ultraviolet Irradiation on capacitance-voltage characteristics of low-k-porous organosilicate dielectrics," *Applied Physics Letters*, Vol. **96**, 052901 (2010).

[9] H. Zheng, S. W. King, V. Ryan, Y. Nishi, and J. L. Shohet, "Bandgap measurements of low-k porous organosilicate dielectrics using vacuum ultraviolet irradiation," *Applied Physics Letters*, Vol. **104**, 062904 (2014).

[10] X. Guo, D. Pei, H. Zheng, S. W. King, Y.-H. Lin, H.-S. Fung, C.-C. Chen, Y. Nishi, and J. L. Shohet, "Measurements of Schottky barrier at the low-k SiOC:H/Cu interface using vacuum ultraviolet photoemission spectroscopy," *Applied Physics Letters*, Vol. **107**, 232905 (2015).

[11] J. Asmussen, "Electron-Cyclotron Resonance Microwave Discharges for Etching and Thin-Film Deposition," *Journal of Vacuum Science & Technology A*, Vol. **7**, pp.883-893 (1989).

[12] K. Suzuki, S. Okudaira, N. Sakudo, and I. Kanomata, "Microwave Plasma Etching," *Japanese Journal of Applied Physics*, Vol. **16**, pp.1979-1984 (1977).

[13] J. Asmussen, T. A. Grotjohn, P. Mak, and M. A. Perrin, "The design and application of electron cyclotron resonance discharges," *Ieee Transactions on Plasma Science*, Vol. **25**, pp.1196-1221 (1997).

[14] S. Matsuo and M. Kiuchi, "Low Temperature Chemical Vapor Deposition Method Utilizing an Electron Cyclotron Resonance Plasma," *Japanese Journal of Applied Physics*, Vol. **22**, L210 (1983).

[15] R. J. Shul, S. P. Kilcoyne, M. H. Crawford, J. E. Parmeter, C. B. Vartuli, C. R. Abernathy, and S. J. Pearton, "High temperature electron cyclotron resonance etching of GaN, InN, and AlN," *Applied Physics Letters*, Vol. **66**, pp.1761-1763 (1995).

[16] M. T. Nichols, "The Effects of Processing Induced Damage on Electrical Conduction Mechanisms and Time-Dependent Dielectric Breakdown of Low-k Organosilicates," Doctor of Philosophy Thesis, University of Wisconsin, Madison, 2013.

[17] M. T. Nichols, K. Mavrakakis, Q. Lin, and J. L. Shohet, "The effects of plasma exposure and vacuum ultraviolet irradiation on photopatternable low-k dielectric materials," *Journal of Applied Physics*, Vol. **114**, 104107 (2013).

[18] K. Nojiri, "Dry Etching Technology for Semiconductors". (Springer International Publishing, Switzerland, 2015).

[19] X. Guo, J. E. Jakes, M. T. Nichols, S. Banna, Y. Nishi, and J. L. Shohet, "The effect of water uptake on the mechanical properties of low-k organosilicate glass," *Journal of Applied Physics*, Vol. **114**, 084103 (2013).

[20] K. Vanstreels and A. M. Urbanowicz, "Nanoindentation study of thin plasma enhanced chemical vapor deposition SiCOH low-k films modified in He/H2 downstream plasma," *Journal of Vacuum Science & Technology B*, Vol. **28**, pp.173-179 (2010).

[21] C. Gaire , Y. Ou, H. Arao, M. Egami, A. Nakashima, R. C. Picu, G. Wang, and T. Lu, "Mechanical properties of porous methyl silsesquioxane and nanoclustering silica films using atomic force microscope," *Journal of Porous Materials*, Vol. **17**, pp.11-18 (2010).

[22] D. S. Stone, "Elastic rebound between an indenter and a layered specimen: Part I. Model," *J Mater Res*, Vol. **13**, pp.3207-3213 (1998).

[23] D. S. Stone, K. B. Yoder, and W. D. Sproul, "Hardness and elastic modulus of TiN based on continuous indentation technique and new correlation," *Journal of Vacuum Science & Technology A*, Vol. **9**, pp.2543-2547 (1991).

[24] X. Guo, J. E. Jakes, S. Banna, Y. Nishi, and J. L. Shohet, "Effect of water uptake on the fracture behavior of low-k organosilicate glass," *Journal of Vacuum Science & Technology A*, Vol. **32**, 031512 (2014).

[25] W. C. Oliver and G. M. Pharr, "An improved technique for determining hardness and elastic modulus using load and displacement sensing indentation experiments," *J Mater Res*, Vol. **7**, pp.1564-1583 (1992).

[26] J. J. Wortman and R. A. Evans, "Young's Modulus, Shear Modulus, and Poisson's Ratio in Silicon and Germanium," *Journal of Applied Physics*, Vol. **36**, pp.153-156 (1965).

[27] A. Grill, "Porous pSiCOH Ultralow-k Dielectrics for Chip Interconnects Prepared by PECVD," *Annu Rev Mater Res*, Vol. **39**, pp.49-69 (2009).

[28] J. E. Jakes , C. R. Frihart, J. F. Beecher, R. J. Moon, P. J. Resto, Z. H. Melgarejo, O. M. Suárez, H. Baumgart, A. A. Elmustafa, and D. S. Stone, "Nanoindentation near the edge," *J Mater Res*, Vol. **24**, pp.1016-1031 (2009).

[29] K. Tapily, J. E. Jakes, D. Gu, H. Baumgart, and A. A. Elmustafa, "Nanomechanical study of amorphous and polycrystalline ALD HfO2 thin films," *International Journal of Surface Science and Engineering (IJSURFSE)*, Vol. **5**, 193 (2011).

[30] H. Li and J. J. Vlassak, "Determining the elastic modulus and hardness of an ultra-thin film on a substrate using nanoindentation," *J Mater Res*, Vol. **24**, pp.1114-1126 (2009).

[31] L. G. Wang, M. Ganor, S. I. Rokhlin, and A. Grill, "Nanoindentation analysis of mechanical properties of low to ultralow dielectric constant SiCOH films," *J Mater Res*, Vol. **20**, pp.2080-2093 (2005).

[32] David Briggs and Martin P Seah, "Practical surface analysis by Auger and X-ray photoelectron spectroscopy". (John Wiley & Sons Ltd, Chichester, 1983).

[33] J. F. Watts and J. Wolstenholme, "An introduction to surface analysis by XPS and AES". (John Wiley & Sons Ltd, England, 2003).

[34] J. Schweppe, R. D. Deslattes, T. Mooney, and C. J. Powell, "Accurate Measurement of Mg and Al K-Alpha-1,2 X-Ray-Energy Profiles," *J Electron Spectrosc*, Vol. **67**, pp.463-478 (1994).

[35] X. Guo, H. Zheng, S. W. King, V. V. Afanas'ev, M. R. Baklanov, J. F. de Marneffe, Y. Nishi, and J. L. Shohet, "Defect-induced bandgap narrowing in low-k dielectrics," *Applied Physics Letters*, Vol. **107**, 082903 (2015).

[36] C. D. Wagner, L. E. Davis, M. V. Zeller, J. A. Taylor, R. H. Raymond, and L. H. Gale, "Empirical atomic sensitivity factors for quantitative analysis by electron spectroscopy for chemical analysis," *Surf Interface Anal*, Vol. **3**, pp.211-225 (1981).

[37] D. Pines, "Collective Energy Losses in Solids," *Reviews of Modern Physics*, Vol. **28**, pp.184-198 (1956).

[38] P. Nozières and D. Pines, "Electron Interaction in Solids. Characteristic Energy Loss Spectrum," *Physical Review*, Vol. **113**, pp.1254-1267 (1959).

[39] M. T. Nichols, W. Li, D. Pei, G. A. Antonelli, Q. Lin, S. Banna, Y. Nishi, and J. L. Shohet, "Measurement of bandgap energies in low-k organosilicates," *Journal of Applied Physics*, Vol. **115**, 094105 (2014).

[40] H. Winter, P. J. Durham, and G. M. Stocks, "Theory of valence-band XPS spectra of random alloys: application to Ag x Pd 1-x," *Journal of Physics F: Metal Physics*, Vol. **14**, 1047 (1984).

[41] S. Rondon, A. Proctor, M. Houalla, and D. M. Hercules, "Use of XPS Valence Bands to Infer Structural Information about the Molybdenum Phase in Carbon-Supported Molybdenum Catalysts," *The Journal of Physical Chemistry*, Vol. **99**, pp.327-331 (1995).

[42] D. A. Zatsepin, P. Mack, A. E. Wright, B. Schmidt, and H. J. Fitting, "XPS analysis and valence band structure of a low-dimensional SiO2/Si system after Si+ ion implantation," *Physica Status Solidi (a)*, Vol. **208**, pp.1658-1661 (2011).

[43] S. W. King, B. French, and E. Mays, "Detection of defect states in low-k dielectrics using reflection electron energy loss spectroscopy," *Journal of Applied Physics*, Vol. **113**, 044109 (2013).

[44] X. Guo, S. W. King, H. Zheng, P. Xue, Y. Nishi, and J. L. Shohet, "Effects of vacuum-ultraviolet irradiation on copper penetration into low-k dielectrics under bias-temperature stress," *Applied Physics Letters*, Vol. **106**, 012904 (2015).

[45] A. Grill and D. A. Neumayer, "Structure of low dielectric constant to extreme low dielectric constant SiCOH films: Fourier transform infrared spectroscopy characterization," *Journal of Applied Physics*, Vol. **94**, pp.6697-6707 (2003).

[46] G. Das, G. Mariottoa, and A. Quarantab, "Microstructural Evolution of Thermally Treated Low-Dielectric Constant SiOC : H Films Prepared by PECVD," *Journal of The Electrochemical Society*, Vol. **153**, pp.F46-F51 (2006).

[47] Thermo Nicolet Corporation, "Introduction to Fourier Transform Infrared Spectrometry," *www.thermonicolet.com*, Vol., (2001).

[48] P. L. King, M. S. Ramsey, P. F. McMillan, and G. Swayze, "Laboratory Fourier transform infrared spectroscopy methods for geologic samples". (Mineralogical Association of Canada, London, Ontario 2004).

[49] Keit Spectrometers, "http://keit.co.uk/ftir-spectrometer-technology/," Vol.

[50] M. He, S. Novak, L. Vanamurthy, H. Bakhru, J. L. Plawsky, and T. Lu, "Cu penetration into low-k dielectric during deposition and bias-temperature stress," *Applied Physics Letters*, Vol. **97**, 252901 (2010).

[51] S. W. King, M. French, M. Jaehnig, M. Kuhn, and B. French, "X-ray photoelectron spectroscopy investigation of the Schottky barrier at low-k a-SiO(C):H/Cu interfaces," *Applied Physics Letters*, Vol. **99**, 202903 (2011).

[52] D. Pei, M. T. Nichols, S. W. King, J. S. Clarke, Y. Nishi, and J. L. Shohet, "Time-dependent dielectric breakdown measurements of porous organosilicate glass using mercury and solid metal probes," *Journal of Vacuum Science & Technology A*, Vol. **32**, 051509 (2014).

Chapter IV

VUV-induced Damage to Low-k Organosilicates

In this Chapter, the effects of VUV photon-irradiation-induced changes to low-k a-SiOC:H organosilicate thin films are investigated. As detailed in Chapter III, use of a synchrotron beamline as a VUV photon source enables one to measure the VUV-induced damage to low-k organsilicates as function of photon energy. First, modifications to mechanical properties of a-SiOC:H thin film from VUV irradiation are examined using nanoidentation. The damage mechanisms are determined based on the FTIR and XPS measurements. Next, VUV-induced leakage currents and moisture uptake in organosilicate films are investigated. The goal of this chapter is to clearly determine the effects of VUV-irradiation on intrinsic low-k a-SiOC:H organosilicates. In particular, VUV-induced mechanical modifications will be emphasized. Finally, this chapter will attempt to elucidate the mechanisms of energy-dependent damage effects from VUV irradiation.

4.1 VUV-induced Mechanical Modifications

The object of this section is to measure VUV-induced modifications to the mechanical properies of porous low-k a-SiOC:H organosilicates, and how this compares with energetic charged-particle-induced damage during plasma processing. To determine this, nanoindentation tests, as detailed in Chapter III, were made on a variety of a-SiOC:H samples after exposure to VUV photons from a synchrotron or to an ECR argon plasma. Changes of hardness (H), elastic modulus (E_s) and crack threshold (C_T) were measured. Crack threshold is defined as the ratio of the indentation depth to the film thickness at which crack is observed for the first time to the film thickness.

Monochromatic photon exposures were made at the University of Wisconsin Synchrotron Radiation Center and the Taiwan National Synchrotron Radiation Research Center using an apparatus described in the previous chapter. Photon energies were specifically selected to mimic those emitted by plasmas used to low-k processing, as listed in **Table 4-1**.

Table 4-1 Summary of the VUV photon energy used to examine the VUV-induced damage.

Photon Energy	VUV Spectral Line	Plasma Feed Gas	Photon Fluence
6.1 eV	202.6 nm	C_2F_6	4×10^{15} photons/cm^2
10.2 eV	121.6 nm	CHF_3	4×10^{15} photons/cm^2
11.8 eV	104.8 nm	Ar	4×10^{15} photons/cm^2

Photons of 11.8 eV energy were used to mimic the strong VUV argon lines at 104.8 nm and 106.6 nm.[1,2] Photons of 10.2 eV energy were used to mimic a CHF_3 discharge (trifluoromethane, a typically used feed gas for low-k dielectric etch). Such a discharge emits a strong VUV hydrogen line at 121.6 nm. [2] Photons of 6.1 eV energy were used to mimic C_2F_6 discharges (hexafluoroethane, another typically used feed gas for low-k dielectric etch). This discharge emits a strong VUV carbon-fluorine line at 202.6 nm, as summarized in the following table.[2] For each irradiation, the total photon fluence impinging on the sample was approximately 4×10^{15} photons/cm^2, which is close to those produced during typical plasma processing.[2,3]

4.1.1 Mechanical-Property Changes Produced by VUV Irradiation

The low-k organosilicates used here are 640-nm porous a-SiOC:H (k=2.65). These were produced with a plasma-enhanced chemical-vapor-deposited (PECVD) process on <100> p-type silicon wafers. The deposition took place in a capacitively coupled plasma reactor utilizing a 13.56 MHz RF source in the presence of several inert and reactive gases with an organosilane precursor. The thickness of 640 nm was chosen because it can lower the effects from the underlying Si substrate during nanoindentation testing.

After VUV exposure, nanoindentation tests were carried out at room temperature on these low-k dielectrics using a Hysitron TriboIndenter® equipped with a diamond Berkovich tip and operated in open-loop control. Stone's elastic model[4] was applied to the measured results to minimize the effects from the Si substrate, as has been discussed in Chapter III. **Table 4-2** summaries the changes in the hardness (H), the elastic modulus (E_s) and the film-crack threshold (C_T) after VUV exposure, in which the percentage changes of

these properties were all calculated based on the same measurements made on the pristine (no exposure) samples.

Table 4-2 Summary of the changes in hardness (H), elastic modulus (Es) and crack threshold (CT) of a-SiOC:H after VUV exposure of several energies. The percentage changes of the VUV-exposed samples were calculated based on the results of pristine (no exposure) samples. Data in the table has been published as in Reference [3].

sample	VUV exposure	Hardness (GPa)	Elastic Modulus (GPa)	Crack threshold
a-SiOC:H	no exposure	0.35 ± 0.02	5.5 ± 0.2	0.66
a-SiOC:H	6.1 eV	0 ± 1 %	0 ± 1 %	0 ± 2 %
a-SiOC:H	8.0 eV	1 ± 1 %	0 ± 1 %	0 ± 2 %
a-SiOC:H	8.5 eV	8 ± 1 %	3 ± 1 %	6 ± 2 %
a-SiOC:H	11.8 eV	12 ± 1 %	4 ± 1 %	8 ± 2 %

From Table 4-2, it is observed that VUV-irradiation with energies of 10.2 and 11.8 eV increases the film hardness by 11% and 12%, respectively, and it also increases the film elastic modulus by 3% and 4%, respectively. For the crack threshold, which is defined as the ratio of indentation depth to film thickness at which cracking is observed for the first time [5], increases of 9% and 8%, respectively, were observed for these samples. However, after VUV-irradiation with photons of energy 6.1 eV and fluence of 4×10^{15} photons/cm^2, the film hardness and modulus were almost unchanged, suggesting that VUV-induced mechanical modifications to low-k a-SiOC:H thin films, including hardness, elastic modulus and crack threshold, are energy-dependent. As will be discussed in the following text of this Chapter, the VUV-induced chemical changes and electrical modifications have also shown this energy dependence.

Usually the mechanical properties of the film are related to the skeleton structure of the material. The variations of the hardness and/or elastic modulus indicate the occurrence of structural changes.[6],[7],[8] Thus, to confirm the nature of the Si-O, Si-C and C-O/H chemical bond structures in the films after VUV irradiation by photons of as a function of photon energy, FTIR and XPS measurements were made on the samples after VUV exposure, as will be discussed in the following material.

4.1.2 Chemical Analysis of Damage Mechanisms

Figure 4-1 shows the differential FTIR spectrum of the a-SiOC:H after VUV irradiation with several photon energies. This was obtained by subtracting the FTIR spectrum of a pristine sample from that of a VUV-exposed sample. After both 10.2 eV and 11.8 eV photon irradiation, structural rearrangements (conversion of the Si-O-Si chemical bonds from cage structure to network structure, carbon depletion and also decrease of Si-OH bonds) are observed in the spectra, as evidenced by the significantly decreased bond densities of Si-$(CH_3)_n$ (1250~1280cm^{-1}, 760~870cm^{-1}), Si-O-Si cage (~1130cm^{-1}) and Si-OH (890~990cm^{-1}) structures in a-SiOC:H films.

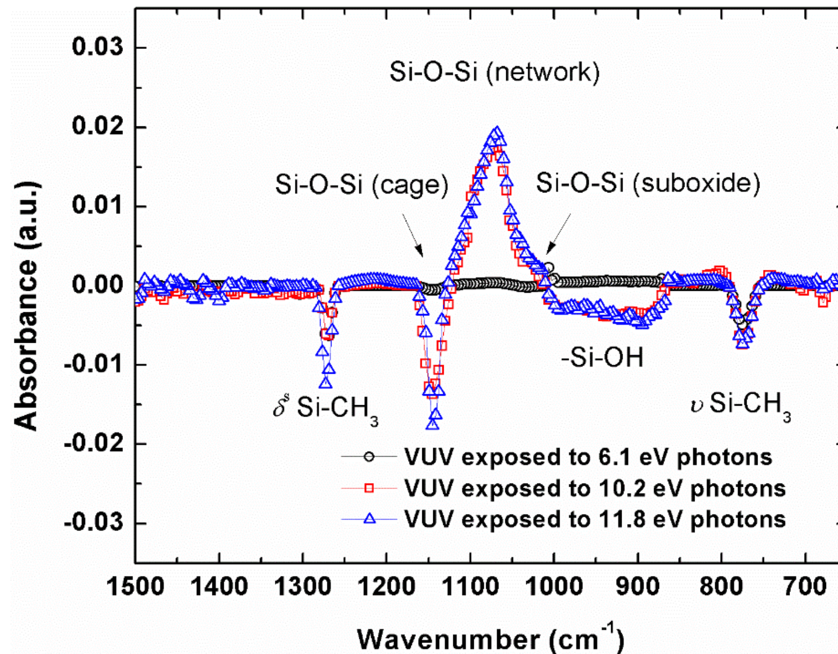

Figure 4-1 Differential FTIR spectrum of VUV-irradiated a-SiOC:H organosilicates with several photon energies. Here 'δ^S' corresponds the bending vibrational mode and 'υ' corresponds the stretching vibrational mode.[3]

On the other hand, an increase in the peak intensity of the Si-O-Si network (~1063cm^{-1}) and the Si-O-Si suboxide (~1023cm^{-1}) structures after both 10.2 eV and 11.8 eV photon irradiation was seen. However, for a 6.1 eV exposed sample, only the bond densities of Si-$(CH_3)_n$ (1250~1280cm^{-1}, 760~870cm^{-1}) were found to decrease. Since both the film hardness, elastic modulus and crack threshold did not change for 6.1 eV exposed a-SiOC:H, one can conclude that Si-$(CH_3)_n$ bonds do not affect the mechanical properties. Thus, the increased mechanical properties including the hardness, elastic modulus and crack threshold, as observed in the 10.2 and 11.8 eV exposed samples, should come from the increased concentration of the Si-O-Si network and suboxide structures. This agrees with A. Grill's report [9] that the methyl group (-CH_3) is only attached to Si as a terminal

group and not bridged to a network structure. Thus, the mechanical property changes in the film must be related to the Si-O-Si skeleton structure, which is usually defined as the series of atoms bonded together that form the essential structure of the compound and are referred to the Si-O-Si structure for low-k a-SiOC:H thin films.[10] (A skeletal structure of a compound is q series of atoms bonded together that form the essential structure of the material.)

As can be seen from the differential FTIR in **Figure 4-1**, the Si-O-Si skeleton structure changes can be described from two aspects: (1) conversion from cage structures to network structures; (2) formation of new crosslinked Si-O-Si structures from reactions of non-crosslinked structures.

For the conversion from cage structures to network structures, it has been reported that in organosilicates, deep UV radiation with a wavelength shorter than 150 nm (E_{photon} > 8.26 eV) can induce a structural rearrangement by converting the existing Si-O-Si cage type structure (Si-O-Si bond angle is 150° or greater) into a Si-O-Si network type structure (Si-O-Si bond angle is 144°).[11],[12] This structural rearrangement can only be initiated by UV/VUV irradiation with wavelengths shorter than the absorption edge of the Si-O-Si network, because only VUV photons with energy larger than the Si-O-Si bond strength can rearrange the bond structure.[3] This threshold of photon energy coincidentally corresponds with the Si-O bond dissociation energy (8.3 eV). That means only photons with energy higher than 8.3 eV can trigger the $Si\text{-}O_2$ bond (known as the silica bond) conversion from the Si-O-Si cage structure to the Si-O-Si network structure.

Figure 4-2 shows a schematic for the Si-O-Si cage structure and the Si-O-Si network structure. Of the two bond states, the Si-O-Si network structure (cross-linked ladder and linear-chain structures), as illustrated in **Figure 4-2**, is more energetically stable than the cage structure. The relative amounts of cage-type and network-type bonding structures affect mechanical properties such as hardness and modulus.[3] Higher network-type bond concentrations tend to produce a higher-modulus film. Thus, the film mechanical properties change because the concentration of energetically stable network structures within the film increases after irradiation.

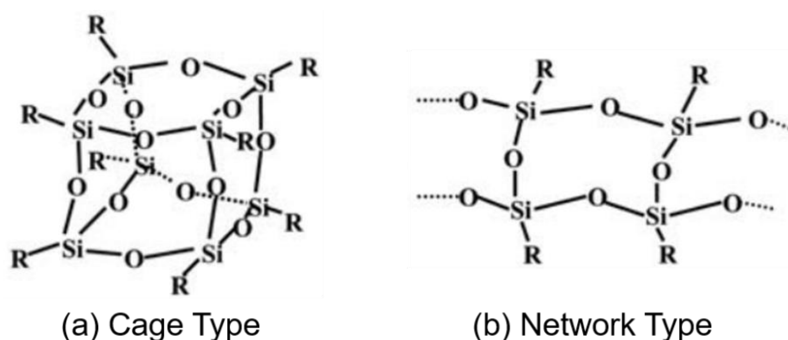

Figure 4-2 A generalized schematic for the Si-O-Si bond struetures: (a) Cage structure; (b) Network structure (cross-linked ladder and linear chain structures). R in the figure represents the -CH_3 (methyl group). [13],[14]

For the formation of new bridging Si-O-Si structures from reactions with non-bridging structures, two mechanisms have been proposed when using VUV photons expose the low-k organosilicates:[12], [15] (a) a photon-assisted reaction of one silanol and one methyl group, as shown in Equation (**4-1**) [12], or (b) a condensation reaction of two silanol groups, as shown in Equation (**4-2**) [15]:

$$O_3{\equiv}Si\text{-}OH + H_3C\text{-}Si{\equiv}O_3 + h\nu \rightarrow O_3{\equiv}Si\text{-}O\text{-}Si{\equiv}O_3 + H^+ + CH_3^+, \quad (4\text{-}1)$$

$$O_3{\equiv}Si\text{-}OH + HO\text{-}Si{\equiv}O_3 + h\nu \rightarrow O_3{\equiv}Si\text{-}O\text{-}Si{\equiv}O_3 + H^+ + OH^-, \quad (4\text{-}2)$$

Both of these photon-assisted reactions, as illustrated above, increase the number of bridging ≡Si-O-Si≡ bonds by depleting either the non-bridging ≡Si-OH bonds or the ≡Si-CH_3 bonds. As a result, the degree of crosslinking in the films is increased and causes the mechanical property changes. It is not clear which reaction mechanism is dominant inside of low-k a-SiOC:H when exposed to high-energy VUV photons. However, since both reactions include the silanol group (-Si-OH), they need the high-energy VUV photons to dissociate the Si-O bond first and then the reactions are triggered by the VUV-dissociated Si-O bond, which has a lower activation energy than that of Si-O bond without VUV exposure.[3]. It is plausible that there is a threshold photon energy for VUV-induced mechanical property changes and it corresponds to the dissociation energy of Si-O chemical bond (8.3 eV). Thus, only photons with energies larger than this threshold can cause mechanical property changes.

To further verify this threshold energy, 8.0 eV VUV photons (which are lower in energy than the 8.3 eV dissociation energy of the Si-O bond) and 8.5 eV photons (which are slightly higher in energy than 8.3 eV), were used to irradiate the sample with the same fluence. The reason we chose 8.0 eV and 8.5 eV is because near 8.3 eV, the energy resolution of the VUV beam from the synchrotron is ~0.1 eV, as discussed in Chapter III, and a step of 0.2 eV can make sure that there is minimal energy overlap during VUV irradiation. The measured mechanical-property changes are also listed in **Table 4-1** Summary of the VUV photon energy used to examine the VUV-induced damage. It can be

seen that after 8.0 eV photon irradiation, no obvious changes in film hardness, modulus and crack threshold were observed, just as was the case for the 6.1 eV photon-irradiated samples. However, after 8.5-eV photon irradiation, the film hardness was found to increase 8% and the elastic modulus and crack threshold increased 3% and 6% respectively, which is comparable to that found for 10.2 and 11.8 eV photon-irradiated samples. Therefore, one can conclude that VUV photons with an energy of 8.3 eV (the dissociation energy of the Si-O chemical bond) or higher can cause changes of the mechanical properties in a-SiOC:H thin film, while VUV photons with energy less than 8.3 eV do not have this effect as discussed above.

Figure 4-3 shows the XPS spectra of the O 1s, C 1s and Si 2p electron orbitals of a-SiOC:H thin films after VUV irradiation with a range of photon energies. No significant changes were seen for 6.1 eV exposed a-SiOC:H except some mild carbon depletion, compared with a pristine sample. For 10.2 and 11.8 eV photon-irradiated samples, both the Si 2p core-level peak and O 1s core-level peak shift to higher binding energy. This is seen as follows. Deconvolution of the Si 2p and O 1s peaks by Gaussian fitting, as shown in **Figure 4-3**, indicates an increase in the concentration of the bridging Si-O-Si bond structures (102.5 eV [16]) and the enhancement of degree of crosslinking inside of a-SiOC:H samples. This occurs because the Si 2p XPS peak of the bridging Si-O-Si bond is at 102.5 eV while the Si 2p peak of the non-bridging bond is at 101.4 eV, and thus the shifting of the Si 2p peak to higher energy indicates an increase of the bridging Si-O-Si bonds. This further corroborates the proposed structural rearrangement generated within the dielectrics as described earlier and illustrated in Equation (**4-1**) and Equation (**4-2**).

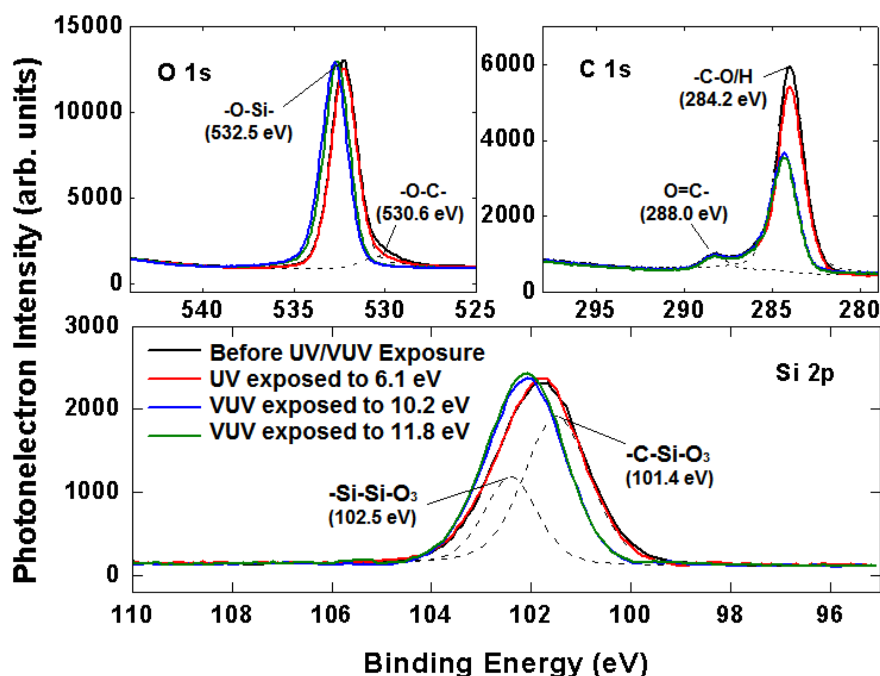

Figure 4-3 XPS spectra showing the changes of the O 1s, C 1s and Si 2p electron orbitals of as-deposited samples after synchrotron irradiation with several photon energies. The dashed lines are the decomposition results after fitting the spectrum with the Gaussian peaks of the unexposed samples.

It should be noted that in real plasma-processing steps, like dual-damascene etch, the mechanical changes produced by VUV photons might be not uniform in the vertical direction because the photon fluence on the dielectric surface is always larger than that in the bulk [17]. These non-uniform mechanical changes can generate physical stresses that are accumulated inside of the material and cause reliability issues, such as increased leakage currents and shortened time-dependent breakdown times. It should also be noted that no significant compositional change or film densification was observed in this case. This is quite different from plasma-induced Si-O-Si structural rearrangements, as will be discussed as follows.

4.1.3 Comparison with Ar Plasma Exposed a-SiOC:H

The same measurements were carried with Ar ECR plasma exposure on a-SiOC:H samples to examine the plasma-induced mechanical property changes and to compare the modifications from energetic ions and VUV photons. The separation between them is explained as follows. (1) In an Ar plasma, we have VUV and ions. We already studied and know how VUV affects the mechanical properties of a-SiOC:H. The difference of mechanical properties between VUV-exposed and Ar-plasma-exposed samples must come from ions. (2). In an Ar plasma, the RF-induced bias can be adjusted to measure the ion-induced mechanical properties change as a function of ion energy.

The work in this section is important because (1) results about reported plasma-induced damage from recent work are not consistent: Vanstreels [18] reported that He/H_2 plasma exposure results in a decrease in both hardness and elastic modulus of a-SiOC:H, while Broussous et al. [19] observed increased hardness and elastic modulus after He plasma exposure It is likely that the difference in results can be explained because the separation of the roles of different components in the plasma was not determined. However,, the work in this thesis does make this separation and night help to answer why they are contrary results. (2) few other works have separated the roles of energetic ions and VUV photons when examining the effects of plasma exposure on the mechanical properties of low-k materials.

Plasma exposures were made in an electron-cyclotron-resonance (ECR) plasma reactor operating with a 400 W, 2.45 GHz microwave power source and 875 Gauss magnetic field, as described previously. The sample chuck was located approximately 30-

cm downstream from the resonant layer. The chuck can be biased using a 100 W radio-frequency (RF) source and an L-type matching network. By varying RF-bias power, a DC bias in the range of 0 to -100 V can be placed on the sample chuck, through which control of the ion-impact energy from the plasma can be accomplished.[3] When there was no bias, the sample surface had a floating potential near zero and the typical energy of ions that reached the film surface was relatively low (10 to 40 eV).[20] In contrast, under -100 V_{DC} bias, the ion bombardment energy was more than one-hundred eV. Nanoindentation tests were made on the plasma-exposed samples following the same procedures. The measured results are listed in **Table 4-3**.

Table 4-3 Summary of the changes in hardness (*H*), elastic modulus (E_s) and crack threshold (C_T) of a-SiOC:H after Ar plasma exposure.

sample	exposure	% changes in hardness	% changes in modulus	% changes in crack threshold
a-SiOC:H	none	0	0	0
a-SiOC:H	plasma no bias	16 ± 1	4 ± 1	12 ± 2
a-SiOC:H	plasma -100V bias	23 ± 1	6 ± 2	16 ± 2

As can be seen, after plasma exposure (no bias), there is a 16% increase in hardness, a 4% increase in modulus and a 12% increase in the crack threshold, compared with that for a pristine a-SiOC:H sample. For samples exposed to a -100 V_{DC} r.f. bias, the hardness increased by 23%, the modulus increased by 6% and the crack threshold increased by 16%. Differential FTIR, as illustrated in **Figure 4-4**, show that the bond intensities of the Si-O-Si network (~1063cm^{-1}), the Si-O-Si cage (~1130cm^{-1}) and the Si-OH bond (890~990cm^{-1}) increased while those of the Si-(CH_3) bond (1250~1280cm^{-1}, 760~870cm^{-1}) and the Si-O-Si suboxide (~1023cm^{-1}) structures decreased after Ar plasma exposure (both for no bias

and -100 V_{DC} bias). These differential FTIR results agree with those observed by Shi et. al. [21], showing significant methyl depletion and a pronounced enhancement of the Si-O-Si network-bond structure.

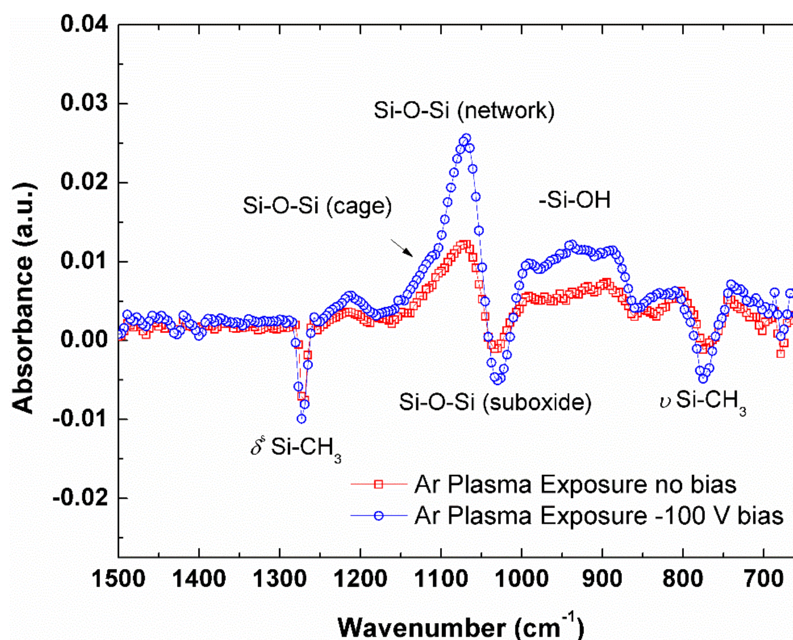

Figure 4-4 Differential FTIR spectrum of plasma-exposed porous organosilicate dielectric films with floating potential or a -100 V_{DC} bias applied to the sample chuck.[3]

It should be noted that the FTIR-bonding configuration changes might be produced from a synergy between the effects of energetic charged particles and VUV photons from Ar plasma.[3] Prager et al [11] pointed out that energetic UV/VUV photon irradiation can depopulate the Si-O-Si cage bond (Si-O-Si bond angle is 150° or greater) by forming a more energetically stable Si-O-Si network bond (with an Si-O-Si bond angle of 144°). However, our FTIR results show an increased Si-O-Si cage-bond intensity. Therefore, this infers that bombardment of energetic ions induces film-surface densification and is responsible for the increased Si-O-Si cage-bond density in the film surface.

These higher-energy ions can induce film densification in three ways[22]: (1) the physical bombardment of ions transfers their momentum to the Si-O-Si backbone structures and densifies them; (2) the concomitant densification of the Si-OH bonds induces film shrinkage; (3) impurity radicals/ions in the Ar plasma can react with or sputter off the -Si-CH_3 groups on the porosity walls and can induce a collapse of the pore structures.[22] To confirm these proposed mechanisms, XPS was also performed on the a-SiOC:H before and after plasma exposure, as shown in **Figure 4-5**.

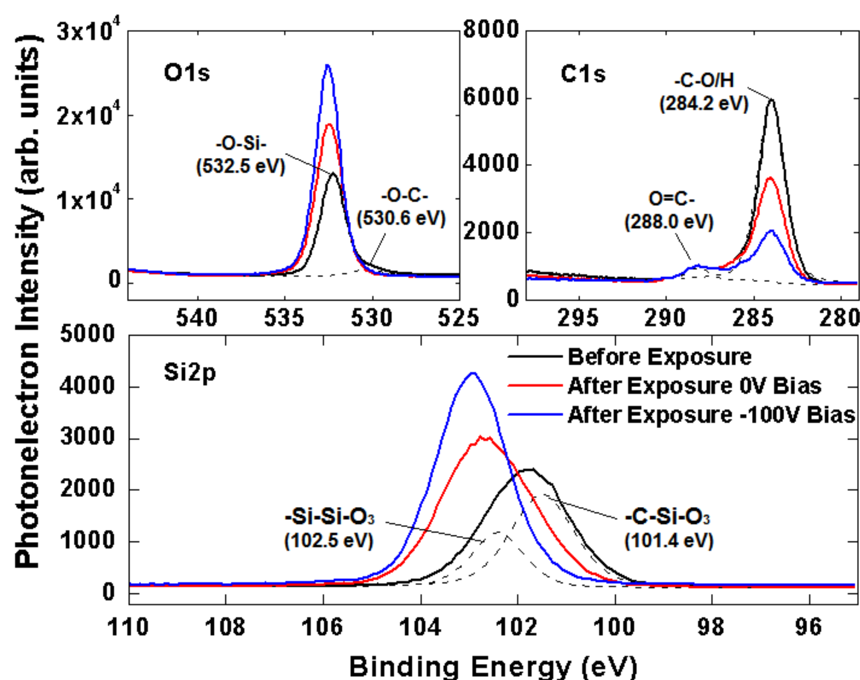

Figure 4-5 XPS spectra showing the changes of O 1s, C 1s and Si 2p electron orbitals of as-deposited samples after plasma exposure without bias or a -100 V DC bias applied to the sample chuck.

In the Ar plasma-exposed samples, several changes were observed in these spectra. The intensity of the C 1s peak decreases after plasma exposure and the decrease is more significant in the -100 V_{DC} RF-biased sample, indicating that energetic ions increase carbon

depletion in the film. This is consistent with the Si-CH_3 peak decreasing in the FTIR results as described above. The Si 2p peak has a significant shift to higher binding energies. For an unbiased plasma-exposed sample, the Si 2p peak center moves to 102.8 eV. Deconvolution results show the Si-O_4 bond (103.0 eV), as well as the Si-O_3 bond (101.4 eV) and the Si-Si-O_3 bond (102.5 eV) are formed on the sample surface. For a -100 V_{DC} RF-biased plasma-exposed sample, the Si 2p electron-orbital spectrum has a perfect Gaussian-shaped peak centered at 103.0 eV (Si-O_4 bond) with a full width at half maximum (FWHM) of 1.81 eV, indicating that a Si-O-Si network-structure layer is formed at the sample surface. In addition, a significantly increased intensity, for both O 1s and Si 2p peaks, is observed, which indicates densification of the film surface.

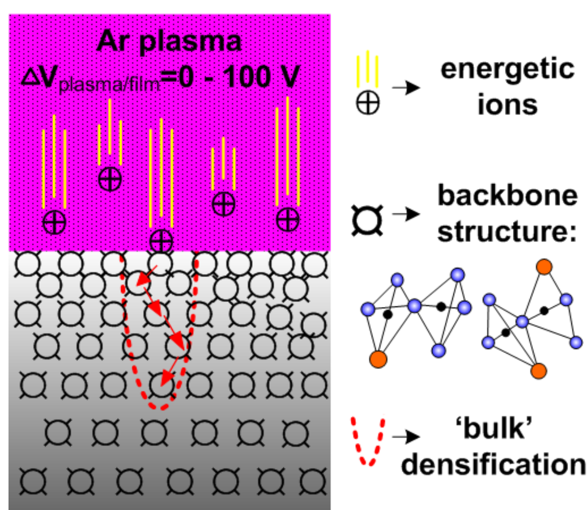

Figure 4-6 Physical model of ion bombardment-induced film bulk densification.

Based on both FTIR and XPS results, it can be concluded that energetic ions affect the a-SiOC:H properties mainly through physical bombardment, during which the ions transfer their momentum to the Si-O-Si backbone and transform them to more stable Si-O-Si network structures. In the meanwhile, the concentration of the Si-O-Si network

structures is increased. The mechanism for ion bombardment-induced film bulk densification is illustrated in **Figure 4-6**. Using an x-ray reflectivity (XRR) fitting based on multiple layer structures, Shi et al.[21] reported a "bulk" densified layer of 30 nm in plasma-exposed ultra low-k dielectric films (k = 2.2) with the film density increasing by 20%, compared with the undensified layer at the film bottom.

4.2 VUV-induced Leakage Currents

The level of leakage currents under external DC electric bias is a very important parameter of low-k ILD thin films, because they are directly related to the device reliability and power consumption in the BEOL. An ideal metal-interconnect dielectric should exhibit excellent electrical-insulating properties with leakage currents typically $< 10^{-8}$ A/cm^2 (up to electric fields of 4-6 MV/cm)[23],[24] and dielectric breakdown strengths $\geqslant$ 6-8 MV/cm.[25],[26] For porous a-SiOC:H thin films, the leakage currents are highly dependent on the material structure, like bandgap energy[27], defect states/density etc. [28] They are also dependent on fabrication technology, such as the deposition precursor[29], the porosity[30] and post UV curing [31], etc. **Section 4.1** shows VUV-induced mechanical modifications to a-SiOC:H thin films. It is necessary to also examine the effects of VUV irradiation on the leakage currents in a-SiOC:H.

A 100-nm a-SiOC:H (k = 3.2) thin film deposited on a Si wafer using PECVD was used for the leakage current measurements after VUV photon irradiation. The conditions of VUV irradiation are same as described in **Section 4.1**, where photon energies were set to 6.1 eV, 10.2 eV and 11.8 eV and total photon fluence was 4×10^{15} photons/cm^2. Since the bandgap energy of the sample used here is measured to be around 8.0 eV,[32] it also

enables one to compare the leakage currents after VUV photon irradiation with energy less than the bandgap energy (6.1 eV) with that of photons with energies higher than the bandgap energy (10.2 eV and 11.8 eV). After VUV irradiation, a MIS structure, with the Ti/Ag electrode, was fabricated as described in Chapter III and used to get the I-V characteristics at room temperature. The voltage ramp rate was 1 V/s for all measurements.

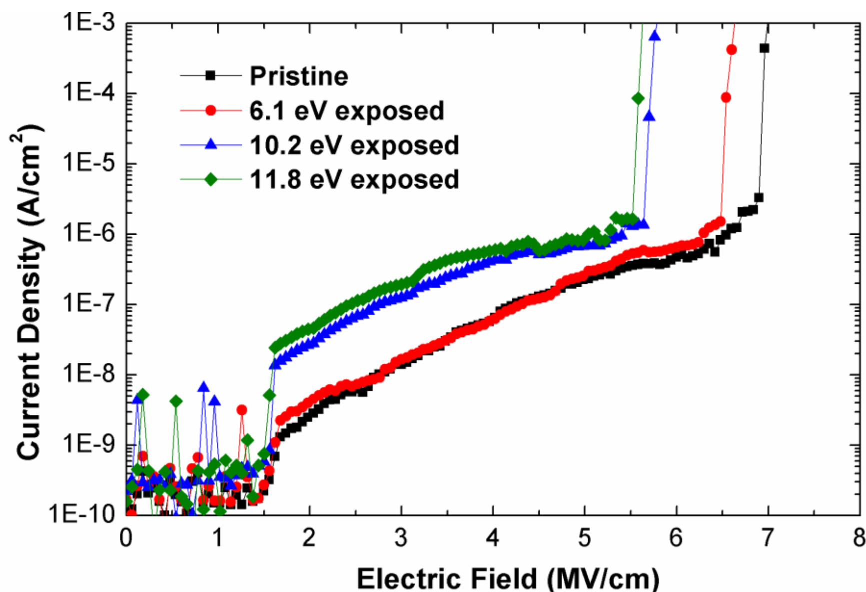

Figure 4-7 Comparison of leakage currents for pristine and VUV photon-irradiated a-SiOC:H thin films for several photon energies.

Figure 4-7 shows the leakage currents measured from both pristine and VUV photon irradiated a-SiOC:H thin film for several photon energies. These results are based on 10-time measurements on several spots on each a-SiOC:H sample. Over the entire range of electric fields analyzed, the 6.1 eV exposed samples were observed to have the same leakage current magnitude as that of the pristine samples. For samples irradiated with 10.2 eV and 11.8 eV photons, an increased magnitude of leakage current was observed when electric fields were larger than 1.5 MV/cm. At the same time, the instantaneous breakdown

voltage was also observed to decrease for 10.2 eV and 11.8 eV photons exposed a-SiOC:H. For the pristine sample, the instantaneous breakdown voltage is around 7.0 MV/cm, while for 10.2 eV photons exposed a-SiOC:H, the breakdown voltage decreased to 5.7 MV/cm and for the 11.8 eV exposed sample, it decreased to 5.5 MV/cm.

Similar results were also observed by Dongfei Pei in his recent work [33] on measuring the leakage currents of low-k ILD samples irradiated with 7 eV, 9 eV, 12 eV and 15 eV photons, in which he claimed that the leakage currents were related to VUV-induced chemical defects inside of the a-SiOC:H thin films. The similar results were obtained for both low-k (Dongfei Pei) and dense (this work) a-SiOC:H films. The FTIR and XPS measurements on VUV-irradiated samples, as depicted in **Section 4.1**, also explain what is evidenced in the I-V characteristics. That is,for 6.1 eV exposed a-SiOC:H, no significant changes were found in the chemical structures of a-SiOC:H; while for 10.2 eV and 11.8 eV exposed samples, both -Si-OH and -Si-CH_3 groups were damaged.

For example, the generated H^+ and OH^- ions from the VUV photon-assisted reactions, as illustrated in Equation (**4-2**), can serve as charge carriers in low-k organosilicates. Due to their high mobility, they can easily cause increased electric-current leakage as the density of the defects inside the low-k dielectrics increase.

At low electric fields, especially when the E-field is less than 1.0 MV/cm, it is not easy to draw a reliable conclusion from the I-V curves, shown in **Figure 4-7**, because of data fluctuations even though the results are averaged based on 10 repeat measurements. It is not clear whether the fluctuations come from the background noise, or whether it is a

result from competition between the various conduction mechanisms because of shallow traps[34],[35] , bulk defects [36],[37], or absorbed moisture.[38]

4.3 VUV-induced Moisture Uptake

Hydrophobicity of the thin film surface is another important property of the low-k a-SiOC:H organosilicates used for ILDs. Plasma-induced damage causes a-SiOC:H to be hydrophilic, instead of being hydrophobic, and to absorb moisture from the gas ambient. This will result in changes to mechanical properties[5], increased leakage currents [38], degradation of adhesion[39], *etc*. Here, the effects of VUV irradiation on the surface hydrophobicity and moisture uptake of a-SiOC:H thin films are investigated in this section, by examining the water contact angle and the H_2O-related FTIR spectrum of a-SiOC:H before and after VUV irradiation with several photon energies.

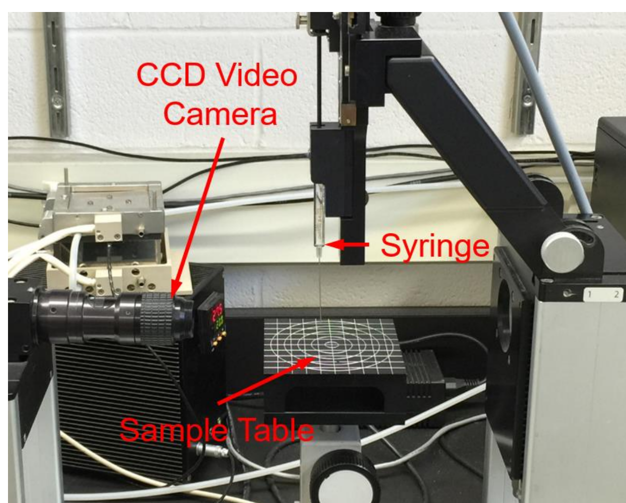

Figure 4-8 Photograph of the OCA 15 plus Contact-Angle Measurement System.

Water contact-angle measurements were made using a video-based optical contact angle measuring instrument, Data Physics OCA 15 Plus, with an automatic liquid dispenser

at ambient temperature, as depicted in **Figure 4-8**. The sample table is manually movable in the horizontal direction and more precisely adjustable in the vertical (z-axis) direction via a hand wheel. A high-speed video system with a USB camera (87 images/s sample rate), on the left of the sample table, is used to record the measurements, which can provide both the static and dynamic contact angle on the surface of the specimen. In this work, the sessile drop method was used by measuring the contact angle of 2 μL droplets of distilled water (polar liquid) on the surface of pristine and VUV-irradiated a-SiOC:H thin film. Five drops per sample were immediately analyzed. For each drop, the contact angle was measured manually and was repeated three times to allow a mean and standard deviation to be calculated.

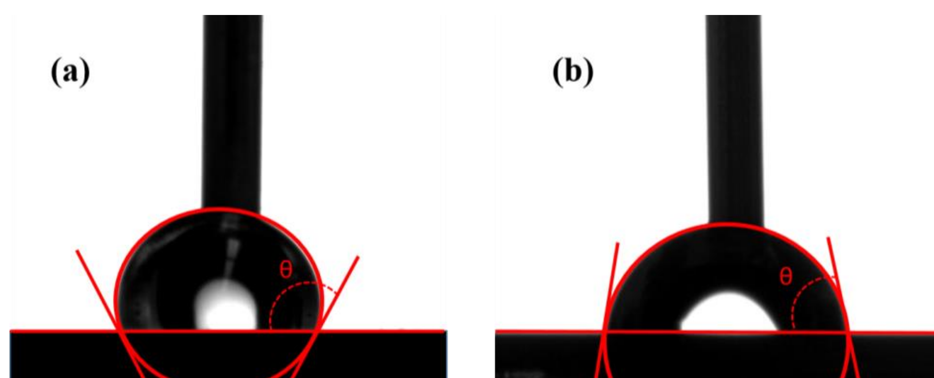

Figure 4-9 Sessile drop testing on a-SiOC:H thin films using distilled water: (a) pristine sample; (b) 6.1 eV VUV photon irradiated sample.

Generally, if the water contact angle is smaller than 90°, the solid surface is considered hydrophilic, and if the water contact angle is larger than 90°, the solid surface is considered hydrophobic. **Figure 4-9** shows one example of sessile drop testing on pristine and 11.8 eV photon exposed a-SiOC:H thin films. The sample shown in the picture is 100-nm porous a-SiOC:H with a porosity of 35% and a k-value of 2.2. As can be

observed here, the pristine sample, with a contact angle of $\theta = 115^o \pm 2^o$, is hydrophobic; while after 6.1 eV exposure, it becomes to hydrophilic with a contact angel of $\theta = 78^o \pm 2^o$. **Table 4-4** lists the measurements on the a-SiOC:H thin films with different porosities and k-values before and after VUV-photon irradiation. To be consistent with previous work, VUV photon energies were still set to be 6.1, 10.2, and 11.8 eV, and the total photon fluence impinging on the sample surfaces was 4×10^{15} photons/cm^2.

Table 4-4 Water contact angle measured on pristine and VUV-exposed a-SiOC:H.

Samples	Pristine	6.1 eV	10.2 eV	11.8 eV
#1 a-SiOC:H nonporous, k=3.2	$126^o \pm 2^o$	$80^o \pm 2^o$	$54^o \pm 2^o$	$46^o \pm 2^o$
#2 a-SiOC:H 25% porosity, k=2.5	$119^o \pm 2^o$	$65^o \pm 2^o$	$45^o \pm 2^o$	$41^o \pm 2^o$
#3 a-SiOC:H 35% porosity, k=2.2	$115^o \pm 2^o$	$78^o \pm 2^o$	$42^o \pm 2^o$	$38^o \pm 2^o$

As shown in **Table 4-4**, the pristine a-SiOC:H thin films under study are all hydrophobic with a measured water contact angle larger than 90°, for both porous and nonporous samples. This is because of the super-hydrophobic $-CH_3$ group present inside of the low-k organosilicates, as reported by Shamiryan et al.[40] However, after VUV photon exposure, the water contact angle decreases below 90°, indicating the samples have become hydrophilic. This phenomenon, unlike the VUV-induced mechanical changes and leakage currents, which are only observed on 10.2 eV and 11.8 eV exposed samples, occur to all VUV-photon energy exposures samples under investigation, including 6.1, 10.2, and 11.8 eV. That might be because VUV irradiation removes the original hydrophobic groups ($-CH_3$) and subsequently creates free-radical sites (-SiO2•) within the material. The -SiO2•

groups are not as hydrophobic as the -CH_3 groups, causing a-SiOC:H to be hydrophilic. These hydrophilic groups enable significant amounts of water to be absorbed from ambient air following water diffusion into the SiCOH bulk through interconnected pores.[41] Since 6.1 eV photons can also remove the -CH_3 groups from a-SiOC:H, as shown by the differential FTIR and XPS results in **Section 4.1**, the contact angle also decreases after 6.1 eV exposure, though the decrease is not as significant as for the 10.2 and 11.8 eV exposed samples.

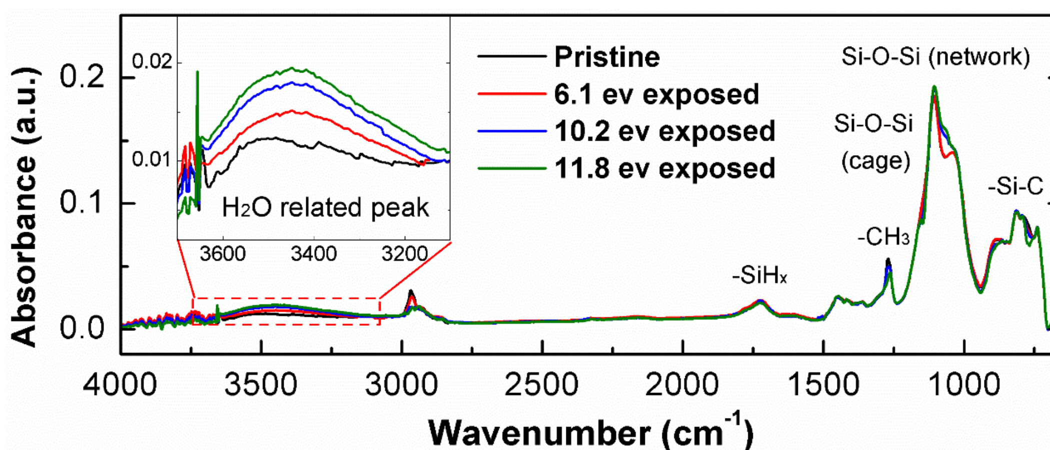

Figure 4-10 FTIR spectra of pristine and VUV-photon irradiated a-SiOC:H thin film with various energies. Inset shows the H_2O-related peak changes after VUV irradiation.

The FTIR spectra measured from pristine and VUV photon-irradiated a-SiOC:H thin film with various energies support the results of the water contact-angle measurements. As illustrated in **Figure 4-10**, besides the changes to the Si-O-Si skeleton structures, the H_2O-related peak also changes after VUV irradiation, which is emphasized in the inset figure. In the FTIR spectrum range of 3200-3800 cm^{-1}, the highest increases of the water-related peaks are observed for both 10.2 and 11.8 eV photon-exposed a-SiOC:H. The 6.1 eV exposed sample shows a mild increase compared with the pristine sample. **Table 4-5**

gives the information about the waveumbers for H_2O related FTIR peaks in PECVD a-SiOC:H low-k films. The increase of the H_2O-related FTIR peaks either can be either from physisorbed and chemisorbed water[42], or from hydroxyl terminals (-OH) [43]. It is not clear which one is dominant. An FTIR instrument, equipped with a humidity-controllable chamber and a temperature-programmable oven, could be used to examine the physisorbed and chemisorbed water, by annealing the samples at 190 °C and 400 °C respectively.

Table 4-5 H_2O related FTIR peak wavenumbers for PECVD a-SiOC:H low-k films.[43]

Wavenumber (cm^{-1})	Comment
3300-3600	H-bonded H_2O (physisorbed and chemisorbed H_2O)
3650-3800	Stretching modes of isolated and terminal -OH
3690	Hydroxyl terminals
3750	Isolated surface silanols Si-OH (sharp peak)
3200-3650	H-bonded Si-OH in chain (Si-OH stretching)

Even hydrogen-bonded water components (physisorbed and chemisorbed water) can be desorbed at a specific annealing temperature, without changing or damaging the chemical structure and integrity of the a-SiOC:H thin films. However, the hydroxyl terminals (-OH) will still exist inside of the a-SiOC:H thin films and deteriorate their dielectric properties.[5],[38],[44]

4.4 Summary

In this Chapter, VUV-induced damage to a-SiOC:H thin films was measured after exposing the samples to monochromatic synchrotron VUV radiation with a range of photon energies. Their mechanical properties, electrical properties, along with their

hydrophobicity were measured as a function of VUV photon energy. We have discovered a threshold photon energy for VUV-induced mechanical and electrical damage. Results indicate the VUV-induced mechanical and electrical damage have the same threshold photon energy. Several conclusions can be made:

1. VUV-induced mechanical modifications to a-SiOC:H are energy-dependent. The energy threshold is related to the dissociation energy of the Si-O chemical bond (8.3 eV). VUV irradiation with photon energies above this value could change the mechanical properties of a-SiCOH, either by converting the Si-O-Si cage structures to network structures or by creating bridging bonds (such as the Si-O-Si bond) from non-bridging bonds (such as the -Si-OH and -Si-CH_3 bonds). VUV photons below this threshold energy are not able to affect the mechanical properties of a-SiCOH.

2. VUV-induced chemical property changes were measured with FTIR and XPS, and have been also shown to be energy-dependent. After both 10.2 eV and 11.8 eV photon irradiation, there are significantly decreased bond densities of the Si-$(CH_3)_n$ (1250~1280cm^{-1}, 760~870cm^{-1}), Si-O-Si cage (~1130cm^{-1}) and Si-OH (890~990cm^{-1}) structures in a-SiOC:H films. On the other hand, an increase in the peak intensity for the Si-O-Si network (~1063cm^{-1}) and the Si-O-Si suboxide (~1023cm^{-1}) structures after both 10.2 eV and 11.8 eV photon irradiation was seen. However, for a 6.1 eV exposed sample, only the bond density of Si-$(CH_3)_n$ was found to decrease.

3. VUV irradiation can increase the leakage currents in a-SiCOH under electric field stress, especially under high electric-field conditions (> 1.5 MV/cm). This effect was observed for photons of 10.2 and 11.8 eV, but not for 6.1 eV. The increased magnitude of the leakage currents come from VUV-induced chemical defects inside the a-

SiOC:H thin films. The threshold energy value is related to the Si-O dissociation energy. The electrical properties deteriorate for photon energies above the threshold.

4. VUV irradiation can change the surface of a-SiOC:H from hydrophobic to hydrophilic, as evidenced by measuring of the water contact angle of the low-k dielectric materials. It will cause moisture uptake from the ambient and further degrade of the low-k dielectric material, such as increased leakage current and decreased breakdown voltage, which has to be avoided. FTIR results show that water uptake takes place in the 6.1, 10.2 and 11.8 eV exposed samples and is more significant when the photon energy is higher. This can be the case because VUV irradiation removes the original hydrophobic groups (-CH_3) and creates free-radical sites (-SiO_2•) within the material. The VUV-created -SiO_2• groups are not as hydrophobic as the -CH_3 groups, causing a-SiOC:H to be hydrophilic.

4.5 References

[1] H. Ren, G. A. Antonelli, Y. Nishi, and J. L. Shohet, "Plasma damage effects on low-k porous organosilicate glass," *Journal of Applied Physics*, Vol. **108**, 094110 (2010).

[2] J. R. Woodworth, M. E. Riley, V. A. Arnatucci, T. W. Hamilton, and B. P. Aragon, "Absolute intensities of the vacuum ultraviolet spectra in oxide etch plasma processing discharges," *J Vac Sci Technol A*, Vol. **19**, pp.45-55 (2001).

[3] X. Guo, J. E. Jakes, S. Banna, Y. Nishi, and J. L. Shohet, "Effects of plasma and vacuum-ultraviolet exposure on the mechanical properties of low-k porous organosilicate glass," *Journal of Applied Physics*, Vol. **116**, 044103 (2014).

[4] D. S. Stone, "Elastic rebound between an indenter and a layered specimen: Part I. Model," *J Mater Res*, Vol. **13**, pp.3207-3213 (1998).

[5] X. Guo, J. E. Jakes, M. T. Nichols, S. Banna, Y. Nishi, and J. L. Shohet, "The effect of water uptake on the mechanical properties of low-k organosilicate glass," *Journal of Applied Physics*, Vol. **114**, 084103 (2013).

[6] A. I. Medved' and A. E. Bryukhanov, "The variation of Young's modulus and the hardness with tempering of some quenched chromium steels," *Metal Science and Heat Treatment*, Vol. **11**, pp.706-708 (1969).

[7] S. Weiner and H. D. Wagner, "The Material Bone: Structure-Mechanical Function Relations," *Annual Review of Materials Science*, Vol. **28**, pp.271-298 (1998).

[8] W. C. Oliver and G. M. Pharr, "Measurement of hardness and elastic modulus by instrumented indentation: Advances in understanding and refinements to methodology," *J Mater Res*, Vol. **19**, pp.3-20 (2004).

[9] A. Grill, V. Patel, K. P. Rodbell, E. Huang, S. Christiansen, and M. R. Baklanov, "Characteristics of low-k and ultralow-k PECVD deposited SiCOH films.," *Mater Res Soc Symp P*, Vol. **716**, pp.569-574 (2002).

[10] S. M. Gates, G. Dubois, E. T. Ryan, A. Grill, M. Liu, and D. Gidley, "Adjusting the Skeleton and Pore Structure of Porous SiCOH Dielectrics," *Journal of the Electrochemical Society*, Vol. **156**, pp.G156-G162 (2009).

[11] L. Prager, P. Marsik, L. Wennrich, M. R. Baklanov, S. Naumov, L. Pistol, D. Schneider, J. W. Gerlach, P. Verdonck, and M. R. Buchmeiser, "Effect of pressure on efficiency of UV curing of CVD-derived low-k material at different wavelengths," *Microelectronic Engineering*, Vol. **85**, pp.2094-2097 (2008).

[12] F. Iacopi, C. Waldfried, K. Houthoofd, E. P. Guyer, D. M. Gage, G. Carlotti, Y. Travaly, T. Abell, O. Escorcia, G. Beyer, I. Berry, R. H. Dauskardt, and K. Maex, "UV-assisted curing: an effective technique for toughening low-k organosilicate films," Advanced Metallization Conference 2005 (AMC 2005), Colorado Springs, CO, 2005.

[13] Nancy Klymko, "Vibrational Spectroscopy Of Ultra-Low-k Dielectric Materials," *FUTURE FAB International-METROLOGY ANALYSIS*, Vol. **17**.

[14] Nigel P. Hacker, "Organic and Inorganic Spin-On Polymers for Low-Dielectric-Constant Applications," *MRS Bulletin*, Vol. **22**, pp.33-38 (1997).

[15] M. G. Albrecht and C. Blanchette, "Materials issues with thin film hydrogen silsesquioxane low K dielectrics," *Journal of the Electrochemical Society*, Vol. **145**, pp.4019-4025 (1998).

[16] T. P. Nguyen and S. Lefrant, "XPS study of SiO thin films and SiO-metal interfaces," *Journal of Physics: Condensed Matter*, Vol. **1**, 5197 (1989).

[17] V. M. Donnelly and A. Kornblit, "Plasma etching: Yesterday, today, and tomorrow," *Journal of Vacuum Science & Technology A*, Vol. **31**, 050825 (2013).

[18] K. Vanstreels and A. M. Urbanowicz, "Nanoindentation study of thin plasma enhanced chemical vapor deposition SiCOH low-k films modified in He/H2 downstream plasma," *Journal of Vacuum Science & Technology B*, Vol. **28**, pp.173-179 (2010).

[19] L. Broussous, G. Berthout, D. Rebiscoul, V. Rouessac, and A. Ayral, "Mechanical properties of a plasma-modified porous low-k material," *Microelectronic Engineering*, Vol. **87**, pp.466-469 (2010).

[20] W. Chen, Y. Morikawa, M. Itoh, T. Hayashi, K. Sugita, H. Shindo, and T. Uchida, "Very uniform and high aspect ratio anisotropy SiO2 etching process in magnetic neutral loop discharge plasma," *Journal of Vacuum Science & Technology A*, Vol. **17**, pp.2546-2550 (1999).

[21] H. L. Shi, H. Huang, J. J. Bao, J. J. Liu, P. S. Ho, Y. F. Zhou, J. T. Pender, M. D. Armacost, and D. Kyser, "Role of ions, photons, and radicals in inducing plasma damage to ultra low-k dielectrics," *Journal of Vacuum Science & Technology B*, Vol. **30**, 011206 (2012).

[22] H. Cui, R. J. Carter, D. L. Moore, H. G. Peng, D. W. Gidley, and P. A. Burke, "Impact of reductive N2 / H2 plasma on porous low-dielectric constant SiCOH thin films," *Journal of Applied Physics*, Vol. **97**, 113302 (2005).

[23] S. W. King, "Dielectric Barrier, Etch Stop, and Metal Capping Materials for State of the Art and beyond Metal Interconnects," *Ecs J Solid State Sc*, Vol. **4**, pp.N3029-N3047 (2015).

[24] J. Batey and E. Tierney, "Low-temperature deposition of high-quality silicon dioxide by plasma-enhanced chemical vapor deposition," *Journal of Applied Physics*, Vol. **60**, pp.3136-3145 (1986).

[25] S. Lombardo, J. H. Stathis, B. P. Linder, K. L. Pey, F. Palumbo, and C. H. Tung, "Dielectric breakdown mechanisms in gate oxides," *Journal of Applied Physics*, Vol. **98**, 121301 (2005).

[26] T. Usui, C. A. Donnelly, M. Logar, R. Sinclair, J. Schoonman, and F. B. Prinz, "Approaching the limits of dielectric breakdown for SiO2 films deposited by

plasma-enhanced atomic layer deposition," *Acta Materialia*, Vol. **61**, pp.7660-7670 (2013).

[27] M. T. Nichols, W. Li, D. Pei, G. A. Antonelli, Q. Lin, S. Banna, Y. Nishi, and J. L. Shohet, "Measurement of bandgap energies in low-k organosilicates," *Journal of Applied Physics*, Vol. **115**, 094105 (2014).

[28] M. T. Nichols, K. Mavrakakis, Q. Lin, and J. L. Shohet, "The effects of plasma exposure and vacuum ultraviolet irradiation on photopatternable low-k dielectric materials," *Journal of Applied Physics*, Vol. **114**, 104107 (2013).

[29] M. T. Nichols, "The Effects of Processing Induced Damage on Electrical Conduction Mechanisms and Time-Dependent Dielectric Breakdown of Low-k Organosilicates," Doctor of Philosophy Thesis, University of Wisconsin, Madison, 2013.

[30] A. Zenasni, V. Jousseaume, O. Gourhant, L. Favennec, and P. Maury, "Porosity generation using hydrogen plasma assisted thermal curing for ultra low k material," *Microelectronic Engineering*, Vol. **85**, pp.2102-2104 (2008).

[31] B. C. Bittel, P. M. Lenahan, and S. W. King, "Ultraviolet radiation effects on paramagnetic defects in low-k dielectrics for ultralarge scale integrated circuit interconnects," *Applied Physics Letters*, Vol. **97**, 063506 (2010).

[32] X. Guo, H. Zheng, S. W. King, V. V. Afanas'ev, M. R. Baklanov, J. F. de Marneffe, Y. Nishi, and J. L. Shohet, "Defect-induced bandgap narrowing in low-k dielectrics," *Applied Physics Letters*, Vol. **107**, 082903 (2015).

[33] Dongfei Pei, "The Effects of Vacuum Ultraviolet Irradiation on the Electrical Properties of Porous Low-k Organosilicate Glass," Doctor of Philosophy Thesis, University of Wisconsin-Madison, 2016.

[34] J. M. Atkin, E. Cartier, T. M. Shaw, R. B. Laibowitz, and T. F. Heinz, "Charge trapping at the low-k dielectric-silicon interface probed by the conductance and capacitance techniques," *Applied Physics Letters*, Vol. **93**, 122902 (2008).

[35] K. F. Schuegraf and C. M. Hu, "Hole Injection SiO2 Breakdown Model for Very-Low Voltage Lifetime Extrapolation," *IEEE Transactions on Electron Devices*, Vol. **41**, pp.761-767 (1994).

[36] Y. H. Kim, S. K. Lee, and H. J. Kim, "Low-k Si-O-C-H composite films prepared by plasma-enhanced chemical vapor deposition using bis-trimethylsilylmethane precursor," *J Vac Sci Technol A*, Vol. **18**, pp.1216-1219 (2000).

[37] D. Restaino, S. Molis, A. Grill, V. Patel, M. W. Lane, T. Cheng, A. Demos, S. M. Gates, D. Kioussis, N. Klymko, H. Liu, S. Nguyen, V. Nguyen, J. C. Patel, S. Reiter, H. Shobha, J. Widodo, K. Yim, and D. Edelstein, "Optimized interfacial strength for dense and porous SiCOH," *Mat Res S C*, Vol. **23**, pp.419-426 (2008).

[38] C. Kubascha, H. Ruelkeb, U. Mayerb, and J. W. Barthaa, "Leakage Current and Breakthrough Measurements on Moisturized SiCOH," *Ecs J Solid State Sc*, Vol. **4**, pp.N3118-N3121 (2015).

[39] X. Guo, J. E. Jakes, S. Banna, Y. Nishi, and J. L. Shohet, "Effect of water uptake on the fracture behavior of low-k organosilicate glass," *Journal of Vacuum Science & Technology A*, Vol. **32**, 031512 (2014).

[40] D. Shamiryan, M. R. Baklanov, S. Vanhaelemeersch, and K. Maex, "Comparative study of SiOCH low-k films with varied porosity interacting with etching and cleaning plasma," *Journal of Vacuum Science & Technology B*, Vol. **20**, pp.1923-1928 (2002).

[41] J. Shoeb and M. J. Kushner, "Damage by radicals and photons during plasma cleaning of porous low-k SiOCH. II. Water uptake and change in dielectric constant," *Journal of Vacuum Science & Technology A*, Vol. **30**, 041304 (2012).

[42] J. Proost, M. Baklanov, K. Maex, and L. Delaey, "Compensation effect during water desorption from siloxane-based spin-on dielectric thin films," *Journal of Vacuum Science & Technology B*, Vol. **18**, pp.303-306 (2000).

[43] M. R. Baklanov, J. F. de Marneffe, D. Shamiryan, A. M. Urbanowicz, H. L. Shi, T. V. Rakhimova, H. Huang, and P. S. Ho, "Plasma processing of low-k dielectrics," *Journal of Applied Physics*, Vol. **113**, 041101 (2013).

[44] X. Guo, S. W. King, H. Zheng, P. Xue, Y. Nishi, and J. L. Shohet, "Effects of vacuum-ultraviolet irradiation on copper penetration into low-k dielectrics under bias-temperature stress," *Applied Physics Letters*, Vol. **106**, 012904 (2015).

Chapter V

VUV-induced Cu Migration into a-SiOC:H and Time-Dependent Breakdown of Cu/Low-k Interconnects

In Chapter IV, VUV-induced damage to intrinsic low-k a-SiOC:H thin films and the associated damage mechanisms were presented. In this Chapter, we extend this work to study VUV-induced damage to Cu/low-k a-SiOC:H dielectric interconnect structures. State-of-the-art low-k dielectric materials, which have the potential to be a next-generation Cu capping-layer dielectrics, are used in this work. The organization of this Chapter is as follows. First, the effects of VUV irradiation on Cu migration into low-k a-SiOC:H organosilicates under bias-temperature stress (BTS) or temperature stress (TS) are presented. A specific low-k a-SiOC:H was investigated due to its relevance as both an

interlayer dielectric and as a potential Cu capping-layer material. Next, the extrinsic (including of Cu migration effects) time-dependent dielectric breakdowns of low-k a-SiOC:H dielectrics (TDDB) are measured, based on a Ti/a-SiOC:H/Cu MIM structure. TDDB characteristic lifetimes are compared for intrinsic (without includes Cu migration) and extrinsic a-SiOC:H breakdown. Lastly, the effects of VUV irradiation on the extrinsic TDDB of a-SiOC:H are examined. A comparison of extrinsic TDDB is made between pristine and VUV photon-exposed samples in order to investigate possible new or exacerbated failure mechanisms introduced by VUV irradiation to low-k a-SiOC:H thin films.

5.1 Dense a-SiOC:H as a Low-k Capping Layer

Capping layers in Cu/low-k interconnects, which are usually SiC_xN_y (k ~ 5.0 - 7.0), are needed (1) to prevent in-diffusion of moisture and other aqueous cleaning chemicals which will cause corrosion of Cu wires and ILD layers [1],[2]; (2) to prevent Cu out-diffusion into overlying metal layers [3]; (3) to passivate the top surface of the Cu lines to enhance electromigration (EM) resistance [4]; (4) to improve interlayer adhesion, etc.[5] As already discussed in Chapter I, when the size of ICs continues to downscale, the relative contribution of the capping layer (which is usually a-SiCxNy thin film with a k-value of 4.5 ~7.0) k-value to the interlayer capacitance increases, and thus there is a critical requirement for alternative low-k materials to serve as capping layers. The reason for this is that the k-value of the traditional capping layer is in the range of 4.5 ~7.0. From

continuous downscaling, not only the interlayer dielectric, but also the capping layer dielectric, need to be low-k materials, in order to reduce the RC delay.

Thus, some specific low-k a-SiOC:H materials, which were provided by Dr. Sean King from Intel Corporation that have the potential to serve as both interlayer dielectrics and as potential Cu capping-layer materials, were analyzed. The samples are nonporous a-SiOC:H with a k-value of 3.2 and a density of 1.5 ± 0.1 g/cm^3, which is relatively dense compared with porous low-k organosilicates (~ 1.1 g/cm^3) that are used as interlayer dielectrics [6]. **Table 5-1** summarizes some of the key material properties for the a-SiOC:H dielectric materials used in this work. These are: film composition, dielectric constant, refractive index, porosity, mass density, Young's modulus and intrinsic film stress. More details about the samples are also available in Sean King *et al.*'s recent publications[7],[8],[9].

The low-k a-SiOC:H dielectrics were deposited by plasma-enhanced chemical-vapor deposition (PECVD) on 300-mm diameter (100) Si wafers. A commercially available PECVD tool utilized in 45-nm low-k/Cu interconnect manufacturing was used. Radiofrequency power was applied to ignite and sustain the plasma at both high and low frequencies (13.56 MHz and 200 - 400 kHz, respectively). The deposition temperature was of the order of 400 ^{o}C, and the process gases utilized included various silane, methlysilane, and methylsiloxane feedgas sources diluted in gases such as He, O_2, CO_2, and/or other oxidizing gases. No sacrificial porogen or post UV-curing were utilized. This inhibits moisture uptake of the samples by significantly reducing the concentration of the hydrophilic groups from porogen residuals in the dielectric.

Table 5-1 Summary of properties for the PECVD low-k a-SiOC:H thin films investigated in this study. RI = Refractive index at 673 nm.[6]

Film	k (± 0.1)	RI (± 0.01)	Porosity	Density (g/cm^3)	Young's Modulus (GPa)	Film Stress (MPa)
a-$SiO_{1.2}C_{0.35}$:H	3.2	1.44	0	1.5 ± 0.1	11 ± 1	50 ± 5

As a capping layer, the low-k a-SiOC:H dielectric has to contact to the Cu wires directly. Because of this, Cu will diffuse into the low-k dielectrics during the deposition of Cu electrodes on a-SiOC:H using either e-beam evaporation or sputter deposition[10], some of the dense low-k a-SiOC:H thin films were deposited on Cu thin-film substrates, for the purpose of investigating the behaviors of Cu migration into a-SiOC:H and the extrinsic TDDB of Cu/low-k interconnects.

The layout of the a-SiOC:H/Cu film stacks is illustrated in **Figure 5-1 (a)**. Details about the fabrication processes are as follows. First, the Cu was electrochemically plated (ECP) on a Cu seed and a TaN adhesion layer sputter-deposited on a 300-mm diameter (100) Si substrate on which 100 nm of thermal oxide had been previously grown. After this, the ECP Cu was chemically mechanically polished (CMP) to a thickness of 350 nm. Prior to a-SiOC:H deposition, H_2 plasma pre-treatment was performed *in-situ* to remove Cu corrosion inhibitors left behind by the Cu CMP process and to reduce Cu surface oxides formed by ambient exposure. Finally, a-SiOC:H thin films were deposited at a thickness of 100 nm on the 350-nm Cu film at temperatures of 400 °C using a standard PECVD tool

as described above. XPS depth profiles, as shown in **Figure 5-1 (b)**, indicate no detectable Cu existing inside of the low-k dielectrics after deposition.

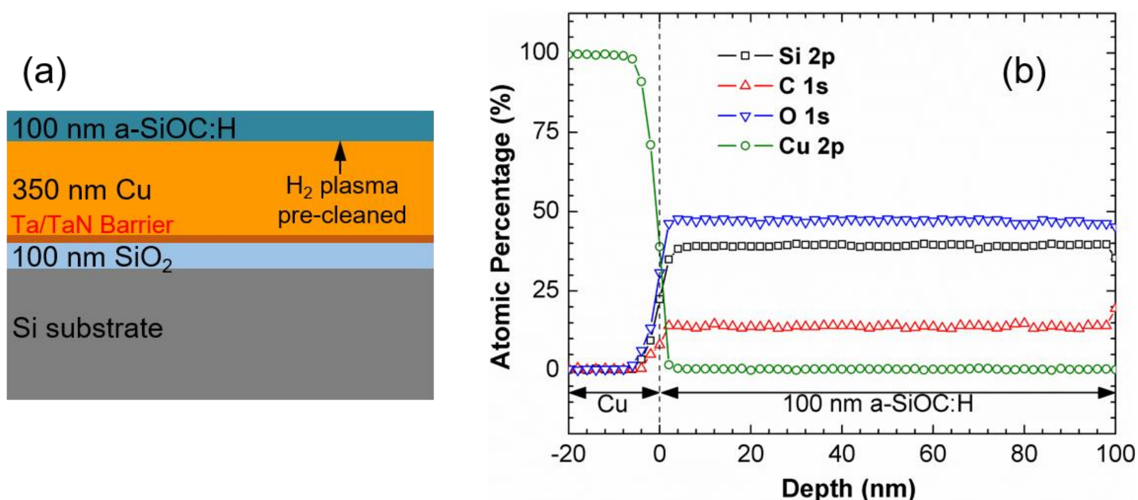

Figure 5-1 (a) Drawing of the a-SiOC:H/Cu film stacks utilized in this work; (b) XPS depth profile of the 100-nm a-SiOC:H thin film after deposition.

5.2 Cu Migration into a-SiOC:H from VUV Irradiation

To study the effects of VUV irradiation on Cu migration into low-k organosilicates, the a-SiOC:H/Cu film stacks, as discussed above, were exposed to VUV photons at the UW-Madison Synchrotron Radiation facility using the system described in Chapter III. The VUV photon energy was set at 9.0 eV (137 nm). The value of 9.0 eV was chosen because the reported penetration depth at these photon energies through amorphous silica-based dielectrics has been estimated to be ~200 nm,[11] which is larger than the thickness of the low-k dielectric thin films used here. Consequently, the entire bulk of the low-k

dielectric could be chemically modified with 9.0 eV VUV photon irradiation. The total photon fluence impinging on the sample was approximately 4.0×10^{15} photons/cm^2.[12]

After VUV irradiation, a hexagonal pattern of 300-nm Ti electrodes was deposited on the sample using e-beam evaporation, forming a Ti/a-SiOC:H/Cu capacitor, as described in Chapter III. Since the diffusivity of Ti into a-SiOC:H is much smaller than that of Cu,[13] utilizing these Ti electrodes can effectively avoid contamination of the low-k dielectrics from the side on which they were deposited. As a control, Ti electrodes were also fabricated on pristine a-SiOC:H/Cu film stacks. To examine Cu diffusion during bias-temperature stress (BTS), an electric field of 2.5 MV/cm, produced with a negative bias on the Ti electrodes, was applied to the Ti/SiCOH/Cu capacitors at a temperature of 225°C for 5.0 hours and 10.0 hours, respectively. After that, the Ti electrodes were sputtered away using a beam of Ar^+ ions (3.0 keV) and XPS depth profiles were obtained by scanning over an area of about 1.5 × 1.5 mm, as detailed in Chapter III. The sample was rotated during Ar^+ ion sputtering (1.5 keV) to minimize sputter-induced roughening. The sputter-removal rate was about 0.2 nm/sec.[12] After each sputter step, the XPS core-level spectra of the selected elements (Si 2p, O 1s, C 1s and Cu 2p) were recorded.

5.2.1 Cu Migration Rate in Pristine and VUV-exposed a-SiOC:H

Figure 5-2 shows the XPS depth profiles of Cu in both pristine and 9.0 eV VUV-irradiated a-SiOC:H after BTS. As illustrated in **Figure 5-2 (a)**, after 5.0 hours of BTS, significant penetration of Cu into the low-k dielectric films was observed: the penetration depth of Cu into a-SiOC:H was measured to be 30 nm for pristine samples and 44 nm for VUV-irradiated samples. For the samples that underwent 10.0 hours of BTS, as shown in

Figure 5-2 (b), the Cu profile of the 9.0 eV exposed sample extended an additional ~20 nm farther into a-SiOC:H than it did into the pristine sample. By using the expression $R_{Cu}=d^2/2t$,[14] where R_{Cu} is the Cu migration rate, d is the penetration depth and t is the temperature stressing time, the estimated migration rate of Cu at 225°C was found to be 2.5×10^{-16} cm^2/s in the pristine sample and 5.4×10^{-16} cm^2/s in the 9.0-eV-exposed sample.

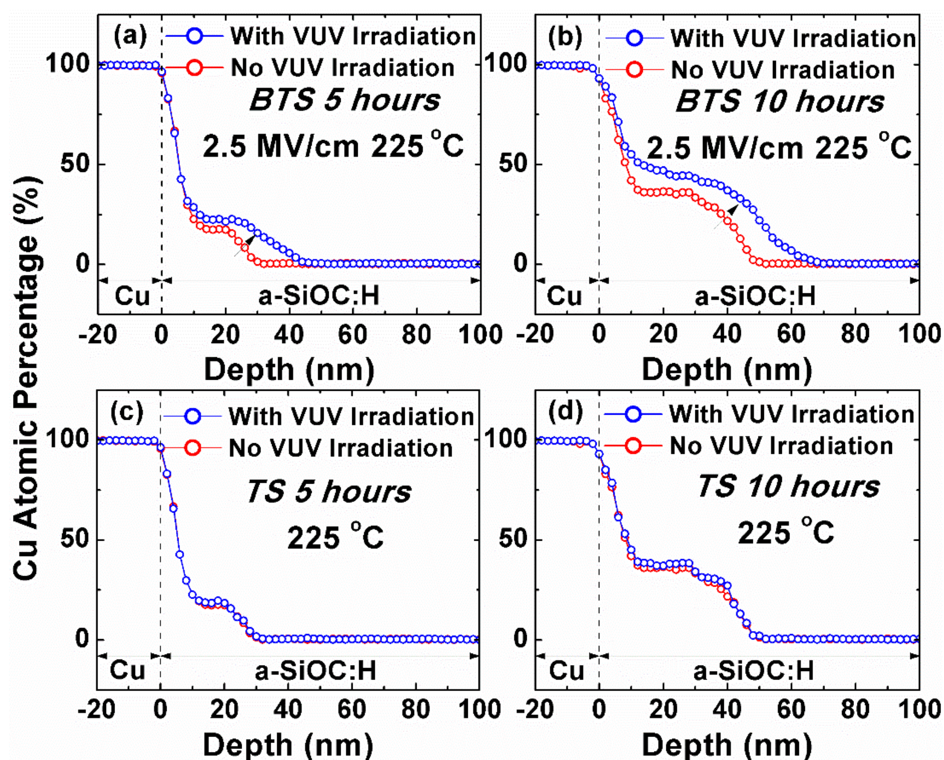

Figure 5-2 XPS depth profiles of Cu in pristine and 9.0 eV exposed a-SiOC:H after BTS/TS treatment. (a) 5.0 h BTS; (b) 10.0 h BTS; (c) 5.0 h TS and (d) 10.0 h TS.

For comparison, Cu profiles in both the pristine and the 9.0-eV-exposed samples under *only* temperature-annealing stress (TS) *without electric-field bias* were also examined, as shown in **Figure 5-2 (c)** and **(d)**. The samples were annealed at a temperature of 225°C for 5.0 hours and 10.0 hours respectively, with no electric bias applied to the

electrodes. Under only TS, the Cu distribution profiles in pristine and 9.0 eV exposed a-SiOC:H were seen to be almost the same. The calculated Cu migration rate under TS is 2.5×10^{-16} cm^2/s in both pristine and 9.0 eV exposed a-SiOC:H.

For a comparison, the same measurements were made on a film stack consisting of porous a-SiOC:H(100 nm)/a-SiCN(4 nm)/Cu. The VUV-exposure condition was identical to what had been used earlier, with a photon energy of 9.0 eV and a photon fluence of 4×10^{15} photons/cm^2. **Figure 5-3** shows the XPS depth profiles of Cu inside both pristine and 9.0-eV VUV-irradiated a-SiOC:H film stack after TS (225°C) and BTS (2.5 MV/cm and 225°C) treatment for 24 hours.

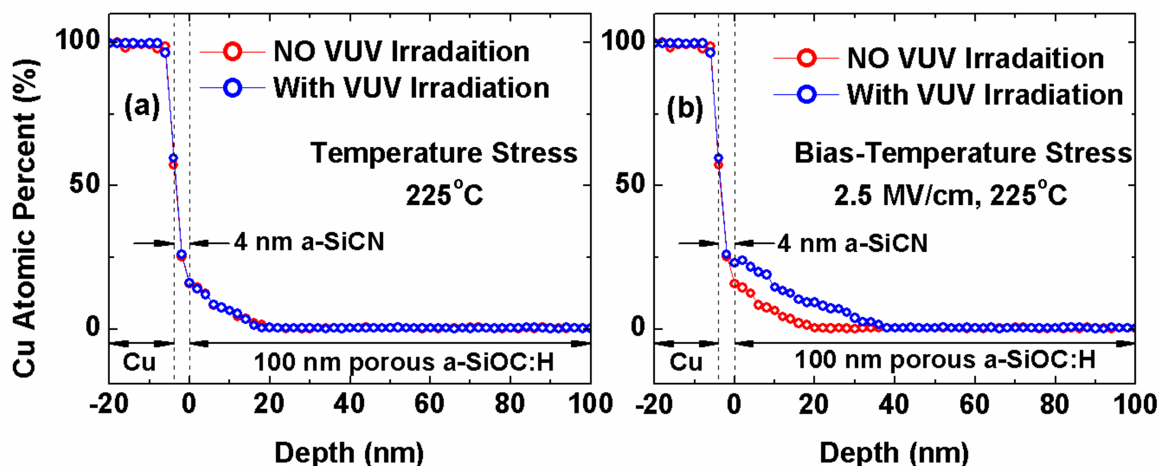

Figure 5-3 XPS depth profiles of Cu in pristine and VUV exposed a-SiOC:H(100nm, 35% porous)/a-SiCN(4nm)/Cu film stack after TS/BTS treatment. (a) 24 hours TS (b) 24 hours BTS. The VUV photon fluence is 4×10^{15} photons/cm^2.

As depicted in **Figure 5-3** (a), after 24-hour temperature stressing (225°C), it was seen that Cu penetrated through the 4-nm a-SiCN layer and entered into the porous a-SiOC:H. No change in the Cu distribution profile was observed in pristine and 9-eV

exposed samples. However, after 24-hour *bias*-temperature stressing (2.5 MV/cm and 225°C), it was observed that Cu migrated farther into the 9.0-eV VUV photon-exposed sample than than it did in the pristine sample, as depicted in **Figure 5-3** (b). This is similar to the case where no a-SiCN capping layer existed between Cu and the low-k a-SiOC:H thin films.

5.2.2 VUV-induced Cu Oxidation and Mechanism Discussion

The above results indicate that 9.0 eV VUV irradiation exacerbates Cu migration into a-SiOC:H when the electric field was applied. Previous work has shown that for the migration of Cu to be enhanced by an electric field, the Cu must be ionized first. Hence, we postulate that within the 9.0 eV exposed a-SiOC:H, the diffused Cu has been ionized. To further verify this, XPS was performed on both the pristine and the 9.0 eV exposed samples. It should be noted that the previous XPS results shown in Chapter IV are from porous a-SiOC:H and the VUV exposure energies were 6.1, 10.2, and 11.8 eV respectively. The XPS results shown in the following are from nonporous (dense) a-SiOC:H and the VUV exposure energy was 9.0 eV, with a fluence of 4×10^{15} photons/cm^2.

Figure 5-4 (a) shows the XPS spectra of the Cu 2p core level, which are calibrated with reference to the C 1s peak at 285 eV. The Cu 2p XPS spectrum from the pristine sample exhibits two major peaks at binding energies of 932.7 and 952.45 eV, which correspond to the Cu $2p_{3/2}$ and Cu $2p_{1/2}$ levels respectively, revealing that the diffused Cu exists primarily in the atomic state.[15] However, two satellite peaks were observed at 964.7 and 945.6 eV in the Cu 2p core-level spectra of the 9.0 eV exposed samples. These satellite peaks are from Cu oxides (CuO or Cu_2O),[16] indicating that part of the Cu

diffused into VUV-irradiated a-SiOC:H is in ionic form (Cu^+). Due to its electropositive characteristic, the migration of Cu^+ into a-SiOC:H will be accelerated by the electric field. Since there were no detectable Cu 2p satellite peaks for Cu diffused into pristine a-SiOC:H, the Cu^+ ions must be formed via a VUV photon-assisted reaction within the a-SiOC:H, as evidenced by the C 1s, Si 2p and O 1s XPS peaks shown in **Figure 5-4 (b)-(d)**.

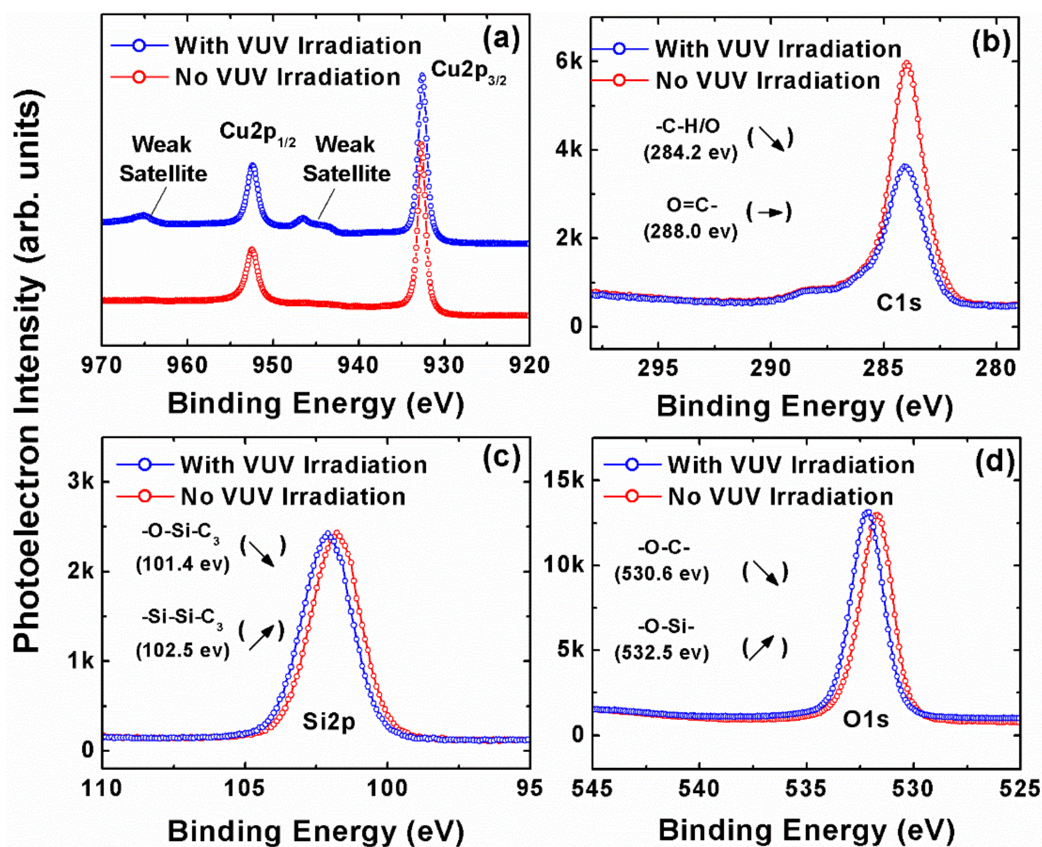

Figure 5-4 Core-level XPS spectra of pristine and 9.0 eV exposed a-SiOC:H samples after BTS: (a) Cu 2p; (b) C 1s; (c) Si 2p and (d) O 1s. VUV-exposure conditions are as follows: photon energy is 9.0 eV; photon fluence is 4×10^{15} photons/cm^2.

FTIR measurements were made on the samples in an enclosure filled with dry N_2, to examine the characteristic changes in the film after 9.0 eV VUV exposure. The FTIR spectrum in **Figure 5-5** shows that the bond densities of -Si-$(CH_3)_x$ (1250-1280 cm^{-1}, 760-870cm^{-1}), Si-O-Si cage structure (-1130 cm^{-1}), and -CH_x (2875-2930 cm^{-1}, 760-870cm^{-1}) structures decreased while the peaks of the Si-O-Si network (1063cm^{-1}) structures increased after 9.0 eV exposure. These results agree well with what was described in Chapter IV. Moreover, the broad band at higher wavenumbers of the FTIR spectrum, is related to the formation of -OH groups and to the incorporation of water within the film.[17] For clarity, the spectra ranging between 3000 and 3800 cm^{-1} are also presented in the inset of **Figure 5-5**. It is seen that after the 9.0 eV exposure, the intensity of the -OH related features increased moderately compared with the pristine sample.

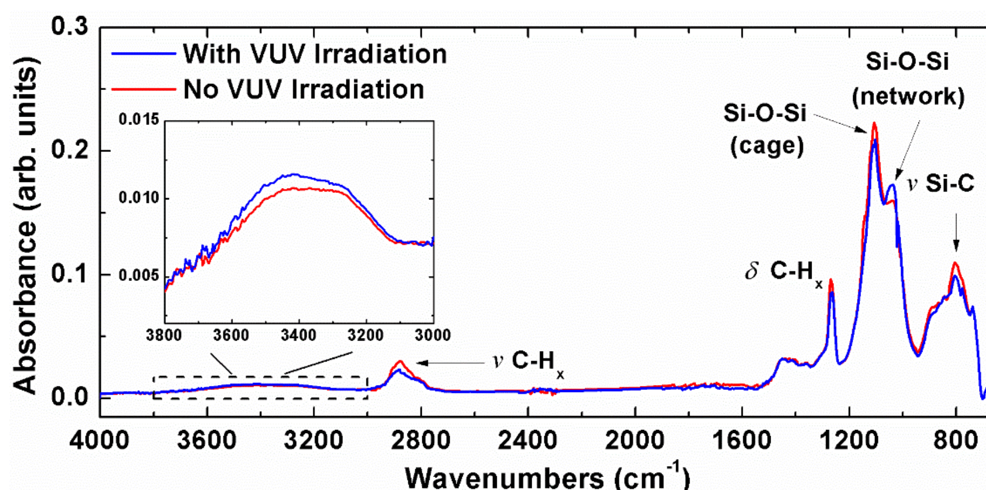

Figure 5-5 FTIR spectrum of pristine and 9.0 eV exposed a-SiOC:H samples. Here, "*δ*" indicates the bending vibrational mode and "*v*" indicates the stretching mode.

Under the combined action of moderate temperatures (150 - 300 ^oC) and an external electric field (0.5 - 5.0 MV/cm),[18] the negatively charged hydroxyl ions (OH^-) generated

were able to diffuse rapidly within the dielectric film because of their higher mobility compared with that of sodium, Cu, or other metals.[19] The hydroxyl ions (OH^-) that reach the Cu/a-SiOC:H surface may react with Cu to form $Cu(OH)_2$, which is not stable and can easily decompose to form CuO/Cu_2O. [18] Such formed Cu oxides can become a source of Cu^+ ions that are available for diffusion. Under BTS (the Cu layer is used as anode and biased positively) there are two driving forces for Cu^+ migration: diffusion caused by a concentration gradient and drift caused by an electric field. Thus, the migration of positively charged Cu^+ into a-SiOC:H will be accelerated when an electric field is applied with Cu as the anode. When Cu is used as the anode, Cu^+ ions drift into the dielectric; when Cu is used as a cathode, there is no Cu^+ ion drift. Both diffusion and drift exist, because a bias-stress electric field was applied. When the Cu layer is biased positively the Cu^+ ions will drift into the dielectric layer. On the other hand, for Cu existing as atomic states, the electrostatic acceleration would be negligible since it these are electrically neutral. This explains why there is a higher calculated Cu migration rate and a deeper Cu penetration depth in 9.0 eV VUV-irradiated a-SiOC:H than that seen in pristine a-SiOC:H, even though the BTS conditions were the same (225°C, 2.5 MV/cm). However, under the same TS condition, the calculated Cu migration rate remains the same for both samples.

5.2.3 Effects of Photon Energy on Cu Migration Rate in a-SiOC:H

As discussed in Chapter IV, the negatively charged hydroxyl ions (OH^-) could originate from a condensation reaction of two silanol groups taking place inside of a-SiOC:H under VUV irradiation with a photon energy higher than the Si-O dissociation energy (8.3 eV) [20]:

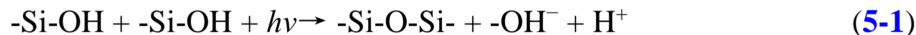

$$\text{-Si-OH + -Si-OH} + h\nu \rightarrow \text{-Si-O-Si- + -OH}^{-} + \text{H}^{+} \quad (5\text{-}1)$$

Therefore, the VUV-induced enhanced Cu migration into a-SiOC:H is likely to depend on the VUV photon energy. **Figure 5-6** shows the comparison of Cu migration rate in pristine, 7.0, 9.0, and 12.0 eV exposed a-SiOC:H thin films. The migration rate was calculated using the same method under same BTS (2.5 MV/cm, 225°C) and TS (225°C) conditions, as previously described. As can be seen in **Figure 5-6**, for 7.0 eV exposed a-SiOC:H, there was no significant change of Cu migration compared with the pristine sample, even when an external electrical field was applied. However, for 9.0 and 12.0 eV exposed samples, the calculated Cu migration rate under BTS increased significantly, indicating that a threshold energy, between 7 and 9 eV, exists for VUV-induced enhancement of Cu migration.

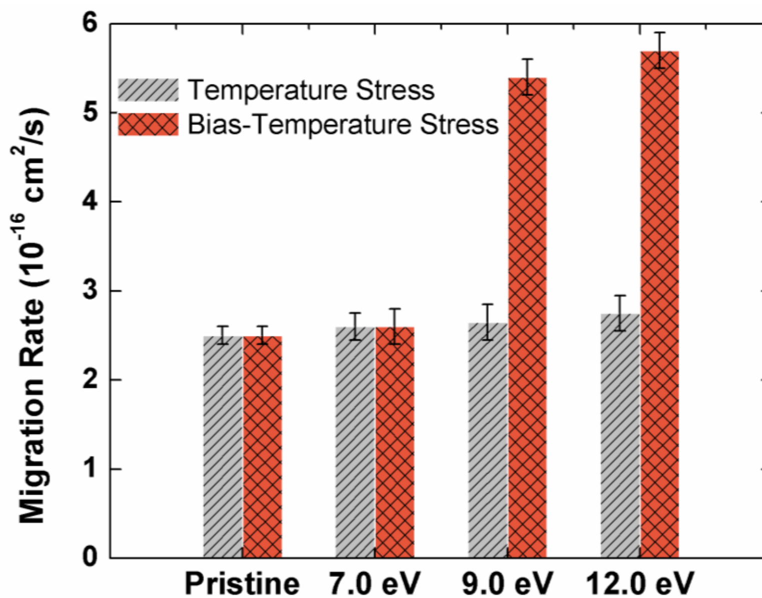

Figure 5-6 Calculated Cu migration rate into a-SiOC:H as a function of VUV photon energy.

Based upon the mechanisms proposed in Equation (5-1) and the FTIR results in **Figure 5-5**, it is possible to claim that the enhancement of Cu migration originates from the generation of hydroxyl ions (OH^-) after VUV exposure and the threshold energy for this is related to the Si-O dissociation energy, which is close to 8.3 eV. The VUV exposure time was around 2 hours. Thus, during the two-hour time period, the VUV exposure keeps generating OH- ions and the generated OH- ions continuously react with the Cu.

Additionally, the same BTS/TS treatments were made on no-plasma pre-cleaned a-SiOC:H/Cu film stacks, in which the surface of the 350-nm Cu layer was *not* treated with H_2 plasma before the deposition of a-SiOC:H, as illustrated in **Figure 5-1** (a). Since Cu corrosion inhibitors are left behind from Cu CMP processing, then the Cu surface can be oxidized by ambient exposure and it becomes a source of Cu^+ ions. In the presence of an external electric field, [21] it was found in the Cu/no plasma pre-cleaned/a-SiOC:H samples, under BTS, that the Cu penetration depth was larger than the depth for those samples treated only with TS. This agrees well with the results for the 9.0 eV VUV-irradiated samples and further verifies Cu oxidation in VUV-irradiated a-SiOC:H.

In summary, 9.0 eV VUV irradiation was found to enhance Cu diffusion into low-k a-SiOC:H under bias-temperature stress. This effect was correlated with the number of hydroxyl free-radical sites generated by VUV photon irradiation in the dielectric. Further analysis shows that there is a threshold energy, which is related to Si-O dissociation energy, for the VUV-induced enhancement of Cu migration.

5.3 TDDB of Cu/Low-k Dielectric Interconnects

As discussed in Chapter III, TDDB of low-k a-SiOC:H thin film is an important factor for the reliability of advanced Cu/low-k interconnects. The mechanism of the dielectric breakdown can be classified as either intrinsic or extrinsic.[22] Intrinsic failure occurs when the dielectric fails due to its own defects, such as broken bonds or dipole-dipole interaction of defects under the influence of an electric field [23] or thermal stress [24], as well as plasma-processing-induced degradation of the chemical, mechanical, and electrical properties of the dielectric.[25],[26] The extrinsic failure mechanism is attributed to failures induced by extrinsic defects, such as Cu migration from the Cu electrode. Much work in the past studied the TDDB of intrinsic low-k a-SiOC:H thin films and also the effects of plasma exposure [25] and/or VUV irradiation [27] on the TDDB characteristics of a-SiOC:H. Since we have shown that VUV-induced enhancement of Cu migration into a-SiOC:H occurs, we will extend the work to determine the extrinsic TDDB of VUV-exposed a-SiOC:H by taking into account the effects from Cu migration.

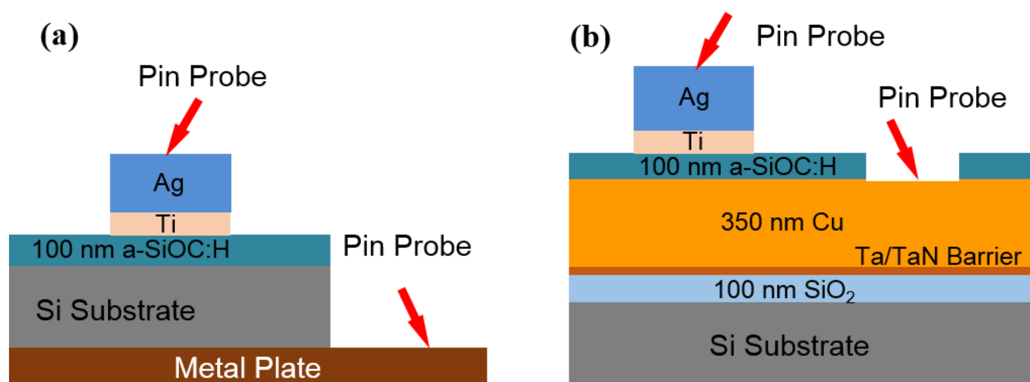

Figure 5-7 Schematic illustrating the (a) MIS and (b) MIM structure used for TDDB measurements.

TDDB measurements were made using the MIS and/or MIM structures as described in Chapter III. The MIS structure (Ag/Ti/a-SiOC:H/Si), shown in **Figure 5-7** (a), was used to measure the TDDB of intrinsic low-k a-SiOC:H dielectrics, while the MIM structure (Ag/Ti/a-SiOC:H/Cu), shown in **Figure 5-7** (b), was used to measure the TDDB of extrinsic Cu/low-k a-SiOC:H interconnects. Details of the fabrication processes for the MIM structure were described in Chapter III. For each TDDB measurement, a constant voltage was applied across the sample via two pin probes connected to the electrodes, and the current was measured as a function of time until breakdown occurred [28]. A temperature-controlled heater was used to heat the sample. The applied voltage was ramped at a rate of 1 V/s with a settling time of 250 ms until the desired voltage was reached. A failure criterion was set when the leakage current reached 10^{-4} A, to be consistent with other TDDB measurements on low-k dielectrics. [29], [27]

Weibull statistical distributions were used for TDDB lifetime projections, because they are the preferred tools for analysis of long-term failure data, and can project a "worst-case" scenario [30], which can more accurately predict expected lifetimes by increased sensitivity to less-probable breakdown events. The Weibull cumulative probability distribution function, which is expressed as F(t) in Equation (**5-2**) and shows that the probability of TTF (time-to-failure) is smaller than *t* and is given by, This probability is F(t), not TTF(t) which is the Weibull cumulative distribution function

$$F(t)_{Weibull} = 1 - \exp\left[-\left(\frac{t-\tau}{\theta}\right)^{\beta}\right] \quad (\mathbf{5\text{-}2})$$

in which τ is known as the minimum time at which failure can occur. β is the shape parameter (also known as the Weibull slope) which is equal to the slope of the line in a

probability plot using the Weibull scale [29] and is related to the breakdown mechanism. θ is the scale parameter (also referred to as the characteristic or dielectric lifetime). If t is the TTF, τ is the minimum possible value of TTF, which should be zero. The distribution then turns into a two-parameter Weibull distribution and the cumulative distribution function becomes:

$$F(t) = 1 - \exp\left[-\left(\frac{t}{\theta}\right)^{\beta}\right] \tag{5-3}$$

Taking the natural logarithm of both sides and simplifying Equation (5-3), by multiplying both sides by negative one and again taking the natural logarithm, leads to the following expression [29]

$$\ln\left(-\ln\left(1 - F(t)\right)\right) = \beta\ln(t) - \beta\ln(\theta) \tag{5-4}$$

The shape parameter β and the scale parameter θ (also referred to as the 63.2% TTF characteristic dielectric lifetime, because when $t = \theta$, $F(\theta) = 63.2\%$) can be determined using median-rank regression [31], using the following approximation:

$$Y(t_i) = \frac{i-0.3}{N+0.4} \tag{5-5}$$

in which $Y(t_i)$ is the estimated proportion of the samples that will have failed by time t_i, N is the total number of samples in the data set, i is the rank (the sequence of the data in the data set in ascending order) of the sample, and t_i is the breakdown time of the sample in ascending sequence. Using median-rank estimates, the set of measured time-to-breakdown data for a given applied electric field can be fit using linear regression to Equation (5-4). From this, the shape parameter β can be determined numerically from the slope of the

regression line. θ can also be determined from the 63.2% TTF characteristic lifetime, using $F(\theta) = 63.2\%$.

5.3.1 Intrinsic TDDB of Low-k a-SiOC:H Dielectrics

Intrinsic TDDB of low-k a-SiOC:H was measured on pristine a-SiOC:H thin films using the Ti/a-SiOC:H/Si MIS structure as shown in **Figure 5-7**(a). The TDDB measurement temperature was chosen to be 120 ^{o}C for several reasons. First, it can help remove absorbed moisture from the ambient. Second, under the same electrical stress, it takes a much shorter time for the film to break down at this temperature than at room temperature [32], which saves time for the measurement. Two values of the electric field, 4.0 MV/cm and 5.0 MV/cm, were used. The Ti metal electrode was biased positively during the measurement.

Figure 5-8 shows a Weibull plot of the breakdown time for pristine a-SiOC:H (k=3.2, mild density ρ =1.5 g/cm^3) under 4.0 MV/cm and 5.0 MV/cm electric fields. These data are based on at least 10 measurements. In the Weibull plot, the vertical axis is ln(-ln(1-F)) and the "0" value of the vertical axis corresponds to the 63.2% TTF characteristic dielectric lifetime. That is, when ln(-ln(1-F)) = 0, the probability of breakdown F is 63.2% and the corresponding breakdown time is 63.2% TTF. For example, in **Figure 5-8**, the horizontal dashed line, which is ln(-ln(1-F)) = 0, represents the 63.2% breakdown probability, and the intersection of the horizontal dashed line with the linear fit of the data points (solid line) corresponds to the location of the 63.2% sample breakdown. Therefore the 63.2% TTF can be obtained as shown by the arrow in **Figure 5-8**. For pristine a-SiCOH,

the 63.2% TTF is estimated to be 2.2 ± 0.1 × 10^4 s under an electric field of 4.0 MV/cm and to be 8.4 ± 0.1 × 10^3 s under an electric field of 5.0 MV/cm.

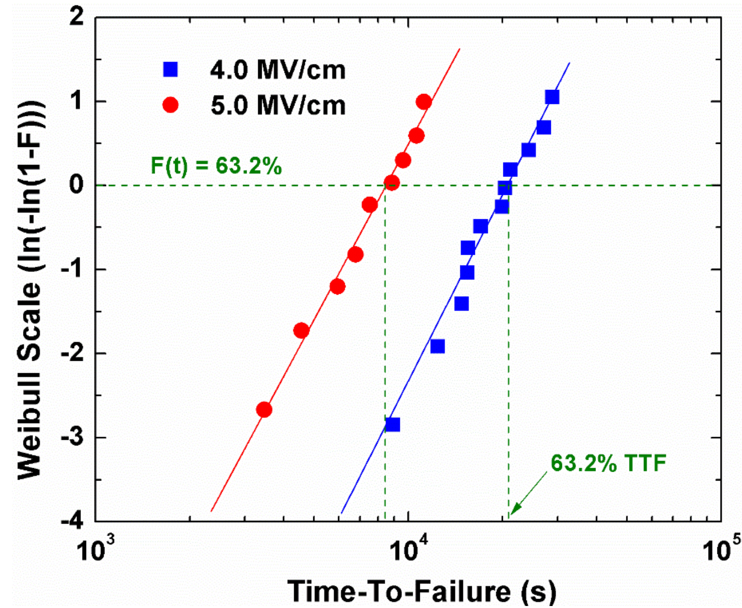

Figure 5-8 Plots of time-to failure (TTF) for pristine a-SiOC:H under 4.0 MV/cm and 5.0 MV/cm electrics field using the Weibull scale.

Additionally, in the Weibull plot, if the horizontal axis is set to be the natural logarithm of t, the shape factor β is equal to the slope of the curve and can be accessed by a linear fit to the data points. If β is greater than 1, the failure probability increases with time.[33],[34] Higher β values mean a better predication of the time-to-failure (TTF) and is a desired characteristic for the Weibull distribution plot.[33] For pristine samples, the value of β is approximately 2.7 ± 0.2 for the 4.0 MV/cm field and 2.6 ± 0.2 for the 5.0 MV/cm field In theory, the range of beta can be from 0 to infinity, because beta is defined as equal to the slope of the Weibull plot, which means the maximum value of beta is infinite. However, experimentally, the value of beta is usually less than 10. Reported values

of beta from publications are in the range of 1 ~ 5. Any value greater than 1 is reasonable. The value of beta varies with sample property and test structure.

The effects of Ar plasma exposure and VUV irradiation on the intrinsic TDDB characteristics of low-k a-SiOC:H thin films have been well studied in the Ph.D. thesis of Dongfei Pei [27]. With his permission, some of his experimental results are repeated here, as shown in **Figure 5-9**. Compared with the pristine film, the TDDB lifetimes of a-SiOC:H irradiated by 7-eV photons do not display much difference from the pristine-film results. However, TDDB degradation was observed for a-SiOC:H irradiated by 9, 12, and 15 eV photons. Since TDDB is directly related to the trap-state concentration in the dielectric film, he claimed that 7 eV does not appear to be high enough to change the trap-state concentration. However, as the photon energy goes higher, the photons are then able to force a transition from the trap states and cause TDDB degradation. He also compared the TDDB property of Ar plasma exposed samples with VUV-exposed samples, which are also plotted in **Figure 5-9**. In his work, the Ar plasma-exposed film shows more TDDB degradation. There are two possible reasons for this difference: 1) The VUV photon fluence of the Ar-plasma may be higher than that of the VUV exposure. 2) The charged-particle bombardment during the Ar-plasma exposure may cause additional damage.

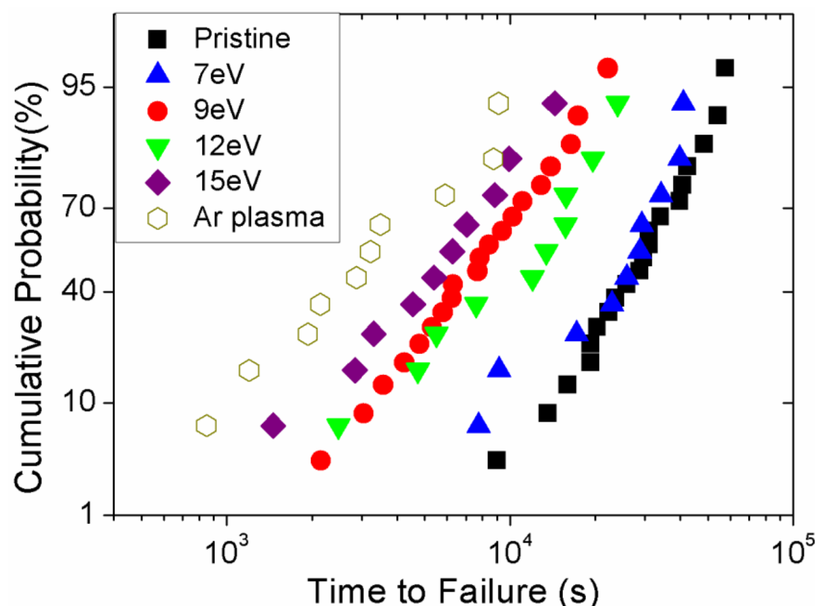

Figure 5-9 Probability plot of the TDDB lifetime of plasma and VUV exposed a-SiOC:H thin films. Data from Dongfei Pei's Ph.D. thesis [27].

5.3.2 Extrinsic TDDB of Cu/Low-k a-SiOC:H Interconnects

Extrinsic TDDB of the low-k a-SiOC:H was measured on the a-SiOC:H/Cu film stacks using the Ag/Ti/a-SiOC:H/Cu MIM structure as shown in **Figure 5-7** (b). The samples used here were 100-nm a-SiOC:H (k=3.2, ρ =1.5 g/cm^3) thin-film PECVD-deposited on a H_2 plasma pre-cleaned 350-nm Cu layer. The temperature for the extrinsic TDDB measurement was also kept at 120 ^{o}C for the same reason as mentioned in the intrinsic TDDB measurement. At this temperature, Cu will diffuse into the a-SiOC:H thin films with an approximate rate of 4.2×10^{-16} cm^2/s, which is calculated using the methods described in **Section 5.2**. An electric field of 4.0 MV/cm was used and the Cu metal electrode was biased positively, which was used as anode, during the measurement. In such

a configuration, it is possible for the Cu ions, if they exist, to drift into the low-k film under the influence of the electric field, which is exactly the case as in damascene structures.[35]

Figure 5-10 shows the results for the extrinsic TDDB of a-SiOC:H by taking into account the effects of Cu diffusion, based on the measurements made on 10 samples. TDDB degradation was observed for extrinsic a-SiOC:H breakdown, as evidenced by the leftward shift of the Weibull plot, compared with the intrinsic a-SiOC:H breakdown without Cu diffusion. The calculated 63.2% TTF for the extrinsic a-SiOC:H breakdown was $1.2 \pm 0.1 \times 10^4$ s, which is approximately half of the 63.2% TTF for the intrinsic a-SiOC:H breakdown ($2.2 \pm 0.1 \times 10^4$ s). Because the Cu layer in the sample was pre-cleaned with H_2 plasma resulting in the Cu-oxide inhibitors being removed, the diffused Cu mainly exists in the atomic state. This was verified with XPS measurements of the samples, in which no satellite peaks (related to Cu+ ions) were observed near the Cu 2p core-level peaks [12], indicating no detectable Cu+ ions existed in the sample after initial deposition. Additionally, the temperature utilized in this measurement (120°C) is below the threshold value (~ 200°C), above which Cu ionic current will be observed [36]. The observed shorter TDDB lifetime should therefore be attributed to diffusion alone of Cu *atoms* rather than the diffusion or drift of Cu ions.

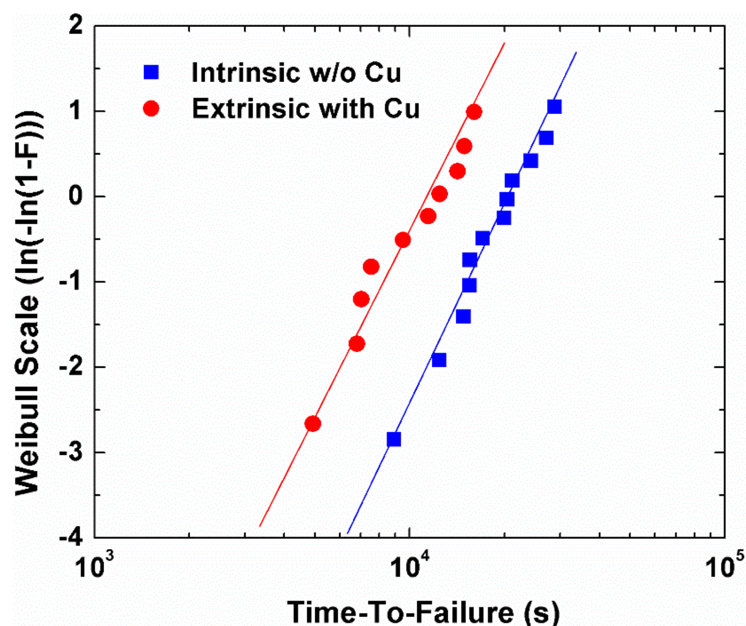

Figure 5-10 Weibull plot of the TTF for intrinsic and extrinsic a-SiOC:H breakdown. Here "intrinsic" refers to the case that does not include Cu migration; "extrinsic" refers to the case includes Cu migration.

This is also seen in the results obtained when using Cu as the cathode, which will be detailed as follows. Under these conditions, the diffused Cu atoms can accumulate in the region near the Cu electrode and shorten the distance between anode and cathode. This means, for the same applied potential, the electric field would rise within the low-k dielectric and hasten the dielectric breakdown.[37] This is is still diffusion, not drift. Diffusion of the Cu atoms will create a layer of Cu inside of the dielectric, which will shorten the distance between the two electrodes. For the sample applied voltage, the electric field would increase because the distance between the electrodes deceases. This can explain why there is a shorter TDDB lifetime in the a-SiOC:H/Cu film stacks than that for intrinsic a-SiOC:H thin films under same bias-temperature condition.

5.4 TDDB for Cu/Low-k Interconnects from VUV Irradiation

The effects of VUV irradiation on the extrinsic TDDB of Cu/a-SiOC:H interconnects were also investigated. Monochromatic VUV irradiation with an energy of 9.0 eV and a total fluence of 4×10^{15} photons/cm^2 was performed on an a-SiOC:H thin film (k=3.2, ρ =1.5 g/cm^3) *before* the Ag/Ti/a-SiOC:H/Cu MIM structures were fabricated. A photon energy of 9.0 eV was chosen because it is larger than the observed threshold energy of VUV-induced damage to a-SiOC:H and also because it has a relatively large penetration depth in a-SiOC:H (> 100nm).

TDDB measurements were made under two sets of conditions. The first condition was obtained by applying a positive potential or bias to the Cu electrode in the Ag/Ti/a-SiOC:H/Cu MIM structure. This is also referenced as using the Cu as an anode in this work. In this case, Cu ions can drift into the low-k a-SiOC:H thin film. The second set of conditions was obtained by applying a negative potential or bias to the Cu electrode, corresponding to using the Cu as a cathode, in which Cu ions will not enter the low-k dielectric since the electric field is forcing them away from the low-k dielectric. XPS measurements do not show the existence of Cu ions inside of the low-k dielectric when Cu was used as a cathode, indicating that no ion diffusion occurs. It is likely this is the case because the concentration of Cu ions is very low, compared with the concentration of Cu atoms, which makes diffusion of Cu ions negligible. Under both conditions, the electric field was 4.0 MV/cm and the temperature was 120°C. The results of the measurements, on

both pristine and 9.0-eV VUV-exposed samples, are shown in **Figure 5-11** using the Weibull scale. Ten samples were measured for each case.

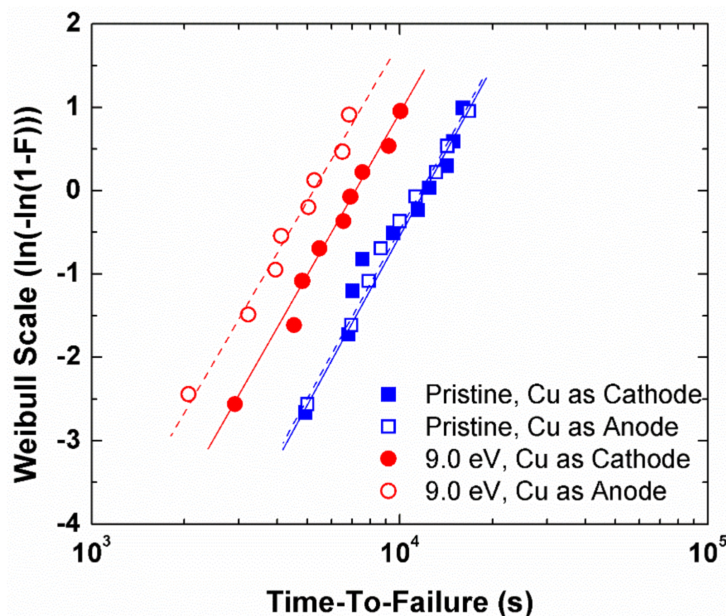

Figure 5-11 Weibull plots of the extrinsic TDDB lifetimes for pristine and 9.0 eV VUV-exposed a-SiOC:H thin films.

For the pristine sample, no difference in the probability curve was observed whether the Cu was used as an anode or cathode. The calculated 63.2% TTFs of the a-SiOC:H film for the two cases (anode and cathode conditions on the Cu) do not display much difference. However, TDDB degradations were observed for 9.0-eV exposed samples, as the probability curves were seen to move to the left. What's more, after 9.0 eV VUV irradiation, the TDDB curve measured using Cu as the anode deviates from that measured using Cu as the cathode, and shows a more severe degradation. This deviation can come from the generation of Cu^{+} ions in 9.0 eV exposed samples, because our previous work [12] has shown that hydroxyl ions (OH^{-}) will be generated in a-SiOC:H after 9.0 eV VUV

irradiation and consequently form CuO/Cu_2O, acting as a Cu^+ ion source once an external electric field is applied. For the 9.0-eV exposed samples, when the Cu is used as an anode, the Cu ions drift into the low-k dielectric and can play a role in the TDDB breakdown.

In order to show the roles of Cu migration in TDDB and the effects of VUV irradiation more directly, the calculated 63.2% TTF for all samples measured in this work are compared in **Figure 5-12**. It shows that diffusion of Cu atoms into a-SiOC:H degrades the TDDB lifetime and there is no difference whether the Cu is used as an anode or a cathode. Nine-eV VUV irradiation further degrades the TDDB lifetime. The most notable degradation of 63.2% TTF is found when the Cu electrode is used as an anode in the 9.0 eV exposed sample. XPS analysis of the pristine and VUV-exposed sample shows this is related to the VUV-induced oxidization of Cu layers inside of the sample.

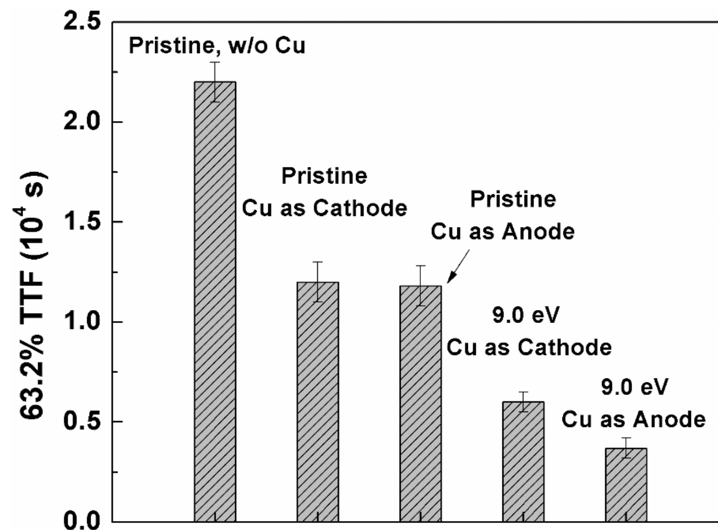

Figure 5-12 63.2% TTF for pristine and for 9.0 eV VUV exposed a-SiOC:H/Cu film stacks.

5.5 Summary

In this chapter, VUV-irradiation-induced Cu migration into low-k a-SiOC:H dielectrics and time-dependent breakdown of a-SiOC:H/Cu structures were investigated. Relative dense a-SiOC:H thin films with a k value of 3.2 and a density of 1.5 g/cm^3 were used due to their relevance as both as an interlayer dielectric and potential Cu capping-layer materials. Cu diffusion in pristine and VUV-exposed samples were compared. Intrinsic (does not include Cu migration) and extrinsic (includes Cu migration). TDDB of a-SiOC:H and the effects of VUV irradiation were measured using a MIM electrical-contact structure. A summary of the results is as follows:

1. Nine-eV VUV irradiation can enhance Cu migration into low-k a-SiOC:H under bias-temperature stress. Under a BTS condition of 120°C and 2.5 MV/cm, Cu migration ratewas calculated to be 2.5×10^{-16} cm^2/s in a pristine a-SiOC:H dielectric and 5.4×10^{-16} cm^2/s in 9.0-eV exposed samples. Cu oxidization was observed in 9.0-eV exposed samples using XPS and this effect was correlated with the hydroxyl free-radical sites (OH$^-$) generated by VUV photon irradiation in the dielectrics, as evidenced by XPS and FTIR measurements.

2. Cu migration in VUV-exposed a-SiOC:H dielectrics depends on the VUV photon energy. A threshold VUV photon energy was found by measuring the Cu migration rate as a function of photon energy, which is related to the Si-O dissociation energy (8.3 eV). Above this value, VUV irradiation will enhance the progress of Cu migration into a-SiOC:H in the presence of an electric field. Below this value, no significant changes were observed.

3. Extrinsic TDDB of a-SiOC:H, measured by taking in account the effects of Cu migration into the dielectric, were investigated under various conditions based on a MIM structure configuration and compared with the intrinsic TDDB characteristics of a-SiOC:H. In the pristine samples, no detectable Cu^{+} ions exist at the Cu/dielectric interface. Diffusion of Cu atoms into pristine a-SiOC:H can degrade the TDDB lifetime. While no difference in TDDB times was observed whether the Cu was used as an anode or a cathode, because no detectable Cu^{+} ions exist either in the bulk of a-SiOC:H or at the interface between Cu and a-SiOC:H.

4. The Cu diffusion-induced TDDB degradation might come from the higher electric-field strength for a given applied voltage within the dielectric. In this case, diffused Cu atoms accumulate near the location of the Cu and shorten the distance between the anode and the cathode, resulting in an increase of the electric field under same voltage bias.

5. Extrinsic TDDB of a-SiOC:H deteriorates after 9.0 eV VUV irradiation. The most notable degradation of the 63.2% TTF time was found when the Cu electrode was used as an anode in a 9.0-eV exposed sample. This is believed to be related to the Cu^{+} ions created by VUV irradiation, because 9.0 eV is above the previously observed threshold.

5.6 References

[1] C. Kubasch, H. Schumacher, H. Ruelke, U. Mayer, and J. W. Bartha, "Fourier Transform Infrared Spectroscopy of Moisturized Low-k Dielectric Materials," *IEEE Transactions on Electron Devices*, Vol. **58**, pp.2888-2894 (2011).

[2] Y. Cheng, W. Chang, and Y. Wang, "Moisture effect on electromigration characteristics for copper dual damascene interconnection," *Journal of Vacuum Science & Technology B*, Vol. **28**, pp.1322-1325 (2010).

[3] M. Vogt, M. Kachel, M. Plotner, and K. Drescher, "Dielectric barriers for Cu metallization systems," *Microelectronic Engineering*, Vol. **37-38**, pp.181-187 (1997).

[4] H. Miyazaki, H. Kojima, and K. Hinode, "Passivation effect of silicon nitride against copper diffusion," *Journal of Applied Physics*, Vol. **81**, pp.7746-7750 (1997).

[5] W. Shao, S. G. Mhaisalkar, T. Sritharan, A. V. Vairagar, H. J. Engelmann, O. Aubel, E. Zschech, A. M. Gusak, and K. N. Tu, "Direct evidence of Cu/cap/liner edge being the dominant electromigration path in dual damascene Cu interconnects," *Applied Physics Letters*, Vol. **90**, 052106 (2007).

[6] S. W. King, B. French, and E. Mays, "Detection of defect states in low-k dielectrics using reflection electron energy loss spectroscopy," *Journal of Applied Physics*, Vol. **113**, 044109 (2013).

[7] S. W. King, D. Jacoba, D. Vanleuvena, B. Colvina, J. Kellya, M. Frencha, J. Bielefeldb, D. Duttac, M. Liuc, and D. Gidleyc, "Film Property Requirements for Hermetic Low-k a-SiOxCyNz:H Dielectric Barriers," *Ecs J Solid State Sc*, Vol. **1**, pp.N115-N122 (2012).

[8] S. W. King, D. Jacob, D. Vanleuven, B. Colvin, J. Kelly, G. Xu, M. French, D. Dutta, and D. Gidley, "Role of Nano-Porosity in Plasma Enhanced Chemical Vapor

Deposition of Hermetic low-k a-SiOCN:H Dielectric Barrier Materials," *Ecs Transactions*, Vol. **45**, pp.27-45 (2013).

[9] S. W. King, "Dielectric Barrier, Etch Stop, and Metal Capping Materials for State of the Art and beyond Metal Interconnects," *Ecs J Solid State Sc*, Vol. **4**, pp.N3029-N3047 (2015).

[10] M. He, S. Novak, L. Vanamurthy, H. Bakhru, J. L. Plawsky, and T. Lu, "Cu penetration into low-k dielectric during deposition and bias-temperature stress," *Applied Physics Letters*, Vol. **97**, 252901 (2010).

[11] J. R. Woodworth, M. E. Riley, V. A. Arnatucci, T. W. Hamilton, and B. P. Aragon, "Absolute intensities of the vacuum ultraviolet spectra in oxide etch plasma processing discharges," *J Vac Sci Technol A*, Vol. **19**, pp.45-55 (2001).

[12] X. Guo, S. W. King, H. Zheng, P. Xue, Y. Nishi, and J. L. Shohet, "Effects of vacuum-ultraviolet irradiation on copper penetration into low-k dielectrics under bias-temperature stress," *Applied Physics Letters*, Vol. **106**, 012904 (2015).

[13] J. D. McBrayer, R. M. Swanson, and T. W. Sigmon, "Diffusion of Metals in Silicon Dioxide," *Journal of The Electrochemical Society*, Vol. **133**, pp.1242-1246 (1986).

[14] D. Brogioli and A. Vailati, "Diffusive mass transfer by nonequilibrium fluctuations: Fick's law revisited," *Phys Rev E*, Vol. **63**, 012105 (2000).

[15] M. Yin, C. Wu, Y. Lou, Cl. Burda, J. T. Koberstein, Y. Zhu, and S. O'Brien, "Copper Oxide Nanocrystals," *Journal of the American Chemical Society*, Vol. **127**, pp.9506-9511 (2005).

[16] J. Ghijsen, L. H. Tjeng, J. van Elp, H. Eskes, J. Westerink, G. A. Sawatzky, and M. T. Czyzyk, "Electronic structure of Cu2O and CuO," *Physical Review B*, Vol. **38**, pp.11322-11330 (1988).

[17] X. Guo, J. E. Jakes, S. Banna, Y. Nishi, and J. L. Shohet, "Effect of water uptake on the fracture behavior of low-k organosilicate glass," *Journal of Vacuum Science & Technology A*, Vol. **32**, 031512 (2014).

[18] O. R. Rodriguez, W. Cho, R. Saxena, J. L. Plawsky, and W. N. Gill, "Mechanism of Cu diffusion in porous low-κ dielectrics," *Journal of Applied Physics*, Vol. **98**, 024108 (2005).

[19] A. B. Duso and D. D. Y. Chen, "Proton and Hydroxide Ion Mobility in Capillary Electrophoresis," *Analytical Chemistry*, Vol. **74**, pp.2938-2942 (2002).

[20] X. Guo, J. E. Jakes, S. Banna, Y. Nishi, and J. L. Shohet, "Effects of plasma and vacuum-ultraviolet exposure on the mechanical properties of low-k porous organosilicate glass," *Journal of Applied Physics*, Vol. **116**, 044103 (2014).

[21] S. W. King, M. French, M. Jaehnig, M. Kuhn, and B. French, "X-ray photoelectron spectroscopy investigation of the Schottky barrier at low-k a-SiO(C):H/Cu interfaces," *Applied Physics Letters*, Vol. **99**, 202903 (2011).

[22] S. S. Hwang, S. Y. Jung, and Y. C. Joo, "Characteristics of leakage current in the dielectric layer due to Cu migration during bias temperature stress," *Journal of Applied Physics*, Vol. **104**, 044511 (2008).

[23] Y. L. Li, Z. Tokei, J. Van Aelst, L. Carbonell, M. R. Baklanov, O. Richard, H. Bender, G. Groeseneken, and K. Maex, "Plasma ash modulation of TDDB thermal

activation energy in damascene SiOC:H," *Semicond Sci Tech*, Vol. **22**, pp.320-325 (2007).

[24] E. T. Ogawa, J. Kim, G. S. Haase, H. C. Mogul, and J. W. McPherson, "Leakage, breakdown, and TDDB characteristics of porous low-k silica-based interconnect dielectrics," Reliability Physics Symposium Proceedings, 41st Annual. 2003 IEEE International, Texas, 2003.

[25] M. T. Nichols, H. Sinha, C. A. Wiltbank, G. A. Antonelli, Y. Nishi, and J. L. Shohet, "Time-dependent dielectric breakdown of plasma-exposed porous organosilicate glass," *Applied Physics Letters*, Vol. **100**, 112905 (2012).

[26] T. Imada, Y. Nakata, S. Ozaki, Y. Kobayashi, K. Yoshikawa, and T. Nakamura, "TDDB characteristics of low-k dielectrics after plasma damage recovery process," *Mat Res S C*, Vol. **23**, pp.557-561 (2008).

[27] Dongfei Pei, "The Effects of Vacuum Ultraviolet Irradiation on the Electrical Properties of Porous Low-k Organosilicate Glass," Doctor of Philosophy Thesis, University of Wisconsin-Madison, 2016.

[28] J. L. Hoyt, H. M. Nayfeh, S. Eguchi, x030A, I. berg, G. Xia, T. Drake, E. A. Fitzgerald, and D. A. Antoniadis, "Strained silicon MOSFET technology," Electron Devices Meeting, 2002. IEDM '02. International, 2002.

[29] M. T. Nichols, "The Effects of Processing Induced Damage on Electrical Conduction Mechanisms and Time-Dependent Dielectric Breakdown of Low-k Organosilicates," Doctor of Philosophy Thesis, University of Wisconsin, Madison, 2013.

[30] F. Chen, O. Bravo, D. Harmon, M. Shinosky, and J. Aitken, "Cu/low-k dielectric TDDB reliability issues for advanced CMOS technologies," *Microelectronics Reliability*, Vol. **48**, pp.1375-1383 (2008).

[31] A. B. Isaev and A. V. Smirnov, "Robust Maximum-Likelihood Algorithms for the Plotting of Linear-Regression on Samples with Correlated Observations," *Meas Tech+*, Vol. **31**, pp.827-831 (1988).

[32] F. Chen, O. Bravo, K. Chanda, P. McLaughlin, T. Sullivan, J. Gill, J. Lloyd, R. Kontra, and J. Aitken, "A comprehensive study of low-k SiCOH TDDB phenomena and its reliability lifetime model development," *Int Rel Phy*, Vol., pp.46-53 (2006).

[33] E. Y. Wu and R. P. Vollertsen, "On the Weibull shape factor of intrinsic breakdown of dielectric films and its accurate experimental determination. Part I: theory, methodology, experimental techniques," *IEEE Transactions on Electron Devices*, Vol. **49**, pp.2131-2140 (2002).

[34] E. Y. Wu, J. Sune, and W. Lai, "On the Weibull shape factor of intrinsic breakdown of dielectric films and its accurate experimental determination. Part II: experimental results and the effects of stress conditions," *IEEE Transactions on Electron Devices*, Vol. **49**, pp.2141-2150 (2002).

[35] L. Zhao, M. Pantouvaki, K. Croes, Z. Tőkei, Y. Barbarin, C. J. Wilson, M. R. Baklanov, G. P. Beyer, and C. Claeys, "Role of copper in time dependent dielectric breakdown of porous organo-silicate glass low-k materials," *Applied Physics Letters*, Vol. **99**, 222110 (2011).

[36] K. Yeap, M. Gall, Z. Liao, C. Sander, U. Muehle, P. Justison, O. Aubel, M. Hauschildt, A. Beyer, N. Vogel, and E. Zschech, "In situ study on low-k

interconnect time-dependent-dielectric-breakdown mechanisms," *Journal of Applied Physics*, Vol. **115**, 124101 (2014).

[37] J. L. Plawsky, W. N. Gill, and R. S. Achanta, "Impact of interfacial solubility on penetration of metals into dielectrics and the mechanism of failure," *Journal of Materials Science: Materials in Electronics*, Vol. **23**, pp.48-55 (2012).

Chapter VI

Band Alignment for Cu/Low-k Dielectric Interconnects

In Chapter V, the VUV-induced enhancement of Cu migration into a-SiOC:H and consequent deterioration of the TDDB lifetime of a-SiOC:H/Cu film stacks were presented. Electrical degradation of a-SiOC:H/Cu structures was observed for photon energies greater than or equal to 9.0 eV with a photon fluence of 4.0×10^{15} photons/cm^2. For metal interconnects, the extent of band alignments between the metal conductor and the insulating dielectrics are essential for determining electrical leakage[1], breakdown[2], and other reliability issues, such as power consumption and device lifetime.[3],[4] In this regard, this Chapter concentrates on the investigation of the electronic band alignment for Cu/a-SiOC:H interconnects. A band diagram, illustrating the barrier potential at the Cu/a-SiOC:H interface, alignments of the valence and conduction bands in the dielectric and the

energy levels of processing-induced defect states, will be presented in this Chapter. Such diagrams are essential to explain and predict some of the reliability issues for Cu/a-SiOC:H interconnects. These include the VUV-induced leakage currents in a-SiOC:H presented in Chapter IV and the degradation of TDDB as presented in Chapter V.

The organization of this Chapter is as follows. First, as one of the most common interfaces present in damascene Cu/low-k interconnect structures, the Schottky barrier potential that appears at the Cu and low-k dielectric interfaces is measured using VUV photoemission spectroscopy.[5] Next, the bandgap energy and valence-band edge are measured with core-level XPS [6] and valence-band XPS [7] respectively. Since trap and defect states in low-k dielectrics are also important to Cu/low-k interconnect reliability [8], we additionally present defect-induced bandgap narrowing in low-k a-SiOC:H dielectrics. Finally, the combined band alignment and defect energy-level diagrams are presented, allowing insight into the many reported electrical leakage mechanisms and reliability issues in low-k dielectrics and integrated low-k/Cu interconnects. It should be noted that the low-k dielectrics under study are state-of-the-art dense low-k a-SiOC:H, which have the potential to be used as a low-k capping-layer dielectric.

6.1 Measurement of the Schottky Barrier Potential at the Cu/a-SiOC:H Interface

Electron transport across the low-k interlayer dielectric and Cu wire interface causes line-to-line leakage current across Cu/low-k interconnects, as shown in **Figure 6-1**,

while electron transport across the low-k capping-layer dielectric and Cu line interface causes layer-to-layer leakage.[9] To fully explore the possible leakage paths for low-k/Cu interconnects, one must therefore examine the barrier potential between Cu and dielectrics used both as interlayer (*i.e.* low-k a-SiOC:H) and Cu capping-layer dielectrics (either a-SiC_xN_y or dense low-k a-SiOC:H).

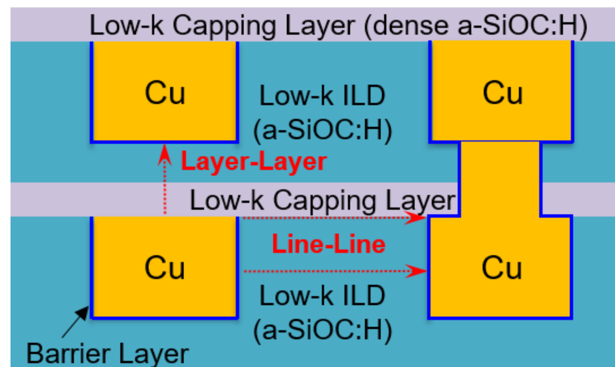

Figure 6-1 Schematic illustrating line-to-line and layer-to-layer current in a damascene Cu/low-k interconnect structure.

In low-k a-SiOC:H dielectrics, VUV irradiation can cause photoinjection, photoconduction, and photoemission of electrons depending on the incident photon energy and the dielectric thickness, as previously discussed in Chapter II.[10],[11] VUV photons can excite electrons into the conduction band from the valence band or from defect states in the bandgap of the dielectric. The electrons can travel in the dielectric and/or the substrate depending on their energy.[12],[13] When the irradiated photon energy is greater than the band-gap energy plus the electron affinity, electrons from the valence band and/or defect states in the bandgap of the dielectric, can be photoemitted and escape from the film surface [10], leaving positive charge trapped within the dielectric.[14] When the photon

energy is less than the bandgap (E_g) of the dielectric, some of the photons can penetrate into the substrate, because the absorption of photons by the dielectric material (energy < E_g) is now weak. Based on the results from Woodworth *et al.*, [15] when the photon energy is less than the bandgap of the dielectric, the photon absorption coefficient is less than 10^3 cm^{-1}, while when energy is larger than the bandgap, the absorption coefficient is approximately 10^6 cm^{-1}, which is at least 10^3 times larger than that in the case of photon energy < E_g.

Photo-generated electrons from the substrate that have energies higher than the substrate/capping-layer dielectric barrier potential, can be injected into the bulk dielectric layer and deplete the previously mentioned accumulated positive charge produced by photoemission.[11],[13] The lowest photon energy having a charge-depleting effect should correspond to the potential barrier present at the substrate/capping-layer dielectric interface.[16] The measured substrate/photoemission current usually changes with photon energy because of the excitation of electrons from specific electronic states to energies into or above the conduction band of the dielectric layer. It should be noted that the photoemission current cannot go to zero under VUV irradiation because there will always be a steady-state photoemission current from the electrons that are photoinjected from the underneath substrate.[17]

Figure 6-2 shows the VUV photoemission spectrum measured from a 100-nm a-SiOC:H thin film deposited on an H_2 plasma pre-cleaned Cu layer previously exposed to 12-eV photons with several different photon fluences. The 100-nm a-SiOC:H thin films are identical to those used in Chapter V. Monochromatic VUV exposures were made using

the synchrotron radiation apparatus as described in Chapter II. The incident VUV photon beam, with a cross-section of 3.0×0.1 cm^2, was oriented normally to the surface of the sample at a pressure of 10^{-8} Torr. The 12-eV photons are used to photoemit the electrons from the valence band and/or defect states in the material, resulting a build-up of positive charge in the material. The energy of 12 eV was chosen because this dielectric has a high photoemission efficiency at this energy.[5]

Before and after the 12-eV photon irradiation, VUV photoemission spectroscopy, was measured. Under this condition, the photon-beam exit slit from the monochromator was set to 0.3 mm so that the photon flux was approximately two orders of magnitude smaller than that for the 12 eV photon exposures and thus did not significantly affect the measured characteristics of the dielectric layer. The photoemission current was monitored with a Keithley 486 picoammeter and was normalized by dividing the measured photoemission current by the incident VUV photon flux measured with the calibrated photodiode.

As shown in **Figure 6-2**, when the photon fluence increases, the magnitude of the VUV-photoemission spectrum/current decreases and reaches a steady state when the irradiation photon dose is or greater than 5.0×10^{15} photons/cm^2. This is because, with increasing VUV photon fluence, most of the electrons have been photoemitted and thus there are few electrons left within the defect states available to be photoemitted when the VUV photoemission spectroscopy scan was made after VUV irradiation. When the photoemission current was approximately equal to the photoinjection current, a steady state was reached. This indicates that no more trapped charges will be generated in the dielectric, and the photoemitted electron flux will equal the flux of photoinjected electrons.[11],[13]

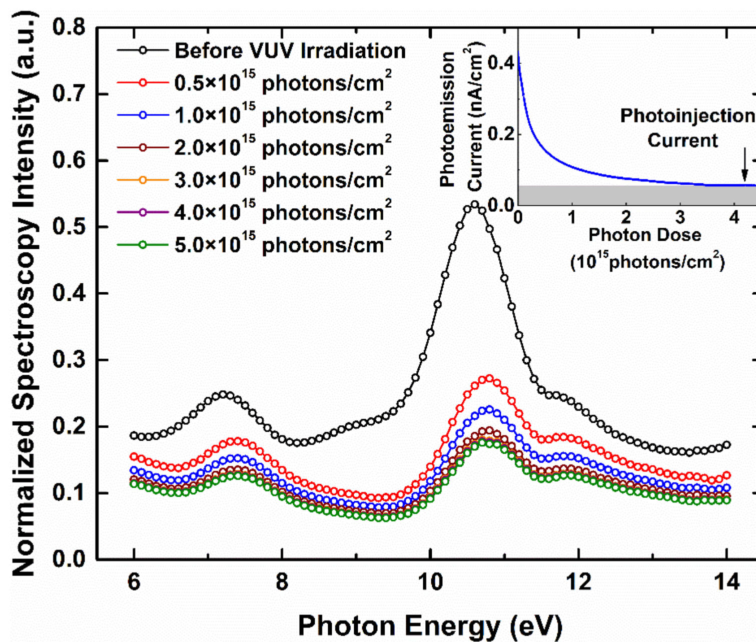

Figure 6-2 VUV photoemission spectrum measured from a 100-nm a-SiOC:H thin film exposed to 12 eV photons with various fluences. The inset figure is the measured photoemission current during 12-eV irradiation as a function of photon fluence.

To investigate the photon-energy range that can repopulate the accumulated charge after 12 eV irradiation, each sample was re-exposed to VUV photons with specific energies from 4.5 to 8.1 eV in steps of 0.2 eV, since a photon energy of 8.1 eV is approximately the bandgap energy of the low-k dielectric.[7] The VUV re-exposure was performed at the same location on the sample with the same fluence of 5.0×10^{15} photons/cm^2, as was the case for the 12 eV exposure.

VUV photoemission spectroscopy was again measured after the second exposure. Figure 6-3 (a)-(d) shows the measured VUV photoemission spectroscopy of 12 eV

irradiated samples with steady-state photoinjection followed with 4.5, 4.7, 4.9 and 8.1 eV re-exposure with same photon dose.

As illustrated by these results, for sufficient 12-eV irradiation to reach steady-state photoinjection current, the experimentally measured VUV photoemission spectrum of the re-exposed samples with energies of 4.7 eV, or lower than that. To confirm this, data for 4.5, 4.6, and 4.7 eV were obtained for comparison (4.5 eV is the lowest energy we can have when using the Seya-beam in the Synchrotron). The data for 4.5 and 4.7 eV are plotted in Figure 6-3, part (a) and (b). They overlap and are nearly identical to that of the 12 eV irradiation to steady-state photoinjection current samples.

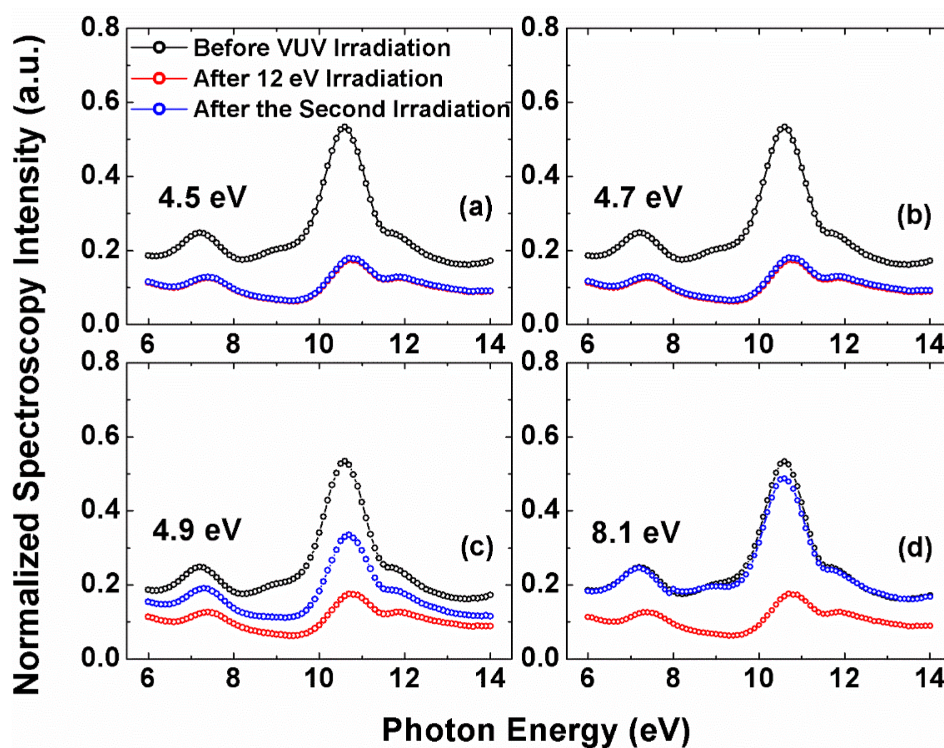

Figure 6-3 VUV photoemission spectroscopy measured on a-SiOC:H/Cu film stack before and after 12 eV exposure followed by re-irradiation with photon energies of 4.5, 4.7, 4.9 and 8.1 eV with a photon fluence of 5×10^{15} photons/cm^2.

Doubling the photon fluence does not show any difference in the results. We have measured the VUV-photoemission spectroscopy as a function of photon fluence, as shown in **Figure 6-2**. Once the photon fluence is higher than 4×10^{15} photons/cm^2, the intensity of the VUV photoemission spectrum will not change. That is, the measured VUV photoemission spectra overlap each other. However, for 4.9 eV and higher energy re-irradiated samples, there is an increase of the intensity of the photoemission spectrum. When 8.1 eV photons were used for re-exposure, the highest increase in the photoemisson spectrum was observed. In fact, the spectrum of the 8.1 eV re-exposed sample is nearly identical to the VUV photoemission spectroscopy of an unexposed sample. Higher photon energies were not used because photons with energies higher than the bandgap energy of the dielectric will induce trapped-charge accumulation inside the dielectric, rather than charge depletion. The bandgap energy of the dielectric is approximately 8.1 eV. Thus, only photons with energy equal to or less than this value will deplete the charge within a sample.

These effects can be further explained by noting that electrons photoemitted from the Cu substrate produced by photons with energies less than 4.7 eV do not have sufficient energy to overcome the a-SiOC:H/Cu interface barrier to be injected into a-SiOC:H dielectric. It should be noted that these photons, which have energy less than 4.7 eV, can make the dielectric a photoconductor. That is, any electrons (or holes) produced do not have enough energy to be emitted or injected, but they can deplete the existing charges inside the dielectric.

It should also be noted that at room temperature, the thermal energy of the electrons is 0.026 eV, which is very small compared to the photon energy, and also is in the range of measurement error of this method (± 0.1 eV). However, we have already taken the effect

of electron thermal energy into account at the beginning. In the inset in **Figure 6-2**, which shows the photoinjection current as a function of photon fluence, the photoinjection current approaches to a constant value that is not zero. When the photon fluence is larger than 4×10^{15} photons/cm^2. This current comes from electron tunneling through the dielectric/Cu interface, due to the thermal energy. This will not make a different in the final result, because we are comparing the relative change of the VUV spectroscopy intensity, not its absolute value.

Thus, these electrons are not able to repopulate the traps in the dielectric that were depopulated during the 12-eV exposure. Therefore, the VUV photoemission spectrum is identical to that for the 12-eV irradiated samples, which had reached steady state of photoinjection versus photoemission. However, if the photoemitted electrons from the Cu substrate have energies larger than the potential barrier present at the a-SiOC:H/Cu interface, they can be injected into the dielectric and then refill defect states within the dielectric. This provides sources of electrons that can be photoemitted during the VUV spectroscopic scan, making the intensity of the VUV photoemission spectrum increase, like that shown in **Figure 6-3 (c)** and **(d)**. Therefore, the potential of the Schottky barrier at a-SiOC:H (k=3.2)/Cu interfaces should be between 4.7 eV and 4.9 eV, that is 4.8 ± 0.1 eV.

To examine the validity and accuracy of the above values, the method of Grant and Waldrop [18], which relies on core-level and valence-band XPS measurements, was also utilized to measure the Schottky barrier potential present at the same a-SiOC:H (k=3.2)/Cu interface.[19] By referencing the XPS Si 2p core level of the low-k a-SiOC:H to its valence-band maximum and then measuring how the position of the core levels changes with the

addition of Cu, the Schottky barrier present at the a-SiOC:H (k=3.2)/Cu interface was determined to be within a range of 4.7 eV to 5.2 eV, which is consistent with the result obtained using VUV photoemission spectroscopy. The method shown here can also be used for the case when a-SiC_xN_y is used as capping layer.

6.2 Defect-induced Bandgap Narrowing of Low-k Organosilicates

Numerous electrically based measurements have shown a direct correlation between trap/defect state concentrations [20], leakage currents [21], breakdown voltages [22], and TDDB failures of low-k materials.[23] In most cases, these electrical degradations in dielectrics are dependent on the depths and locations of trap states within the bandgap. To address this issue, a number of empirical measurements have recently been devoted to determine the effective bandgap energy and to delineate the location of extended gap/defect states of the low-k dielectrics.[6],[24],[25]

For the same reason, the bandgap energy and valence-band edge (VBE) of the low-k dielectrics were measured using core-level XPS [6] and valence-band XPS [7] respectively, which have been described in detail in Chapter III. The results are shown in **Table 6-1**. The a-SiOC:H materials examined involved various compositions and dielectric constants that are representative of low-k capping layer or low-k ILDs currently utilized or being considered for future applications. After the films were produced, XPS measurements were made on the surface using a micro-focused monochromatic Al Kα X-

ray source with a centroid photon energy of 1486.6 eV. During the measurement, a flood gun, which can generate a combination of low energy electrons (0.1 to 5.0 eV) and low energy Ar^+ ions, was used to neutralize any charge that built up at the surface during the photoelectron emission process, or static charge from handling prior to analysis. Spectra were collected with a collection angle of 60° relative to the surface normal. The pass energy of the analyzer was set as 21 eV with a corresponding absolute resolution less than 0.5 eV.

Table 6-1 Summary of properties for a-SiOC:H films under study. (PECVD = Plasma-enhanced chemical-vapor deposition, OS = Organosilane, AOS = Alkoxysilane, VBE = Valence-band edge)

Film #	Deposition and precursor	k-Value (± 0.1)	Density (g/cm^3)	Porosity (%)	Bandgap (± 0.3 eV)	VBE
1	PECVD-OS	3.2	1.5±0.1	0	8.1	4.1
2	PECVD-AOS	2.5	1.3±0.1	25	8.0	4.0
3	PECVD-AOS	2.2	1.1±0.1	34	8.3	4.2

The depth of information of the XPS measurement, (also known as "sampling depth", referring to the maximum depth from which an X-ray excited electron can escape. This depth depends on the material properties and the inelastic mean free path (IMFP) of electrons that varies with the element analyzed. For Al Kα x-ray activated O 1s photoelectrons, the corresponding inelastic mean free path (λ_p) in SiO_2-like oxides is approximately 30-40 Å. [7] According to the Beer-Lambert law,[26] 95% of the signal obtained with XPS originates from within three attenuation lengths (usually referred to as "λ_p", defined as the distance in which the signal intensity attenuates to 1/e of its original value, e.g., $I = I_0 * \exp(-d/\lambda_p)$, of the surface ($3\ \lambda_p$), which gives a sampling depth of 45-60

Å for a 60° electron exit angle. Each sample was measured 10 times. For each measurement, the spectrum was scanned 50 times. Then, the bandgap energy of the sample was determined by extrapolating a linear fit to the leading edge of the electron energy-loss spectrum and by locating the onset of inelastic energy loss relative to the core-level peak.[6],[25] The accuracy of this method can be ~ 0.5 eV or less if the electron density in the valence band near surface is laterally homogeneous and the largest source of error is due to uncertainty in the process of linear extrapolation.[6]

For a-SiOC:H films (k=3.2), the bandgap energy was calculated to be 8.1 ± 0.3 eV by subtracting the binding energy of O 1s peak at 532.6 eV from that of the onset of inelastic losses.[23] This value agrees with the reported bandgap energy of 8.2 eV for a-SiCOH film (k=3.2) measured by reflection electron energy loss spectroscopy (REELS).[25] The valence-band edge (VBE) of the a-SiOC:H film (k=3.2) film was determined to be approximately 4.1 eV. Measured results on other samples are also listed in **Table 6-1**.These values provide a necessary energy reference for calculating the depths of trap states with the band gap, the interfacial energy-barrier heights, [5] as well as the possible conduction mechanisms in the materials.[27]

In most cases, the creation of defects and vacancies within the bandgap will cause a reduction of the bandgap by formation of additional electronic states either above the valence band or below the conduction band that overlap with one or the other of these two bands.[7] For example, a conduction-band tail may arise and extend below the conduction-band edge (CBE) in the presence of vacancies and defect centers near the conduction-band edge.[28] However, the valence-band edge (VBE) may also lift upwards

due to an excess of electronic states originating nearby from disorder and imperfection of the materials.[29] Both of these can lead a decrease in the bandgap.

A number of electron-spin-resonance (ESR) measurements of porous/non-porous low-k dielectrics have shown that defects within these materials are silicon dangling bonds [30], neutral or positively charged oxygen vacancies and carbon residues,[31],[32] all of which can generate states near the mid bandgap.[33] In addition, the Si-Si dangling bonds can generate a bonding state in the lower band gap and an antibonding state near the CBM. Oxygen vacancies possess a "shallow" bound state 1-2 eV below the CBM, while non-bridging oxygen can introduce states just above the VBE.[33] The effects of these additional electronic states on the experimental bandgap of low-k dielectrics are largely unknown. Considering this, the defect-induced bandgap-narrowing phenomenon in low-k dielectrics must be investigated.

6.2.1 Bandgap Narrowing in Low-k a-SiOC:H Thin Films

To investigate defect-induced bandgap narrowing and also to measure the energy levels of the defects within the bandgap, a 4.0 keV Ar^+ ion-sputtering beam, from the monatomic argon-ion source in the XPS analyzing chamber as described earlier in Chapter III, was utilized *in-situ* to create defects on the sample surface, following the work of King *et al*.[25] The ion-beam current was 15 $\mu A/cm^2$ and the sputtering time was 30 seconds. XPS measurements with the same procedure were then made on the ion-sputtered spot of the sample to get a comparison to the bandgap energy before and after ion sputtering.

Figure 6-4 shows the inelastic-loss spectra near the O 1s core-level peak collected from a 100-nm thick a-SiCOH film (k=3.2) before and after *in-situ* Ar^+ ion sputtering, which had been calibrated with reference to the C 1s peak at 284.8 eV. The low-k a-SiOC:H thin film used here is identical to the samples used for the Schottky-barrier measurements, as described earlier in this Chapter. It is deposited on a H_2 plasma pre-cleaned Cu/Ta(TaN)/Si film stack using PECVD. To see how the sputtering-induced charging affects the uniformity of the potential distribution across the oxide surface, the full width at half maximum (FWHM) of the O 1s peak was examined on each sample. No comparable broadening of the O 1s emission line was observed after ion sputtering.

By tracking the intersection of the leading edge (*solid straight line*) and the background level (*dashed horizontal line*) of the electron energy inelastic loss spectra, as shown in **Figure 6-4**, the onset of inelastic losses was found to occur at 539.4 eV for the ion-sputtered samples. To quantify the uncertainties of the linear extrapolation, least-square-fitting regression lines with 95% confidence were constructed (*dotted straight lines*) to the inelastic-loss peak leading edge, by which the errors of the linear extrapolation were estimated to be ± 0.3 eV with 95% confidence. According to these analyses, the bandgap of the sample after ion sputtering was calculated to be 6.8 ± 0.3 eV, which is lower by 1.3 eV compared with the bandgap of pristine a-SiOC:H film (8.1 ± 0.3 eV).

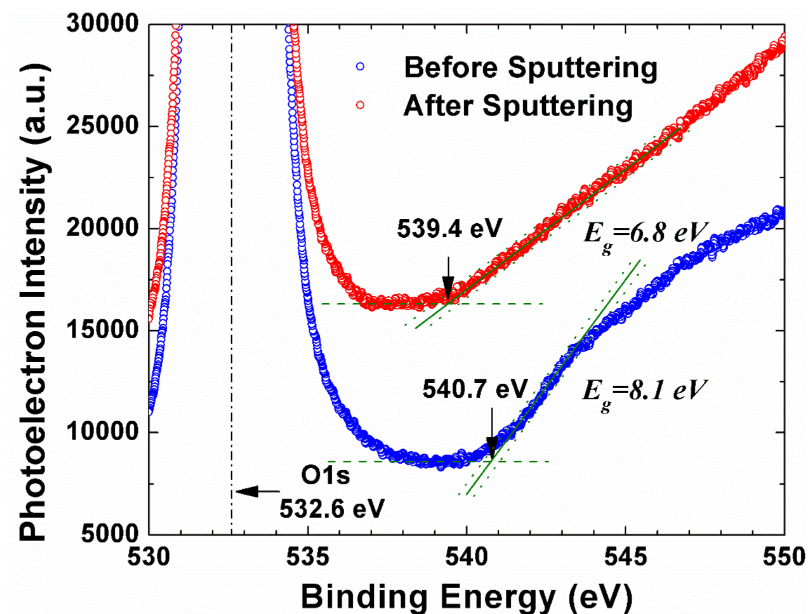

Figure 6-4 Bandgap measurements of a-SiOC:H (k=3.2) film before and after ion sputtering by linearly fitting to electron energy loss spectra with 95% confidence interval.[23]

Table 6-2 shows the bandgap measurements of all of the samples. As can be seen, after 4 keV ion-beam sputtering, the bandgap energies of the a-SiCOH films were all reduced. The reduction ranges from 1.3 eV to 2.2 eV depending on the film composition. These reductions cannot be ascribed to measurement errors alone and suggest that additional states must have been created within the bandgap. Thus, valence-band XPS measurements were made to examine the valence-band density of states of each sample.

Table 6-2 Summary of bandgap energy and valence-band edge position before and after ion sputtering for the a-SiOC:H films under study. To remain consistent, the valence-band edge (VBE) positions here are all referred to the Fermi level (“ 0 ” eV.), and a negative value of VBE means it is below the Fermi level.

Film #	Before ion sputtering		After ion sputtering	
	Bandgap (±0.3 eV)	VBE (±0.1 eV)	Bandgap (±0.3 eV)	VBE (±0.1 eV)
1	8.1	− 4.1	6.8	− 2.8
2	8.0	− 4.0	6.2	− 2.2
3	8.3	− 4.2	6.1	− 2.0

6.2.2 Uplifting of the Valence Band Edge in a-SiOC:H

By linearly fitting to the rising edge of the spectra, as shown in **Figure 6-5**, the valence-band edge (VBE) of the a-SiCOH film can be determined. For pristine samples, this value is approximately 4.1 eV. However, for the ion-sputtered sample, additional electronic states were detected above the VBE, resulting in a shift of the VBE towards to 2.8 eV, as illustrated by the arrow in **Figure 6-5**. Since no broadening was observed for the FWHM of the O 1s peak after sputtering, the apparent “tail” of the electron-energy distribution must originate from the sputtering-induced defects, rather than any local fluctuations of electrostatic potential across the film surface caused by sputtering.

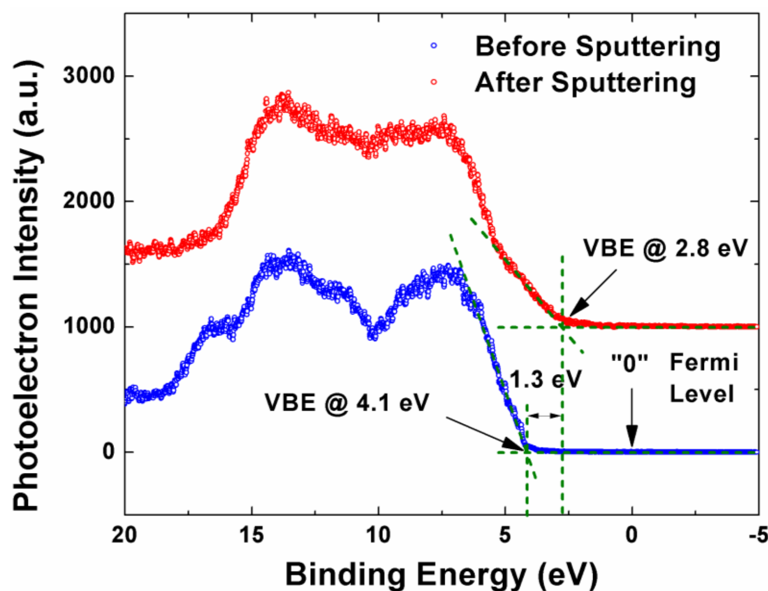

Figure 6-5 Valence band XPS spectra of a-SiOC:H (k=3.2) film before and after ion sputtering, where the “0” binding energy corresponds to the Fermi level.

A schematic representation of the density of states is depicted in **Figure 6-6**, to show the changes of the band structures after ion sputtering. One can see that in the ion-sputtered sample, a valence-band tail appears and extends above the VBE. The up shifting of the VBE was calculated to be 1.3 eV by subtracting the VBE value of the ion-sputtered sample from that of the pristine sample, which is in excellent agreement with the bandgap reduction, suggesting that the bandgap narrowing after sputtering must be attributed to the uplifting of the valence band.

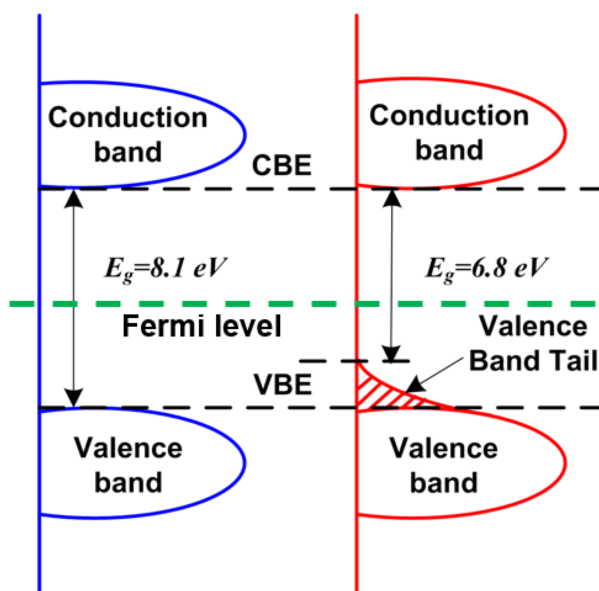

Figure 6-6 Schematic representation of the density of states of a-SiOC:H (k=3.2) film before and after ion sputtering.

6.2.3 Defects in a-SiOC:H as Measured with Electron-Spin Resonance

To obtain insight into the nature of defects generated during ion sputtering, ESR measurements were carried out on a-SiCOH thin films before and after ion sputtering. **Figure 6-7** shows the conventional first-derivative absorption spectra of the ESR signal from the samples with the applied magnetic field **B** oriented parallel to the sample surface. The values of the *g*-factor and the linewidth of the defect center were determined by fitting the spectra into a Lorentzian derivative line shape using least squares. Control spectra were measured on the pristine sample and were observed to exhibit signals only originating from silicon dangling bonds (Si_{db}), as shown by the blue curve in **Figure 6-7**. These silicon dangling-bond defects, similar to the bulk E' centers, are usually from the

underlying a-SiCOH/Si interface with no measurable density of paramagnetic defects pertaining to the low-k dielectric layer itself.[34],[35]

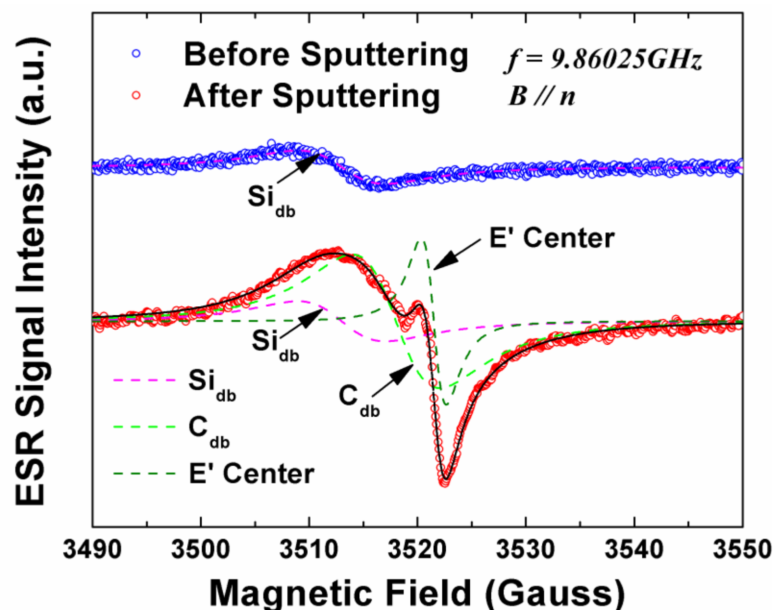

Figure 6-7 ESR signals measured on a-SiOC:H (k=3.2) film before and after ion sputtering.

However, after ion sputtering, the intensity of the Si_{db} defect (silicon dangling bonds) increased. However, splitting off H from a Si-H bond in the oxide also results in the same signal.[36] In this case (non-porous PECVD oxide) this may happen simply because of electron-hole pair generation and hole trapping on the Si-H bonds.[37] In addition, peaks with much higher intensities emerged in the ESR spectra. The predominant peak is characterized with a *g*-factor of 2.0006 and an approximate linewidth of 2 G. These have been attributed to surface oxygen vacancies (SOV), in which the defects are usually positively charged in the paramagnetic state.[31] The other signal at g = 2.0026 with an approximate linewidth of 7 G is identified as that from carbon-dangling-bonds (C_{db}) back-bonded to C or Si atoms.[32]

These observations are consistent with ESR results reported by previous authors [31,32]. That is, ion sputtering-induced defects in low-k dielectrics generate oxygen/silicon vacancies analogous to the oxygen-deficient/silicon dangling bond centers in bulk SiO_2 and carbon-dangling-bonds in carbon silicide clusters. The SOV (surface oxygen vacancy) has been previously identified as a defect that creates sub-gap surface defects at approximately 5.0 and 7.2 eV, [25] which are located in the upper half of the bandgap and close to the CBE. The silicon dangling bonds possess a highly localized state near the mid-bandgap, lying near the isolated sp^3 or p hybrid energies[33] that will not contribute to states below the Fermi level.

As a result, the states near VBE must originate from sputtering-induced carbon-related defects, which have been shown to give rise to "deep" energy levels near the VBE of the SiO_2-like skeleton in a low-k dielectric material.[38],[39] Usually, the excessive carbon-dangling bonds at the interfaces result in electron states distributed in the lower half of the bandgap.[38] In addition, electronic states associated with a-C:H layers can be found in the same energy range.[39] It should be pointed out that the ESR experiments used here only detect the fraction of the sputtering-induced defects with an unpaired electron while diamagnetic entities escape ESR detection. Nevertheless, the Si carbide and oxicarbide clusters generally represent the most stable bonding configurations and may be produced by ion sputtering in densities sufficient to cause the formation of the VB "tail" as seen here. These results have been published in *Applied Physics Letters*.[7].

6.3 Band Diagram for Cu/Low-k a-SiOC:H Interconnects

In this section, we summarize and combine the above results, including the barrier potential at Cu/a-SiOC:H interface, the bandgap energy and the defect-induced valence-band uplifting of a-SiOC:H, with our work on VUV-induced Cu migration to present a series of schematic flat-band diagrams illustrating the various possible paths for electron transport in Cu/low-k damascene structures and to explain the VUV-induced electrical degradations of Cu/low-k interconnects. The low-k dielectric used here is dense low-k a-SiOC:H (1.5 g/cm3, k = 3.2), which has been considered as a potential low-k capping-layer dielectric.

To illustrate the barrier for electron injection from a Cu wire into a low-k a-SiOC:H capping layer dielectric, as well as the interlayer dielectrics in Cu/low-k damascene structures, we present in **Figure 6-8** the band alignments at Cu/low-k a-SiOC:H interfaces. If the density of surface trap/defect states in low-k dielectrics is small (in the level of 5.0 ~ 6.0×10^{11} cm^{-2} or less)[40], the degradation influence from the surface states are negligible and the barrier potential at the Cu/a-SiOC:H interface is 4.8 ± 0.1 eV, as shown in **Figure 6-8 (a)**. An added voltage of 4.8 ± 0.1 V or greater is necessary to overcome the barrier thus created for electron injection from the Cu wire into a-SiOC:H.

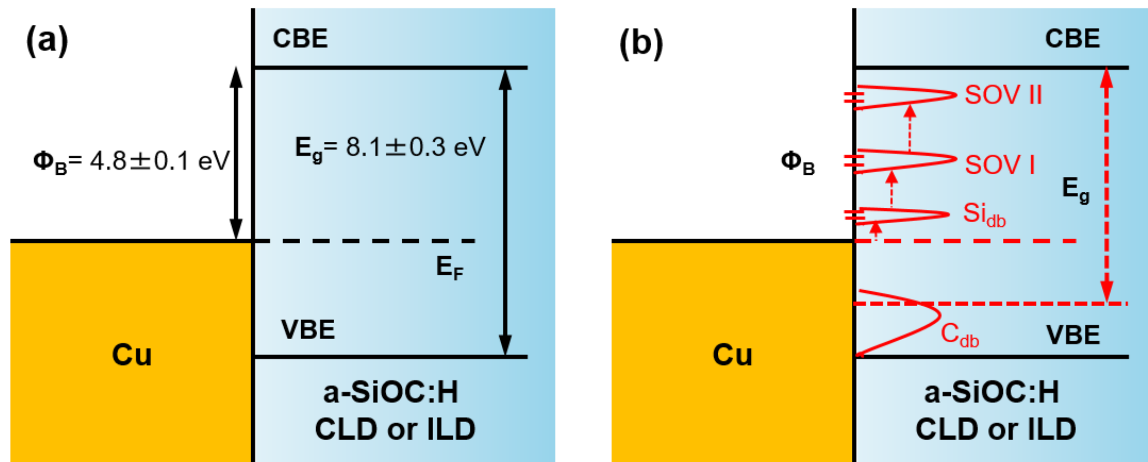

Figure 6-8 Schematic band diagram of a Cu/low-k damascene structure: (a) band diagram w/o surface states; (b) defect-induced changes to the band diagram.

However, as shown and discussed previously, VUV photons and/or ions from a processing plasma can cause generation of defect states within a low-k a-SiOC:H dielectric. Considering both Schottky and Poole-Frenkel type leakage mechanisms, barrier heights of 0.7 - 1.5 eV have been reported [41],[42] for leakage currents predominantly along the interface between the low-k a-SiOC:H and the Cu layer. The overall lower barrier heights for the SiOC:H/Cu interface is likely due to differences in Fermi level pinning at the metal/dielectric interface that is typically attributed to interface gap states.[19] That can be explained by the defect-induced variation of the band diagram of Cu/low-k a-SiOC:H interfaces, as depicted in **Figure 6-8 (b)**. The defect-induced variation of the band diagram will be discussed in detail in the following paragraph, based on the energy levels of defect states within the samples.

Table 6-3 summarizes the energy levels of these trap/defect states within the bandgap of low-k a-SiCO:H dielectrics. In a real damascene Cu/a-SiOC:H structure, electrons can be injected from Cu into the trap/defect states within the bandgap of a-SiOC:H, rather than into the conduction bands directly, as shown by the arrows in **Figure 6-8(b)**. This can happen in both non low-k capping layer dielectrics (*e.g.* a-SiC_xN_y:H) and low-k capping layer dielectrics (e.g. dense a-SiOC:H).[8] In these scenarios, the barrier potential at the a-SiOC:H/Cu interface is substantially reduced by the presence of the interface states.

Table 6-3 Summary of the energy levels of trap/defect states within the bandgap of a-SiOC:H. The energy level location is referred to the valence-band edge (VBE).

Defects	Comments	Energy Level
C_{db}	Carbon related defects	0.7 - 3.0 eV [38]
Si_{db}	Silicon dangling bonds	4.3 - 4.9 eV [33]
SOV I	Surface oxygen vacancy type I	5.0 -6.0 eV [19],[33]
SOV II	Surface oxygen vacancy type II	7.2 -7.6 eV [19],[33]

For example, based on the band diagram as shown in Figure 6-8 and the energy levels of the defect states listed in **Table 6-3**, we can calculate that the barrier height for electrons to transport to Si_{db} states (4.3 eV above the valence-band edge) from the Cu layer [3.3 eV above the valence-band edge. The value was obtained by subtracting the barrier height at the Cu/dielectric interface (4.8 eV) from the dielectric bandgap energy (8.1 eV)] is approximately 1.0 eV. This value is in excellent agreement with the value reported by Mutch *et al*. [8]

On the other hand, we have shown that VUV irradiation (9.0 eV or greater) can cause the oxidation of Cu wire by forming a CuO/Cu_2O thin layer between the Cu and a-SiOC:H interface [43], which will further exacerbate Cu migration into the low-k a-SiOC:H and deteriorate the TDDB lifetime of the dielectric. With this in mind, we next update the band diagram by introducing a thin layer of Cu/Cu_2O between the Cu and the low-k a-SiOC:H dielectric (which can be considered as a potential capping layer), as shown in **Figure 6-9**. For low-k a-SiOC:H, it does not matter if it is used as an interlayer dielectric or a capping-layer dielectric, because the energy levels of the defect states within the bandgap are always same [8], as shown in Figure 6-9. This is true for both porous and nonporous samples.

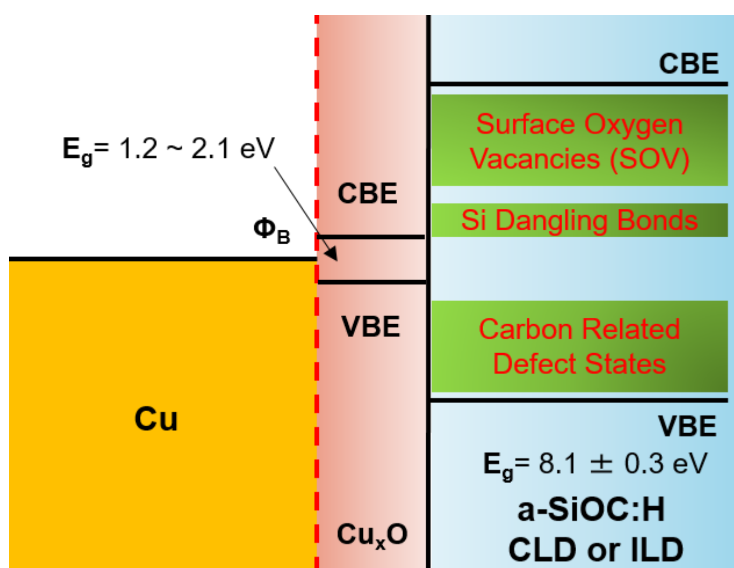

Figure 6-9 Schematic band diagram with VUV-induced Cu oxides layer and relevant defect/trap positions illustrating the barrier for electron injection from Cu wire into the low-k a-SiOC:H CLD or ILD.

The reported bandgap energy for Cu oxides is in the range of 1.2 to 2.1 eV.[44],[45] As can be seen, the conduction-band minimum of the CuO layer generally aligns with the Si dangling-bond defects in the low-k a-SiOC:H dielectric. Electrons are likely to cross this interface and to move inside the dielectric due to the presence of defect states below the CBE. These conduction pathways enable Poole-Frenkel conduction.[46]

Additionally, with Cu ions drifting into the low-k dielectric under the influence of an externally applied or self-generated electric field, another low-energy conduction pathway for electrons to transport across the low-k dielectric is provided. Over an extended time frame, the drift process causes accumulation of Cu^{+} ion clusters inside the low-k dielectric (in the bulk), resulting in a bending of the conduction band in the bulk of the dielectric, as shown in Figure 1-13 in Chapter I.[47] Electrons are then able to tunnel through the interfacial energy barrier by Fowler-Nordheim tunneling.[48]

In many cases, the barrier heights deduced from the analysis of the current-voltage (IV) characteristics are a small fraction of the interfacial barrier heights measured by XPS or VUV photoemission spectroscopy as shown previously in this work. This discrepancy can now be understood by considering both the dominant trap/defect states likely to be present and their energy levels within the low-k dielectric. It is anticipated that the band diagrams established in this work, as shown in **Figure 6-8** and **Figure 6-9**, will provide an improved platform for developing a complete physics-based determination of low-k/Cu interconnect reliability. This will require *ab initio* simulations to establish a model for how porosity and the spatial distribution of pores affect the band structure of the dielectric. While it should be noted that there are many more complex phenomena limiting the reliability performance of low-k/Cu interconnects that are not covered in these band

diagrams, such as moisture [49],[50] and hydrogen -related failures [51], consideration of such effects is beyond the scope of this work, but represents an important area for future research in low-k/Cu interconnect reliability

6.4 Summary

In this Chapter, the band alignment for Cu/low-k interconnects has been investigated to determine the mechanisms of VUV-induced electrical degradation, such as increased leakage currents, shorter TDDB lifetimes (both intrinsic and extrinsic) and other reliability issues, such as power consumption and device lifetime in integrated low-k/Cu interconnect structures. This is summarized as follows.

1. VUV photoemission spectroscopy has been used to investigate the existence and magnitude of the Schottky barrier present at the interface of low-k a-SiOC:H/Cu interfaces. The Schottky-barrier potential at the a-SiOC:H (k=3.2)/Cu interface was found to be 4.8 ± 0.1 eV. This proposed method of VUV exposure/re-exposure followed by VUV photoemission spectroscopy has been shown to be valid and efficient by comparing the measured results with previously reported values.
2. The bandgap energy and valence band edge (VBE) of low-k a-SiOC:H dielectrics were measured using core-level XPS and valence-band XPS, respectively. Defect-induced bandgap narrowing was observed in various ion-sputtered a-SiOC:H thin films and the reduction of the bandgap energy varies with the properties (such as the density, carbon concentration) of the dielectrics used as the capping layer materials.

3. Valence-band XPS measurements show additional electron states are created near the VBE by ion sputtering and the bandgap reduction originates from the tail extended above the valence band edge (VBE). Electron-Spin-Resonance measurements reveal that the carbon-related defects inside of the low-k dielectrics are responsible for measured bandgap narrowing.

4. Defect-enriched band diagrams are illustrated to show the barrier for electron injection from a Cu wire into the low-k a-SiOC:H capping layer dielectric or interlayer dielectrics in Cu/low-k damascene structures. A thin layer of Cu/Cu_2O is also introduced into the band diagram, in order to include the effect of VUV-induced Cu oxidation at the interface of Cu and a-SiOC:H.

5. The mechanisms of previously observed VUV irradiation-induced increased leakage currents, and degradation of TDDB (both intrinsic and extrinsic) in integrated low-k/Cu interconnect structures were discussed based on the proposed band diagram. This suggests that the defects within the bandgap of the low-k dielectric films are largely responsible for electrical degradation and likely limit the dielectric reliability, because the barrier potential at the a-SiOC:H/Cu interface for charge transport is substantially reduced by the presence of the interface states. For example, as presented earlier in Section 6.3, with the presence of Si_{db} (silicon dangling bond) defect states in the dielectric, the barrier height for electrons to transport into the dielectric layer from the Cu layer reduced to 1.0 eV approximately. This reduced barrier height enables electrons to transport through the insulating dielectric layer readily and cause increased leakage currents and early dielectric breakdown.

6.5 References

[1] J. G. Simmons, "Poole-Frenkel Effect and Schottky Effect in Metal-Insulator-Metal Systems," *Physical Review*, Vol. **155**, pp.657-660 (1967).

[2] M. Lenzlinger and E. H. Snow, "Fowler-Nordheim Tunneling into Thermally Grown SiO2," *Journal of Applied Physics*, Vol. **40**, pp.278-283 (1969).

[3] A. Kerber and E. A. Cartier, "Reliability Challenges for CMOS Technology Qualifications With Hafnium Oxide/Titanium Nitride Gate Stacks," *IEEE Transactions on Device and Materials Reliability*, Vol. **9**, pp.147-162 (2009).

[4] J. R. Yeargan and H. L. Taylor, "The Poole-Frenkel Effect with Compensation Present," *Journal of Applied Physics*, Vol. **39**, pp.5600-5604 (1968).

[5] X. Guo, D. Pei, H. Zheng, S. W. King, Y.-H. Lin, H.-S. Fung, C.-C. Chen, Y. Nishi, and J. L. Shohet, "Measurements of Schottky barrier at the low-k SiOC:H/Cu interface using vacuum ultraviolet photoemission spectroscopy," *Applied Physics Letters*, Vol. **107**, 232905 (2015).

[6] M. T. Nichols, W. Li, D. Pei, G. A. Antonelli, Q. Lin, S. Banna, Y. Nishi, and J. L. Shohet, "Measurement of bandgap energies in low-k organosilicates," *Journal of Applied Physics*, Vol. **115**, 094105 (2014).

[7] X. Guo, H. Zheng, S. W. King, V. V. Afanas'ev, M. R. Baklanov, J. F. de Marneffe, Y. Nishi, and J. L. Shohet, "Defect-induced bandgap narrowing in low-k dielectrics," *Applied Physics Letters*, Vol. **107**, 082903 (2015).

[8] M. J. Mutch, T. Pomorski, B. C. Bittel, C. J. Cochrane, P. M. Lenahan, X. Liu, R. J. Nemanich, J. Brockman, M. French, M. Kuhn, B. French, and S. W. King, "Band

diagram for low-k/Cu interconnects: The starting point for understanding back-end-of-line (BEOL) electrical reliability," *Microelectronics Reliability*, Vol., (2016).

[9] K. Yeap, M. Gall, Z. Liao, C. Sander, U. Muehle, P. Justison, O. Aubel, M. Hauschildt, A. Beyer, N. Vogel, and E. Zschech, "In situ study on low-k interconnect time-dependent-dielectric-breakdown mechanisms," *Journal of Applied Physics*, Vol. **115**, 124101 (2014).

[10] J. L. Lauer, J. L. Shohet, C. Cismaru, R. W. Hansen, M. Y. Foo, and T. J. Henn, "Photoemission and conduction currents in vacuum ultraviolet irradiated aluminum oxide," *Journal of Applied Physics*, Vol. **91**, pp.1242-1246 (2002).

[11] J. L. Lauer, H. Sinha, M. T. Nichols, G. A. Antonelli, Y. Nishi, and J. L. Shohet, "Charge Trapping within UV and Vacuum UV Irradiated Low-k Porous Organosilicate Dielectrics," *Journal of the Electrochemical Society*, Vol. **157**, pp.G177-G182 (2010).

[12] R. J. Powell, "Hole photocurrents and electron tunnel injection induced by trapped holes in SiO2 films," *Journal of Applied Physics*, Vol. **46**, pp.4557-4563 (1975).

[13] H. Sinha, M. T. Nichols, A. Sehgal, M. Tomoyasu, N. M. Russell, G. A. Antonelli, Y. Nishi, and J. L. Shohet, "Effect of vacuum ultraviolet and ultraviolet irradiation on mobile charges in the bandgap of low-k-porous organosilicate dielectrics," *Journal of Vacuum Science & Technology A*, Vol. **29**, 010601 (2011).

[14] H. Sinha, J. L. Lauer, M. T. Nichols, G. A. Antonelli, Y. Nishi, and J. L. Shohet, "Effect of vacuum ultraviolet and ultraviolet Irradiation on capacitance-voltage characteristics of low-k-porous organosilicate dielectrics," *Applied Physics Letters*, Vol. **96**, 052901 (2010).

[15] J. R. Woodworth, M. E. Riley, V. A. Arnatucci, T. W. Hamilton, and B. P. Aragon, "Absolute intensities of the vacuum ultraviolet spectra in oxide etch plasma processing discharges," *J Vac Sci Technol A*, Vol. **19**, pp.45-55 (2001).

[16] H. Zheng, S. W. King, V. Ryan, Y. Nishi, and J. L. Shohet, "Bandgap measurements of low-k porous organosilicate dielectrics using vacuum ultraviolet irradiation," *Applied Physics Letters*, Vol. **104**, 062904 (2014).

[17] G. S. Upadhyaya, J. B. Kruger, and J. L. Shohet, "Vacuum-ultraviolet-induced charge depletion in plasma-charged patterned-dielectric wafers," *Journal of Applied Physics*, Vol. **105**, 053308 (2009).

[18] J. R. Waldrop, R. W. Grant, Y. C. Wang, and R. F. Davis, "Metal Schottky barrier contacts to alpha 6H-SiC," *Journal of Applied Physics*, Vol. **72**, pp.4757-4760 (1992).

[19] S. W. King, M. French, M. Jaehnig, M. Kuhn, and B. French, "X-ray photoelectron spectroscopy investigation of the Schottky barrier at low-k a-SiO(C):H/Cu interfaces," *Applied Physics Letters*, Vol. **99**, 202903 (2011).

[20] B. C. Bittel, P. M. Lenahan, and S. W. King, "Ultraviolet radiation effects on paramagnetic defects in low-k dielectrics for ultralarge scale integrated circuit interconnects," *Applied Physics Letters*, Vol. **97**, 063506 (2010).

[21] J. M. Atkin, E. Cartier, T. M. Shaw, R. B. Laibowitz, and T. F. Heinz, "Charge trapping at the low-k dielectric-silicon interface probed by the conductance and capacitance techniques," *Applied Physics Letters*, Vol. **93**, 122902 (2008).

[22] M. T. Nichols, H. Sinha, C. A. Wiltbank, G. A. Antonelli, Y. Nishi, and J. L. Shohet, "Time-dependent dielectric breakdown of plasma-exposed porous organosilicate glass," *Applied Physics Letters*, Vol. **100**, 112905 (2012).

[23] M. T. Nichols, "The Effects of Processing Induced Damage on Electrical Conduction Mechanisms and Time-Dependent Dielectric Breakdown of Low-k Organosilicates," Doctor of Philosophy Thesis, University of Wisconsin, Madison, 2013.

[24] A. Grill, "Plasma enhanced chemical vapor deposited SiCOH dielectrics: from low-k to extreme low-k interconnect materials," *Journal of Applied Physics*, Vol. **93**, pp.1785-1790 (2003).

[25] S. W. King, B. French, and E. Mays, "Detection of defect states in low-k dielectrics using reflection electron energy loss spectroscopy," *Journal of Applied Physics*, Vol. **113**, 044109 (2013).

[26] R. Cammack, T. Atwood, P. Campbell, H. Parish, A. Smith, F. Vella, and J. Stirling, "Oxford Dictionary of Biochemistry and Molecular Biology", 2nd ed. (Oxford University Press, Oxford, 2008).

[27] T. K. Wong, "Time Dependent Dielectric Breakdown in Copper Low-k Interconnects: Mechanisms and Reliability Models," *Materials*, Vol. **5**, pp.1602-1625 (2012).

[28] B. Rafferty, S. J. Pennycook, and L. M. Brown, "Zero loss peak deconvolution for bandgap EEL spectra," *Journal of Electron Microscopy*, Vol. **49**, pp.517-524 (2000).

[29] F. Devynck, A. Alkauskas, P. Broqvist, and A. Pasquarello, "Charge transition levels of carbon-, oxygen-, and hydrogen-related defects at the SiC/SiO2 interface through hybrid functionals," *Physical Review B*, Vol. **84**, 235320 (2011).

[30] H. Ren, S. L. Cheng, Y. Nishi, and J. L. Shohet, "Effects of vacuum ultraviolet and ultraviolet irradiation on ultrathin hafnium-oxide dielectric layers on (100)Si as measured with electron-spin resonance," *Applied Physics Letters*, Vol. **96**, 192904 (2010).

[31] T. A. Pomorski, B. C. Bittel, P. M. Lenahan, E. Mays, C. Ege, J. Bielefeld, D. Michalak, and S. W. King, "Defect structure and electronic properties of SiOC:H films used for back end of line dielectrics," *Journal of Applied Physics*, Vol. **115**, 234508 (2014).

[32] V. V. Afanas'ev, A. P. D. Nguyen, M. Houssa, A. Stesmans, Z. Tokei, and M. R. Baklanov, "High-resolution electron spin resonance analysis of ion bombardment induced defects in advanced low-k insulators (k=2.0-2.5)," *Applied Physics Letters*, Vol. **102**, 172908 (2013).

[33] E. P. O'Reilly and J. Robertson, "Theory of defects in vitreous silicon dioxide," *Physical Review B*, Vol. **27**, pp.3780-3795 (1983).

[34] J. H. Thomas and S. Hofmann, "Ion bombardment induced changes in silicon dioxide surface composition studied by X-ray photoelectron spectroscopy," *Journal of Vacuum Science & Technology A*, Vol. **3**, pp.1921-1928 (1985).

[35] E. Paparazzo, "X-ray photo-emission and Auger spectra of damage induced by Ar+ ion etching at SiO2 surfaces," *Journal of Physics D: Applied Physics*, Vol. **20**, 1091 (1987).

[36] V. V. Afanas'ev and A. Stesmans, "Charge state of paramagnetic E´ centre in thermal SiO2 layers on silicon," *Journal of Physics: Condensed Matter*, Vol. **12**, 2285 (2000).

[37] S. Shamuilia, V. V. Afanas'ev, Pi. Somers, A. Stesmans, Y.-L. Li, Z. Tokei, G. Groeseneken, and K. Maex, "Internal photoemission of electrons at interfaces of metals with low-k insulators," *Applied physics letters*, Vol. **89**, 2909 (2006).

[38] V. V. Afanas’ev, M. Bassler, G. Pensl, M. J. Schulz, and E. Stein von Kamienski, "Band offsets and electronic structure of SiC/SiO2 interfaces," *Journal of Applied Physics*, Vol. **79**, pp.3108-3114 (1996).

[39] V. V. Afanas’ev, A. Stesmans, and M. O. Andersson, "Electron states and microstructure of thin a-C:H layers," *Physical Review B*, Vol. **54**, pp.10820-10826 (1996).

[40] A.-K. M. Zakzouk, "The Dependence of the SiO2 Defect Density on Both the Applied Electric Field and the Oxide Thickness," *Journal of The Electrochemical Society*, Vol. **126**, pp.1771-1779 (1979).

[41] M. Vilmay, D. Roy, F. Volpi, and J. M. Chaix, "Characterization of low-k SiOCH dielectric for 45 nm technology and link between the dominant leakage path and the breakdown localization," *Microelectronic Engineering*, Vol. **85**, pp.2075-2078 (2008).

[42] Robin C. J. Wang, K. S. Chang-Liao, T. K. Wang, M. N. Chang, C. S. Wang, C. H. Lin, C. C. Lee, C. C. Chiu, and K. H. Wu, "Electrical conduction and TDDB reliability characterization for low-k SiCO dielectric in Cu interconnects," *Thin Solid Films*, Vol. **517**, pp.1230-1233 (2008).

[43] X. Guo, S. W. King, H. Zheng, P. Xue, Y. Nishi, and J. L. Shohet, "Effects of vacuum-ultraviolet irradiation on copper penetration into low-k dielectrics under bias-temperature stress," *Applied Physics Letters*, Vol. **106**, 012904 (2015).

[44] F. K. Mugwang'a, P. K. Karimi, W. K. Njoroge, O. Omayio, and S. M. Waita, "Optical characterization of Copper Oxide thin films prepared by reactive dc magnetron sputtering for solar cell applications," *International Journal of Thin Films Science and Technology*, Vol. **2**, pp.15-24 (2012).

[45] Shinho Cho, "Optical and electrical properties of CuO thin films deposited at several growth temperatures by reactive RF magnetron sputtering," *Metals and Materials International*, Vol. **19**, pp.1327-1331 (2013).

[46] H. Miyazaki, D. Kodama, and N. Suzumura, "Phenomenological classification of stress-induced leakage current and time-dependent dielectric breakdown mechanism," *Journal of Applied Physics*, Vol. **106**, 104103 (2009).

[47] S. Lee, A. S. Oates, and K. M. Chang, "Fundamental understanding of porous low-k dielectric breakdown," 2009 IEEE International Reliability Physics Symposium, Montreal, QC, 2009.

[48] N. Suzumura, S. Yamamoto, D. Kodama, K. Makabe, J. Komori, E. Murakami, S. Maegawa, and K. Kubota, "A new TDDB degradation model based on Cu ion drift in cu interconnect dielectrics," *Int Rel Phy*, Vol., pp.484-489 (2006).

[49] Y. Cheng, W. Chang, and Y. Wang, "Moisture effect on electromigration characteristics for copper dual damascene interconnection," *Journal of Vacuum Science & Technology B*, Vol. **28**, pp.1322-1325 (2010).

[50] C. Kubascha, H. Ruelkeb, U. Mayerb, and J. W. Barthaa, "Leakage Current and Breakthrough Measurements on Moisturized SiCOH," *Ecs J Solid State Sc*, Vol. **4**, pp.N3118-N3121 (2015).

[51] C. Wu, Y. Li, I. Ciofi, Th. Kauerauf, J. Bömmels, I. De Wolf, Zs. Tőkei, and K. Croes, "Towards understanding intrinsic degradation and breakdown mechanisms in SiOCH low-k dielectrics," *Journal of Applied Physics*, Vol. **117**, 064101 (2015).

Chapter VII

Conclusions and Future Directions

The first section of this Chapter provides a summary of the significant results drawn from this work. In the second and final section, suggestions for the future work are given. Alternative solutions to mitigate the VUV-induced damages to Cu/low-k interconnects are also discussed in detail.

7.1 Summary of Results

7.1.1 VUV-induced Mechanical Modifications to a-SiOC:H

VUV photons with energies larger than a specific threshold value was found to be able to cause a significant increase in film hardness along with a small increase in elastic modulus and crack threshold. In the range of 4.5-30 eV (what one can get from the synchrotron), any photons with energies higher than 8.3 eV cause mechanical change. The

energy threshold was identified to be 8.3 eV and is approximately the dissociation energy of the Si-O chemical bond. Thus, VUV irradiation with photon energies above the threshold energy can change the mechanical properties of a-SiOC:H, while VUV photons below this threshold energy are not able to affect the mechanical properties of a-SiOC:H. Two mechanisms have been proposed for these VUV-induced mechanical property changes of a-SiOC:H dielectrics as follows:

(1) VUV photons with energies larger than 8.3 eV can trigger a silica-bond conversion from Si-O-Si cage to Si-O-Si network. Of the two bond states, the latter (cross-linked ladder and linear chain structures) is more energetically stable than the former (polyhedral). Relative amounts of cage type and network type bonds affect the mechanical properties such as hardness and modulus. Higher network-type bonding tends to produce a higher modulus film. Thus the film mechanical properties change because of the increase in the number of energetically stable network structures within the film.

(2) VUV photons with energies larger than 8.3 eV can increase the degree of cross-linking inside of an a-SiOC:H thin film from VUV-assisted reactions in which new bridging Si-O-Si structures are generated from non-bridging structures. The possible reactions are as follows:

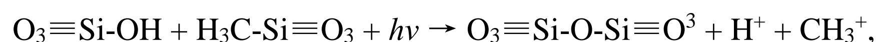

$$O_3\equiv Si\text{-}OH + H_3C\text{-}Si\equiv O_3 + h\nu \rightarrow O_3\equiv Si\text{-}O\text{-}Si\equiv O^3 + H^+ + CH_3^+,$$

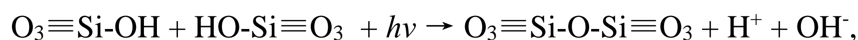

$$O_3\equiv Si\text{-}OH + HO\text{-}Si\equiv O_3 + h\nu \rightarrow O_3\equiv Si\text{-}O\text{-}Si\equiv O_3 + H^+ + OH^-,$$

Both of these photon-assisted reactions, as illustrated above, increase the number of bridging $\equiv$Si-O-Si$\equiv$ bonds by depleting either the non-bridging $\equiv$Si-OH bonds or $\equiv$

$Si-CH_3$ bonds. As a result, the degree of crosslinking in the films is increased and results in mechanical property improvements at the same time. From this point of view, this mechanism may have the potential to be used as a curing process for low-k organosilicates.[1]

7.1.2 VUV-induced Moisture Uptake to a-SiOC:H

VUV-induced moisture uptake in a-SiOC:H has been investigated by examining the water contact angle and H_2O-related FTIR spectra of a-SiOC:H before and after VUV irradiation with several photon energies. Results show that VUV irradiation can change the a-SiOC:H surface from hydrophobic to hydrophilic, permitting moisture uptake from the ambient. This phenomenon has been observed in all VUV-exposed samples (6.1, 10.2 and 11.8 eV) and becomes more significant as the photon energy becomes larger.

This might be the case because VUV irradiation removes the original hydrophobic groups ($-CH_3$) and creates free-radical sites ($-SiO_2\bullet$) within the material. The $-SiO_2\bullet$ groups are not as hydrophobic as the $-CH_3$ groups, causing a-SiOC:H to be hydrophilic. These hydrophilic groups enable significant amounts of water to be absorbed from humid air following diffusion into the a-SiOC:H bulk through interconnected pores. The increase of the H_2O-related FTIR peaks either can be either from physisorbed, or chemisorbed water[2], or from hydroxyl terminals (-OH) [3]. It is not clear which one is dominant. Methods to address this issue are proposed as future work and will be discussed in detail later in this Chapter.

7.1.3 VUV-induced Exacerbation of Cu Migration into a-SiOC:H

A low-k a-SiOC:H sample from Intel (k = 3.2, density of 1.5 g/cm^3), because of its relevance as both an interlayer dielectric and as a candidate Cu capping-layer material, was used to study the effects of VUV irradiation on Cu migration into a-SiOC:H under various bias-temperature stress conditions. This dense low-k a-SiOC:H thin film has the potential to replace traditional capping-layer dielectrics (*e.g.* a-SiC$_x$N$_y$:H with a k value of 4.5 ~ 7.0) and thus to serve as novel capping layer.

It was found that nine-eV VUV irradiation can exacerbate Cu transport into low-k a-SiOC:H under bias-temperature stress (BTS). Under a temperature of 120°C and an electric field of 2.5 MV/cm, the Cu migration rate was calculated to be 2.5×10^{-16} cm^2/s in pristine a-SiOC:H dielectric and 5.4×10^{-16} cm^2/s in 9.0 eV-exposed samples. The calculated high Cu migration rate after VUV irradiation comes from the ion drift in the presence of an electric field, which was not observed in the pristine sample. This is because in the pristine sample, Cu exists in the form of atoms rather than ions. While in 9.0-eV exposed samples Cu oxidization was observed. This effect is correlated with the number of hydroxyl free-radical sites (OH^-) generated by VUV photon irradiation in the dielectric, as evidenced by XPS and FTIR measurements.

Further analysis showed that Cu migration rate under BTS in VUV exposed a-SiOC:H dielectric depends on the VUV photon energy. A threshold VUV photon energy was found by measuring the Cu migration rate as a function of photon energy, which is related to the Si-O dissociation energy (8.3 eV). Above this value, VUV irradiation can cause oxidation of Cu and create Cu^+ ions at the interface between the Cu layer and the

dielectric layer. In the presence of an electric field, the progress of Cu migration into a-SiOC:H will be exacerbated due to the Cu^+ ion drifts. However, XPS depth profile measurements show that VUV irradiation does not affect diffusion of Cu atoms very much in the presence of an electric field, since the XPS depth profile of Cu migration under BS (in the case only diffusion occurs, without ion drifts) did not show a difference between the pristine and VUV-exposed samples. Thus, Cu migration includes diffusion and drift. From the XPS depth profile measurement, VUV irradiation causes enhanced Cu ion drift, but does not affect Cu diffusion very much.

7.1.4 VUV-induced Deterioration of Extrinsic TDDB of Cu/a-SiOC:H

Extrinsic TDDB of a-SiOC:H, (including the effects of Cu migration into the dielectric), were studied under various conditions (with and without VUV photon irradiation) using on a MIM structure configuration. This was compared with the intrinsic (not including the effects of Cu migration) TDDB characteristics of a-SiOC:H.

XPS measurements on a pristine sample show Cu exists in the form of Cu atoms. Diffusion of Cu atoms into a-SiOC:H will degrade the TDDB lifetime. There was no difference whether the Cu electrode was used as anode or cathode. In this case, diffused Cu atoms accumulate near the region of the Cu electrode and shorten the distance between the anode and the cathode, resulting in an increase of the electric field under the same voltage bias. Because Cu atoms are electrically neutral, they do not drift in the presence of an electric field.

Extrinsic TDDB of a-SiOC:H deteriorates after 9.0-eV VUV irradiation. The most significant degradation of the 63.2% time to failure (TTF) was found when the Cu electrode

was used as the anode in a 9.0 eV VUV-exposed sample. This is believed to be related to the Cu^+ ions created by VUV irradiation, because 9.0 eV is above the previous observed threshold, which is 8.3 eV, for oxidation of Cu and creation of Cu^+ ions within the sample. The drift of Cu^+ ions into a-SiOC:H can cause them to act as charge trap centers, raising the local electric field to an extent where the field exceeds the breakdown strength. It can also lower the metal/dielectric interface Schottky barrier to electron injection/tunneling and thereby promote failure.

7.1.5 Measurements of Schottky Barrier at Cu/a-SiOC:H Interface

VUV photoemission spectroscopy was utilized to determine the potential of the Schottky barrier present at low-k a-SiOC:H/Cu interfaces, to fully explore the possible leakage paths for low-k/Cu interconnects. By examining the photoemission spectra before and after VUV exposure of a low-k a-SiOC:H (k = 3.2) thin film fabricated by plasma-enhanced chemical-vapor deposition on a polished Cu substrate, it was found that photons with energies of 4.9 eV or higher can deplete accumulated charge in a-SiOC:H films, while photons with energies of 4.7 eV or less, did not have this effect. These critical values were identified so as to determine the electrostatic potential of the interface barrier between the a-SiOC:H and the Cu layers. Using this method, the Schottky barrier at the low-k a-SiOC:H (k = 3.2)/Cu interface was determined to be 4.8 ± 0.1 eV.

This proposed method of VUV exposure/re-exposure followed by VUV photoemission spectroscopy has been shown to be useful and efficient by showing consistency with previously reported values. It has the potential to be applied to measure the barrier height of other metal/dielectric interface.

7.1.6 Band Diagram for Cu/low-k Damascene Interconnects

The bandgap energy and valence-band edge (VBE) of the low-k a-SiOC:H dielectrics were measured using core-level XPS and valence-band XPS respectively. Defect-induced bandgap narrowing was observed in various ion-sputtered a-SiOC:H thin films and the reduction of the bandgap energy varies with the film composition. Valence-band XPS measurements show that additional electron states are created near the VBE by ion sputtering. The bandgap reduction originates from an electron tail extended above the valence band maximum. Electron-spin-resonance measurements reveal that carbon-related defects inside of the low-k dielectrics are responsible for the measured bandgap narrowing.

The combined band alignment and defect energy-level diagrams are presented so as to illustrate the barrier for electron injection from a Cu conductor into a low-k a-SiOC:H capping layer dielectric or interlayer dielectric in Cu/low-k damascene structures. Mechanisms for the previously observed VUV irradiation-induced increase in leakage currents and the degradation of TDDB in integrated low-k/Cu interconnect structures were discussed based on a proposed band diagram. The diagram suggests that the defects within the bandgap of the low-k dielectric films are largely responsible for electrical degradation and are likely to limit the dielectric reliability.

A thin layer of CuO/Cu_2O was also introduced into the band diagram, to include the effects of VUV-induced Cu oxidation at the interface of Cu and a-SiOC:H. It showed that the conduction-band edge (CBE) of the CuO layer generally aligns with the Si dangling-bond defects in the low-k a-SiOC:H dielectric. Electrons are likely to cross this interface and to move inside the dielectric due to the presence of defect states below the

CBE. These conduction pathways enable Poole-Frenkel conduction.[4] One would anticipate that electrical leakage would likely increase if such a Cu-oxide layer, induced by VUV-photon irradiation during plasma processing, is present in a Cu/low-k damascene structure.

The dense a-SiOC:H (k=3.2) used in this work is a state-of-the-art low-k dielectric material, due to its relevance as both an interlayer dielectric and candidate Cu capping-layer material. Although this a-SiOC:H was primarily studied in this work, the conclusions here may be applied to other Si-based low-k dielectrics with similar chemical compositions but with different k-values or porosities. As long as the future candidates of low-k dielectrics still contain Si-CH_3 groups and Si-O-Si networks, the conclusions of this work will likely apply. Additionally, it is hoped that the defect-enriched band diagrams established in this work will provide an improved platform for understanding of Cu/ low-k interconnect reliability and become a physics-based platform for investigating hydrogen, moisture, and other reliability failures in greater detail.

7.2 Suggestions for Future Work

Over the course of this work, the role of VUV-induced degradation on the reliability and electronic properties of BEOL Cu/low-k organosilicate interconnects has been investigated. All of the results suggest that during the fabrication process, the VUV photons generated during plasma processing can cause a reliability issue to Cu/low-k interconnects.

As a result, there are still challenges for successful integration of Cu wires with low-k dielectrics. In this section, recommendations for future investigations are proposed.

7.2.1 Temperature Dependence of VUV-induced Damages

In this work, all of the VUV irradiation was performed at room temperature. However, it will be useful to look into the temperature dependence of VUV-induced damage. This is because VUV-induced damage involves chemical reactions and diffusion of radicals (like -CH_3 and -OH radicals) of gas-phase molecules (like CH_4 and H_2O). The rate of chemical reaction and diffusivity of molecules significantly depends on the temperature. It was shown that the same plasma processing at lower temperature resulted in less damage to low-k dielectrics.[5]

Understanding the amount and type of VUV-induced damage as a function of temperature (both above and below room temperature) will help to develop and improve cryogenic plasma-processing methods.

7.2.2 Depth Profile of VUV-induced Damage in a-SiOC:H

This work has shown that VUV irradiation can damage both the surface (measured with XPS) and the bulk (measured with FTIR) of a-SiOC:H thin films. However, the mechanism by which the defects change as a function of depth of the film after irradiation with VUV photons of different energies is not clear. For example, it is not clear that the VUV-induced increase of a-SiOC:H hardness is uniform at the surface and in the bulk. Such non-uniform mechanical changes can cause physical stress accumulated inside of the

materials and cause reliability issues, such as increased leakage current and early breakdown.[6], [7]

XPS depth profiles used in this work are a good way to study the Cu distribution profile in a-SiOC:H but they are not well suited to show any depth-dependent damage from VUV irradiation.[8] This is because the XPS depth profile method utilizes high energy Ar^+ ions to sputter the film. The damage created by high-energy Ar^+ sputtering can exceed most VUV-induced damage.[9],[10]

Time-of-Flight Secondary Ion Mass Spectrometry (TOF-SIMS) [11] could be used to accurately analyze the depth profile of each element of the film. For example, measuring the depth profile of carbon using TOF-SIMS can provide information about VUV-induced carbon depletion at different depths.[12] X-ray reflectivity (XRR) measurements could be used to measure the depth profile of the mass density of the film.[13] If the VUV-induced damage is not vertically homogeneous, it could be measured by examining the chemical changes using TOF-SIMS or examining the density changes using XRR.

7.2.3 Moisture-assisted TDDB of Cu/low-k Interconnects

This work has shown VUV irradiation can change the a-SiOC:H surface from hydrophobic to hydrophilic, causing moisture uptake from the ambient, which will further degrade the dielectrics and is undesirable.[3] More generally, both physical bombardment by energetic ions, and their reaction with radicals during plasma processing can result in an increase in the hydrophilic silanol content in low-k dielectrics, causing the same problem.[3],[14] This is not only true for plasma etching processes but might also be true for PECVD processes. Kubasch et al [15] have shown that if water is in the dielectric film,

the leakage-current density increases of about 6 orders of magnitude from the ionization of water molecules under an applied electric field.

However, further research is needed for a complete understanding of the moisture-assisted TDDB of Cu/low-k damascene interconnects. A temperature-programmable oven equipped in a humidity-controllable chamber can be used to study the roles of physisorbed and chemisorbed moisture in TDDB degradation, by annealing the samples at 190 °C and 400 °C respectively.[16] These heating processes drive off the absorbed water. The transport of ionized-water molecules under different water concentration and electric-field conditions, along with the resulting TDDB performance, need to be characterized. It will also be important to find out whether the absorbed water will react with Cu and further degrade the TDDB performance of Cu/a-SiOC:H damascene structures.[14]

7.2.4 Alternative Methods to Mitigate VUV-induced Damage

In the long run, new solutions to mitigate VUV-induced damage are needed. Based on the results observed in this work, VUV photons with energies higher than the threshold value of 8.3 eV will cause increased leakage currents, exacerbated Cu migration and degraded TDDB lifetimes in Cu/low-k dielectrics. At the same time, VUV photons with energies smaller than this threshold did not show significant damage effects. Therefore, one possible way to mitigate VUV-induced damage to Si-based low-k dielectrics is by developing new plasma etchants that do not generate high-energy photons.

In the latest work of Otell et al [17], they suggest using CF_3I as a replacement for CF_4 gas to decrease the plasma-induced damage on low-k dielectrics during etching. They observed that there is almost no VUV emission below 150 nm (energy > 8.3 eV) in a CF_3I

plasma, as shown in **Figure 7-1**, while the other parameters, such as etch rate, selectivity etc, did not show much difference compared to a CF_4 plasma. Furthermore, a CF_3I plasma is environmentally benign and can be generated using the same equipment as CF_4 plasma, without significant additional cost or safety issues. [18]This is an exciting result for mitigating the damage to a-SiOC:H from VUV photon irradiation.

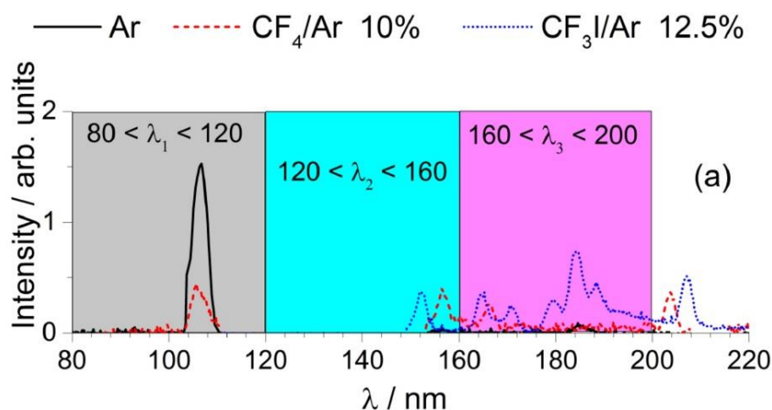

Figure 7-1 VUV emission of CF_3I plasma in the VUV range ($80 \leq \lambda \leq 220$ nm).[17] The different colors represent different ranges of VUV photon wavelengths.

An alternative method to mitigate the process-induced reliability issues of Cu/low-k interconnects is by developing new materials or manufacturing methods for low-k dielectrics to maintain lower k-values without losing mechanical/electrical strength. For example, amorphous hydrogenated boron carbon nitride (a-BCN:H) films [19], exhibiting elastic modulus values between two and ten times greater than those of state-of-the-art Si-based dielectric materials across a wide range of k values, are becoming a recent focus of study.[20],[21]

In particular, optimized a-BCN:H films with moderate k values in the range of 3.0 - 4.0, in addition to having outstanding mechanical properties (modulus of 100-150 GPa,

which are 10 - 20 times larger than that of porous a-SiOC:H), [20],[22] simultaneously exhibit excellent electrical properties (leakage currents of < 10^{-8} A/cm^2 at 2 MV/cm and breakdown voltages > 5 MV/cm).[19] a-BCN:H films in this range also demonstrate resistance to Cu diffusion to at least 600 °C, as well as chemical stability and etch properties suitable for low-k diffusion barrier/etch-stop applications.[19],[23] Cesium ion-implantation has been recently shown to be able to improve the mechanical properties of a-SiOC:H thin film by up to 30% [24], which is either comparable to or better than the effects of UV-curing.[25] This could be a supplement to or a substitution for the currently used UV-curing method for low-k a-SiOC:H films[25]. However, further research is needed to examine the effect of Cs implantation on leakage currents and TDDB lifetimes.

7.3 References

[1] H. Zheng, X. Guo, D. Pei, W. Li, J. Blatz, K. Hsu, D. Benjamin, Y.-H. Lin, H.-S. Fung, C.-C. Chen, Y. Nishi, and J. L. Shohet, "Nonthermal combined ultraviolet and vacuum-ultraviolet curing process for organosilicate dielectrics," *Applied Physics Letters*, Vol. **108**, 242906 (2016).

[2] J. Proost, M. Baklanov, K. Maex, and L. Delaey, "Compensation effect during water desorption from siloxane-based spin-on dielectric thin films," *Journal of Vacuum Science & Technology B*, Vol. **18**, pp.303-306 (2000).

[3] M. R. Baklanov, J. F. de Marneffe, D. Shamiryan, A. M. Urbanowicz, H. L. Shi, T. V. Rakhimova, H. Huang, and P. S. Ho, "Plasma processing of low-k dielectrics," *Journal of Applied Physics*, Vol. **113**, 041101 (2013).

[4] H. Miyazaki, D. Kodama, and N. Suzumura, "Phenomenological classification of stress-induced leakage current and time-dependent dielectric breakdown mechanism," *Journal of Applied Physics*, Vol. **106**, 104103 (2009).

[5] K. Ida, S. Nguyen, S. Lane, N. Klymko, K. Chanda, F. Chen, and et al, "PECVD low-k (similar to 2.7) dielectric SiCOH film development and integration for 65 nm CMOS devices," *Advanced Metallization Conference 2005 (AMC 2005)*, Vol., pp.89-95 (2006).

[6] F. Chen and M. Shinosky, "Soft breakdown characteristics of ultralow-k time-dependent dielectric breakdown for advanced complementary metal-oxide semiconductor technologies," *Journal of Applied Physics*, Vol. **108**, 054107 (2010).

[7] C. Wu, Y. Li, M. R. Baklanov, and K. Croes, "Electrical Reliability Challenges of Advanced Low-k Dielectrics," *Ecs J Solid State Sc*, Vol. **4**, pp.N3065-N3070 (2015).

[8] X. Guo, S. W. King, H. Zheng, P. Xue, Y. Nishi, and J. L. Shohet, "Effects of vacuum-ultraviolet irradiation on copper penetration into low-k dielectrics under bias-temperature stress," *Applied Physics Letters*, Vol. **106**, 012904 (2015).

[9] J. A. Davis, R. Venkatesan, A. Kaloyeros, M. Beylansky, S. J. Souri, K. Banerjee, K. C. Saraswat, A. Rahman, R. Reif, and J. D. Meindl, "Interconnect limits on gigascale integration (GSI) in the 21st century," *Proceedings of the IEEE*, Vol. **89**, pp.305-324 (2001).

[10] S. Natarajan, M. Armstrong, M. Bost, R. Brain, M. Brazier, and et al, "A 32nm Logic Technology Featuring 2nd-Generation High-k plus Metal-Gate Transistors,

Enhanced Channel Strain and 0.171 μm2 SRAM Cell Size in a 291 MB Array," *Int El Devices Meet*, Vol., pp.941-943 (2008).

[11] B. Patrick and L. Weng, in *Microbeam and Nanobeam Analysis*, edited by Daniele Benoit, Jean-Francois Bresse, Luc Van't dack et al. (Springer Vienna, Vienna, 1996), pp. 167-182.

[12] K. Lionti, W. Volksen, T. Magbitang, M. Darnon, and G. Dubois, "Toward Successful Integration of Porous Low-k Materials: Strategies Addressing Plasma Damage," *Ecs J Solid State Sc*, Vol. **4**, pp.N3071-N3083 (2015).

[13] A. Grill, "Plasma enhanced chemical vapor deposited SiCOH dielectrics: from low-k to extreme low-k interconnect materials," *Journal of Applied Physics*, Vol. **93**, pp.1785-1790 (2003).

[14] Y. Cheng, K. Leon, J. Huang, W. Chang, Y. Chang, and J. Leu, "Effect of moisture on electrical properties and reliability of low dielectric constant materials," *Microelectronic Engineering*, Vol. **114**, pp.12-16 (2014).

[15] C. Kubascha, H. Ruelkeb, U. Mayerb, and J. W. Barthaa, "Leakage Current and Breakthrough Measurements on Moisturized SiCOH," *Ecs J Solid State Sc*, Vol. **4**, pp.N3118-N3121 (2015).

[16] X. Guo, J. E. Jakes, M. T. Nichols, S. Banna, Y. Nishi, and J. L. Shohet, "The effect of water uptake on the mechanical properties of low-k organosilicate glass," *Journal of Applied Physics*, Vol. **114**, 084103 (2013).

[17] Z. el Otell, V. Šamara, A. Zotovich, T. Hansen, J. F. de Marneffe, and M. R. Baklanov, "Vacuum ultra-violet emission of CF4 and CF3I containing plasmas and

their effect on low-k materials," *Journal of Physics D: Applied Physics*, Vol. **48**, 395202 (2015).

[18] S. Samukawa, Y. Ichihashi, H. Ohtake, E. Soda, and S. Saito, "Environmentally harmonized CF(3)I plasma for low-damage and highly selective low-k etching," *Journal of Applied Physics*, Vol. **103**, (2008).

[19] B. J. Nordell, T. D. Nguyen, C. L. Keck, S. Dhungana, A. N. Caruso, W. A. Lanford, J. T. Gaskins, P. E. Hopkins, D. R. Merrill, D. C. Johnson, L. L. Ross, P. Henry, S. W. King, and M. M. Paquette, "Conquering the Low-k Death Curve: Insulating Boron Carbide Dielectrics with Superior Mechanical Properties," *Advanced Electronic Materials*, Vol. **2**, 1600073 (2016).

[20] B. J. Nordell, C. L. Keck, T. D. Nguyen, A. N. Caruso, S. S. Purohit, W. A. Lanford, D. Dutta, D. Gidley, P. Henry, S. W. King, and M. M. Paquette, "Tuning the properties of a complex disordered material: Full factorial investigation of PECVD-grown amorphous hydrogenated boron carbide," *Materials Chemistry and Physics*, Vol. **173**, pp.268-284 (2016).

[21] M. T. Alam, M. S. Bresnehan, J. A. Robinson, and M. A. Haque, "Thermal conductivity of ultra-thin chemical vapor deposited hexagonal boron nitride films," *Applied Physics Letters*, Vol. **104**, 013113 (2014).

[22] B. J. Nordell, S. Karki, T. D. Nguyen, P. Rulis, A. N. Caruso, S. S. Purohit, H. Li, S. W. King, D. Dutta, D. Gidley, W. A. Lanford, and M. M. Paquette, "The influence of hydrogen on the chemical, mechanical, optical/electronic, and electrical transport properties of amorphous hydrogenated boron carbide," *Journal of Applied Physics*, Vol. **118**, 035703 (2015).

[23] G. Rampelberg, K. Devloo-Casier, D. Deduytsche, M. Schaekers, N. Blasco, and C. Detavernier, "Low temperature plasma-enhanced atomic layer deposition of thin vanadium nitride layers for copper diffusion barriers," *Applied Physics Letters*, Vol. **102**, 111910 (2013).

[24] Y. Kayaba, K. Kohmura, H. Tanaka, Y. Seino, T. Odaira, F. Nishiyama, K. Kinoshita, S. Chikaki, and T. Kikkawa, "Electrical reliabilities of highly cross-linked porous silica film with cesium doping," *Journal of the Electrochemical Society*, Vol. **155**, pp.G258-G264 (2008).

[25] W. Li, D. Pei, X. Guo, M. K. Cheng, S. Lee, Q. Lin, S. W. King, and J. L. Shohet, "Effects of cesium ion-implantation on mechanical and electrical properties of organosilicate low-k films," *Applied Physics Letters*, Vol. **108**, 202901 (2016).